Al-Si-N Transparent Hard Nanostructured Coatings

Inauguraldissertation

zur
Erlangung der Würde eines Doktors der Philosophie
vorgelegt der
Philosophisch-Naturwissenschaftlichen Fakultät
der Universität Basel

von

Aude Pélisson
aus Nantua (Frankreich)

Dübendorf, 2009

UNI
BASEL

Genehmigt von der Philosophisch-Naturwissenschaftlichen Fakultät auf Antrag von:

Prof. Dr. Hans Josef Hug
Prof. Dr. Peter Oelhafen
Dr. Jörg Patscheider
Prof. Jochen M. Schneider, Ph.D.

Basel, den 28/04/2009

Prof. Dr. Eberhard Parlow, Dekan

Druck: Empa Druckerei

The important thing in science is not so much to obtain new facts as to discover new ways of thinking about them.

Sir William Bragg (1862 – 1942)

The scientist is not a person who gives the right answers, he is one who asks the right questions.

Claude Lévi-Strauss (1908 –)

Preface

The work presented in this doctoral thesis has been carried out 2005–2009 at the laboratory for Nanoscale Materials Science of Empa, the Swiss Federal Laboratories for Materials Testing and Research, in Dübendorf (CH) and to some extent (nanoindentation testing) at Empa, Thun (CH).

Financial support for the first two years of this project was provided by the Alcan Technology Fonds, Project no. 0410.

Abstract

This thesis analyses the properties of Al-Si-N thin films. Based on the expected immiscibility of aluminum nitride (AlN) and silicon nitride (Si_3N_4), the hardness and the optical transparency of each single phase, transparent nanostructured films with enhanced hardness are expected to form.

Al-Si-N thin films were prepared by closed field unbalanced magnetron sputtering from pure Al and Si targets in an Ar/N_2 reactive atmosphere. The films were deposited at 200°C and 500°C onto silicon, cemented carbide, glass and UV-grade fused silica, in order to investigate their chemical, morphological, structural, mechanical, optical and thermal properties. The chemical composition was varied from pure AlN to Al-Si-N with a Si concentration of 23 at.%, as determined by X-ray photoelectron spectroscopy. The deposition conditions were set to provide a sufficient amount of nitrogen resulting in fully nitrided layers, i.e. transparent and containing about 50 at.% of nitrogen. Despite an excellent base pressure of the deposition chamber ($< 10^{-6}$ Pa), an oxygen concentration of 0.5–2.0 at.% was measured in the films.

The structural and morphological properties of the films were studied by X-ray diffraction (XRD), scanning electron microscopy and transmission electron microscopy (TEM). Up to 15–20 at.% of Si, the films are crystalline with the hexagonal – wurtzite – structure of AlN and a strong (002) texture. Pure AlN films show a strong columnar morphology that progressively diminishes upon incorporation of silicon in the films. In parallel, the mean crystallite size within the columns decreases from 60 nm in pure AlN to about 30 nm at 6 at.% of Si and 5 nm at 12 at.% of Si. Altogether, it is shown that the investigated ternary material system consists in three composition regimes with different sets of properties that are determined by the silicon content and independent from the deposition temperature: for Si contents below 6 at.%, the Si atoms substitute Al atoms in the AlN wurtzite lattice, as revealed by a linear decrease of the *c* lattice parameter in XRD data. Exceeding the solubility limit of 6 at.%, the thin films consist of $Al_{0.44}Si_{0.06}N_{0.5}$ nanocrystallites surrounded by a thin SiN_y grain boundary (GB) layer: a nanocomposite structure is formed. In the silicon concentration range from 6 to about 12 at.% of Si, the SiN_y layer thickness is constant and equals to 0.25 nm ($\sim$ 1 monolayer), while the crystallite size decreases inversely proportional to the Si content. Above 12 at.% of Si, the growth mode changes and the SiN_y layer thickness increases with the Si content. The films become progressively X-ray amorphous with chemical and mechanical properties approaching those of pure silicon nitride.

The hardness and biaxial residual stress of the films were studied by nanoindentation and mechanical profilometry, respectively. While hardness is about 20–25 GPa in pure AlN and $\mathrm{SiN_y}$, it reaches 32 GPa in Al-Si-N thin films at 8–12 at.% of Si, concentration at which a negligible residual compressive stress (< 0.5 GPa) is measured. This hardness enhancement over a broad composition range is explained by the interplay of several hardening mechanisms: on the one hand, the formation of an Al-Si-N solid solution and the grain refinement cause a reduction of dislocation activity within the crystalline phase; on the other hand, as the two-phase nanocomposite structure is formed, the presence of $\mathrm{SiN_y}$ at the GBs hinders deformation by GB sliding. The optical properties of the films are moreover only little influenced by variations of the film composition: a refractive index in the range 2.00–2.12 at 633 nm wavelength, corresponding to 80 % light transmission, is measured. The structural, mechanical and optical properties of the films are stable upon annealing for 2h at 1000°C in argon.

Al(-Si-)N/$\mathrm{SiN_y}$ multilayer coatings were deposited as a model system to study interfacial properties which are difficult to access in 3D nanocomposite structures. XRD and high-resolution TEM reveal that up to 0.7–1.0 nm ($\sim$ 2.5–3.5 monolayers) of crystalline silicon nitride can be epitaxially stabilized on an AlN (001) surface. This finding reinforces the assumption of an ordering of the $\mathrm{SiN_y}$ GB layer and the formation of coherent interfaces in Al-Si-N nanocomposite coatings. It provides an explanation for the moderate hardness enhancement obtained in Al-Si-N coatings that probably results of a gradual structural transition at the interfaces. Moreover finite solubility in the Al-Si-N system is associated to a moderate thermodynamic driving force for phase separation. This probably calls for a composition gradient at the interfaces, all the more as a non-equilibrium deposition process is used. Interfaces in the Al-Si-N system are therefore expected to be penetrable obstacles e.g for dislocations upon plastic deformation. If incorporated at the grain boundaries, oxygen impurities may also lower the interface cohesion energy and facilitate GB sliding.

The present work shows that optically transparent coatings can be produced of Al-Si-N with a hardness exceeding 30 GPa at low deposition temperatures. The investigations presented in this thesis provide a thorough understanding of the material and of the evolution of its properties with the silicon content in the films.

Zusammenfassung

Diese Promotionsarbeit untersucht die Eigenschaften von dünnen Al-Si-N Schichten. Aufgrund der erwarteten Unmischbarkeit von Aluminium Nitrid (AlN) und Silizium Nitrid (Si_3N_4) sowie der Härte und optischen Transparenz jeder einzelnen dieser zwei Phasen, erwartet man die Bildung harter, transparenter und nanostrukturierter Schichten.

Solche Al-Si-N Schichten wurden mittels closed field unbalanced magnetron sputtering abgeschieden. Reine Al und Si Targets wurden in einer reaktiven Ar/N_2 Atmosphäre zerstäubt. Die Filme wurden bei 200°C und 500°C auf Silizium, Wolfram Karbid, Glass und UV Qualität Siliziumoxyd abgeschieden, um ihre chemischen, morphologischen, strukturellen, mechanischen, optischen und thermischen Eigenschaften zu untersuchen. Die chemische Zusammensetzung der Filme wurde von reinem AlN zu Al-Si-N mit einem Si Gehalt von 23 at.% (anhand von Röntgen Photoelektronen Spektroskopie bestimmt) variiert. Die Abscheidebedingungen wurden so gewählt, dass genügend Stickstoff vorhanden war, um völlig nitridierte Schichten zu erhalten, das heißt Schichten, welche mindestens 50 at.% Stickstoff enthielten und deshalb transparent sind. Trotz eines ausgezeichneten Hintergrunddrucks in der Abscheidekammer ($< 10^{-6}$ Pa), wurde in den Schichten eine Sauerstoffkonzentration von 0.5–2.0 at.% gemessen.

Struktur und Morphologie der Schichten wurden anhand von Röntgendiffraktion, Raster- und Tranmissionselektronenmikroskopie studiert. Bis zu einer Si Konzentration von 15–20 at.%, bleiben die Filme kristallin, wobei die einzig sichtbare Phase, die des Wurtzit-AlN mit einer stark ausgeprägten (002) Textur ist. Das reine AlN zeigt eine starke säulenförmige Morphologie, welche mit zunehmender Inkorporation von Si in den Schichten nach und nach verschwindet. Parallel dazu, nimmt die mittlere Kristallitgröße von 60 nm in reinem AlN und 30 nm bei 6 at.% Si zu 5 nm bei 12 at.% Si ab. Eine detaillierte Analyse dieser Resultate offenbart, dass das ternäre Al-Si-N System in drei Bereiche unterteilt werden kann, deren Eigenschaften durch den Si Gehalt und nicht durch die Abscheidetemperatur bestimmt sind. Für Si Konzentrationen unter 6 at.%, wird in den Röntgendiffraktionsmessungen gezeigt, dass Si-Atome einen Al Gitterplatz einnehmen, was durch die lineare Abnahme des Gitterparameters c sichtbar wird. Oberhalb einer Löslichkeitsgrenze von 6 at.%, bestehen die Schichten aus $Al_{0.44}Si_{0.06}N_{0.5}$ Nanokristalliten, die in einer intergranularen SiN_y Schicht eingebettet sind: es bildet sich eine Nanokompositstruktur. Im Si-Konzentrationsbereich von 6 bis etwa 12 at.% bleibt die Dicke der SiN_y Schicht konstant bei 0.25 nm ($\sim$ 1 Monolage), während die Größe der Kristallite invers-proportional zum Siliziumgehalt abnimmt. Oberhalb von 12 at.% ändert sich der Wachstumsmodus und die Dicke der SiN_y Schicht nimmt dann mit dem Siliziumgehalt zu. Die Schichten werden für Röntgenstrahlen nach und nach amorpher und entwickeln chemische und mechanische Eigenschaften, die sich denen von reinem Siliziumnitrid nähern.

Die Härte der Schichten sowie deren biaxialer Spannungszustand wurden anhand von Nanoindentation sowie mechanischer Profilometrie untersucht. Während die Härte in der Größenordnung 20–25 GPa in den reinen AlN und $\mathrm{SiN_y}$ Schichten liegt, erreicht sie 32 GPa in den Al-Si-N Schichten mit 8–10 at.% Si. Bei dieser Konzentration wird ein vernachlässigbarer residueller Spannungszustand gemessen ($<$ 0.5 GPa). Diese über einen weiten Si Konzentrationsbereich gemessene Härtezunahme, wird durch die simultane Wirkung verschiedener Mechanismen hervorgerufen: einerseits wird die Versetzungsaktivität in den immer kleiner werdenden Al-Si-N Kristalliten unterdrückt, was durch die Bildung einer festen Lösung weiter unterstützt wird; andererseits verhindert bei einer Zwei-Phasen-Nanokompositstruktur das intergranulare $\mathrm{SiN_y}$ eine Verformung durch Aufeinandergleiten der Kristallite. Außerdem werden die optischen Eigenschaften der Schichten kaum durch die veränderte Zusammensetzung beeinflusst: es wurde ein Brechungsindex zwischen 2.00 und 2.12 bei einer Wellenlänge von 633 nm gemessen, was einer optischen Transmission von etwa 80 % entspricht. Die strukturellen, mechanischen und optischen Eigenschaften der Schichten bleiben nach einem zwei-stündigen Tempern bei 1000°C unter Argonatmosphäre stabil.

Da die Grenzflächeneigenschaften in einer dreidimensionalen Nanokompositstruktur schwer zu bestimmen sind, wurden als Modellstruktur $\mathrm{Al(\text{-}Si\text{-})N/SiN_y}$ Multischichten abgeschieden. Deren Studium anhand von Röntgendiffraktion und hoch auflösender Transmissionselektronenmikroskopie zeigt, dass bis zu 0.7–1.0 nm ($\sim$ 2.5–3.5 Monolagen) kristallines Siliziumnitrid epitaktisch auf einer AlN (001) Schicht stabilisiert werden kann. Dieses Resultat unterstützt die Hypothese, dass kohärente $\mathrm{Al\text{-}Si\text{-}N/SiN_y}$ Grenzflächen in den Nanokompositschichten gebildet werden, und dass die intergranulare $\mathrm{SiN_y}$ Schicht eine Kristallstruktur besitzt. Auf diese Weise kann auch die moderate Härtezunahme in den Al-Si-N Schichten erklärt werden, welche wahrscheinlich ihren Ursprung in dem kontinuierlichen Übergang der Struktur an den Grenzflächen nimmt. Außerdem kann man die endliche Löslichkeit der Al-Si-N Phase einer moderaten thermodynamischen Phasentrennungskraft zuordnen. Aus diesem Grund ist ein Zusammensetzung-Gradient an den Grenzflächen wahrscheinlich, umso mehr, da die verwendete Abscheidetechnik von dem thermodynamischen Gleichgewicht weit entfernt ist. In den Al-Si-N Nanokompositschichten, bilden also die Grenzflächen durchlässige Hindernisse für Versetzungen was eine plastische Verformung des Materials ermöglicht. Auch zwischen den Kristalliten inkorporierte Sauerstoffatome können die Trennungsenergie der Grenzfläche erniedrigen und das intergranulare Gleiten erleichtern.

In dieser Arbeit wird gezeigt, dass optisch transparente Beschichtungen aus Al-Si-N bei tiefen Abscheidetemperaturen und mit einer Härte von mehr als 30 GPa hergestellt werden können. Die in dieser Arbeit präsentierten Untersuchungen erlauben es, ein grundlegendes Verständnis des Materialsystems sowie der Entwicklung seiner Eigenschaften als Funktion des Siliziumgehaltes zu gewinnen.

Résumé

Ce travail de thèse est consacré à l'étude des propriétés de couches minces Al-Si-N. Du fait de l'immiscibilité attendue des nitrures d'aluminium (AlN) et de silicium (Si_3N_4), de la dureté et de la transparence optique de chacune de ces phases, la formation de couches dures, transparentes et nanostructurées est attendue.

Les couches d'Al-Si-N ont été produites par pulvérisation de cathodes magnétron non-équilibrées disposées en champ fermé. Des cibles d'Al et de Si sont utilisées et pulvérisées dans une atmosphère réactive d'Ar/N_2. Les films ont été déposés à 200°C et 500°C sur des substrats de silicium, carbure de tungstène, verre et silice UV, afin d'explorer leurs propriétés chimiques, morphologiques, structurelles, mécaniques, optiques et thermiques. Leur composition chimique, mesurée par spectroscopie des photoélectrons X, est variée de l'AlN pur à l'Al-Si-N contenant 23 % at. de silicium. Les conditions de dépôt sont ajustées de façon à ce que la quantité d'azote fournie suffise à l'obtention de couches complètement nitrurées, c.à.d. transparentes et contenant environ 50 % at. d'azote. En dépit de l'excellente pression de base atteinte dans la chambre de dépôt ($< 10^{-6}$ Pa), une concentration de 0.5–2.0 % at. d'oxygène est mesurée dans les couches.

Les propriétés structurelles et morphologiques des couches ont été étudiées par diffraction de rayons X (XRD), microscopie électronique à balayage et microscopie électronique en transmission (TEM). Jusqu'à 15–20 % at. de Si, les couches sont cristallines et la seule phase identifiée est celle de l'AlN wurtzite avec une forte texture (002). L'AlN pur présente une morphologie colonnaire marquée qui disparait progressivement par incorporation du silicium dans les couches. En parallèle, la taille moyenne des cristallites constitutives de chaque colonne décroit de 60 nm dans l'AlN pur, à environ 30 nm à 6 % at. de Si, et 5 nm à 12 % at. de Si. Une analyse détaillée de ces résultats révèle que le système ternaire Al-Si-N peut être divisé en trois régimes de composition, dont les propriétés sont déterminées par la teneur en Si et sont indépendantes de la température de dépôt. Pour une teneur de moins de 6 % at. de Si, l'incorporation d'atomes de silicium en substitution de l'aluminium dans la maille hexagonale d'AlN est révélée en XRD par la décroissance linéaire du paramètre de maille *c*. Au dessus d'une limite de solubilité identifiée à 6 % at., les couches minces sont constituées de nanocristallites d'$Al_{0.44}Si_{0.06}N_{0.5}$ entourées d'une couche intergranulaire de SiN_y: une structure nanocomposite est formée. Pour une concentration en Si variant de 6 à environ 12 % at. de Si, l'épaisseur de la couche de SiN_y reste constante et égale à 0.25 nm (∼ 1 monocouche), tandis que la taille des cristallites décroit de façon inversement proportionnelle à la teneur en silicium. Au dessus de 12 % at., le mode de croissance change et l'épaisseur de la couche de SiN_y augmente avec la teneur en Si. Les couches deviennent progressivement amorphes aux rayons X et présentent des propriétés chimiques et mécaniques se rapprochant de celles du nitrure de silicium pur.

La dureté des couches ainsi que leur contrainte biaxiale résiduelle ont été étudiées respectivement par nanoindentation et par profilométrie mécanique. Alors que la dureté est de l'ordre de 20–25 GPa dans l'AlN et le $\mathrm{SiN_y}$ purs, elle atteint 32 GPa dans les couches d'Al-Si-N contenant 8–10 % at. de Si, concentration à laquelle une contrainte résiduelle en compression négligeable ($<$ 0.5 GPa) est mesurée. Cet accroissement de la dureté distribué sur une large plage de composition résulte de l'action simultanée de plusieurs mécanismes: d'une part, la formation d'une solution solide d'Al-Si-N et la diminution de la taille des grains entraine une réduction de l'activité de dislocation dans la phase cristalline; d'autre part, lorsque qu'une structure nanocomposite biphasée est formée, la présence de $\mathrm{SiN_y}$ aux joints de grains empêche une déformation par glissement des grains les uns sur les autres. Les propriétés optiques des couches sont par ailleurs peu influencées par les variations de composition : un indice de réfraction compris entre 2.00 et 2.12 à une longueur d'onde de 633 nm est mesuré, ce qui correspond à une transmission optique d'environ 80 %. Les propriétés structurelles, mécaniques et optiques des couches sont stables après un recuit de 2h à 1000°C sous argon.

Afin de servir de modèle pour l'étude des propriétés d'interface, difficilement accessibles dans une structure nanocomposite tridimensionnelle, des multicouches d'Al(-Si-)N/$\mathrm{SiN_y}$ ont été déposées. Leur étude en diffraction X et en TEM haute résolution montre que jusqu'à 0.7–1.0 nm ($\sim$ 2.5–3.5 monocouches) de nitrure de silicium cristallin peuvent être stabilisés par épitaxie sur une surface d'AlN (001). Ce résultat renforce l'hypothèse de la formation d'interfaces Al-Si-N/$\mathrm{SiN_y}$ cohérentes dans les couches nanocomposites, et de l'existence d'un ordre cristallin dans le $\mathrm{SiN_y}$ intergranulaire. Cela explique, par-là même, l'accroissement de dureté modéré obtenu pour le système Al-Si-N, qui résulte vraisemblablement d'une transition structurale graduelle aux interfaces. De plus, l'existence d'une solubilité non nulle dans l'Al-Si-N est associée à une force motrice thermodynamique de séparation de phase modérée. Par conséquent, l'existence d'un gradient de composition aux interfaces est probable, d'autant plus qu'un procédé de dépôt hors équilibre thermodynamique est utilisé. Dans les couches nanocomposites d'Al-Si-N, les interfaces constituent donc des obstacles pénétrables à une déformation plastique par mouvement de dislocations. Dans le cas d'une incorporation aux joints de grains, les impuretés d'oxygène peuvent également causer une diminution de l'énergie de cohésion d'interface et faciliter le glissement aux joints de grains.

Dans ce travail, il est montré que des revêtements optiquement transparents peuvent être fabriqués à base d'Al-Si-N à faible températures de dépôt et avec une dureté supérieure à 30 GPa. Les investigations présentées dans cette thèse permettent de dresser une image détaillée du matériau et de l'évolution de ses propriétés en fonction de sa teneur en silicium.

Contents

List of abbreviations

Deposition techniques

CFUBMS: Closed Field Unbalanced Magnetron Sputtering
CVD: Chemical Vapor Deposition
DIBS: Dual Ion Beam Sputtering
HIPIMS: High Power Impulse Magnetron Sputtering
HPPMS: High Power Pulsed Magnetron Sputtering
IBAD: Ion Beam Assisted Deposition
MBE: Molecular Beam Epitaxy
MOVPE: Metal Organic Vapor Phase Epitaxy
LPCVD: Low Pressure CVD
PACVD: Plasma Assisted CVD
PLD: Pulsed Laser Deposition
PVD: Physical Vapor Deposition
UBMS: Unbalanced Magnetron Sputtering

Characterization techniques

AES: Auger Electron Spectroscopy
AFM: Atomic Force Microscopy
EDX: Energy Dispersive X-ray Analysis
EELS: Electron Energy Loss Spectroscopy
EPMA: Electron Probe Micro-Analysis
ERDA: Energy Recoil Detection Analysis
ESCA: Electron Spectroscopy for Chemical Analysis
EXELFS: Extended Energy Loss Fine Structure
FTIR: Fourier Transform Infra Red
HRTEM: High Resolution TEM
SE: Spectroscopic Ellipsometry
SEM: Scanning Electron Microscopy
STEM: Scanning TEM
TEM: Transmission Electron Microscopy

XPS: X-ray Photoelectron Spectroscopy
XRD: X-Ray Diffraction
XRR: X-Ray Reflectometry

Miscellaneous

BE: Binding Energy (XPS context)
BF: Bright Field (TEM context)
DF: Dark Field (TEM context)
DFT: Density Functional Theory
DC: Direct Current
ED: Electron Diffraction (TEM context)
fcc: Face centered cubic (Crystallography)
FED: Field Emission Display
FFT: Fast Fourier Transformation
FWHM: Full Width at Half Maximum
GB: grain boundary
hcp: hexagonal close-packed (Crystallography)
HF: High Frequency
HR: High-Resolution
IR: Infrared
ISE: Indentation Size Effect (nanoindentation testing context)
ITO: Indium Tin Oxide
LED: Light Emitting Diode
ML: monolayer
NIST: National Institute of Standards and Technology
PE: photoelectron
PF: Pole Figure (XRD context)
RC: Rocking curve (XRD context)
RF: Radio Frequency
rms: root mean square
SAD: Selected Area Diffraction (TEM context)
SZM: Structure Zone Model
UHV: Ultra High Vacuum
UV: Ultra Violet
w: wurtzite (Crystallography)

Part I

Introduction

Chapter 1

Preamble and project definition

1.1 Motivation

Over the last 20 years, nanostructured coatings based on transition metal nitrides and carbides have attracted increasing interest. Thanks to the tailoring of their structure and composition, these coatings show improved mechanical, chemical and tribological properties [Holl 86] [Vepr 95] [Musi 00] [Pats 03] [Vepr 05] [Mayr 06a]. They are mostly attractive for industrial applications in high speed machining (cutting, punching, forming, etc.) [Cava 06] [Csel 07] [Vepr 08], but are also used for wear applications (e.g. for automotive components [Gahl 01] [Treu 05] or for biomedical implants [Haue 03] [Leva 07]) and decorative applications [Rein 94] [Cons 99]. In particular, coatings based on a combination of Ti, Cr, Al and Si nitrides and carbides (e.g. Ti-N, Cr-N, Ti-C-N, Ti-Al-N, Ti-Cr-N, Ti-Al-C-N, Cr-Al-Si-N and Ti-Al-Si-N) are currently available on the market to be used as protective hard coatings for machining tools [Csel 07] [Vepr 08]. One of the most promising coating is the nanocomposite structure made of nanocrystalline Ti-Al-N embedded in an amorphous silicon nitride matrix[1] [Holu 99] [Nied 99] [Vepr 04a] [Parl 04a] [Mart 05]. With such a structure, the hardness of TiN is doubled (from 24 GPa for TiN to 40–45 GPa for TiAlSiN), as well as its maximum application temperature (from 600°C for TiN to $>$ 1000°C for TiAlSiN) [Csel 05]. The tool life time can hence be considerably improved.

Due to their metallic nature, however, traditional hard coating systems

---

[1] e.g. nACo® from PLATIT - Switzerland (`http://platit.com/coatings/coating-types/breakthrough-coatings/naco`) and MARWIN® SI from SHM - Czech Republic (`http://www.shm-cz.cz/en/products/pvd-coatings/marwin-si`)

such as *nc*-TiN/*a*-SiN$_x$ (*nc*: nanocrystalline, *a*: amorphous) are optically opaque and cannot be used in applications requiring optical transparency. Here a new class of hard nanocomposite coatings is proposed that relies on the combination of group III nitrides, such as GaN, AlN, BN, and silicon nitride. Due to the large band gap of group III nitrides, these materials are optically transparent in the visible range of light. In addition improved mechanical properties are expected whenever a three-dimensional network made of group III nitride nanocrystallites embedded in an amorphous silicon nitride matrix can be formed. Among group III nitrides, AlN shows good mechanical and anti-oxidation properties and can be easily deposited by sputtering. According to the existing Al-Si-N ternary phase diagram [Weit 90], AlN and Si_3N_4 are expected to be immiscible: the formation of a two-phase *nc*-AlN/*a*-SiN$_x$ composite coating is thus expected if Al and Si are co-deposited in a reactive atmosphere containing nitrogen.

In this work, the suitability of the Al-Si-N system for new optically transparent nanostructured coatings with improved mechanical properties is explored, following the general design rules of hard (phase-separated) nanocomposite coatings originally defined by Veprek [Vepr 95] [Vepr 05]. In view of industrial applications such as protective coatings in the glass industry, Al-Si-N coatings were prepared by low temperature ($\leq 500°C$) reactive magnetron sputter deposition. The deposition technique can be scaled up for large industrial deposition units. Moreover the possibility to deposit the coatings at low temperature – e.g. below 500°C, the glass transition temperature of float glass – is of great technological interest as compared to another transparent hard material, Al_2O_3, which can be only fabricated at high deposition temperatures.

1.2 Structure of the present research work

The objectives of this thesis are to deposit Al-Si-N coatings, investigate their microstructural and chemical properties, and correlate these properties to the mechanical and optical properties of the films, so as to get a thorough understanding of the Al-Si-N system deposited by low temperature reactive sputtering. Following this study, the results are compared to the design rules for hard nanocomposite coatings proposed by Veprek, and are used to used to give a broader perspective on hardening mechanisms in nanocomposite coatings.

The present manuscript is divided as follows:

In Chapter 2, a short review is given on the design and classification of hard nanostructured coatings. Special attention is devoted to the material selection criteria and to the hardening mechanisms of composite coatings. This is followed by a section on the Al-Si-N system, where the state of knowledge on the thermodynamics and the local chemistry of Al-Si-N at the beginning of this work is presented. A list of the potential and current applications of Al-Si-N coatings is also provided.

As already mentioned, the Al-Si-N coatings studied in this work were prepared by reactive magnetron sputtering. An introduction to this deposition technique and to the commonly obtained thin film microstructures is given in Chapter 3. The chemical, structural, mechanical and optical properties of the coatings were investigated by X-ray photoelectron spectroscopy (XPS), X-ray diffraction (XRD), scanning and transmission electron microscopy (SEM, TEM), nanoindentation testing, mechanical profilometry and UV-visible spectroscopy. All these characterizations techniques are briefly presented in Chapter 4.

The experimental results obtained on Al-Si-N thin films are reported in Chapter 5. The films were deposited with increasing Si content by confocal unbalanced magnetron co-sputtering of Al and Si targets in a reactive atmosphere containing nitrogen. Two deposition temperatures were used: 200°C and 500°C. The experimental procedures used to prepare the films are reported at the beginning of this chapter.

To obtain a better insight into the role and properties of interfaces in the Al-Si-N three-dimensional nanocrystalline systems, nanoscaled multilayer samples were used as simplified two-dimensional model systems. Several series of multilayers consisting of alternate layers of AlN (or Al-Si-N) and SiN_y were prepared using similar deposition conditions to the ones used for isotropical nanocomposite coatings in Chapter 5. The details of the multilayer sample preparation as well as the results of XRD, X-ray reflectometry (XRR), high-resolution TEM, nanoindentation and profilometry experiments are reported in Chapter 6. Implications on the properties of Al-Si-N nanocomposite thin films are discussed.

In the conclusion of this work (Chapter 7) a broader view on the way to build hard nanostructured coatings is given, based on the knowledge gained from Al-Si-N thin films. It is proposed to adopt a more fundamental and global approach for future developments in the field of hard coatings.

Chapter 2

Basics and state of the art

2.1 Hard nanostructured coatings: a short review

Hard nanostructured coatings can be divided into two main classes: hard multilayer (and superlattice[1]) coatings, which are composite coatings with a composition and phase modulation in one direction of space i.e. the growth direction, and so-called hard nanocomposite coatings, the structure of which is modulated in all three direction of space, with a characteristic length at the nanometer scale (Fig. 2.1). Such coatings are often based on a combination of binary, ternary and sometimes quaternary nitride and carbide systems, whose microstructure is optimized so as to produce coatings showing e.g. enhanced hardness [Holl 86] [Vepr 95] [Musi 00] [Pats 03] [Vepr 05] [Mayr 06a], toughness [Leyl 04] [Zhan 07f], thermal stability and oxidation resistance [Hult 00] [Mann 01] [Rave 07] [Vepr 05] [Mayr 06a]. In this section, the basic strategies for the design of new hard coatings are described and examples of nanostructured coatings are given. Since the present work deals with nanocomposite hard coatings, special attention will be given on the specific design rules proposed for such coatings.

2.1.1 Material selection and microstructural design

The development of hard nanostructured coatings relies on basic considerations in material selection and in the ways to improve the mechanical properties (especially hardness) of single-phase and multi-phase coatings. The criteria used for the selection of a particular material (or material

---

[1] i.e. heteroepitaxial multilayer structure with an individual layer thickness of nanometer scale.

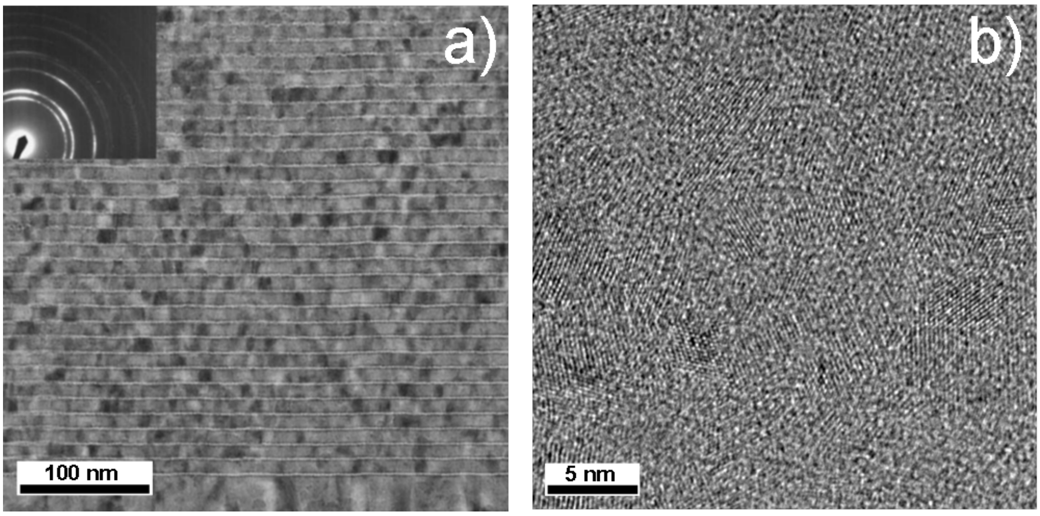

Figure 2.1: (a) Cross-sectional micrograph and selected area diffraction (SAD) pattern from a TiN/SiN_x *multilayer system with a bilayer thickness of 11.5 nm and a* SiN_y *thickness of 1.7 nm [Sode 05]. (b) High-resolution TEM micrograph of a Ti-Al-Si-N nanocomposite thin film with high Al + Si content (*$Ti_{0.42}Al_{0.50}Si_{0.08}N$*). A mixture of* fcc *Ti-Al-N and hexagonal wurtzite AlN crystalline nanograins with different orientations is visible. They are presumably surrounded by a thin amorphous* SiN_x *matrix [Parl 04b].*

combination) and its processing depend on the substrate material and on the actual application of the coating. In general, important parameters to be considered are the intrinsic hardness of the selected material, the adhesion to the substrate, the residual stress in the deposited film, the cohesion between different phases in the case of multi-phase coatings, and of course the interactions with the environment in the chosen application [Holl 86] [Loff 94] [Holl 95]. In many wear applications, the hardness (= *the resistance to plastic deformation*) is considered of primary importance, even if toughness (= *the ability to absorb energy up to fracture*) can be equally important. Hard materials can be selected among nitrides, borides, carbides and oxides of transition metals and of group III and IV elements. Typical materials chosen for single-phase hard coatings are TiC, WC, SiC, TiN, TiCN, Al_2O_3 and TiB_2.

As a guideline for material selection, Holleck proposed in [Holl 86] a classification of hard coatings according to their bond nature. Three groups were distinguished: metallic hard materials (nitrides, carbides and borides of transition metals), covalent hard materials (nitrides, carbides and borides of Al, Si, and B, as well as diamond) and ionic (ceramic) hard materials (oxides of Al, Zr etc.). A schematic representation of this classification is given in Figure 2.2. The nature of the bond between elements is related to specific properties characteristic of each group. In particular, metallic hard materials tend to have a higher elastic modulus and a small electrical resistivity. In addition they show a good adhesion to metallic substrate, used e.g. for machining applications[2]. The hardest materials are found among covalent coatings (diamond, cubic boron nitride), that also show the lowest linear thermal expansion coefficients (however not necessarily adapted to the metallic substrates if high temperature applications are considered). Ionic materials show the best chemical inertness but are also very brittle.

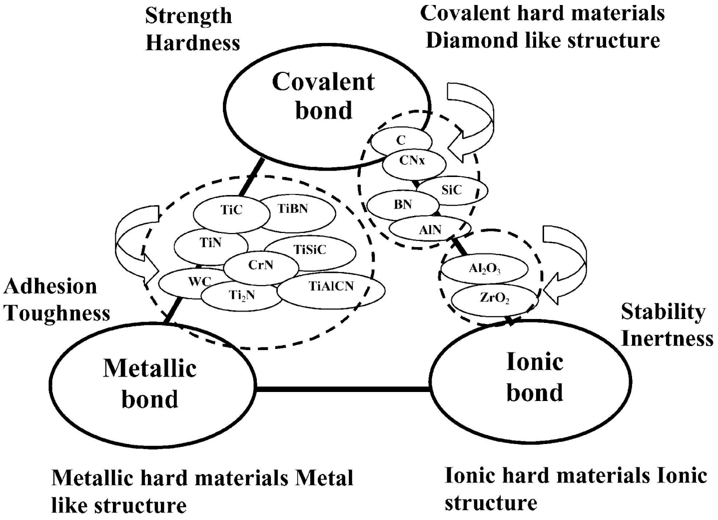

Figure 2.2: Change of material properties as a function of the chemical bonding. The hard materials shown in this scheme can be combined to form nanostructured coatings with e.g. enhanced hardness, toughness and oxidation resistance [Holl 99].

Hard coatings can be deposited using chemical vapor deposition (CVD) or physical vapor deposition (PVD) techniques. The great advantage of PVD techniques, for instance, is the large flexibility in the type of materials that can be grown, the cleanliness of the process (the material properties can be strongly influenced by the introduction of impurities), and the possibility to control the microstructure of the coatings[3]. Already 20 years ago Holleck [Holl 86] and Sundgren [Sund 86] acknowledged the high potential of the combination of several (hard) materials to form multiphased hard coatings

---

[2] In the tool industry, typical substrates are cemented carbide (WC-Co) and high speed steel (HSS).

[3] See also Chapter 3.

with a controlled microstructure[4]. The importance of the microstructure on the mechanical properties, especially the hardness, was stressed by both authors. In particular, it is mentioned that strong (high cohesive energy) and defect-free (no impurities or voids) grain boundaries, a small grain size and the build-up of internal stress (e.g. due to the incorporation of interstitial atoms using ion bombardment during the film growth) can favor a high hardness. The role of non-equilibrium (metastable) structures such as supersaturated structures to synthesize hard multi-phase coatings was also pointed out. The various hardening mechanism available to design coatings with enhanced hardness are described in the next sub-section. The general strategies proposed for the material selection and the control of microstructural features described in [Holl 86] and [Sund 86] paved the way for the development of new nanostructured hard coatings.

2.1.2 Hard materials and hardening mechanisms

As to the hardness, protective coatings are generally divided into hard ($20\ \text{GPa} < H < 40\ \text{GPa}$) and superhard ($H \geq 40\ \text{GPa}$) coatings. There is a large number of hard materials among nitride, carbide and oxide materials, as mentioned above, but there are only few known intrinsically superhard materials, namely diamond (~ 90 GPa), cubic boron nitride *c*-BN (~ 50 GPa), and possibly a few other binary and ternary compounds from the B-C-N system [Vepr 99] [Krok 04]. The high intrinsic hardness of these materials is related to a high binding energy (bond strength), a high degree of covalent bonding and a short interatomic distance [Kisl 86] [Gao 03] [Simu 06] [Li 08] [Guo 08]. According to these criteria, is was in particular postulated that a C_3N_4 phase could be even harder than diamond itself, since the C–N bonds are slightly shorter than C–C bonds [Krok 04]. This was supported by the calculation of the bulk modulus of a β- C_3N_4 polymorph that was found almost as high as that of diamond [Liu 89]. However this material could never be deposited with the expected mechanical properties. Recently, it was found by first principle calculations that, despite their high elastic modulus, C_3N_4 solids may actually have a low strength, much

---

[4] The term *microstructure* is used as the widely accepted concept of the existence of a structure at a small scale, originally at the micrometer scale, but here applied to structures rather of nanoscale nature. By *structure* is meant the existence of lattice point defects, dislocations, voids, impurities, grain boundaries (in one, two or three directions in layered, columnar and equiaxed structures respectively), the formation of different material phases (possibly not in thermodynamic equilibrium) and the resulting phase distribution in the composite material, the existence of a crystallographic texture, of surface roughness, the grain size etc.

lower than that of diamond [Zhan 06]. Unfortunately, both diamond and *c*-BN are metastable high pressure and high temperature phases, which strongly limits their fabrication and utilization. Amorphous diamond-like carbon (*a*-C:H, DLC) and amorphous $\mathrm{CN_x}$ are then preferred. However, the chemical affinity (high solubility) of carbon with iron (steel), silicon and other alloys limits the application of carbon-based hard coatings to e.g. the machining of aluminum and wood [Musi 00]. For these reasons, materials with extrinsic hardness, i.e. hardness determined by their microstructure, are subject to intense research efforts, all the more as the large variety of material combination and structural design strategies gives almost infinite possibilities for the development of hard and superhard coatings with tailored properties.

For the design and the control of the microstructure of hard coatings, it is important to known the different mechanisms that can lead to the hardening of a crystalline material, mainly acting by hindering or the retarding the deformation generated by dislocation movements. These mechanisms are reviewed e.g. in [Arzt 98], [Mayr 06a], [Rave 07] and [Zhan 07f]. In the case of crystalline thin films, they can be divided into i) grain boundary hardening, ii) solid solution hardening, iii) age hardening and iv) hardening by energetic ion bombardment.

Grain boundary hardening In metal and alloy (crystalline) films, a decrease of the grain size below 1 µm hinders the multiplication and the movement of dislocations, creating dislocation pile-ups at grain boundaries, so that the hardness of the material is increased according to the Hall-Petch relationship [Hall 51] [Petc 53]: $H = H_0 + kd^{-1/2}$, with H the hardness, H_0 the intrinsic hardness, k a constant and d the grain size. The phenomenon is especially prominent for $d < 50 - 100$ nm. For $d \lesssim 10 - 20$ nm the dislocation activity is entirely blocked due to the absence of dislocation sources (at least one dislocation loop must fit into the grains [Arzt 98]) and another deformation mechanism comes into play. The material shows then a "reverse Hall-Petch" behavior, that is to say a decrease of hardness with decreasing the grain size. The origin of this reverse effect is still subject to debates [Tjon 04]. In nanocrystalline metals, this effect is essentially attributed to a grain boundary sliding mechanism [Schi 98] [Van 02]. In nanocrystalline ceramics, however, grain boundary sliding, grain rotations and intergranular slip-stick events (formation of intergranular dislocations) can interplay, with the possiblity of a cooperative mechanical response from grains coupled by a disordered (amorphous) intergranular grain boundary phase [Szlu 05]. In all cases, a low cohesive energy at grain boundary, as well as the existence of porosity or the presence of impurities are responsible for weak grain boundaries, which results in a softening of the material. A way to prevent this phenomenon consists in strengthening the grain boundary, which can be achieved by the formation of an intergranular phase made of a distinct (immiscible) material. This intergranular phase, also called matrix phase or tissue phase, must form strong (high cohesive energy) and defect free interfaces with the nanocrystalline phase to be able to block grain boundary sliding. It must also be thin enough so that crack propagation is efficiently inhibited by numerous deflections at the surface of the crystalline grains. Such arguments constitute the basic design principles of hard and superhard nanocomposite coatings, as will be described in further details in section 2.1.4. The composite made of nc-TiN/a-SiN$_x$ is often used a model system for such coatings. A similar hardening can be achieved by the self-organization of a nanocolumnar (anisotropic) structure in superhard overstoichiometric TiB$_{2.4}$ thin films, where TiB$_2$ columns are encapsulated in a B-rich thin tissue phase [Mayr 05].

Grain boundaries in the form of planar interfaces also play an important role in multilayer structures, although the hardening mechanisms that come into play are different than for nanocrystalline materials. When the bilayer thickness Λ of a periodic multilayer structure is in the range of $\approx$ 5–10 nm, a significant hardness enhancement can be achieved. Dislocation blocking at the layer interface and a Hall-Petch strengthening were identified as the dominant effects that explain hardening [Chu 95] [Yash 99]. The dislocation blocking is caused by the difference in shear modulus of the individual layers, as proposed by Koehler [Koeh 70]. Dislocations preferably remain in the layer with the lower shear modulus, where the dislocation line energy is lower, and a minimum shear stress is needed to force the dislocation motion across the interface. This effect can cause significant hardness enhancement if the layers are thin enough so that dislocation generation and motion cannot occur within each individual layers. As for the Hall-Petch relation – for which it is assumed that dislocations cannot move across grain boundaries –, it is only applicable for multilayer systems composed of materials having different dislocation slip-systems, that is non-isostructural multilayers (individual layers have different crystallographic structures). This effect shows however a breakdown at a critical layer thickness the order of 10–20 nm, reminiscent of what was previously described for nanocrystalline materials [Arzt 98] [Yash 99].

Solid solution hardening Solid solution hardening comes from the lattice distortion generated by the insertion of atoms of the alloying element (solute atoms) either in interstitial or substitutional lattice positions. The resulting strain and stress fields impede the dislocation motion, increasing the yield strength of the material. The shear stress needed to move a dislocation increases with the solute concentration and with the strain caused by the solute (in turn dependent on the size of the solute atoms). The limit to this effect corresponds to the solubility limit of the solute. The solubility limit can be increased by the use of a non-equilibrium growth process such as kinetically limited PVD deposition at low substrate temperature [Holl 88]. A supersaturated metastable solid solution can then be deposited [Mayr 06a] [Zhan 07f]. The most prominent example in the field of hard coatings is the deposition of a metastable fcc $Ti_{1-x}Al_xN$ solid solution with an Al content up to $x \approx 0.7$, whereas the solid solubility of Al in TiN is normally limited to a few atomic percents [Hult 00] [Mayr 06c] [Mayr 07b]. Besides Ti-Al-N, Ti-C-N, Cr-Al-N and Cr-Zr-N are further examples [Zhan 07f].

Age hardening (Also called "precipitation" or "dispersion strengthening" [Arzt 98]) Age hardening is a widely used process for the strengthening of bulk materials. It is achieved by precipitation of a second phase from a supersaturated metastable phase. This mechanism can be accelerated and controlled by a post-deposition annealing treatment. The alloy composition and the careful control of the growth of precipitated particles enables to maximize the strengthening effect, which results from the balance between the "cutting" (on small penetrable particles) and the "bowing" or "by-passing" (on large impenetrable particles) stress to be overcome for dislocation motion. Indeed the cutting stress that operates for solute atoms and coherent precipitates is proportional to $\sqrt{R}$, with R the radius of the particle, while the by-passing stress (Orowan mechanism) of particles impenetrable for dislocations varies as $1/R$ (for a constant volume fraction of particles)[5] [Arzt 98]. Age hardening was for example reported for Ti-Al-N alloys, that undergo a spinodal decomposition[6] into nanometer-sized coherent cubic domains of

---

[5] The Orowan stress actually varies as $1/L$ with L being the obstacle spacing. The by-passing of impenetrable obstacles is equivalent to the condition that a dislocation loop must fit between two obstacles (particles). For a constant volume fraction of particles of radius R and homogeneous dispersion, $L \propto R$ [Arzt 98].

[6] The *spinodal decomposition* is a strong thermodynamically driven and diffusion rate-controlled phase segregation. This type of phase segregation occurs in $A_{1-x}B_x$ binary systems when the second derivative of the Gibbs free energy of the mixed phase is negative, which means that the system is inherently unstable and does not require nucleation and grain growth to decompose. Spinodal decomposition leads to the formation of a self-

fcc TiN and fcc AlN [Mayr 03] [Mayr 07a]. Note that if additional thermal activation is provided to the latter system, a phase transformation into the thermodynamically stable fcc TiN and wurtzite AlN can occur that results in a hardness decrease [Mayr 03]. This demonstrates the need for a careful control of the age hardening process. Recently, thermally induced self-hardening of nanocrystalline Ti-B-N [Mayr 06b] and Zr-Al-N [Sanj 06] thin films was also reported.

Hardening by energetic ion bombardment Ion bombardment during the film growth can be used to densify and modify the morphology of the films [Matt 89]. It usually results in a better adhesion of the film to the substrate and is often correlated to an increasing compressive biaxial residual stress in the deposited film. During energetic ion bombardment, defects are created by collision cascades, resulting in permanent atomic displacement (creation of interstitials, vacancies) below the film surface, and implantation of gas atoms. These point defects can interact and lead to the formation of one- (dislocations), two- (grain boundaries, twins) or three- (voids, cracks, particles) dimensional defects. These defects are in turn related to the existence of macro- and micro-stress in the films. In particular an apparent linear relationship between hardness and residual compressive stress was reported for several single-phase coatings (e.g. TiN, CrN) deposited by PVD methods [Mayr 06a]. However, it is now known that this is not the compressive stress itself that is responsible for the hardening effect, but the defects responsible for the residual stress that also acts as effective barriers for dislocation motion and generate a hardness enhancement. Hardness enhancement due to ion bombardment can be easily achieved at low deposition temperatures of a few hundred degrees (typically $\lesssim$ 300°C) [Vepr 05]. However hardening by energetic ion bombardment yields coatings with low thermal stability [Vepr 05] [Mayr 06a]. Annealing, indeed, leads to the recovery of deposition-induced lattice defects by migration and recombination [Hult 00] [Mayr 06a]. This annihilation of defects results in turn in the relaxation of the biaxial compressive residual stress and in a decrease of hardness.

Because of their limited thermal stability, hard coatings relying on defect hardening are not appropriate for coating applications in the tool industry where operating temperatures may exceed 1000°C [Mayr 06a]. On contrary, grain boundary hardening and the formation of a nanocomposite structure, as described above, can enable equivalently good mechanical properties, with

---

organized composition-modulated structure at the nanometer scale [Vepr 05] [Mayr 06a].

in addition good thermal stability due to the stabilizing role of the intergranular (”tissue”) phase with respect to crystallization and grain growth. As for age hardening, it can represent a valuable ability of hard coatings (such as Ti-Al-N) for self-adaptation to thermal load. All the above described hardening mechanisms are useful tools in the hand of the coating engineer and researcher. These tools can be used and combined to develop new multifunctional coatings with improved mechanical properties. For instance, hard coatings intended for industrial applications as protective coatings against wear must show an outstanding combination of mechanical (hardness, toughness) and chemical (oxidation resistance) properties. Because high working temperatures are common in the tool industry with likely significant deterioration of the mechanical properties, the issue of the thermal stability of hard coatings and the ways to improve it were recently emphasized in several review papers [Vepr 05] [Mayr 06a] [Rave 07]. In addition and as already mentioned, hardness is not necessarily the unique parameter that quantifies the performance of wear resistant coatings. A high toughness can be of equal importance. Unfortunately, high hardness and high toughness cannot always be achieved simultaneously since very hard materials are usually brittle materials with a bad adherence to the substrate. This issue was recently raised and specific design strategies were proposed to prepared ”hard yet tough” materials [Leyl 00] [Leyl 04] [Zhan 07f].

2.1.3 Currently developed hard nanocomposite coatings

Many interesting reviews can be found in the literature about hard and superhard nanostructured coatings. They deal with the material combinations, structures and properties, the associated design concepts and the recent progresses in the field: [Musi 00] [Musi 01c] [Musi 02b] [Zhan 03] [Vepr 05] [Mayr 06a] [Rave 07] [Stue 08]. Among these publications, several classifications of hard nanostructured coatings are proposed, according to the type of hardening mechanism used and to the type of nanostructure and composition. The most widely studied nanocomposite systems are listed below. Note that the given classification is not exhaustive. Readers interested in multilayer and superlattice coatings shall find valuable information in [Musi 00], [Stue 08] and references therein.

The main groups of hard and superhard nanocomposite coatings can be defined as:

1. *nc*-MeN/nitride, boride or carbide hard phase (e.g. *a*-$\mathrm{SiN_x}$ [Vepr 96]

[Dise 98] [Nied 99] [Mart 05] [Sand 06c], TiB_2 [Mayr 06b] [Mayr 06a], etc.), where the second phase is a minority phase (e.g. *nc*-TiN/*a*-SiN_x, with hardness maximum at a Si content of about 10 at.% [Vepr 05]);

2. *nc*-MeN/*a*-SiN_x with a high (≥40–50 at.%) Si content (e.g. *nc*-TaN/*a*-SiN_x with ≥40 at.% of Si [Zema 04]);
3. *nc*-MeN/metal soft phase (e.g. Cu, Ni, Fe, Mo, Y, Ag, Co etc. [Musi 01c] [Musi 02a]), for example Zr-Cu-N [Musi 99], Al-Cu-N [Musi 01a], Zr-Ni-N [Musi 01b] [Karv 01];
4. *nc*-MeC/*a*-C (e.g. *nc*-TiC/*a*-C:H [Voev 97] [Zehn 04] [Pei 05]).

In the above classification, MeN denotes a transition metal nitride or a solid solution based on a transition metal nitride (Me=Ti, W, V, Zr, Cr, [$Ti_{1-x}Al_x$], [$Cr_{1-x}Al_x$], [$Zr_{1-x}Al_x$], etc.).

Nanocomposite coatings of groups 1 and 3 can show superhardness ($H \geq$ 40 GPa); their exact structural and mechanical properties strongly depend on the composition and on the condition of preparation. The SiN_x matrix (group 1), for example, can enable superior thermal stability and oxidation resistance by efficiently blocking grain coarsening [Nied 99] [Vepr 04a]. In coatings of group 3, the introduction of metal atoms is clearly related to a hardness increase. However the exact origin of hardness and superhardness in such coatings remains unclear since the same hardness can be obtained with very different microstructures (small/large grain size, strong/weak texture etc.). In particular the hardness enhancement cannot be attributed to the formation of a nanocomposite structure similar to the coatings of group 1 [Karv 01]. The coatings of group 2 are X-ray amorphous and show high thermal stability and oxidation resistance (> 1000°C), with a hardness in the range 20–40 GPa [Musi 07] [Musi 08b]. Nanocomposites of group 4, based on a-C or a-C:H, show excellent frictional behavior because the amorphous carbon transforms into nanocrystalline graphite, which acts as a solid lubricant [Haue 00] [Pats 01] [Pats 03].

2.1.4 Design rules for nanocomposite hard coatings

The first strategies for the design of hard coatings were introduced by Koehler [Koeh 70]. He predicted that epitaxial multilayer heterostructures could be strengthened if they consist of alternative layers of low and high elastic modulus, with a bilayer period Λ in the nanometer range. Due to the limitations of vacuum technology in these days, the concept could be verified only about twenty years later when sufficiently advanced vacuum technology became available. Progresses were then rapidly done in the field of nanometer scale multilayered hard coatings [Shin 92] [Yash 99]. However, the strong dependence of the achieved hardness on Λ, on the quality of the heteroepitaxial growth and on the incorporation of impurities can cause large variation in the coating properties when they are fabricated in industrial deposition units. Indeed gradual target erosion can lead to small variations of the deposition rate. Moreover high deposition temperature, single crystalline substrates and low background pressures are required, which is not industrially viable. In addition, multilayer structures show inherently anisotropic properties. The deposition of single-layer nanocomposite coatings was initially proposed as a way to avoid these problems [Vepr 95]. The isotropic microstructure of nanocomposite coatings should form automatically during deposition. To date, detailed design rules where proposed only for nanocomposite coatings of type *nc*-MeN/*a*-$\mathrm{SiN_x}$ and essentially by Vepřek an co-workers [Vepr 95] [Vepr 99] [Nied 01] [Vepr 05] [Vepr 07a].

The concept for the design of stable superhard nanocomposites according to Vepřek is the following:

- Stable nanocomposite coatings can be fabricated with an isotropic composition modulation at the nanometer range achieved by strong, thermodynamically driven, and diffusion rate-controlled spinodal phase segregation during deposition, that leads to a self-organization of the film microstructure.
- The film microstructure consists of a hard transition metal nitride (MeN) nanocrystalline phase, embedded in a thin matrix, typically amorphous, of an immiscible material. This second (minority) phase should show a high structural flexibility to fully cover the crystallites of the first (majority) phase and form a dense structure. *a*-$\mathrm{Si_3N_4}$ or *a*-BN are typically recommended for the matrix phase.
- Crystallites should be small enough so as to prevent dislocation activity; the matrix phase should be thin enough so as to reduce crack formation and propagation. The matrix phase should moreover act as a glue between the nanocrystals of the majority phase so as to hinder grain boundary sliding, i.e. the interfaces between the two phases should be strong (high cohesive energy), and defect-free (no voids, no impurity). The close relationship between hardness and microstructure is illustrated in Figure 2.3.

- In the case of *nc*-MeN/*a*-SiN$_x$ composite films deposited by reactive plasma PVD or CVD methods, the nitrogen activity should be sufficiently high (partial pressure $\geq 1 \times 10^{-3}$ mbar) to promote the formation of the transition metal nitride phase (instead of the formation of a silicide phase) and hence provide the thermodynamical driving force for phase segregation. Since spinodal decomposition is diffusion rate-controlled, a sufficiently high deposition temperature T (500–600°C) is needed to achieve full segregation (fast diffusion) during deposition.

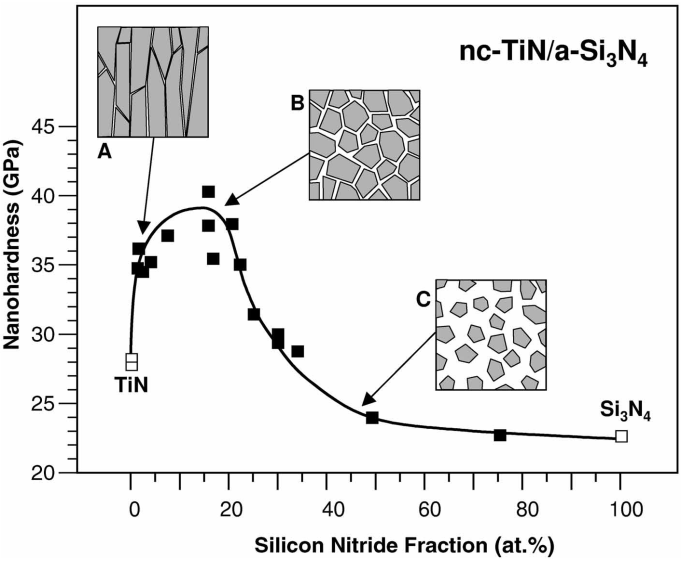

Figure 2.3: Simultaneous evolution of the nanohardness and the coating microstructure as the fraction of silicon nitride in nc-TiN/a-Si$_3$N$_4$ hard nanocomposite coatings is increased [Pats 03]. (A) The hardness increases due to the grain refinement induced by the introduction of silicon nitride. However material deformation can still occur by dislocation movements within the crystalline TiN phase and/or grain boundary sliding. (B) The hardness reaches a maximum as the dislocation activity is hindered in crystalline grains with a diameter D < 10 nm. The formation of a silicon nitride tissue phase with strong interface with TiN crystallites moreover prevents deformation by grain boundary sliding. Nanocracks are quickly stopped due to their frequent deviation at grain boundaries. (C) The propagation of nanocracks in the amorphous silicon nitride phase of increasing volume becomes progressively the dominant deformation process and hardness reaches the value found in pure silicon nitride.

When all these conditions are fulfilled, the hardness achieved can greatly exceed that predicted by a rule of mixture (i.e. linear interpolation between the bulk hardness of each individual phase material). According to Veprek, the maximum hardness is achieved when the matrix phase content, say a-SiN$_x$, approximately corresponds to the percolation threshold (long range connectivity) in the three-dimensional network of the nanocomposite, that is when the surface coverage of the crystallites equals approximately one monolayer of the matrix phase, independent on the exact grain size (that should anyway be kept small). The period of the segregated system (i.e. the grain size) results from the balance between the decrease of Gibbs free energy associated to phase separation and the increase of elastic strain energy at grain boundaries. By spinodal decomposition of immiscible materials, a regular structure is obtained with narrow size distribution of crystallites, sharp and strong (flaw free) interfaces. This is different from the structure expected if phase segregation would occur according to nucleation and growth process: one would expect a larger size distribution of crystallites. Hard coatings achieved by spinodal decomposition of immiscible phases are thermodynamically stable, which means that they are inherently thermally stable.

The design rules developed by Vepřek proved to be successful for the fabrication of many different hard and superhard coatings. However, the strict deposition conditions of sufficiently nitrogen activity and substrate temperature, and of high coating purity are often difficult to fulfill for industrial applications. In this case, incompletely segregated systems can be deposited with a lower hardness than if the above conditions would have been entirely fulfilled. If the deposition conditions are far from those prescribed by Vepřek, or more generally (i.e. also for systems different than the nc-MeN/a-SiN$_x$ system) if the deposition conditions do not allow spinodal decomposition, then the segregation occurs by successive steps of crystallite nucleation and growth, simultaneous diffusion and segregation of the second compound/element at the surface until a critical surface coverage is achieved that blocks the crystallite growth and forces repeated nucleation. This segregation in kinetically limited conditions was suggested by Barna, Petrov *et al.* [Barn 98] [Petr 03] and Patscheider [Pats 01] [Pats 03]. Sandu *et al.* recently described the formation and evolution of a nanocomposite structure in Zr-Si-N and Nb-Si-N systems deposited in such non-equilibrium conditions [Sand 06c] [Sand 08]. They reported a structural evolution as a function of the Si content divided into three composition regions. At low Si content hardness enhancement is obtained by solid solution hardening. By increasing the Si content, the (possibly metastable) solubility limit α of Si in the transition metal nitride is exceeded and the silicon atoms are segregated at the crystallite surface to form a SiN$_x$ tissue layer with increasing surface coverage of the Me-Si-N crystallites (transition region).

When further increasing the Si content, a constant SiN_x coverage is observed together with an inverse proportionality of crystallite size to Si content. The authors found that the pair (α, surface coverage) was dependent on the deposition parameters (deposition temperature, nitrogen pressure). This behavior is much different to that proposed by Vepřek. The results obtained by Sandu *et al.* illustrate the complexity of the morphology and hence hardness control in nanocomposite coatings deposited in conditions similar to industrial conditions.

At present, there is however no definite methodology to select a specific combination of materials and to chose the deposition conditions to produce a given coating microstructure with specific properties. Research in the field of hard nanocomposite coatings is still mainly empirical, proceeding by a so-called coating development (i.e. the systematic analysis of coating systems and the optimization of the deposition parameters to improve the properties of each coating) [Loff 94]. Prediction in the evolution of coating properties as a function of their composition and, for example, of a thermal treatment is in its infancy [Mayr 07a]. However, recent efforts toward the understanding of the critical properties of interfaces in nanocomposite systems [Vepr 07a] [Hao 06b] [Hult 07] [Sode 07a] on the one hand, and the definition of new routes for microstructural design (e.g. by use of post-deposition annealing [Mayr 06a]) on the other hand, should soon lead to improved and widen concepts for the design of multifunctional hard nanostructured coatings. In this regard, *ab initio* (first-principle) and thermodynamic calculations are valuable tools, now used in the field of hard coatings to predict e.g. decomposition thermodynamics and phase stabilities [Mayr 06c] [Mayr 07b] [Alli 07] [Zhan 07c] [Zhan 07d] [Zhan 07e] [Zhan 08a] [Zhan 08b] [Shen 08] [Alli 08] and interfacial bonding (energy, geometry, strength) [Hao 06a] [Hao 06b] [Hult 07] [Zhan 07a] [Zhan 07b].

2.2 The Al-Si-N system

2.2.1 The Al-Si-N phase diagram

The Al-Si and Al-N phase diagrams reported in [ASM 96] give AlN as the only stable binary phase. AlN does exist in the stable hexagonal wurtzite form and the metastable cubic NaCl form [Wrie 86]. In the Si-N system [Hill 92] [ASM 96], the only silicon nitride stable phase is reported with the Si_3N_4 stoichiometry. Si_3N_4 occurs into two hexagonal crystallographic forms: α-Si_3N_4 and β-Si_3N_4 [Grun 79] [ASM 96]. β-Si_3N_4 is usually considered as the stable form of Si_3N_4. The α- and β-Si_3N_4 forms both contain distorted Si–N_4-tetrahedra (i.e. Si four-fold bond coordination) and planar N–Si_3 units (i.e. N three-fold bond coordination). The crystalline structures of wurtzite AlN and β-Si_3N_4 are outlined in Appendix A (p. 198). In 1999, a novel high pressure polymorph of Si_3N_4 with a spinel (cubic) structure was discovered [Zerr 99]. This new form was initially given the name "c-Si_3N_4" ("c" for cubic), but later preferentially referred as γ-Si_3N_4 by analogy to other modifications of oxides. In this structure, nitrogen atoms form a (distorted) cubic, closed-packed (*fcc*) array where silicon atoms occupy interstitial sites in both tetrahedral and octahedral coordination in a 1:2 ratio [Krok 04]. The coordination number of two thirds of the Si atoms is hence increased from 4 to 6, as compared to α- and β-Si_3N_4, and the coordination number of all N atoms is increased from 3 to 4. The γ-Si_3N_4 is predicted to be twice as hard as the α- and β-Si_3N_4 forms (i.e. nanohardness $\gtrsim$ 30 GPa). This form was found to be metastable at ambient pressure up to at least 700 K.

The Al-Si-N ternary system has only been little studied up to now. The few data and attempts to elaborate a ternary phase diagram conclude that neither a ternary compound nor a solid solution are present in the system [Rogl 92], i.e. a mixture of AlN and Si_3N_4 is supposed to be formed, provided enough nitrogen is available. The only ternary phase diagram ever reported is shown in Figure 2.4 [Weit 90].

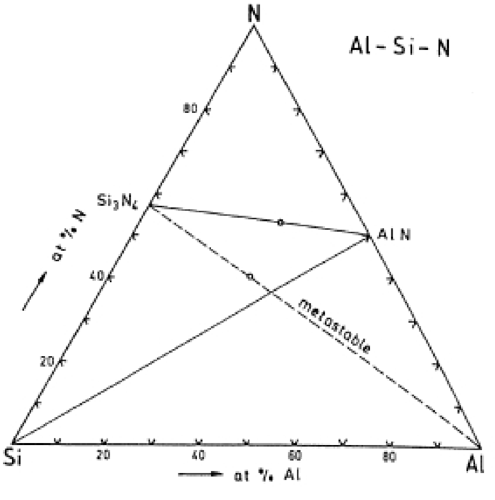

Figure 2.4: Isothermal section of the Al-Si-N system at 600°C [Weit 90].

The original studies conducted on Al-Si-N – and used to draw Figure 2.4 – consisted actually in bringing into contact pure Al and Si_3N_4 surfaces at

600°C and performing XRD, TEM and AES at the interface between the two materials [Weit 90] [Naka 86] [Bren 89]. Thermodynamic data indicate that the reaction $Si_3N_4 + 4Al \rightarrow 4AlN + 3Si$ is favorable, even at room temperature [Weit 90] [Bren 89]. However, after the formation of a thin layer of AlN on top of Si_3N_4, this layer acts as a strong diffusion barrier, making it difficult to reach the thermodynamic equilibrium. All experiments do not even detect such an AlN layer and conclude to a metastable equilibrium between silicon nitride and aluminium. The diffusion barrier formed by AlN would be so strong as to prevent the reaction, even after prolonged annealing.

Hillert *et al.* tried to predict the properties of the quasi-binary a Si_3N_4-AlN section in the Al-Si-N system [Hill 92]. The authors calculated a quasi-binary Si_3N_4-AlN phase diagram by neglecting the solubility of AlN in Si_3N_4 and of Si_3N_4 in AlN, and assuming an ideal solution model to the liquid phase. This model was based upon a ionic two-sublattice model of type $(Al^{3+})_p(N^{3-},SiN^0_{4/3})_Q$ where $Q = 3$ and p is varied with the composition. It was used so as to calculate the Gibbs free energy of the liquid solution from the assumed properties of pure AlN and pure Si_3N_4. From there, a Si_3N_4-AlN binary phase diagram was calculated and an eutectic liquid was predicted in the Si_3N_4-AlN system at 2269 K and 64.3 mol% of AlN. However the equilibria with the gas phase were neglected in the previous calculation. New calculations including the gas phase showed that the eutectic liquid decomposes by sublimation for a pressure lower than 6.7 bar. In addition it is showed that no liquid solution of AlN and Si_3N_4 at any composition can exist under ordinary pressure since both AlN and Si_3N_4 decompose by sublimation before they melt under a pressure of 1 bar. In particular Si_3N_4 decomposes into liquid Si and gaseous N_2 of 1 bar at 2114 K, that is at a temperature lower than the eutectic temperature given above. This explains the present lack of experimental information on the AlN-Si_3N_4 phase diagram.

The work of Spencer and Holleck is further note worthy [Holl 88] [Spen 90] [Spen 01]. They used thermodynamical calculation methods to predict not only stable but also metastable phase formation during the physical vapor deposition (PVD) of nitride, carbide and boride coatings. Unfortunately, no work was carried out on the Al-Si-N system. Kaufman also developed thermodynamical calculations for quasi-binary and quasi-ternary phase diagrams of ceramic systems, but did not publish any calculation for the AlN-Si_3N_4 system [Kauf 88].

2.2.2 Potential applications of Al-Si-N coatings

Potential applications of the Al-Si-N system are mainly based on the properties of AlN. AlN is transparent in the visible range of light and has the widest band gap (6.2 eV) within the group-III nitrides. Its refractive index is about 2.0 at a wavelength of 633 nm [Joo 99]. AlN is a hard covalent nitride with a good oxidation resistance. Oxidation of AlN causes the formation of a dense protective layer of Al_2O_3 that prevents fast penetration of oxygen into the bulk AlN material. The small electron affinity of AlN makes it also easy to extract electrons from the surface to vacuum. Starting from pure AlN, Si is added either as a dopant, to create n-type AlN, or is added to form Si_3N_4, a refractive hard material that provides additional oxidation resistance due to the microstructure of the Al-Si-N composite.

The potential applications, as found in the literature, are the following:

- Heavily Si-doped AlN is considered as an interesting material for optoelectronic applications in the deep UV spectral domain. It could be used in field-emission devices such as flat panel displays, the so-called field emission displays (FEDs) [Kasu 00] [Tani 04]. The Si-doping was found to drastically enhance the field-emission in AlN. Si-doped AlN is also interesting in n-AlN/p-diamond heterostructure diodes for UV-light emitters [Misk 03], as well as AlN p-i-n (p-type/intrinsic/n-type) homojunction Light Emitting Diodes (LED) [Tani 06a] [Tani 06b]. Interest in the doping efficiency of Si in AlN and the associated compensation mechanisms, as well as the optimum growth conditions, gave rise to a considerable amount of published data, both experimental [Tani 01] [Kasu 01] [Goen 01] [Tani 02] [Ive 05] [Herm 05] [Herm 06] [Monr 06] [Lebe 06] and theoretical [Bogu 97] [Matt 97] [Stam 02].

- Al-Si-N was proposed as a dielectric for dielectric-metal-dielectric type transparent heat-mirrors [Chib 05] [Chib 08]. Transparent heat-mirrors have a high infrared (IR) reflectivity (i.e. low heat emissivity) and a high transmission in the visible range of light. They are used for thermal power conversion (combined with a heat absorber), architectural windows, solar water-heating devices and transparent windows for furnaces. The DMD (D: dielectric, M: metal) or DMDMD multilayer structures are commonly used due to the flexibility of their design and their tunable spectral selectivity in the IR and in the visible [Fan 74] [Fan 85]. The infrared reflectivity is provided by the metallic (M) layer(s). Ag or Ag-alloys are typically used here. The dielectric (D) layers serve as transparent (protective) antireflection layers that increase the transmission in visible without lowering the infrared reflectivity of the metallic layer. Oxide materials (ITO[7], ZnO, TiO_2, etc.) are typically chosen. However, heat mirrors based on oxide dielectric materials suffer from environmental instabilities between the oxide and silver atoms; namely the silver atoms migrate and tend to oxide at the interface. Several oxygen-free materials were proposed to improve the interface properties. Among them, Al-Si-N was reported to be a promising candidate: it shows similar properties (optical transmission in the visible and shading coefficient[8]) as ITO-based multilayers. Chiba *et al.* reported a transmission in the visible of 79.7% and a shading coefficient of 0.50 for an AlSiN (43 nm)/$Ag_{95.8}Cu_{2.2}Nd_2$ (11 nm)/AlSiN (86 nm)/$Ag_{95.8}Cu_{2.2}Nd_2$ (11 nm)/AlSiN (43 nm) transparent low emissivity coating [Chib 08]. The Al-Si-N films were deposited by DC magnetron sputtering of an $Al_{30}Si_{70}$ target in a reactive atmosphere of Ar and N_2.

- The suitability of $AlSi_xN_y$ ($x \sim 0.31$, $y \sim 0.51$) was demonstrated as embedded layer for attenuated phase-shifting masks in the 193 nm lithography technology [Lin 00]. Phase-shifting masks are photomasks that take advantage of the interference generated by phase differences to improve image resolution in photolithography. Conventional photomasks are made of a quartz plate covered with opaque chrome features that form the pattern to be reproduced on a semiconductor wafer. In an attenuated phase-shifting mask, certain chrome features are replaced by another material (e.g. Al-Si-N in the present case) that lets a few percents of the light through, this weak transmitted light being however insufficient to expose the resist on the wafer. In addition the thickness of this semi-opaque material is chosen so that the transmitted light in the coated area of the quartz plate is 180° out of phase with the light transmitted through the uncoated quartz regions of the photomask. The resulting light interference increases the intensity contrast, thus sharpening the imprint in the exposed photoresist and increasing the resolution of the pattern transfer. To be suitable for such an application, Al-Si-N must show good etch selectivity with respect to the resist and the mask substrate (for the fabrication of the mask), as well as exposure durability to light irradiation (during photolithography), which

---

[7] Indium-tin-oxide

[8] The amount of the sun's heat transmitted through a given window compared with that of a standard 1/8-inch-thick single pane of glass under the same conditions, which is given a value of 1. The less solar heat is transmitted by a window, the lower its shading coefficient and the greater its shading ability.

was verified by Lin *et al.* [Lin 00].

- Al-Si-N layers were proposed as protective layers against corrosion for magneto-optical disks that employ rare earth transition metal alloy films [Maen 90] [Asan 87] [Miao 97]. The large refractive index of Al-Si-N was reported to be favorable to enhance a large Kerr effect[9]. The low temperature required for the RF sputter deposition of Al-Si-N films is suitable for such an application.

- AlN-Si_3N_4 codeposits prepared by CVD were identified as potential anti-oxidation coatings by Henry and co-workers [Henr 93] [Henr 95] [Mart 95] [Maze 97] [Henr 97] [Perr 97]. Chemical and structural characterizations of the codeposit were performed (see next section); XPS and thermogravimetric studies revealed that the oxidation of the codeposit was much slower than the oxidation of pure AlN, and that AlN and Si_3N_4 phases were simultaneously oxidized. The slow rate of oxygen diffusion was attribute to the formation of a mixed oxide phase of the mullite type (i.e.: $3Al_2O_3$, $2SiO_2$). Recently, Musil *et al.* reported data on the hardness, oxidation resistance and thermal stability of Al-Si-N sputtered films [Musi 08a]. The films were found to keep their mechanical properties up to an annealing temperature of 1000°C even after 4h, and to have an oxidation temperature as high as 1000–1100°C, which is much better than that of Ti-Al-N films, for example.

- Shortly after the present project was started, *nc*-AlN/*a*-SiN_x nanocomposites films were first proposed as potential optical protective coatings [Li 05], thanks to the hardness and transparency of AlN and according to the design methodology of nanocomposite films.

The most promising application of Al-Si-N – and the one that is subject to the most intense investigations – is in field emission devices. Light Emitting Diodes with a low emission wavelength of 210 nm were recently successfully fabricated by Taniyasu *et al.* [Tani 06a]. Such coatings are deposited at high temperature with a high crystalline quality.

---

[9] The Kerr effect is a change in the refractive index of a material in response to an electric field. The magneto-optical Kerr effect is the phenomenon that light reflected from a magnetized material has a slightly rotated plane of polarization. This effect is used for the reading function of (rewritable) magneto-optical disks: the change of light polarization enables to see magnetized domains and read the binary data stored in the magnetic media. The magneto-optical Kerr effect can be enhanced by decreasing the reflectivity of the magnetic sample, e.g. by coating the surface of a magnetic sample with a dielectric film.

As shown before, the first investigations on sputtered Al-Si-N coatings to be used as protective coatings were published already 20 years ago, but seemingly did not attract much interest in the thin films scientific community. Due to the large amount of scientific and technical efforts devoted to the production of new multifunctional hard coatings, the Al-Si-N system is subject to new interest, especially over the last 3 years.

2.2.3 Investigations on the local chemistry

As mentioned above, the Al-Si-N system is mainly investigated in the form of Si-doped AlN, that is to say for low silicon concentrations, much below one atomic percent. From quantum molecular dynamics calculations the substitutional configuration of Si on the cation Al site is the ground state (energetically most stable state) for Si-doped AlN [Bogu 97]. The existence of a ternary alloy or of a solid solution at higher silicon concentrations was excluded in the construction of the ternary phase diagram (Fig. 2.4). There is, however, only little thermodynamical data on the system, so that detailed investigations on the local chemistry in deposited Al-Si-N films are needed, all the more as the formation of metastable phases can be expected from depositions at high deposition rate and/or low deposition temperature [Spen 90] [Spen 01]. Here is an overview of the principal chemical investigations conducted on the Al-Si-N system.

In 1990, Maeno *et al.* proposed some indications for an Al-Si-N solid solution using XPS and Electron Probe Micro-Analysis (EPMA) data [Maen 90]. Al-Si-N and Al-Si-O-N films were deposited by RF sputtering from an AlSi target; the deposition temperature was not specified in the publication. The Al/(Al+Si) ratios explored were in the range 0.47–0.63. Pure Si_3N_4 and pure AlN were also deposited for comparison. The refractive index of Al-Si-N layers was found to vary with the Si content and all the samples were X-ray amorphous. XPS photoelectron peaks were fitted using three base components attributed to different bonding states, namely Al^0, Al–N–Si and Al–O on the one hand, Si^0, Si–N–Al, and Si–N–O on the other hand. Using EPMA data, the authors elaborated a model of composition and concluded to a mixture of AlN and Si_3N_5, rather than a mixture of AlN and Si_3N_4. They suggest this to be regarded as a the result of the substitution of AlN for Si in Si_3N_4. Due to a lack of experimental information and scientific argumentation however, such a conclusion should be considered with care.

A few years later, Henry and coworkers started investigations on AlN-Si_3N_4 co-deposits [Henr 93]. Low pressure CVD at high temperature (between 1000°C and 1300°C) was used to deposit Al-Si-N films on SiC. The precursors used were $AlCl_3$, $SiCl_4$ and NH_3, with N_2 as a carrier gas. One of the most detailed study was published by Mazel *et al.* [Maze 97]. The results of TEM (Bright Field/Dark Field/Electron Diffraction), high-resolution TEM (HRTEM), Electron Energy Loss Spectroscopy (EELS), Extended Energy Loss Fine Structure (EXELFS), XRD and SEM investigations were reported. Two samples were deposited at 1100°C. The first one, with an Si:Al ratio equal to 2 (as determined by EELS), was found to be amorphous, whereas the second one, corresponding to Si:Al = 1, was composed of nanocrystals of an average size of 5 nm and showing the AlN wurtzite structure, as determined by electron diffraction and XRD. Plasmon energy loss peaks (EELS) were recorded at intermediate positions between those of AlN and Si_3N_4, so that the authors concluded to the formation of a mixture of AlN and Si_3N_4. As an additional proof, EXELFS was performed on both samples and used to calculate Al–N, Al–Al, Si–N and Si–Si bond lengths. The latter were found to be very close to both experimental and theoretical bond lengths in pure AlN and Si_3N_4. Although not explicitly mentioned by the authors, this excludes the formation of an Al-Si-N solid solution in the studied films, since bond lengths would be expected to follow a Vegard law otherwise. A third sample was deposited at 1000°C with a higher Al content than in the two previous ones. Silicon segregation at the surface was reported on this sample. In addition, Si-rich and Al-rich samples were grown at 1300°C. The deposited structures were identified as α-Si_3N_4 and wurtzite AlN respectively, each with potential inclusions of the second nitride (not detectable by XRD). In a second publication, the same group reported results for samples deposited at 1100°C and EPMA, XRD and XPS characterization techniques [Henr 97]. Si_3N_4 was in all case identified as amorphous whereas AlN was well crystallized. Five compositions were studied (namely 100, 40, 20, 5 and 0 at.% of Al) and their Auger parameters were calculated using the Al $KL_{2,3}L_{2,3}$ and Si $KL_{2,3}L_{2,3}$ transitions. The Auger parameters were apparently not sensitive to variations in the composition. A broadening of the Auger peaks in Al-Si-N suggested however the presence of more chemical bonds than only Si–N_4 and Al–N_4 found in AlN and Si_3N_4. This was attributed to a large contribution of interface domains, associated to the possible formation of Si–N_xAl_y tetrahedra (with $x + y = 4$), as supported by the presence of a shoulder on the high energy side of the Si KLL signal.

Taniyasu *et al.* reported the formation of an Al-Si-N ternary alloy up to a few atomic percents of silicon in the wurtzite AlN lattice [Tani 01] [Kasu 01]. The authors grew Si-doped AlN at 900°C by low pressure Metal Organic Vapor Phase Epitaxy (MOVPE) from trimethylaluminum, silane and ammonia on SiC substrates. The lattice constants a and c of the deposited - strained - Al-Si-N layers were determined with a very good accuracy of 0.01% by high-resolution XRD. From there, the strain-free lattice parameters a_0 and c_0 were calculated, assuming a biaxial residual stress of the coating and using the elastic constants and the c_0/a_0 ratio of pure AlN. The a_0 and c_0 parameters thus calculated were found to linearly decrease with an increase of the Si content. Such a decrease followed to a good approximation the Vegard law, namely here a linear interpolation between the Al–N and the Si–N bond lengths. The authors concluded to the formation of an $\mathrm{Al_{1-x}Si_xN}$ solid solution in the range[10] $0 \leq \mathrm{x} < 0.12$ by substitution of Si atoms on Al sites in the AlN wurtzite lattice. For $\mathrm{x} > 0.12$, a progressive decrease and finally disappearing of the Al-Si-N diffraction peaks was observed. The authors suggested as an explanation either a maximum solubility of Si in AlN, or the presence of Si atoms on N sites or on interstitial sites. Note that oxygen was found to be below the detection limit in Auger Electron Spectroscopy (AES).

Hermann *et al.* deposited highly Si-doped AlN using plasma assisted Molecular Beam Epitaxy (MBE) at a substrate temperature of 860°C on sapphire [Herm 05]. N_2 was introduced with a RF plasma source, whereas Al and Si atoms were evaporated from effusion cells. The chemical composition was control by modifying the Si flux. The concentration of Si in the samples was ranging from 5.0×10^{19} cm^{-3} to 5.2×10^{21} cm^{-3}, as revealed by Energy Recoil Detection Analysis (ERDA)[11]. An average oxygen concentration of 8×10^{19} cm^{-3} was found in the samples. Growth under Al-rich conditions led to a strong Si surface segregation with a silicon concentration gradient over the layer thickness, whereas the silicon concentration was found to be homogeneous under N-rich conditions. High-resolution XRD and Atomic Force Microscopy (AFM) studies revealed that the crystalline quality was deteriorated for a silicon concentration of $[\mathrm{Si}] > 1.1 \times 10^{21}$ cm^{-3}, as evidenced by a sudden increase of both the FWHM of the rocking curve of the AlN (002) diffraction peak and of the root-mean-square (rms) surface roughness. The authors claimed that this "might be due to the formation of an AlSiN alloy". This deterioration of the crystalline quality was accompanied by a decrease of the activation energy of the conductivity and an increase of the room temperature conductivity. The authors suggested the formation of an

---

[10] corresponding to 0–6 at.% of Si over the total composition of Al-Si-N in term of Al, Si and N atomic content.

[11] A concentration of $[\mathrm{Si}] = 5.2 \times 10^{21}$ cm^{-3} corresponds to about 5.4 at.% of Si, taken over the total Al, Si and N composition.

impurity band at high Si concentrations. For lower Si concentrations, the authors suggested the formation of Si DX centers [12], related to a Si-induced compressive stress that relaxes for [Si] $> 5.3 \times 10^{20}$ cm^{-3}. This suggestion is based on theoretical calculations (cf. [Bogu 97]) according to which the N-rich growth conditions favor the Si_{Al} incorporation (i.e. the incorporation of a Si atom on an Al lattice site) over the Si_N incorporation, which is favored by Al-rich growth conditions. To summarize, the reported data suggest that the formation of an $\mathrm{Al}_{1-\mathrm{x}}\mathrm{Si}_{\mathrm{x}}\mathrm{N}$ solid solution is possible in N_2-rich growth conditions, whereas Si segregation is favored by Al-rich growth conditions. The authors stay however inconclusive regarding the formation of a solid solution and the solubility limit of Si in AlN. They mention nevertheless in [Herm 05] that no indications for Si saturation was found when increasing the Si flux. In [Herm 06] they moreover report that "under nitrogen-rich growth conditions silicon can be homogeneously incorporated up to Si concentrations of [Si] $= 5.2 \times 10^{21}$ cm^{-3}", which can be understood as the formation of an Al-Si-N solid solution. This would be in agreement with the solubility limit of 6 at.% reported by Kasu *et al.* in [Kasu 01], even if Hermann *et al.* do not literally identify the above reported concentration as a solubility limit.

Besides these three main studies of Henry *et al.*, Taniyasu *et al.* and Hermann *et al.*, all conducted on high temperature CVD deposition processes, little was reported on the local chemistry in the Al-Si-N system. Few studies were published on Al-Si-N films deposited by low temperature PVD techniques. However, as a consequence of the ternary phase diagram given in Figure 2.4, the possible existence of a solid solution was little if not at all considered in the reported investigations. XRD peaks that only indicate the presence of stable wurtzite AlN, and XPS photoelectron peaks very close to the ones expected for $\mathrm{Si}_3\mathrm{N}_4$ and AlN were easily taken as a proof for the formation of an AlN-$\mathrm{Si}_3\mathrm{N}_4$ two-phase mixture [Mart 01] [Bend 02] [Musi 02b] [Li 05]. In all cases, AlN was found crystalline, whereas $\mathrm{Si}_3\mathrm{N}_4$ was identified as amorphous, as a consequence of the low deposition temperature. These few studies tend to say that there is no ternary compound, at least at low deposition temperatures, but they actually provide no strong indication that supports this statement. From the published data, it cannot be concluded if a mixture of AlN and $\mathrm{Si}_3\mathrm{N}_4$ or a ternary Al-Si-N solid solution (or both) was produced.

---

[12] Namely Si atoms moving off the substitutional Al site towards an interstitial position, associated with an important lattice distortion and the formation of a deep donor level [Chad 88] [Moon 90] [Bran 03] [Wall 04].

Since the present work deals with the preparation and characterization of Al-Si-N hard nanocomposite coatings, the results of the only study ever carried out on the subject before 2005[13] should be reported here. This work was published in 2005 by Li *et al.* [Li 05]. The authors claimed to have deposited nc-AlN/a-SiN$_x$ nanocomposite films by asymmetrical dipolar pulsed DC power magnetron sputtering from Al and Si target under an Ar/N$_2$ mixture at 200°C. A RF bias was applied to the Si and glass substrate during deposition. AlN and SiN$_x$ were deposited in turn by rotating the substrate holder, facing alternatively one target and the other, and varying the staying time in front of the Al target. Ten samples were deposited with compositions ranging from pure AlN to pure SiN$_x$. In their paper, the Si content is unfortunately partly specified in term of "staying time", and partly in term of "Si target duty ratio", without giving either a correspondence between the two "units" or a direct measure of the silicon concentration. TEM investigations on two samples revealed a grain size of the order of 4–10 nm. It is however not clear whether the samples are multilayered or show an isotropic nanostructure. The authors proposed that a higher Si content lead to the formation of smaller AlN crystalline grains by hindering the nucleation of AlN. Hardness measurements (technique not specified) showed a hardness enhancement for an intermediate Al-Si-N composition (corresponding to 40% of Si target duty ratio) with a maximum of 30 GPa. Estimations (details not specified) of the mean grain separation at this composition showed that only a few monolayers of SiN$_x$ separate the crystallites. Transmission in the visible spectral range was found greater than 85% for a thickness of 1.2 μm, independent of the grain size and of the composition. These promising results are however tarnished by the lack of clear descriptions of the deposition and characterization conditions, as well as a limited critical discussion of the results.

To complete this overall picture of the Al-Si-N system, the role of oxygen needs to be discussed. AlSiON films are for example considered as promising for optical and optoelectronics applications. In particular the index of refraction of these films was found to be tunable by varying the composition between AlSiN$_x$ (n = 2.20) and AlSiNO$_x$ (n = 1.65) [Mart 01] [Bend 02]. In the mentioned studies, the films were deposited by filtered cathodic arc deposition from an Al/Si alloy target under N$_2$/O$_2$ gas flow. The hardness of the films was found to be strongly dependent on their oxygen content. The hardness decreases from 22 GPa for AlSiN$_x$ to 18 GPa for an oxygen

---

[13] Since 2005, only two publications dealt with Al-Si-N hard nanocomposite coatings: [Peli 07] (Pélisson *et al.*, i.e. this work) and [Musi 08a] (Musil *et al.*).

content of about 15 at.% in AlSiON. This was measured by nanoindentation using a Berkovich indenter. Note that oxynitride systems based on the Al-Si-O-N quaternary system, including the so-called "sialon" ceramics, are widely studied and have gained considerable technological, importance similar to silicon nitride and silicon carbide systems [Cao 91] [Chen 97] [Rose 99] [Krok 04]. Al-Si-O-N based systems are principally synthesized by sintering, usually making use of sintering additives such as Li, Ca, Mg, Y. A detailed XPS study of such an oxynitride system is for example reported by Schneider *et al.* [Schn 97].

As a conclusion, Si-doped AlN deposited at high temperature is extensively studied, but the local chemistry in Al-Si-N systems containing more than a few atomic percents of silicon is not well understood. In particular, no study on the local chemical composition of PVD samples deposited at low temperature is available. Concerning films deposited at high temperature, the formation of a solid solution is reported for Si atomic concentrations below about 6% [Kasu 01]. From the reported data, this solubility limit may actually be as low as 4 at.% [Tani 01], but it could also be higher than 6 at.%, since no crystallographic data is available for a higher Si concentrations, that would enable to check this upper limit. No further study was conducted on this issue. Evidence for Si surface segregation (Al-rich deposition conditions) on the one hand, and homogeneous two phase mixture of AlN and Si_3N_4 (N-rich deposition conditions) on the other hand, is also found in the literature.

Part II

Experimental methods

Chapter 3

Thin film deposition method

Al-Si-N thin films were deposited by reactive closed field unbalanced magnetron sputtering (CFUBMS). This is one of the many different modes of physical sputter deposition, that ranges from conventional DC and RF sputtering [Ohri 02] [Ross 03] to DC pulsed reactive magnetron sputtering [Spro 98] and now to the development of high power pulsed magnetron sputtering[1] (HPPMS) [Kouz 99] [Spro 05] [Helm 06]. In this chapter the basics of magnetron sputtering, CFUBMS and reactive sputtering are introduced, together with some insights into the obtained film morphology.

3.1 Reactive magnetron sputtering

3.1.1 Sputtering process

Sputtering is a physical vapor deposition (PVD) process that involves the kinetic ejection of atoms from a solid source known as target. This is the result of a sequence of energetic collisions with accelerated ions from a gas phase. The mass and energy of the incident particles determine the regime of the resultant collision process. At incident energies in the 50–2000 eV range, near-surfaces atoms are displaced in a random collision sequence and may receive enough kinetic energy to overcome the surface binding energy and be emitted from the target. This is known as the "collisional" or "knock-on" sputtering regime, and this the one used for thin film deposition [Ross 03]. At incident energies of 2–50 keV, collision cascades may break atomic bonds in a larger region near the impact point. This regime is however not used for thin film deposition. For incident energies larger than 50 keV, the incident particles may penetrate deeply below the surface before they release their

---

[1] also called high power impulse magnetron sputtering (HIPIMS)

energy. The incident particles are implanted in the material and the sputter yield (yield = *number of emitted particles / number of incident particles*) drops since little energy is released near the target surface. These and further interactions due to ion bombardment are schematically illustrated in Figure 3.1. Once particles are emitted, they travel in the evacuated chamber with their initial velocity until they either collide with a residual gas particle or until they impinge on a nearby surface (in particular on the substrate material) and condense to form a thin film.

In sputter deposition, the ion bombardment of the target surface is typically achieved in a plasma environment or in a ion beam configuration. In the plasma system, a plasma of neutral (e.g. Ar) and/or reactive (e.g. N_2) gas is created between an anode and a cathode (diode configuration). The anode is usually the grounded chamber wall, which is in electrical contact with a so-called ground shield placed in the vicinity of the target. The target material is biased negatively and constitutes the cathode. Positive ions in the plasma near the cathode region are accelerated at high energy onto the cathode surface and cause the sputtering of the target surface. In this diode configuration, the plasma is sustained by the emission of secondary electrons from the cathode surface caused by ion bombardment. These electrons are quickly accelerated in the gas phase and cause additional ionization of gas atoms.

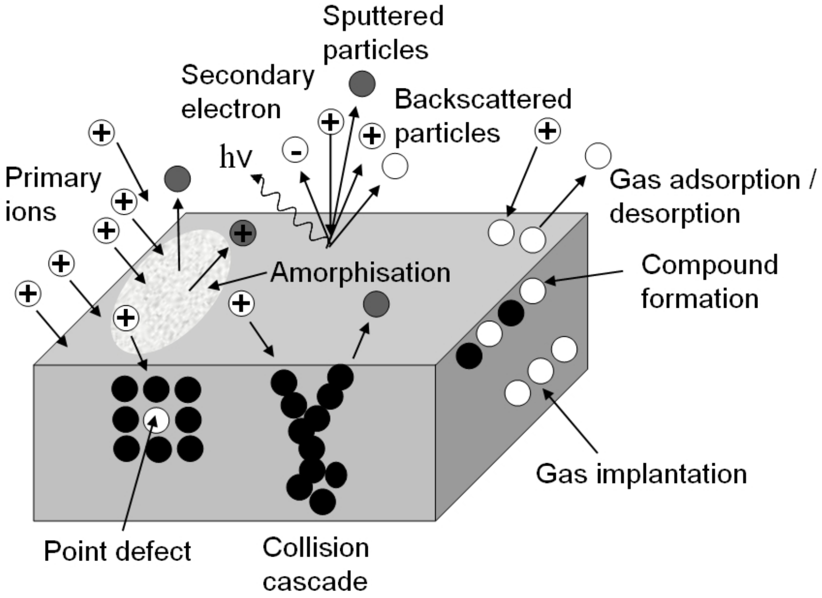

Figure 3.1: Interactions due to ion bombardment on the sputter target.

3.1.2 Magnetron sputter deposition

Originally DC diodes were used to vaporize target material at rates much higher than corresponding to their thermodynamical vapor pressure. However this configuration was very inefficient due to the poor utilization of secondary electrons emitted from the target and the resulting low plasma density. Increasing the chamber pressure allowed to increase the coupling of secondary electrons with the plasma, although without any improvement of the deposition rate, due to the increasing number of in-flight scattering collisions of sputtered atoms and the background gas. The introduction of RF diodes not only facilitated the use of dielectric targets, but also resulted in a better coupling of the energy of electrons to the plasma. Due to their oscillations in the plasma, the energy of electrons was increased through a wave-coupling process and the kinetic energy of secondary electrons was eventually better transferred to the plasma, resulting in a higher plasma density. The main drawback of RF diodes is, however, the need of a high frequency matching network to efficiently couple the power from the power supply into the plasma, meaning additional equipment cost and complexity of use. Hollow cathode diodes were introduced to trap secondary electrons in a hollow cavity and have them oscillate between opposite surfaces of the cathode to increase the plasma density, which was, however, still not an ideal solution. Magnetron plasma devices were proposed in this context so as to increase the efficiency of DC and RF diodes.

Principle When a magnetic field is added near the cathode region, a magnetic confinement of the plasma can be created. The field alters the trajectory of secondary electrons that spiral around the magnetic lines in the vicinity of the target. The electrons are localized on the field lines and their path length is greatly increased by one or several orders of magnitude. This results in a higher probability of ionizing electron-atom collisions and hence in an increased plasma density near the target surface. In turn, the ion bombardment of the target is intensified, leading to higher sputter rates as well as greatly increased deposition rates that are then of interest for industrial applications. Indeed the beneficial effect of the magnetic field on the plasma density enables to reduce the operating pressure down to a few μbar. In this pressure region the sputtered particles can fly off in a ballistic trajectory to impinge on the substrate. There is almost no loss of particle directionality and kinetic energy through scattering collision in the gas phase, i.e. there is little or no thermalization of the particles at this pressure. As compared to the basic sputtering mode, magnetron cathodes can be operated at lower discharge voltages (a few hundreds volts against a few kV without magnetron). At the same time much higher current densities can be attained at the cathode: tens to hundreds of mA/cm^2, being three to four order of magnitude larger than without magnetron. Limitations of the power applied to magnetron sputter sources come then either from the current limit of the power supply or from the limited efficiency of heat transfer from the target to the water-cooling system.

In practice, small magnets are arranged in a ellipse-like or a circular ring at the back of the target so that the drift path (Lorentz force) of electrons forms a closed loop. In the case of a planar target with a circular arrangement of magnets, the magnetic field is radial to the surface and the closed-loop path is a broad circular band at the target surface. In this region, the target erosion proceeds faster and an erosion track is progressively formed during sputtering, as shown in Figure 3.2. This zone of intense erosion is often called "the racetrack".

Unbalanced magnetron sputtering In all PVD processes, ion bombardment of the growing film is a critical parameter which strongly influences the film properties. In particular, the use of a low ion bombardment can promote the deposition of dense films with a good adhesion to the substrate. This is in particular beneficial in the deposition of hard, wear-resistant coatings, low friction coatings and corrosion-resistant coatings. Ion bombardment can be achieved by applying a negative bias to the substrate. An increase of the substrate bias causes an increase of the energy of the bombarding ions. This, however, eventually leads to the formation of defects in the growing film (including the incorporation of gas atoms) and to the generation of compressive stresses. Instead, a high flux (> 2 mA/cm^2) of relatively low energy (< 100 eV) ions should be used [Kell 00]. In conventional "balanced" magnetrons, the plasma is strongly confined within a few centimeters above the target surface. The substrate however cannot be placed in this region since it would be subject to concurrent re-sputtering during film growth. Moreover such a short target-to-substrate distance is not suitable for the deposition of homogeneous coatings on larger surfaces, as commonly the case in industry. In contrast the plasma density in regions located further away from the target is insufficient for a beneficial ion bombardment of the growing film. A solution is provided by the use of an unbalanced magnetron configuration. This configuration was first proposed in 1986 by Window and Savvides [Wind 86a] [Wind 86b] [Savv 86], patented in 1990 by Teer Coatings Ltd. and is widely used since then. In this configuration, the magnetic field at periphery of the target is strengthened relative to the central pole. As a result the field lines are not all "closed" but some are directed toward the substrate so that secondary electrons can escape their confinement. The plasma is then extended further away from the target surface to the substrate, creating ideal conditions for ion bombardment. The ion current on the growing film is increased by one order of magnitude (5–10 mA/cm^2 [Kell 00] [Ohri 02]) as compared to a balanced magnetron configuration. The schematic representation of an unbalanced magnetron is given in Figure 3.2.

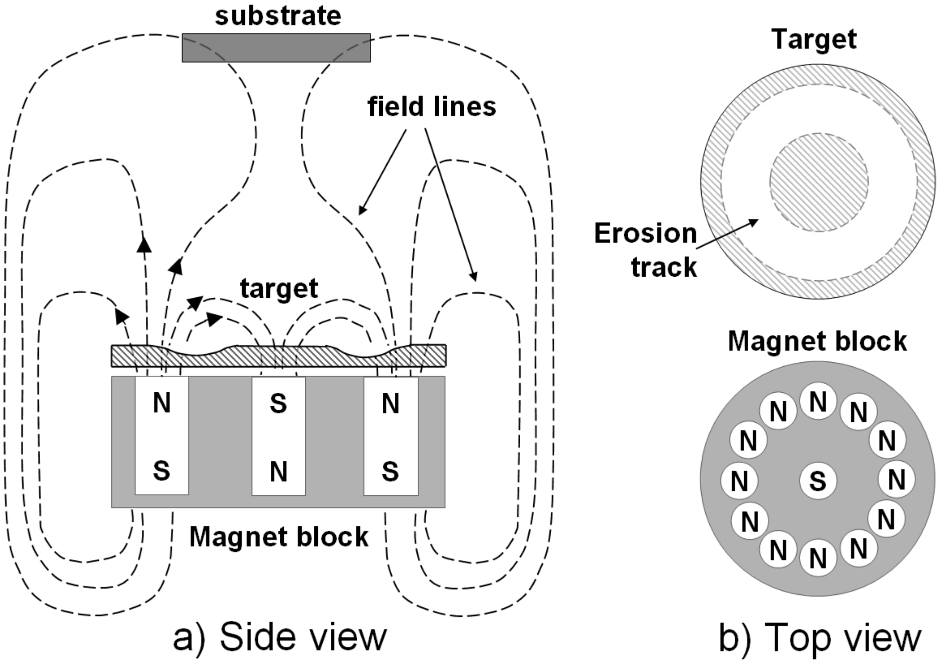

Figure 3.2: Schematic representation of an unbalanced magnetron.

Closed-field unbalanced magnetron sputtering(CFUMS) For the deposition or multicomponent coatings or to uniformly coat complex shapes at acceptable deposition rates, it is often useful to operate several magnetrons at the same time. Adjacent magnetrons can be configured with the same or with opposite magnetic polarities. In the latter case, this configuration is termed "closed-field" since the field lines are closed between the magnetrons, as shown in Figure 3.3. In this way secondary electrons are confined in the region between the target and the substrate, far away from the walls of the deposition chamber. The plasma density is high at the substrate, and the ion-to-neutral particle ratio impinging at the substrate is 2–3 times higher than in a single unbalanced magnetron configuration [Kell 00].

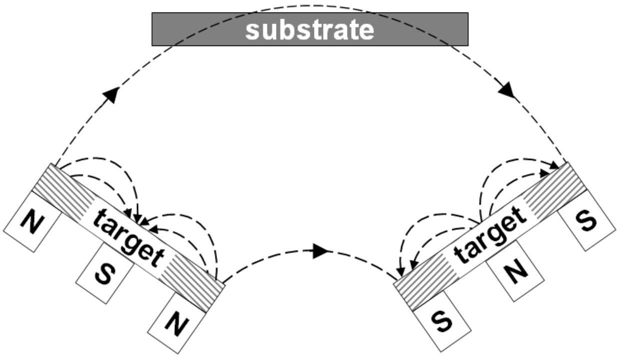

Figure 3.3: Schematic representation of a confocal closed field unbalanced magnetron configuration with two sputter guns.

3.1.3 Reactive magnetron sputtering

Metallic multicomponent films can be deposited from compound targets with the desired stoichiometry. Oxide, nitride, carbide and sulfide compounds can however also be deposited by sputtering from metallic target in the presence of a reactive gas (oxygen, nitrogen, acetylene, etc.) usually mixed with an inert working gas (Ar). Since high purity (ductile) metal targets are easier to manufacture than (brittle) compound target, this is often the preferred solution, all the more as high purity gases are commercially available. In addition, this technique enables the use of DC power, which is much less complex and expensive than RF power. Furthermore the cooling of metallic targets that are thermally conductive is much more efficient, which gives access to higher applied powers to the target.

Depending on the amount of reactive species introduced in the deposition chamber, a solid solution of metal doped with the reactive element can be deposited as well as a compound or a multiphase alloy. A wide range of composition is accessible. The deposition conditions are nevertheless greatly influenced by the reactive gas flow, as shown in Figure 3.4. When the reactive gas flow is low, the reactive species are entirely removed from the gas phase by adsorption at the substrate and the cathode surface (interval AB). As a result the chamber pressure remains constant as if no reactive gas was added. The deposited film is metal-rich. When the gas flow is increased, the concentration of the reactive species in the deposited film increases. In addition, the reactive species start to react with the target surface: the sputter target becomes "poisoned". This results in a reduced sputter yield of the compound target surface as compared to the sputter yield of the pure metallic surface. At constant power applied to the target, this usually leads to an increases of the secondary electron emission, that is to say a decrease of the impedance of the plasma and a decrease of the discharge voltage on the

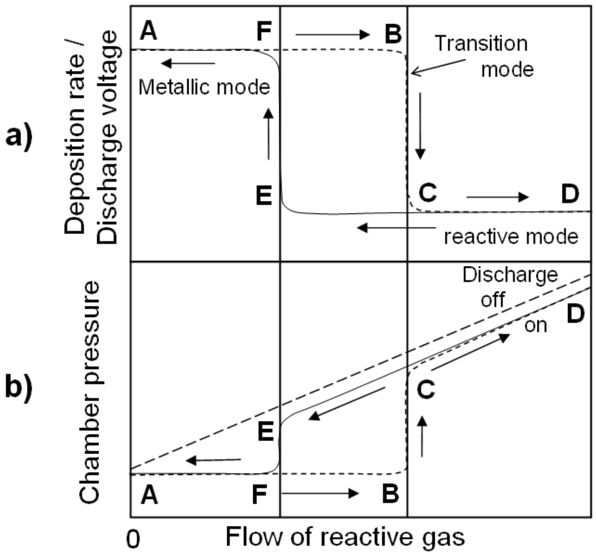

Figure 3.4: Hysteresis behavior of reactive magnetron sputtering (here at constant partial pressure of the non-reactive gas and at constant sputtering power): effect of the reactive gas flow (a) on the deposition rate and the discharge voltage (same qualitative evolution) and (b) on the chamber pressure (or reactive gas partial pressure). The different sputtering modes are indicated.

target (Fig. 3.4a). In turn the deposition rate is also reduced. At moderate reactive gas flows, the surface compound is readily sputtered away from the target surface. In the case of magnetron cathodes, a differential poisoning of the target surface is observed, as the poisoning is more prominent outside than inside the racetrack (erosion track) [Safi 00]. At a critical reactive gas flow, however, the surface of the target is entirely covered by a compound and the sputter yield drops radically (interval BC). As a consequence the pumping rate of reactive species at the target surface also drops, which is evidenced by a sudden increase of the chamber pressure (Fig. 3.4b). The chamber pressure remains anyway lower than if the discharge was off. For a further increase of the flow of reactive gas, the reactive species are in excess and the chamber pressure linearly increases with the gas flow (interval CD). The deposited films are "gas-rich" (i.e. rich in the nonmetal introduced as the gas). When the reactive gas flow is decreased from that high reactive gas flow, the metallic state of the target surface is reached at a much lower flow that the critical flow previously defined due to the lower sputter yield of the poisoned target (interval DE). The difference in sputter yield for the metal and the compound (e.g. Al and AlN) gives rise to the hysteresis effect shown in Figure 3.4. Within the hysteresis region (BCEF loop), the deposition conditions are unstable. Often the desired film composition is achieved only in the reactive mode (interval DE), however with a reduced deposition rate as compared to deposition rate achieved in the metallic mode (interval AB). When higher deposition rates are needed or when an under-stoichiometric composition is aimed at, one needs to work in the transition region (interval BC). This implies to find a way to control the deposition conditions in this region - due to the steep slope, i.e. fast change of film properties upon small flow changes, the flow control of the reactive gas is far from being ideal here. An easy way is to increase the pumping speed of the pumps used to evacuate the chamber during deposition. Above a critical pumping speed, the hysteresis effect can be suppressed and the deposition is stable over the whole range of reactive gas flow and film composition (gradual transition between metallic and reactive modes of sputtering) [Safi 00] [Musi 05] [Berg 05]. This is however not always possible due to the considerable additional costs, in which case alternative fast control procedures are available to work inside the hysteresis region. This includes plasma emission monitoring and voltage control in real time during the reactive sputter process (feedback control system) to work in the transition mode (interval BC) [Safi 00] [Spro 05]. A further issue comes from frequent arcing events occurring on the poisoned target surface. As mentioned before, DC sputtering is often preferred to RF sputtering. A major problem of DC reactive sputtering is however the build-up and accumulation of charges on the poisoned regions of the target surface, resulting in localized arc discharges and eventually target damages. Today's DC power supply units can efficiently suppress micro-arc events on a time scale of microseconds. The suppression of severe arcing however requires the use of more sophisticated procedures, the simplest one being pulsed DC reactive magnetron sputtering (with pulse in the range of 10–300 kHz) [Spro 98] [Safi 00] [Musi 05] [Berg 05] [Spro 05]. All these alternative techniques require either additional equipment and/or time-consuming optimization experiments. As a consequence, reactive sputtering is often simply run in the reactive mode with DC power and flow control of the reactive gas, despite the loss of deposition rate, since the process is stable and the film properties easily reproducible with these deposition conditions.

3.1.4 Deposition chamber used in this study

The deposition machine used in this work is an ATC 1500-F Sputtering System from AJA International, Inc. (USA). A picture of the deposition chamber is given in Figure 3.5, together with a schematic representation of the chamber Figure 3.6. The machine is composed of a small load lock (introduction) chamber and a large deposition chamber (Ø 15", height 13")

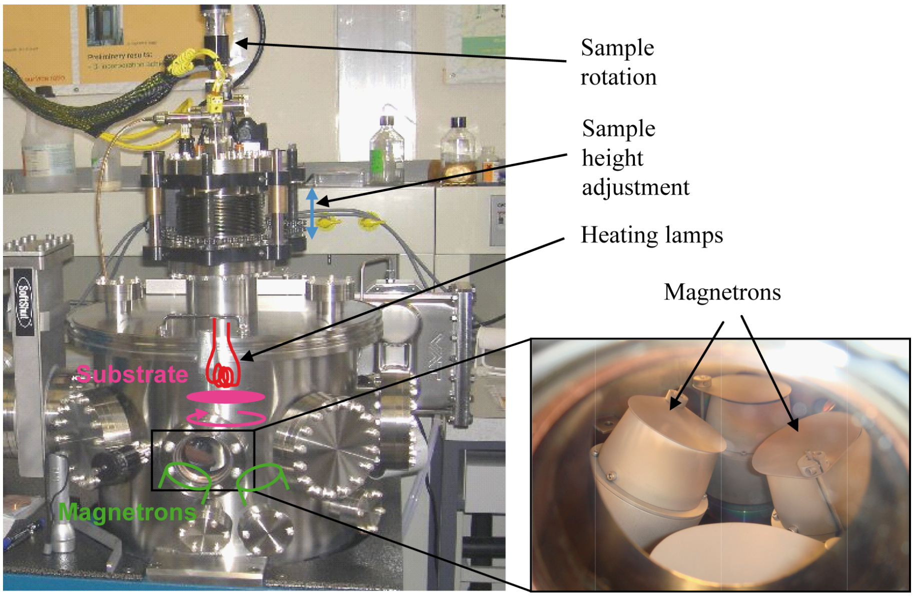

Figure 3.5: UHV sputter deposition chamber equipped with four magnetron guns. In the sputter guns, targets are surmounted by chimney sets closed by shutters.

containing four inclinable magnetron sputter guns. The substrates can be mounted face-down on a heated substrate holder rotating about 12 cm (adjustable height) above the Ø = 5 cm (2") targets. The sputter guns are tilted so that they point toward the center of the substrate holder in a confocal way. The sputter targets (cathodes) are each surrounded by a ground shield (grounded anode) and surmounted by a conical chimney closed by a shutter. The resulting higher pressure obtained in the vicinity of the targets enables to ignite the plasma (shutter closed) and sustain it (shutter opened) at low pressure in the deposition chamber. The sputter targets are operated with DC power. A RF bias can be applied to the substrate, that is suitable when insulating materials are deposited. The gas species, here Ar and N_2, can be injected either directly at the bottom of the chamber, between the magnetron blocks, or at the target surface. For this second option, the gas is injected within the magnetron chimney and homogeneously distributed at the target surface thanks to a gas ring.

The deposition conditions used to elaborate nanocomposite and multilayers thin films based on the Al-Si-N system are given at the beginning of Chapters 5 and 6. After deposition, the films were characterized with the analytical techniques described in Chapter 4.

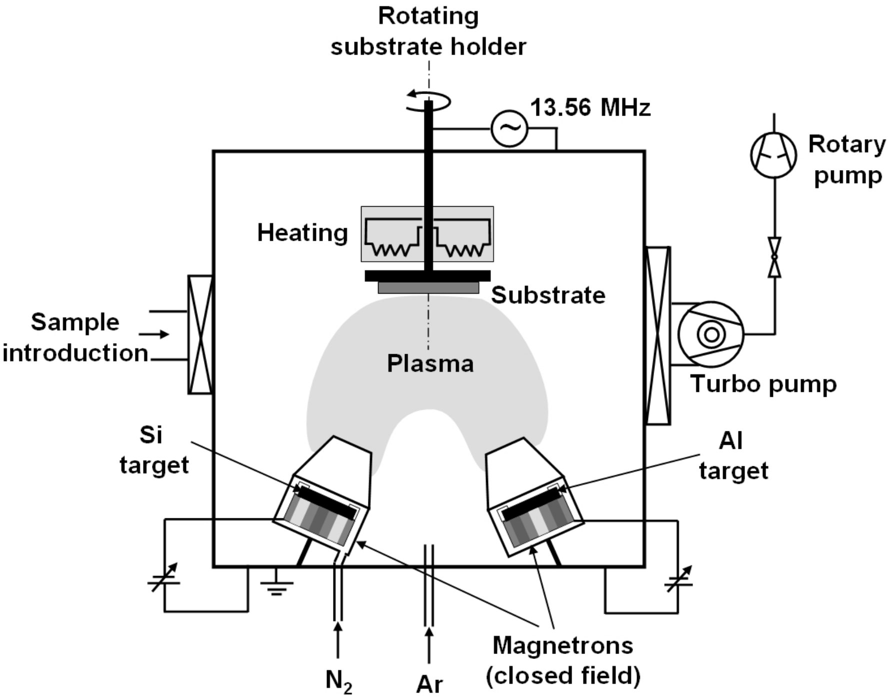

Figure 3.6: Schematic view of the sputter deposition chamber. Two magnetrons were used equipped with a Si target and an Al target. The magnetrons are in unbalanced closed field configuration.

3.2 Film growth and morphology

Major advantages of magnetron sputter deposition over e.g. evaporation or CVD processes is the high deposition rate that can be achieved and the low substrate temperature T_s, often less that 0.2–0.3 of the melting point T_m (in Kelvin). In these conditions films are grown far from thermodynamic equilibrium and kinetic effects play a major role, so that metastable phases can be synthesized [Holl 88]. The film microstructure (grain size, crystallographic orientation, defects, surface and bulk morphology) is the result of the specific deposition conditions used. Surface and bulk diffusion rates are among the most important physical parameters for the control of the microstructural evolution of thin films. The homologous temperature T_s/T_m is generally recognized as the primary parameter that controls diffusion rates and subsequently the film microstructure. Structure Zone Models (SZM), constructed by the compilation of experimental results, have been developed to systematically categorize the structural evolution of thin films during PVD deposition as a function of one (usually the homologous temperature) or several deposition parameters. The second variable usually attempts to describe the influence of the simultaneous bombardment of the growing film with energetic particles: the deposition pressure [Thor 74], the substrate bias [Mess 84] and the ion-to-atom ratio at the substrate [Kell 98] are the chosen parameters. The most famous SZM is shown in Figure 3.7 and was developed by Thornton [Thor 74] [Thor 77].

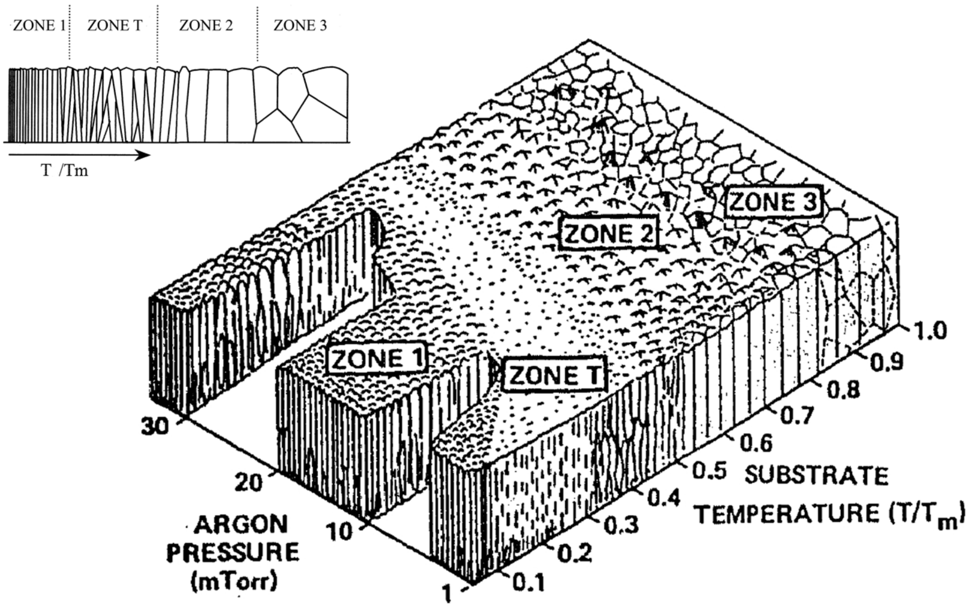

Figure 3.7: Structure zone model developed by Thornton [Thor 77]: schematic representation of the influence of argon pressure and substrate temperature on the morphology of the growing film. T is the absolute temperature and T_m is the melting temperature of the coating material. A profile of the structure model is given in insert to emphasize the main structural characteristics [Barn 98].

This structure zone model is divided into three zones plus a transition zone between zone 1 and zone 2. At low homologous temperatures (zone 1), the adatom mobility is low and the films develop an underdense structure with a fine fiber texture. Atomic shadowing is the dominant process. The columns, either composed of equiaxed grains or amorphous, are separated by pores, or voids. The surface roughness is usually quite prominent. At higher homologous temperatures, surface diffusion becomes significant (zone T). The columnar appearance is retained but the formation of voids is suppressed; the films are dense. Grain coarsening occurs during coalescence of small islands, resulting in an orientation selection of the growing crystallites. Competitive grain growth takes place and the structure is inhomogeneous along the film thickness. Small randomly oriented crystallites near the substrate evolve in larger crystallites with a pronounced texture (preferred crystallographic orientation(s)) as the film grows, giving rise to characteristic V-shape grains. Anisotropic surface diffusivities and adatom potential energies determine which crystallographic orientation will be dominant. Kinetically disadvantaged columns quickly disappears during the growth. This is exacerbated by simultaneous atomic shadowing effects. The grain boundary migration (bulk diffusion) remains however limited in this region. At still higher $\mathrm{T}_s/\mathrm{T}_m$ (zone 2), bulk diffusion becomes significant and grain migration can occur also to minimize interface and surface energies. This phenomenon is added to the initial orientation selection at the initial stages of film growth. As a result the selection is quicker, the grains are larger and the surface roughness decreases. The film structure is homogeneous in thickness: the columns extend from the bottom to the top of the film with grain boundaries perpendicular to the film plane. At again higher substrate temperatures (zone 3), the structure is characterized by equiaxed three dimensional grains (no columnar structure anymore) as the result of bulk diffusion process, recrystallization and grain growth. The structure is fully dense.

Modifications, or updates, of this original model were successively proposed to take into account the evolution of the sputtering systems used. For example a model was developed specifically for closed field unbalanced magnetron systems [Kell 98] [Kell 00], where the $\mathrm{T}_s/\mathrm{T}_m$ values at the zone boundaries are modified. The effects of ion irradiation, on the one hand, and of the introduction of impurities, on the other hand, were specifically studied [Petr 03] [Barn 98]. Low energetic ion bombardment, already mentioned before, can be used to influence the film properties while keeping the substrate temperature low. A bias can be applied to the substrate to increase the ion bombardment of the growing surface so as to densify the structure. However the increasing energy of impinging ions as the bias is increased results in lattice damages, compressive stresses and inert gas incorporation. By increasing the ion flux and keeping the ion energy below the threshold for bulk lattice displacements ($\lesssim$ 20 eV), the texture can be dramatically influenced while limiting the residual stress and avoiding lattice damages. This is one of the great advantages of UBMS systems. Petrov *et al.* presented the distinct effects of ion flux and ion energy on the evolution of the film microstructure [Petr 03]. The authors showed that the use of ion to atom ratios larger than 5 can enable to control the microstructure evolution, in particular the texture evolution, due to the anisotropy of the chemisorption of gas ions on surfaces of different crystallographic orientations. A second refinement of the structure zone model was proposed by Barna *et al.* [Barn 98] [Petr 03].

It takes into account the effect of additives, in the form of impurities or a small amount of alloying species, that can be used to control the structural evolution during growth (crystallite size, morphology and crystallographic texture). Such impurities may be active as inhibitor or promotor of the structure phenomena described previously (surface diffusion, competitive growth etc.). Often, impurities act as grain refiners through a solute (impurity) drag effect on grain boundary motion [Cahn 62] [Mich 99]. At low concentration, the segregation of impurity atoms at the surface and at grain boundaries can greatly reduce the surface diffusion of adatoms and the mobility of grain boundaries, limiting grain coarsening. At higher concentrations, competitive growth can occur due to the anisotropic segregation of impurities at given crystallographic surfaces. At even higher concentrations, complete impurity layers (tissue phase) can entirely cover the surface of growing crystallites, stopping the growth and forcing repeated nucleation of hence random oriented crystallites. The grain size can be decreased in the nanometer range and the columnar structure is lost. The obtained structure is dense and the surface roughness remains low. The two-phase structure moreover ensures a higher thermal stability by efficiently blocking grain coarsening due to the presence of an immiscible phase at the grain boundaries. This effect is used in the deposition of hard nanocomposite coatings [Petr 03] [Musi 01c].

Chapter 4

Characterization methods

4.1 Chemical characterization by X-ray Photoelectron Spectroscopy

X-ray Photoelectron Spectroscopy (XPS) is a semi-quantitative spectroscopic technique that can be used to measure the elemental composition, chemical state and electronic state of the elements of a material (except H and He). The technique is based on the photoelectric effect, namely the ejection of electrons from matter after absorption of energy from electromagnetic radiations such as X-rays. Because the mean free path of electrons in solids is very small, the detected electrons originate from only the top few monolayers of the specimen surface, typically a few nanometers, which makes this technique a unique tool for surface specific studies. XPS was developed in the mid 1960s by the group of K. Siegbahn (Nobel Prize for Physics in 1981) and was first known by the acronym ESCA (Electron Spectroscopy for Chemical Analysis), to account for the fact that not only photoelectrons are detected by this technique, but also Auger electrons. Nowadays, the acronym ESCA regroups several electrons spectroscopies, namely XPS, but also AES (Auger Electron Spectroscopy) and UPS (Ultraviolet Photoelectron Spectroscopy). The XPS technique is widely used both in academic and industrial research environments.

4.1.1 Principle

Basics The technique consists in irradiating a surface under vacuum with monoenergetic soft X-rays and analysing emitted electrons by energy. Mg Kα (1253.6 eV) or Al Kα (1486.6 eV) lines are usually used. The kinetic energy E_k of photoelectrons is related to the electron binding energy of atomic orbitals E_b by:

$$E_k = h\nu - E_b - \phi_s \tag{4.1}$$

where $h\nu$ is the energy of the photons and ϕ_s the spectrometer work function, which is calibrated using reference materials. After a photoelectron is emitted, a relaxation process takes place to fill in the vacancy created in the core level by an electron coming from an upper level. The gain in energy associated to this relaxation can be dissipated either by the emission of a photon, or by emission of an Auger electron (secondary electron), as shown in Figure 4.1.

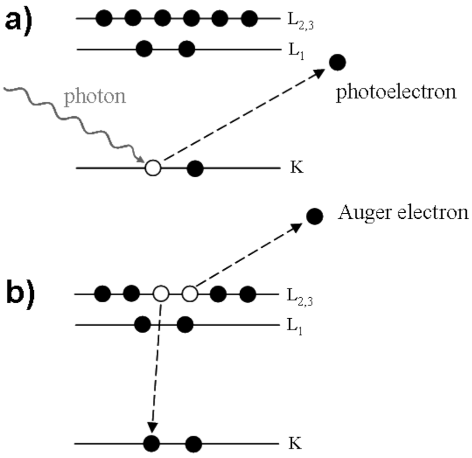

Figure 4.1: The XPS emission process with (a) the ejection of a photoelectron after absorption of a photon, and (b) the relaxation process resulting here in the emission of an Auger $KL_{2,3}KL_{2,3}$ *electron. Both kinds of electrons are detected during XPS analysis [Brig 03].*

XPS spectra An XPS spectrum is a plot of the number of detected electrons against their binding energies. Each element has a specific set of binding energies (BE) that enables its identification. Knowledge of physical and experimental parameters such as photoionization cross-sections, transmission function[1] of the spectrometer and inelastic mean free paths of the emitted electrons enables the quantification of elements through the definition of sensitivity factors. These factors relate the intensity of each peak to elemental concentrations.

An example of survey broad energy spectra measured on an Al-Si-N thin film is given in Figure 4.2.

---

[1] This function gives the ratio between the number of electrons at a given energy transmitted through the spectrometer to the number of electrons entering the entrance aperture of the spectrometer at that energy.

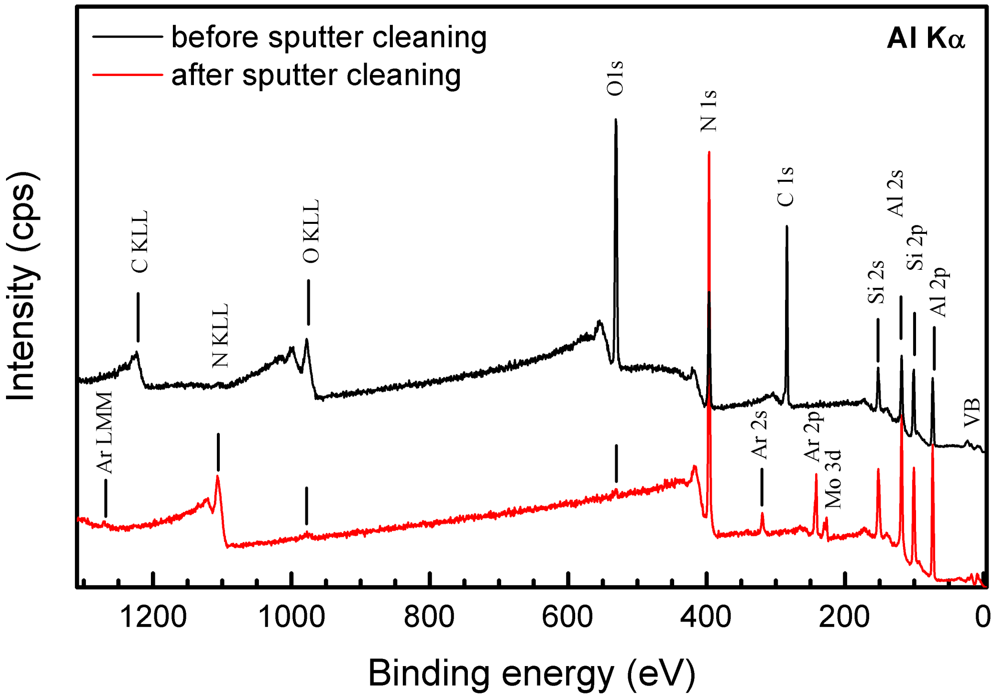

Figure 4.2: XPS survey spectra on an Al-Si-N thin film containing about 16 at.% of Si, recorded before and after Ar$^+$ sputter cleaning (3 kV, 90 s) of the sample surface. An Al Kα monochromatic source was used. Binding energies of Al, Si, N, O and C core photoelectrons are clearly identified. After Ar sputtering, the C1s signal disappears and the O1s signal greatly decreases. Signals from implanted Ar atoms and re-deposited Mo coming from the Mo mask used to clamp the sample appear. Auger electrons from O, N and Ar are also detected. The valence band (VB) is visible in the binding energy region ∼ 0–20 eV.

Several peaks are observed on these survey spectra, that have different origins. The main features are:

- peaks corresponding to the emission of core level photoelectrons, such as Al2p, N1s etc. The photoelectrons emitted come from well defined energy levels, so that the corresponding peaks are very narrow. In the case of p, d and f orbitals, a closely spaced doublet is visible instead of a single peak. This splitting results from spin-orbit coupling effects and the corresponding energy levels are labeled with their total angular momentum (e.g. 1/2 and 3/2 for a p orbital). However for light elements such as Al and Si, the $2p$ doublet peaks are so close that they are treated as one single peak. In the case of argon already, the doublet is visible and can be resolved into e.g. Ar2$p_{3/2}$ and Ar2$p_{1/2}$. Peak shapes can be described as a combination of Lorentzian and Gaussian lines that are related to instrumental and intrinsic effects[2]. The binding energy position enables to identify chemical elements. Interactions with the chemical environment (e.g. oxidation, polarization etc.) can cause small variations in the peak position that enable the identification of the chemical state of each element.

- a valence band at low binding energies (< 20 eV) that corresponds to electrons coming from energy levels close to the Fermi level. Information can be deduced concerning e.g. the formation of specific hybrid orbitals. In the case of Al-Si-N specimens, the valence band consists of broad features that overlap and hardly evolve with the chemical composition. These specimens are moreover insulating, so that the electron density of states at the Fermi level (BE = 0 eV) is close to zero.

- Auger peaks originating from the relaxation of the ionized atom. The peaks are much broader than photoelectron peaks since three electrons are involved in the transition. Auger electrons are characterized by their kinetic energy which is independent on the excitation energy (here Al Kα). For this reason Auger lines will appear on a binding energy plot (such as the one shown in Figure 4.2) to be in different positions when ionizing photons of different energies (i.e. different X-ray sources) are used.

- a non-linear background intensity which is increasing on the high BE side of each peak. This is related mainly to the inelastic scattering of electrons that lose part of their kinetic energy as they pass through the sample into the vacuum. A correction for the background is needed for an accurate determination of both peak position and peak shape. A Shirley iterative procedure was used in this work to calculate the baseline to be subtracted [Brig 03].

The estimated quantitative accuracy of atomic concentrations determined by XPS (for major peaks, using routine work conditions) is of the order of 10% of the concentration values in atomic percents (at.%). The detection limit of contaminations is the order of 0.1 at.%.

---

[2] The line shape of the X-ray source can be approximated by a Lorentzian function. The energy-spread function (resolution) of the electron energy analyser - constant in FAT (Fix Analyser Transmission) mode, i.e. mode when a constant analyser pass-energy is used - can be approximated by a Gaussian line shape. The natural line width of photoelectron peaks - related to the life-time of core vacancies - can be approximated by a Lorentzian function.

Point charge model Physical models were developed to account for initial states (pre-ionization) and final states (post-ionization) effects in the emission process of photoelectrons and Auger electrons. A simple model for the interpretation of chemical shifts of core levels is the *point charge model* that relates the binding energy to the atomic charge [Brig 03] [More 98]:

$$E_b(i) = const + kq + V_M \quad \text{with} \quad V_M = \frac{e}{4\pi\varepsilon_0}\sum_j \frac{q_j}{r_{ij}} \tag{4.2}$$

and where $E_b(i)$ is the binding energy of a particular core level on atom i, k is a constant that expresses the change in the core level energy upon removal of a valence electron, q is the valence charge on atom i and V_M is the Madelung energy, which represents the potential acting on atom i due to the point charges on atoms j situated at distance r_{ij} from atom i. This model only accounts for initial state effects; final state effects however, related for example to the polarization (charge rearrangement) of core and valence electrons as well as surrounding atoms by the core hole created during photoionization, must also be taken into account. A so called relaxation term R divided into intra-atomic R^a (related to core and valence electrons) and extra-atomic R^{ea} contributions is then added to the above expression for E_b. For two atoms placed in different chemical environments, the chemical shift of their binding energies is then given by:

$$\Delta E_b = k\Delta q + \Delta V_M - \Delta R^a - \Delta R^{ea} \tag{4.3}$$

Depending on the type of material system considered (molecular solid, ionic solid etc.), one term may be dominant, or several terms may have comparable amplitude but opposite signs. Note also that the expression above seems to be a sum of independent terms. But in fact, they are related to each other and there is no simple rule to predict the effect of charge transfer on the evolution of the Madelung constant and on relaxation effects [Crug 03].

Auger parameter and Wagner plots The analytical utility of Auger transitions in XPS was first recognized by C. D. Wagner who presented a paper entitled "Auger lines in X-ray photoelectron spectrometry" at the first International Conference on Electron Spectroscopy (Asilomar, CA) in 1971. Auger lines are indeed closely related to final states in the X-ray induced ionization process, involving emission of electrons from the valence band, while photoelectron lines are rather sensitive to initial states in core levels. As a consequence, Auger chemical shifts can be significantly larger than the respective photoelectron binding energy shifts. Complementary information on the chemical environment of atoms can therefore be deduced from Auger lines shape and position.

By combining the most intense photoelectron line and the sharpest Auger line of an element, the so-called *Auger parameter* (concept introduced by Wagner) can be calculated. This parameter is independent of any static charge effect on the studied specimen (see section 4.1.3) and does therefore not require an energy referencing, which makes it very useful in the study of insulator samples. The (modified) Auger parameter α' is defined as the sum of the kinetic energy of the main Auger line and the binding energy of the most intensive photoelectron line:

$$\alpha' = E_k(\text{Auger}) + E_b(\text{photoelectron}) \tag{4.4}$$

The Auger parameter shift between two compounds is related to the final state relaxation energy, in particular the evolution of the valence charge and of extra-atomic contributions [More 98] [Brig 03]. This is illustrated by the following equation [More 98]:

$$\Delta\alpha' = 2[\Delta R^a(\text{valence electrons}) + R^{ea}] \tag{4.5}$$

that describes the shift in the modified Auger parameters as being equal to twice the variation of the relaxation energy.

However, the Auger parameter is still a one-dimensional quantity. Wagner introduced a more useful approach that consists in representing the kinetic energy of the sharpest Auger line together with the binding energy of the most intense photoelectron line in the form of a scatter plot: the so-called "chemical state plot", later also called "Wagner plot". With the definition of the (modified) Auger parameter, the presentation of such a plot is now standardized as follows. The Auger kinetic energy is on the ordinate and the photoelectron binding energy is on the abscissa oriented in the negative direction. The Auger parameter can be read on diagonal lines with slopes -1 (appearing $+1$ in the plot due to the negative direction of the abscissa), as can be seen from the following equation [More 98]:

$$E_k = \alpha' - E_b \tag{4.6}$$

A constant Auger parameter corresponds to similar final state effects in two different compounds. Chemical states with similar initial state effects will appear on a line with slope -3 [More 98], which corresponds to the following expression:

$$E_k = [const + 2(V_M + kq)] - 3E_b \tag{4.7}$$

A shift parallel to lines with −3 slopes corresponds to twice the variation in Madelung energy V_M and in the density of valence electrons, q. Examples of chemical state plots are given in [Wagn 82] [More 98] [Bert 02]. A chemical state plot of nitrogen for Al-Si-N films of various composition deposited in this work is given in Figure 5.14, p. 106.

4.1.2 Analysis conditions

XPS spectra were recorded on a PHI Quantum 2000 microprobe spectrometer with a base pressure of 8×10^{-7} Pa. A monochromatic Al Kα (1486.6 eV) excitation was used. The spectrometer energy scale was calibrated using the Au4f$_{7/2}$, Ag3d$_{5/2}$ and Cu2p$_{3/2}$ photoelectron lines. The FWHM of the Ag3d$_{5/2}$ line was 1.62 eV and 0.6 eV at 117.4 eV and 11.75 eV of pass energy respectively. Simultaneous electron (1.2 eV) and low energy Ar-ion flooding was used to minimize the buildup of static charge on the surface of Al-Si-N insulating specimens during XPS analysis.

The native oxide layer on top of Al-Si-N specimens was removed by Ar$^+$ sputtering at 3 kV for 90 s prior to XPS analysis. Survey spectra in the −5-1310 eV binding energy (BE) range were recorded before and after argon sputtering in 0.5 eV steps and 117.4 eV pass energy. Detailed spectra of the most intense core level lines of the constituents (Al2p, Si2p, N1s) as well as of the most common impurities (C1s and O1s) were recorded after argon sputtering in 0.1 eV steps and 11.75 eV pass energy. The N(KLL) Auger transition was recorded with 0.2 eV steps and 11.75 eV pass energy. The error bars shown in all the graphs reported in this work (section 5.2.1) correspond to the step size of the measurements.

4.1.3 Charge correction procedure

Electrostatic charging occurs as a consequence of impeded charge flow from (photoelectrons, Auger electrons) and to (electron and ion neutralization) the measured area of the analyzed sample. As a consequence, the kinetic energies of detected electrons can be increased or decreased in XPS spectra; this energy shift due to static charging effects is identical for all lines. Charge effects are especially problematic when insulators such as Al-Si-N are investigated and their photoelectron binding energies are compared to binding energy positions reported in the literature to identify chemical states of elements. Careful charge control and charge referencing are therefore crucial for the production of reliable XPS data that can be compared to data produced by other researchers [ASTM 03]. In particular, a detailed description of the charge referencing procedure is mandatory whenever XPS data are published.

Charge referencing is based on the use of reference elements supposed to be free from any chemical effects, i.e. which encounter no chemical shift of a reference photoelectron line due for example to interactions effects (polarization, chemical reaction etc.) with the studied specimen. In addition, the reference photoelectron line used must have a well known binding energy position, which is true an ideal case only. A couple of techniques are used for charge referencing: adventitious carbon present on the sample surface during XPS analysis is the most widely used external referencing element. The National Institute of Standards and Technology (NIST) recommends referencing the C1s binding energy to 284.8 eV [NIST 03]. Authors often set it also at 284.6 eV or 285.2 eV [ASTM 03]. The correct binding energy for the C1s core level depends on the exact nature of the carbon contamination present on the specimen. Sample treatments such as heating or ion sputtering may have a non-negligible effect on the binding energy of C1s electrons [Swif 82]. As a consequence, carbon referenced binding energy data reported in the literature are often scattered [Brig 03] [ASTM 03]. Gold decoration offers an alternative to C1s referencing. It usually consists in the vapor deposition of a thin gold layer on the entire surface of the specimen; the $Au4f_{7/2}$ photoelectron peak, set at 84.0 eV as for bulk gold, is used as charge reference. This technique however suffers from physical limitations related to sub-monolayer surface coverage. In particular, gold coverage less than one monolayer thick may encounter strong relaxation effects by interaction with the substrate [Kohi 84] [Kohi 85]. If the gold coverage is so small that gold particles (clusters) less than about $\sim$ 10 nm are formed, a shift of the $Au4f_{7/2}$ line position to higher binding energies as large as 1 eV is possible on insulating surfaces [Wert 83] [Wert 88] [DiCe 88] [Boye 05]. When Ar^+ sputter cleaning of the specimen surface is applied prior to elemental analysis to remove surface contaminants, adventitious carbon is likely to be entirely removed or chemically altered (e.g. carbide formation), and is no longer available for charge referencing. In the same way traditional gold decoration methods can no longer be used. Implanted Ar, due to its chemical inertness, is believed to be a reliable alternative [Bert 02]. An average line position of $Ar2p_{3/2}$ at 241.82 eV has been recommended [Powe 95]. The Ar2p line can, however, encounter pronounced chemical shifts depending on the material in which the ions are implanted [Citr 74] [More 98]. Although these effects are known, the issue of using Ar as a charge reference is seldom addressed in the literature. A last alternative can be the use of an internal reference element that is assumed not to be subject to a chemical shift. Examples taken from the literature include referencing on the N1s line in AlN specimens [Tayl 81b] or SiN_y-based specimens [Donl 88], on the bulk O1s peak in oxides [Heid 06], on a bulk metal peak for surface nitride, oxide or carbonate layer on a metallic specimen [Tayl 81b] [Heid 06] and on Si2p in sputtered Si-Al-O-N specimens [Schn 97]. In many cases, however, assumptions on the chemical stability of constituting elements of the investigated specimen seem difficult to justify.

In the present study, the native oxide layer on the coating surface was removed by Ar^+ sputtering prior to analysis. Due to the concomitant removal of adventitious carbon from the surface the C1s line could not be use as charge reference. Referencing on implanted argon atoms was therefore attempted, but a large chemical shift (∼1 eV) of the $Ar2p_{3/2}$ photoelectron line was evidenced. In view of these difficulties, a specific gold referencing procedure was designed for charge referencing of Al-Si-N specimens. The Au4f line was recorded in 0.1 eV steps and 11.75 eV pass energy, and the $Au4f_{7/2}$ line taken at 84.0 eV was used as a charge reference. Further details about this charge reference procedure are reported in Chapter 5, section 5.2.1. The practical limitations for the use of adventitious carbon, implanted argon and gold decoration as charge references for the Al-Si-N system are discussed there.

4.1.4 Data processing

Elemental composition was determined using the Multipak software package (version 8.2B). Shirley backgrounds were defined under a region of ±4 eV around photoelectron peaks. The software uses PHI relative sensitivity factors to calculate element concentrations in atomic percentage. Detailed spectra were processed by the CasaXPS software package (version 2.3.10). An iterative Shirley background was removed before line fitting. Line shapes were chosen as Gaussian/Lorentzian products of type GL(p), p representing the amount of pure Lorentzian shape. The parameter p was determined for Al2p, Si2p and N1s lines from best fits (i.e. minimum residual standard deviation) in pure AlN and SiN_y films. GL(40) for Al2p, GL(30) for Si2p and GL(80) for N1s were used in pure AlN and Al-Si-N films. GL(30) for Si2p and GL(50) for N1s were used in pure SiNy. The doublet lines of Ar2p and Au4f, used for charge referencing purpose, were fitted each using two components of identical line shape with the constraint of equal full width at half maximum (FWHM).

4.2 Structural characterization

4.2.1 X-Ray Diffraction

X-ray diffraction (XRD) is a powerful non-destructive technique to investigate the crystallographic phases of a material, with an information depth up to few microns. In addition, information can be derived about the crystalline texture (distribution of preferred orientations), mean crystallite size and residual stress in the studied specimen [Klug 74] [Birk 06].

a) Principle

When X-rays interact with an atom, they can be absorbed or scattered, giving rise then to the emission of a coherent electromagnetic wave of same frequency in all directions of space. On a periodic array of atoms (crystalline matter), the waves emitted by each single atom interfere with each other either constructively or destructively, giving rise to a diffraction pattern characteristic of the crystallographic arrangement of the material. The directions along which interferences are constructive are given by the Laue conditions.

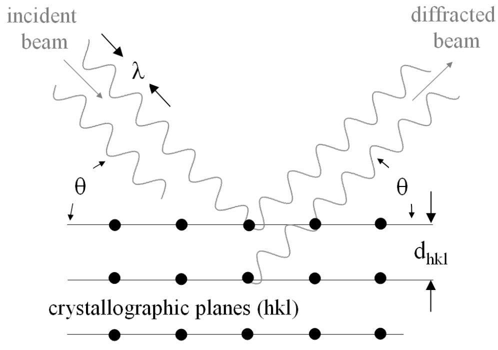

Figure 4.3: Bragg conditions for constructive interferences at a periodic arrangement of atoms.

The Bragg conditions (Fig. 4.3) can be deduced from the Laue conditions and describe in a simple geometrical relationship the conditions for constructive interferences on crystallographic planes of Miller indices (hkl). The Bragg law relates the diffraction angle 2θ to the interplanar distance d_{hkl} in the following way:

$$2d_{hkl}\sin\theta = \lambda \tag{4.8}$$

with λ the wave length of the incident beam.

In an hexagonal crystal system (such as wurtzite AlN), the lattice parameters a and c are related to the interplanar distance d_{hkl} by the following equation:

$$\frac{1}{d_{hkl}^2} = \frac{4}{3}\frac{h^2 + hk + k^2}{a^2} + \frac{l^2}{c} \tag{4.9}$$

b) Measurement apparatus and geometry

Apparatus A Bruker/Siemens D5000 diffractometer in the Bragg-Brentano geometry equipped with an Euler cradle and a Cu X-ray source is used (Figure 4.4). Among the three main radiation lines, most of the Cu Kβ line is absorbed by use of a Ni filter. The CuKα_2 line is removed by the data processing software EVA (from Bruker AXS) using the Rachinger correction procedure [Klug 74]. Reported X-ray data correspond then to a Cu Kα_1 radiation with a wavelength $\lambda = 1.54056$ Å.

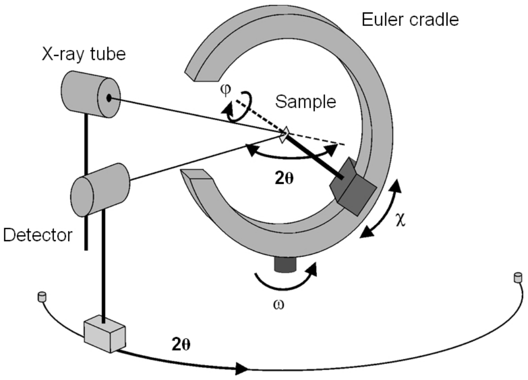

Figure 4.4: Schematic picture of a diffractometer equipped with a X-ray tube and an Euler cradle (ω is often used instead of θ when θ and 2θ movements are unlocked, i.e. independent of each other). (Picture adapted from [Schw 95])

The following measurement geometries are used in this work:

θ-2θ scans The most common measurement performed on thin films to investigate their crystalline structure and texture is the so-called θ-2θ scan. θ is defined as the angle between the sample surface and the incoming X-ray beam. The angle between the incoming beam and the detector is kept at all time at a value of 2θ. As the values of 2θ are scanned, the geometry is such that the recorded information comes from crystallographic planes parallel to the sample surface, and only from these. In this measurement geometry, the scattering plane, defined by the wave vectors, is perpendicular to the sample surface. Since bulk polycrystalline samples, such as sputtered thin films, are composed of small crystallites oriented in a non-random way in space, the θ-2θ scans will not be able to probe all the crystallites, but only those having a diffracting crystallographic plane parallel to the sample surface. However, the recorded diffractogram is usually sufficient to identify the crystallographic phase(s) present in the sample (from the JCPDS-ICDD[3] database), and even to estimate the texture of the sample.

---

[3] Joint Committee on Powder Diffraction Standards/ International Centre for Diffraction Data

Rocking curves Rocking curves (RC) give access to the the angular distribution of a given (hkl) reflex in the θ-2θ diffractogram. It consists in scanning θ (also called then ω) values while keeping the detector at a fixed position of 2θ, corresponding to the position of the reflex to be studied. The FWHM of the recorded rocking curve quantifies the angular distribution of (hkl) planes.

φ and χ scans The measurement of a diffracted signal from a crystallographic plane non parallel to the sample surface requires the alignment of this plane so as to bring it in diffraction (Bragg) conditions. The sample must therefore be moved, which is achieved using two additional rotation movements in the diffractometer. First, the sample can be tilted around an in-plane axis comprised in the scattering plane[4] by an angle χ. Secondly, the sample can be rotated about the normal to its surface by an angle φ. Both angles are shown in Figure 4.4.

c) Crystallographic information

Texture The crystallographic *texture* of a material is the orientation distribution of crystalline grains in a (poly)crystalline sample. As such, the texture cannot be easily quantified by a number, as for other physical properties (density, resistivity, etc.). It is usually described in term of preferred crystallographic orientation. A monocrystal has only one (preferred) orientation - defined as the crystallographic plane that coincides with the surface (e.g. Si (001)); a powder that consists of randomly oriented grains shows no preferred crystallographic orientation and is said to be textureless. Materials deposited by techniques such as PVD or CVD are usually polycrystalline with a non-random orientation of their crystallites. One or several preferred crystallographic orientations can be defined, that are a consequence of the growth process and can be strongly influenced, in some case, by the crystallographic orientation of the substrate (i.e. epitaxy). The texture affects the material properties by introducing structural anisotropy.

The texture can be estimated from θ-2θ scans, but the information deduced from these scans is incomplete, since only crystallographic planes parallel to the sample surface can be probed. A qualitative estimation of the texture consist in calculating peaks intensity ratios and comparing them to JCPDS-ICDD data (given for powders, i.e. textureless samples): any

---

[4] Note that varying the angle θ between the sample surface and the incoming beam corresponds to rotating the sample about an in-plane axis that is perpendicular to the scattering plane for $\chi = 0$.

deviation between the measured ratios and the reference data indicates that the studied specimen is textured. For a quantitative estimation, a *texture coefficient* can be defined from intensity ratios of diffraction peaks.

The determination of the complete texture of a sample requires a measurement in the three-dimensional space. By combining the φ and χ movements described above, crystalline planes that are not parallel to the sample surface can be brought in diffraction conditions. So-called *pole figures* (PF) are measured for a fixed scattering angle (fixed θ-2θ, i.e. constant d_{hkl} spacing) and consist of a series of φ scans (in plane rotations) at different tilt or χ-azimuth angles. The construction of a hkl-pole figure is then based on the stereographic projection of hkl-*poles*, defined as the intersection between [hkl] directions and an imaginary sphere surrounding the sample. Pole figures can be displayed either in 3D, the third dimension representing the intensity in each measurement point, or in 2D, with level lines (contour plot) reproducing the topography (signal intensity) of the 3D view. Example of pole figures are given in Figure 5.17, p. 112. Since a single hkl-pole figure only describes the orientation distribution of one family of planes, two of such pole figures are then required to describe the complete texture of a sample. A further tool exist, that enables to represent the texture in one single picture: it is called the *Orientation Distribution Function* (ODF). However a description of this tool will go beyond the scope of this brief introduction on texture measurement[5].

Grain size and strain broadening The shape and breadth (width) of a pure diffraction line profile are determined by both the mean crystallite size (or distribution of sizes) characterizing the sample, and by the particular imperfections (lattice strain, stacking disorder, point defects) of the crystalline lattice. The experimental line is moreover a convolution of an instrumental line (giving rise to a small instrumental line broadening) and the intrinsic or pure line. For very small crystallite sizes (say $\leq$ 100 nm), the instrumental broadening is negligible.

When several orders of reflection are available in θ-2θ scans, different methods can be applied to separate the crystallite size and the strain broadening [Klug 74]. The Fourier method of Warren and Averbach gives access

---

[5] Interested readers may have a look at the following web site to be introduced in an interactive way into the science of pole figures and orientation distribution functions: `http://aluminium.matter.org.uk/content/html/eng/default.asp?catid=100&pageid=1039432491`.

to a size distribution of crystallites. The Williamson-Hall method uses integral breadths and depends upon explicit assumptions as to the shape and the broadening profiles due to each effect. The first method is more exact, but the second one is much easier to apply. If micro-strain effects can be assumed to be negligible, the Scherrer equation can be used that expresses the breadth β (in 2θ units and in radians) of a single line at position 2θ resulting for a mean crystallite size L [Klug 74]:

$$L = \frac{K\lambda}{\beta \cos\theta} \tag{4.10}$$

The original equation was derived by Scherrer (1918) for the case of small cubic crystals of uniform size. The constant K equals then 0.94 and the FWHM of the diffraction line is taken as the line breadth β.

Other derivations are available. For instance one derivation employs the integral breadth[6] β_i to develop a treatment independent of the crystallite shape and symmetry. This leads to an *effective crystallite dimension* L_{hkl}, defined as the volume average of the crystallite dimension T normal to the reflecting plane (hkl) [Klug 74]:

$$\beta_i(2\theta) = \frac{\lambda}{L_{hkl} \cos\theta} \quad \text{with} \quad L_{hkl} = \frac{1}{V}\int T dV \tag{4.11}$$

Equation 4.11 corresponds to the original Scherrer equation (Eq. 4.10) in which the integral breadth is used instead of the FWHM and $K = 1$. This "modified" expression has a special value in the interpretation of X-ray diffraction patterns of specimens containing crystallites of particular shape (platelike, needlelike and lathlike). Niederhofer *et al.* reported a comparison of the crystallite sizes in Ti-Si-N superhard nanocomposite coatings determined by the Warren-Averbach analysis on the one hand, and the Scherrer equation - both using the FWHM and the integral breadth - on the other hand [Nied 99]. This study clearly shows that (at least) for crystallite sizes smaller than about 20 nm, the Warren-Averbach method and the Scherrer formula with the integral width yield similar crystallite sizes. In contrast the Scherrer formula with the FWHM clearly yields unreliable data.

In the present work on Al-Si-N nanocomposite coatings, only one order of reflection was available in XRD data, so that neither the Warren-Averbach

---

[6] Integrated intensity of the line profile above background, divided by the peak height.

method nor the Williamson-Hall method could be applied. The crystallites in Al-Si-N films were moreover found to be elongated rather than of spherical shape, as revealed by TEM. Eq. 4.11 was therefore used in this work to determine crystallite sizes in Al-Si-N sputtered thin films.

Periodicity and interface quality of multilayer structures Periodic structures such as multilayer films can be characterized using both low angle ($2\theta \leq 15°$) and high angle ($2\theta \geq 15°$) XRD techniques (both in a θ-2θ geometry). The distinction is made since low angle XRD results from the reflection of X-rays at interfaces between distinct materials of different electron densities, independent on the crystallinity of these materials, while high angle XRD uses the diffraction of X-rays on crystallographic planes. Low angle XRD is commonly called X-Ray Reflectometry (XRR) and is presented in the next section. The basics of high angle XRD on multilayer structures are presented here.

The high angle diffraction pattern obtained on multilayers or superlattice systems is a convolution of the crystalline structure and the composition modulation. This gives rise to equally spaced (in reciprocal space) satellite peaks surrounding the main diffraction (Bragg) peak from the film, as shown in Figure 4.5. These satellite features are called *Laue oscillations*. In the case of a periodic structure of bilayer period Λ, the position of the m^{th} order satellite peak is given by a modified form of Bragg's law:

$$\sin\theta_{\pm} = \sin\theta_B \pm \frac{m\lambda}{2\Lambda} \tag{4.12}$$

where $\theta_{\pm}$ and θ_B are the angles of the satellite peak and of the Bragg peak respectively, and λ is the X-ray wavelength [Yash 99].

When several satellite peaks are observed, simulations can be performed to obtain quantitative structural information such as the individual layer thicknesses, the interface widths and the interfacial roughness [Yash 99]. However, in the case of non-epitaxially grown multilayers measured with a non-monochromatic X-ray radiation such as shown in Figure 4.5, this may prove difficult. Moreover the intensity of the satellite peaks quickly decreases with the satellite order in the case of a non square-wave composition modulation, so that higher order satellites may be quickly hidden by the background.

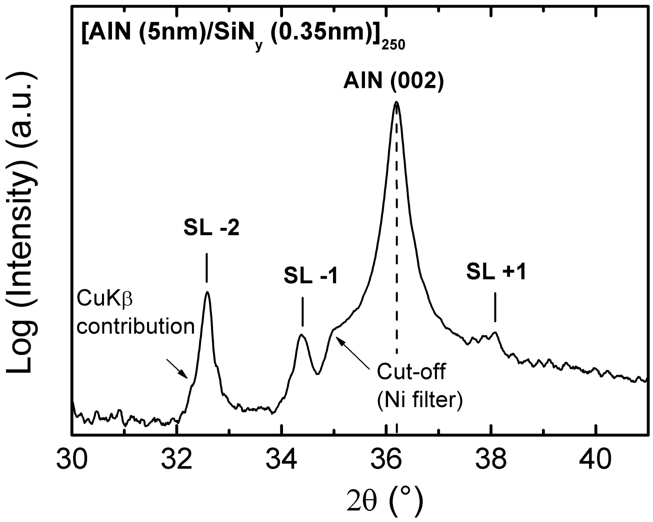

Figure 4.5: High angle X-ray diffraction scan on a [AlN (5 nm)/SiN$_y$ (0.35 nm)]$_{250}$ multilayer film deposited on silicon. A Cu anode was used as X-ray source. Among the three main radiation lines Kα_1, Kα_2 and Kβ, most of the Kβ intensity was filtered out using a Ni filter and the Kα_2 was suppressed from the measurement using a Rachinger correction procedure; the main signal comes then from the Kα_1 line. Marked on the scan are the AlN (002) diffraction peak and three superlattice (SL) peaks surrounding it. Note that the -2 order coincides with a weak residual Kβ diffraction contribution on AlN (002) crystallographic planes.

4.2.2 X-Ray Reflectometry

X-Ray Reflectometry (XRR) is a non-destructive technique, primarily used for thickness determination of thin films between 2 and 200 nm with a precision of the order of 1 Å. In addition, information about roughness and density of the films can be obtained by a fit between simulated and experimental data. XRR measurements were performed using the same Siemens Diffractometer D5000 as used for XRD measurements. The configuration was however modified in front of the detector: the slit holder, comprising anti-scatter slit, Ni Kβ filter and receiving slit, was replaced by a parallel plate collimator (a set of closely spaced thin Cu plates perpendicular to the scattering plane) followed by a flat LiF monochromator. The Leptos software, from Bruker AXS, was used to fit the experimental data.

a) Principle

During a XRR measurement, the sample is irradiated by a monochromatic beam of wavelength λ at grazing incidence θ, and the reflected signal is recorded at angle 2θ (in a θ-2θ geometry). Measurements are typically performed in the 2θ angular range 0–5°. The reflected intensities depend on the the different electron densities in the studied specimen, which correspond to the refractive indexes in classical optics. For incident angles below a critical angle θ_c, total reflection occurs at the surface of the specimen. The recorded intensity is constant and maximal for $\theta < \theta_c$; the critical angle is determined by an abrupt fall in the reflected intensity. Examples of XRR scans on multilayer samples are given in Figure 4.6. The critical angle is $2\theta_c \approx 0.5°$. For $\theta > \theta_c$, X-rays are reflected at the surface and interfaces of the specimen, which gives rise to interference fringes that are angle-dependent. These so called *Kiessig fringes* [Kies 31] are visible in Figure 4.6a. The period of the interference fringes and the decrease in the intensity are related to the film total thickness and to the roughness of the film surface and interface(s) respectively. The critical angle θ_c is related to the (atomic) density of the material.

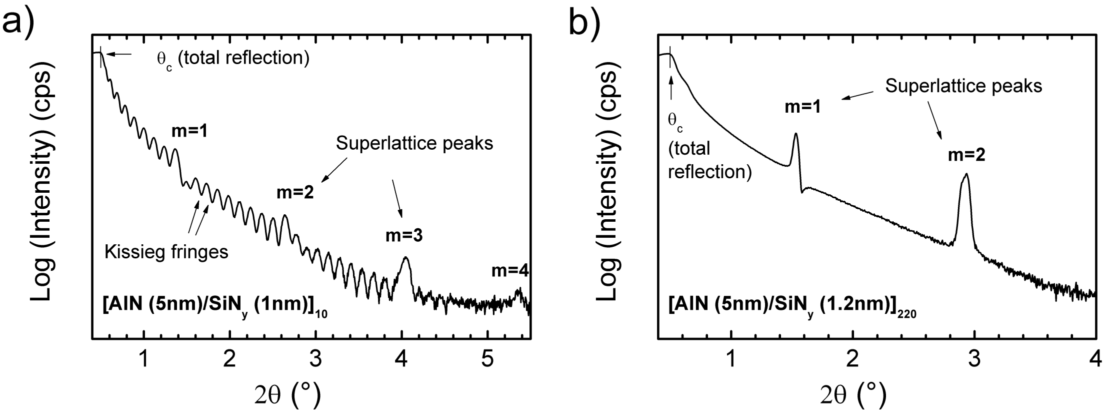

Figure 4.6: X-ray reflectometry scans from two multilayer stacks deposited on silicon with a bilayer period close to 6 nm. (a) [AlN (5 nm)/SiN$_y$ (1 nm)]$_{10}$ (i.e. 60 nm total thickness) and (b) [AlN (5 nm)/SiN$_y$ (1.2 nm)]$_{220}$ (i.e. ∼ 1.4 nm total thickness) multilayer films. In the case of the thicker film (b), the Kiessig fringes have a too small period to be resolved, so that only the superlattice peaks are seen.

For a single film of thickness t on a substrate, the m^{th} order interference maximum is located at:

$$\theta_m^2 = m^2 \frac{\lambda^2}{4t^2} + \theta_c^2 \approx m^2 \frac{\lambda^2}{4t^2} + 2\delta \tag{4.13}$$

with m being an integer. δ is related to the real part of the complex refractive index of the material, given by:

$$\tilde{n} = 1 - \delta + i\beta \tag{4.14}$$

δ represents here the dispersion and β the absorption. δ and β are of the order of 10^{-5} and 10^{-6}, respectively.

For $\theta_m \gg \theta_c$, the thickness can be determined from the difference between two neighboring maxima (or minima) using the following relation:

$$t \approx \frac{\lambda}{2} \frac{1}{\theta_{m+1} - \theta_m} \tag{4.15}$$

A fit over a wide angular range of a few degrees usually enable the determination of the film thickness with a precision better than 1 Å.

XRR on single layers was used in this work to calibrate sputter deposition rates prior to the deposition of multilayer films. Another way to calibrate deposition rates consist in depositing thick films and measure their thickness by mechanical profilometry (see section 4.3.2), or by SEM on a cross-section sample. XRR has the advantage of requiring very thin (i.e. quickly deposited) films, for a measurement and data processing time the order of $\frac{1}{2}$ to 1 h only.

b) Low angle reflection on multilayer structures

In the case of a multilayer film, superlattice peak, that are related to the periodicity of the multilayer structure, superimpose to the Kiessig fringes (Fig. 4.6a). The latter even tend to disappear completely when the total thickness of the film exceeds $\sim$ 150 nm (Fig. 4.6b). The observed superlattice peaks occur at a 2θ position given by a modified form of the Bragg's law [Yash 99]:

$$\sin^2\theta = (m\lambda/2\Lambda)^2 + 2\delta \tag{4.16}$$

where m is the order of the peak, λ the X-ray wavelength, Λ the unknown bilayer period and δ is related to the real part of the volume-averaged complex refractive index of the film. Λ can be determined by plotting $\sin^2\theta$ versus m^2 and fitting to a straight line.

4.2.3 Electron Microscopy

a) SEM

Scanning electron microscopy (SEM) was used to investigate the morphology of the coatings. In this technique, a high energy (typically 5–10 keV) electron beam is scanned across the sample surface. The incident electrons cause low energy secondary electrons to be generated with a yield dependent on the incidence angle. Some of these electrons can escape from the sample surface; the secondary electron image gives information about the sample topography with a lateral resolution of a few nanometers. Chemical contrast is obtained from backscattered electrons. In the case of Al-Si-N, however, no chemical contrast can be expected between AlN and SiN_y regions due to the very small difference in atomic numbers of Al and Si.

Al-Si-N thin films deposited on silicon were observed in cross-section after cleavage of the substrate. Prior to SEM analysis and to avoid unwanted surface static charge effects during imaging, the samples were glued on the SEM sample holder using (conductive) silver paste and then coated with a thin layer of carbon. Pt coating instead of carbon coating was also tried, but resulted in the formation of a cracked brain-like Pt overlayer hiding the morphology of the Al-Si-N specimen. Pictures reported in Chapter 5 were taken by Michael Stiefel on a Hitachi S-4800 Scanning Electron Microscope at a low acceleration voltage of 2 kV (Empa, Dübendorf).

b) TEM

Transmission electron microscopy (TEM) enables the investigation of the microstructure of a sample down to the atomic scale. TEM uses the same basic principles as the light microscope but the small wavelength of electrons (1.97 pm at an acceleration voltage of 300 keV) makes it possible to get a lateral resolution a thousand times better than with a light microscope. In this technique, a beam of electrons is transmitted through a thin specimen of less than ~ 100 nm, interacting with matter as it passes through the sample. An image is formed from the electrons transmitted through the specimen, magnified and focused by an objective lens onto a fluorescent screen or a CCD camera. The contrast on TEM images of crystalline materials is essentially a diffraction contrast.

In this work, cross-sections of selected Al-Si-N samples were prepared by manual mechanical polishing (tripod method) followed by mild ion milling to electron transparency. Both conventional and high-resolution (HR) TEM was then performed. Bright field (BF) images give a general picture of the sample microstructure (voids, columns, grains etc.). Dark field (DF) images of a selected crystalline orientation enable a more accurate estimation of the size and distribution of similarly oriented crystalline domains or grains (but not of single crystallites). Electron diffraction (ED) patterns are used to identify phases and evaluate the texture. In the case of multilayer samples deposited on a single crystalline substrate, electron diffraction enables the orientation of the sample with respect to the electron beam along a zone axis of the substrate perpendicular to the normal to the surface, so that interfaces in the specimen are very precisely aligned with the direction of observation. HR micrographs enable to determine the crystallites shape and size in the thinnest regions of the specimen, and to distinguish well ordered crystalline regions from disordered and presumably amorphous regions. Images reported in Chapters 5 and 6 were taken by Magdalena Parlinska-Wojtan on a Philips CM30 microscope (Empa, Dübendorf).

4.3 Mechanical characterization

4.3.1 Nanoindentation

Indentation techniques are used to determine the hardness of a material. These techniques consist in pressing an indenter of known geometry into a surface under a fixed load. The depth of penetration or the area of the resulting impression can be used as a measure of the resistance against deformation of the studied material. The hardness H of a material is defined as its resistance to plastic deformation and is expressed as the ratio between maximum load P_{max} and contact area A:

$$H = \frac{P_{max}}{A} \tag{4.17}$$

In conventional hardness testing A is measured after the test on the residual imprint in the surface. Different tests can be performed that are distinguished by the geometry of the indenter. Due to differences in the way plastic deformations are induced, hardness values obtained by different techniques cannot easily be compared. It is important to note that hardness is not an intrinsic property of a material but is a sum of many effects contributing to the finally measured hardness. These effects comprise yield strength, grain boundary effects, defect distribution etc. Therefore hardness values are related to standard test procedures.

a) Theory of instrumented indentation testing

The mechanical properties of thin films can be deduced from indentations at very small depth (in the micrometer range or below) using the nanoindentation technique. At such a length scale, the accurate determination of the residual impression would be very difficult using an optical microscope. For this reason, a specific instrumented indentation testing was developed that is based on the dynamically recording of the applied load (inductive actuator) and displacement (capacitive sensor) data as a diamond indenter is driven into the specimen surface. Specimens are typically very smooth and flat. As the indenter is pushed into the material, both elastic and plastic deformation cause the formation of a hardness impression conforming to the shape of the indenter to some contact depth, h_c. As the indenter is withdrawn, only the elastic portion of the displacement is recovered; it is this recovery that allows the determination of the elastic properties of a material. Hardness and Young's modulus (also called elastic modulus or E modulus) are deduced from load-displacement curves, as well as the projected contact area A_c. A typical load-displacement curve and a deformation pattern are given in Figure 4.7.

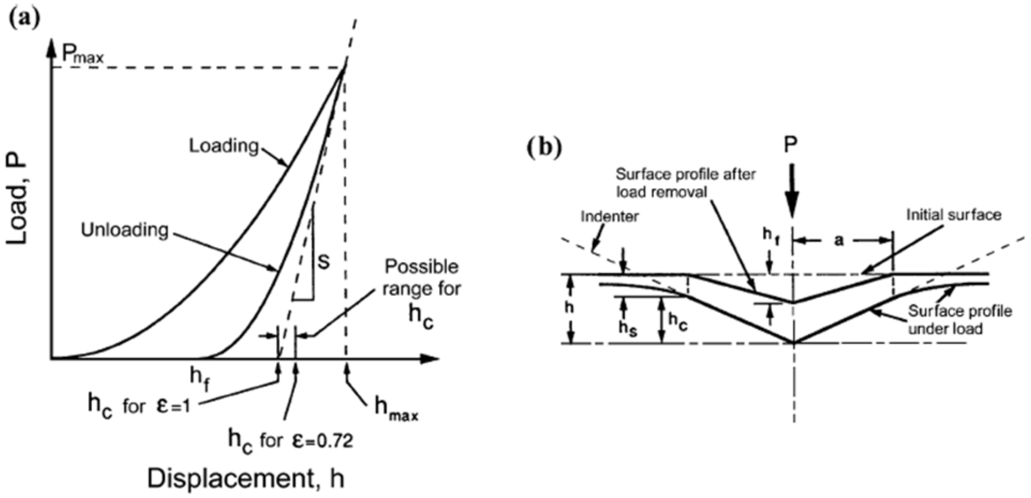

Figure 4.7: (a) Typical load-displacement curve and (b) deformation pattern of an elastic-plastic sample during and after nanoindentation (Pictures taken from [Li 02], but initially published in [Oliv 92]).

The procedure to calculate both H and E is not straightforward. The two most commonly used methods of analysis of indentation test data, namely the "Oliver and Pharr" method and the "Field and Swain" method, and their associated corrections are reviewed in [Fisc 00]. In this work, the procedure developed by Oliver and Pharr [Oliv 92] [Oliv 04] was used for processing of the measured data. This method is now briefly described.

The first step of this procedure consists in fitting the unloading part of the load displacement data to a power-law relation derived from contact mechanics theory:

$$P = B(h - h_f)^m \tag{4.18}$$

with P being the applied load, h the penetration depth into the surface and h_f the final displacement. B and m are empirical fitting parameters, depending on the geometry of the contact and the specimen material [Fisc 06a]. From there, the contact stiffness $S = \mathrm{d}P/\mathrm{d}h$ can be calculated by differentiating the above equation and evaluating it for $h = h_{max}$:

$$S = Bm(h_{max} - h_f)^{m-1} \tag{4.19}$$

The contact stiffness corresponds to the initial portion of the unloading curve, as shown in Figure 4.7a.

Using S, the contact depth h_c can be calculated from:

$$h_c = h_{max} - \varepsilon \frac{P_{max}}{S} \tag{4.20}$$

with ε being a constant that depends on the indenter geometry ($\varepsilon = 0.75$ for a three-sided pyramidal Berkovich indenter). h_c is in turn used to calculate the contact area. $A_c = 24.56 h_c^2$ for a perfect Berkovich indenter, but needs to be calibrated (tip calibration) for non-ideally sharp indenter tips using an area function of the form:

$$A_c = C_0 h_c^2 + \sum_{i=0}^{n} C_i (h_c)^{(1/2)i} \tag{4.21}$$

where C_i (including C_0) are constants determined by curve-fitting procedures.

Using S and A_c, the so-called reduced elastic modulus E_r can be determined:

$$E_r = \frac{\sqrt{\pi} S}{2\beta\sqrt{A_c}} \tag{4.22}$$

with β depending on the indenter geometry (1.034 for Berkovich pyramids). The reduced modulus is related to the indenter elastic modulus E_{ind} and the specimen elastic modulus E by the relation:

$$\frac{1}{E_r} = \frac{1-\nu^2}{E} + \frac{1-\nu_{ind}^2}{E_{ind}} \tag{4.23}$$

with ν and ν_{ind} respectively the Poisson ratio of the specimen and of the indenter material.

It is important to note that the contact stiffness, used for the calculation of the projected contact area and then in both the determination of H and E, is a critical parameter. It can either be determined by fitting the unloading data after measurement of the load-displacement curve, or as a dynamical measurement during recording the load-displacement curve using small oscillations superimposed on the load-unload procedure [Li 02]. The first solution was used here. In this case, it is recommended not to fit the entire unloading curve, but exclude the very top and the bottom of the curve. The Poisson ratio of the specimen must also be known. An uncertainty of ±0.1 produces an error for E of about ±5%. The scattering of values measured on a given specimen with fixed parameter is moreover usually about ±10% or higher.

b) Instrumentation and experimental procedures

Apparatus A MTS Nano Indenter® XP system equipped with a Berkovich tip specially designed for small depth indentation (B1777 type) was used in this work. The Berkovich tip is a three–sided pyramid that has an aspect ratio similar to that of the four–sided Vickers pyramid. The Berkovich tip has a face angle, i.e. the angle between the normal to the sample surface and tip face, of 65.3°. It is well adapted for indentation because it produces plasticity at very low loads and it can be manufactured with good geometrical precision. The nanoindenter is placed on a vibration isolation table in a thermal/sound isolation cabinet to ensure sufficient environmental stability during the measurements. TestWorks 4, also from MTS System Corporation, was used as measurement software. The data were then exported for further processing using the ASMEC IndenterAnalyser (IA) software.

Experimental procedures Al-Si-N films deposited on silicon were tested with nanoindentation. The samples were glued on aluminum cylindrical plots using a thermic glue. The plots were then fixed to the indenter sample tray. The temperature used to melt the glue was about 150–200°C, i.e. the films' properties were not affected. About 40 (or more if needed) measurement points were then chosen on each sample through the built-in microscope of the indenter system, and the measurement conditions were defined. The typical measurement procedure used consisted in loading the sample up to 2 mN within 30 s, then remaining at this load during 30 s to allow a drift measurement, unloading 75% of the maximum load with twice the load rate, and finally holding the load for a second drift correction measurement. Such a test typically lasted about 5 minutes per measurement point. Out of the 40 measured curves examined with TestWorks, 20 were selected to be exported in IA. This selection was essentially based on the quality of the measurement:

low noise (especially for the upper part of the unloading curve), accurate surface detection and quadratic aspect of the initial part of the load curve[7]. Aberrant curves corresponding to possible surface contamination, void in the surface, or showing pop-in like features were eliminated. In the IA software, the zero-point correction was then manually adjusted for each curve, as well as the thermal drift. The final data processing using the Oliver-Pharr method is performed by the software on an average curve calculated from all selected curves that could be corrected in a reliable way, which was usually possible for 15 to 20 of them. Typically, the unloading curves were fitted between 98% and 40–50% of the maximum load. A value of $\nu = 0.25$ was used in all the measurements performed on Al-Si-N films[8]. To ensure that the measurement conditions remained unchanged from one measurement campaign to the next one[9], a reference Al-Si-N sample, belonging to the first measured samples, was measured again at the beginning of each new measurement campaign.

c) Specific issues and general recommendations

Due to the large scattering of calculated values from load-displacement curves, it is recommended to always perform several indentation tests to average them and thereby obtain more reliable results. Apart from this statistical issue it is moreover important to avoid any influence of the substrate. Typically the maximum indentation depth h_{max} should be kept at less than 10% of the film thickness [Bull 05] [Fisc 06a]. This is reasonable in many cases, especially when the film is not too thin (i.e. at least a few µm thick) and the indenter not too blunt (say, radius of curvature $\lesssim$ 100 nm). It is also recommended that h_{max} be larger than 20 times the roughness of the specimen surface. Hardness values should also presented in the range where

---

[7] This should apply to a fully elastic contact (Hertzian contact) between a plane and a conical indenter, which corresponds to $m = 2$ in Equation 4.18. In practice, m is usually found to be lower than 2 (but close to this value) by doing a power law fitting of the initial part of the load curve. This can be related both to the exact shape of the indenter and to the fact that the sides of the residual impression in the specimen do not necessarily remain straight after elastic recovering of the material [Fisc 06a].

[8] This Poisson ratio was calculated using the elastic constants of wurtzite AlN reported in [Tsub 85], under the assumption of an indentation along the c-axis of the crystal. In such a case, the Poisson ratio can be defined as the ratio between in plane strain and axial strain, which leads to $\nu = C_{13}/(C_{11} + C_{12})$ with C_{ij} the elastic constant of h-AlN. Note that the h-AlN system is anisotropic, which means that the elastic properties (E, ν) of the material rely on the crystallographic directions along which a mechanical stress is applied. In the present case, the films were found to be (002) textured (see Chapter 5), so the above assumption is justified.

[9] spaced in time by several months, since the measurement were not performed in Dübendorf, but at Empa in Thun.

they are invariant of the applied load. As for E modulus measurements, one must be aware of the fact that this value is always influenced by the substrate. Several methods are proposed in the literature to remove the substrate influence in the measured hardness. This can be achieved by mean of an extrapolation to zero indentation depth from a set of E modulus measured at different penetration depths [Fisc 06a], or using simple empirical approaches [Bull 05] [Beeg 05].

For indentation at very low penetration depths (less than $\sim$ 200 nm), so-called *Indentation Size Effect* (ISE) may play a significant role. They can be related to (i) the surface preparation of the specimen [Nix 98], (ii) test artifacts (e.g. a non-fully developed plastic zone associated to shallow depth and to a blunt indenter tip[10], pile-up and sink-in that are not accounted for in calculations [Bull 05], non reliable tip calibration for indentation depth smaller than $\sim$ 100 nm), or (iii) material related effects (such as the so-called *strain gradient plasticity*[11] that can result in artificially high hardness values due to geometrical necessary dislocation created at the apex of the indenter tip [Nix 98], or else microstructural scale effects when h_{max} is comparable to grain size or material domains in multiphase materials). Models for ISE have been developed, but often several mechanism are likely to take place and cannot be distinguished.

General recommendations for nanoindentation testing on thin films, both concerning experimental procedures and the correct interpretation of the results, can be found in [Bull 05] [Fisc 06a]. A review of the main ISE effects is provided in [Bull 03]. The specific case of nanocomposite hard coatings is developed in [Schw 05] and [Fisc 06b].

In the present work, the thickness of the coatings tested by nanoindentation was of the order of 1 µm only. Too fulfill the 10% rule of thumb described above, indentation tests were performed at a penetration depth smaller than 100 nm. ISE effects are then likely to be present and could be pointed out from indentation load series performed on few micrometer-thick coatings, as reported in section 5.2.3 p. 123.

---

[10] A typical tip radius is of the order of 50–100 nm.

[11] The term *indentation size effect* is actually partly used as an equivalent of *strain gradient plasticity*, and partly in a more general meaning of depth dependent values measured by nanoindentation. The latter definition is used here.

4.3.2 Residual stress determination by profilometry

The thickness and internal residual stress in the coatings were determined using a Tencor® P-10 Surface Profiler mechanical profilometer. The thickness was determined by measuring the step profile formed between coated and uncoated regions on the substrate, the latter being masked by the metallic clamps used to fix the samples on the sample holder during the deposition process. The biaxial residual stress was calculated using Stoney's equation [Ston 09] after measuring the spherical deflection of samples deposited on silicon. A concave top surface (supporting the film) indicates a thin film under tensile stress, while a convex top surface indicates a thin film under compressive stress. According to Stoney, the residual stress σ_f in a single thin film on a substrate is given by:

$$\sigma_f = \frac{4\rho}{3L^2}\frac{E_s}{(1-\nu_s)}\frac{t_s^2}{t_f} \tag{4.24}$$

with ρ being the spherical deflection, L the length on which the curvature is measured, E the Young's modulus, ν the Poisson's ratio and t the thickness. The subscripts s and f denote the substrate and the film, respectively. From the specifications of $\langle 100 \rangle$ oriented Si-wafer from the company Si-Mat (Germany): $t_s = 380$ µm, $E_s = 130$ GPa and $\nu_s = 0.275$.

4.4 Optical characterization

4.4.1 Transmission measurements by optical spectroscopy

Optical transmission measurements were carried out at normal incidence in the range 190-1100 nm (6.5-1.1 eV) on a UV-vis spectrophotometer (model Cary-50 scan), using the Cary VARIAN UV scan software (version 3.0) for the measurement control. Typical transmission curves on Al-Si-N nanocomposite thin films deposited on UV-grade fused silica are shown in Figure 4.8a. Multiple reflections at the three media interfaces (air/film, film/substrate and substrate/air) are responsible for the interference fringes visible on all the curves (except for the uncoated substrate). The measured optical transmittance is a combination of film and substrate properties. In the case of a single absorbing film deposited on a flat, thick and finite transparent substrate, a simple analysis method enables to derive the refractive index, the absorption coefficient and the thickness of the film from the fringes of a single transmission curve. This method is known as the *envelope method* and was developed by Manifacier *et al.* [Mani 76] and Swanepoel [Swan 83]. The method is briefly summarized here. For a detailed development, see [Swan 83].

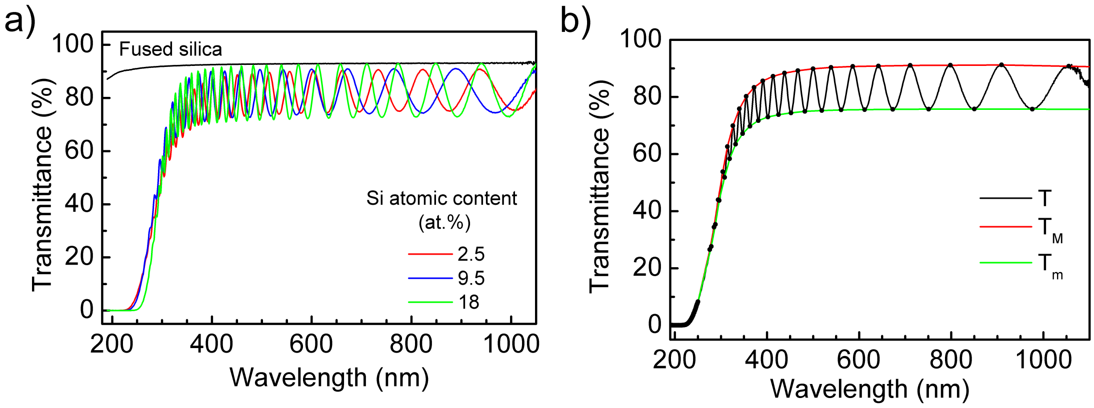

Figure 4.8: (a) Typical transmission curves measured on Al-Si-N nanocomposite coatings of various compositions deposited on UV-VIS grade fused silica; (b) Transmission spectrum of an Al-Si-N film deposited on fused silica together with the envelope curves of interferences maxima, $T_M(\lambda)$*, and minima,* $T_m(\lambda)$*.*

The envelope method Let us consider a film of uniform thickness d and of complex refractive index $\tilde{n} = n - i\kappa$ with n the refractive index of the film and κ its extinction coefficient which is related to the absorption coefficient α using $\kappa = \alpha\lambda/4\pi$. The substrate is infinitely thick compared to the film and has a refractive index s and an absorption coefficient $\alpha_s = 0$.

By measuring an uncoated substrate, the refractive index of the substrate can be determined from the interference free transmission curve using:

$$T_s = \frac{2s}{s^2+1} \tag{4.25}$$

Once s is known, the transmittance T of the system film/substrate is a complex function of n and α. In the case of $\kappa^2 \ll n^2$, the expression for the transmittance is given by [Swan 83]:

$$T = \frac{Ax}{B - Cx\cos\varphi + Dx^2} \tag{4.26}$$

where $A = 16n^2 s$, $B = (n+1)^3(n+s^2)$, $C = 2(n^2-1)(n^2-s^2)$, $D = (n-1)^3(n-s^2)$, $\varphi = 4\pi nd/\lambda$ and $x = \exp(-\alpha d)$.

The maxima T_M and minima T_m of the interference fringes can be written as:

$$T_M = \frac{Ax}{B - Cx + Dx^2} \tag{4.27}$$

$$T_m = \frac{Ax}{B + Cx + Dx^2} \tag{4.28}$$

and are considered continuous function of wavelength λ. They are generated by interpolations through the maxima and minima of the transmission fringes, as shown in Figure 4.8b.

In the region of medium and weak absorption ($T_M \gtrsim 70\%$), the real part of the refractive index can be calculated from the relation:

$$n = [N + (N^2 - s^2)^{1/2}]^{1/2} \tag{4.29}$$

where

$$N = 2s\frac{T_M - T_m}{T_M T_m} + \frac{s^2 + 1}{2} \tag{4.30}$$

Once $n(\lambda)$ is known, the absorbance of the film x can be calculated by an expression of the form $x(n)$ obtained from Eq. 4.27:

$$x = \frac{E_M - [E_M^2 - (n^2 - 1)^3(n^2 - s^4)]^{1/2}}{(n - 1)^3(n - s^2)} \tag{4.31}$$

where

$$E_M = \frac{8n^2 s}{T_M} + (n^2 - 1)(n^2 - s^2) \tag{4.32}$$

The absorption coefficient α and the extinction coefficient κ can be calculated from Eq. 4.31. The film thickness d can be estimated from the positions (λ) and refractive indices of two adjacent maxima (or minima) using the basic equation for the formation of interference fringes $2nd = m\lambda$, with m an integer.

Limitations of the envelope method come from the assumptions made regarding the non absorbing substrate, the low absorption of the layer, the ideally flat interfaces, as well as from the definition of the continuous envelope curves. Improvements of the envelope method are available to account for a surface roughness [Swan 84] or to determine the optical properties of non-uniformly thick absorbing films [Rich 04].

4.4.2 Spectroscopic Ellipsometry

Spectroscopic ellipsometry (SE) measurements can also be carried out to determine the optical properties of thin films. This was attempted here using an Ellipsometer SE850 (from Sentech Instruments GmbH) at the university of Basel (Group of Prof. Dr. P. Oelhafen).

Ellipsometry measures the change of polarization of light upon reflection on a specimen and enables the extraction of the real and imaginary part of the dielectric function (or complex refractive index) [Rose 90]. Ellipsometry measures the ratio of r_s and r_p, the complex Fresnel's reflection coefficients for light polarized perpendicular and parallel to the plane of incidence, which is described by the fundamental equation of ellipsometry:

$$\frac{r_p}{r_s} = \tan(\Psi)\exp(\Delta) \tag{4.33}$$

where the Ψ and Δ, known as the ellipsometric angles, are the experimental quantities measured, that are related to the optical and structural properties of the sample.

Since Ψ and Δ cannot be converted directly into the optical constants, the measured values must be compared to values calculated for an assumed optical model. The sample structure is hence described by a layer model, taking into account each oxide layer and surface roughness as additional individual layers (see e.g. [Khos 05] [Easw 05]). For each layer, a model for the dielectric function must be chosen (e.g. Cauchy or Sellmeier for insulators, Drude for metals, Tauc-Lorentz for amorphous layers, etc.). Effective medium approximations can also be used to account for an anisotropic media such a composite layer (e.g. Al-Si-N two-phase nanocomposite coatings), a porous layer (e.g. sputtered AlN open columnar structure) or a surface roughness (see e.g. [Sanj 05] for SE on optically opaque Nb-Si-N nanocomposite thin films). This becomes quickly excessively complex when a large number of parameters are to be fitted for a single measurement, e.g. n, k (the optical constants) and d (the thickness) for each layer of the model. Assumptions must be made so a to reduce the number of parameters, but this proves difficult in the case of surface oxidized Al-Si-N composite coatings on top of Si wafers covered with a native $\mathrm{SiO_2}$ oxide. Modeling is critical and no model could be found to fit satisfactory the experimental data. After initial trials these complications led to the decision that spectroscopic ellipsometry was not used as a characterization tool for Al-Si-N nanocomposite coatings.

Part III

Experimental results

Chapter 5

Al-Si-N nanocomposite coatings

5.1 Sample preparation

5.1.1 General deposition parameters

Deposition conditions

Al-Si-N samples were deposited by DC unbalanced magnetron sputtering from confocally arranged pure Al (99.99%) and Si (99.999% – B-doped[1]) circular targets of 2" in diameter in an Ar/N_2 reactive atmosphere at a total pressure of about 0.3 Pa. The base pressure of the deposition chamber at room temperature was $\leq 10^{-6}$ Pa. The argon and nitrogen flows were set at 15 sccm and 7 sccm respectively for all depositions. Ar was injected at the bottom of the deposition chamber, while N_2 was injected at the Si target surface. The aim was to form a nitride at the target surface that shall be sputtered instead of pure Si (i.e. poisoned target state). This was found to be necessary to promote a sufficient nitridation of the silicon in the deposited films[2]. No substrate bias was applied, as preliminary tests[2] using RF bias (2.5–5 W, corresponding to 75–100 V) showed a strong residual stress in the coatings, leading to a film delamination on glass substrates.

---

[1] resistivity: 0.005–$0.020\ \Omega \cdot \mathrm{cm}$, i.e. B concentration $\sim 3.0 \times 10^{18}$–$2.0 \times 10^{19}\ \mathrm{cm}^{-3}$.

[2] Preliminary experiments performed by Dr. Franz Josef Haug.

Control of reactive sputtering

I could observe that, for the high pumping speed[3] achieved by the turbomolecular pump mounted on the deposition chamber, the hysteresis effect associated to reactive sputtering was not visible (cf. Fig. 5.1). Within the deposition conditions used in this work, the dwell time (average time spent by gas molecules in the deposition chamber) amounts to 0.3 s (= $pressure \times volume/flow$)[4]. Diserens [Dise 00] observed in an other sputter deposition system that the hysteresis was absent for a dwell time of 1 s, but could be observed for 1.6 s. This is consistent with my observations. The suppression of the hysteresis effect at high pumping speed is a well known effect [Safi 00] [Musi 05]. The change of slope outlined by dashed lines in Figure 5.1 illustrates that the chosen nitrogen flow of 7 sccm is situated just at the cross-section of tangent curves corresponding to the fully metallic mode and the fully reactive mode. The surface of the Al target is then probably partially but not fully poisoned at this nitrogen flow. The poisoning state of the target surface is confirmed by the reduction of the deposition rate by a factor of four between pure Al (N_2 flow = 0 sccm) and AlN (N_2 flow = 7 sccm). This poisoning occasionally caused micro-arcing events at the surface of the targets (mainly on the Al target) during the deposition of Al-Si-N thin films, that could not always be suppressed by the arc suppression system included in the DC power supplies.

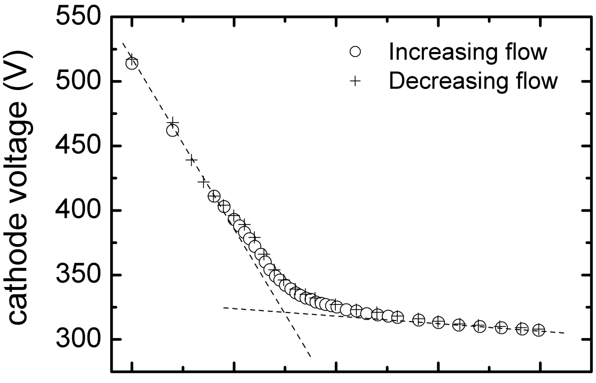

Figure 5.1: Dependence of the cathode voltage of the aluminum target on the flow of reactive gas (N_2) for a fix applied power (200 W) and flow of neutral gas (Ar, 15 sccm).

---

[3] Volume flow rate for $N_2 = 210$ l/s.

[4] with pressure $P = 3 \times 10^{-3}$ mbar, volume of the deposition chamber (Ø 15", height 13") $V = \pi \times (15 \times 2.54/2)^2 \times (13 \times 2.54)/1000 = 37.6$ l and flow $Q = 22$ sccm, with 1 sccm = 1013 mbar $\cdot$ cm$^3 \cdot$ min^{-1} = 1013 mbar × 0.001 l/60 s = 0.01688 mbar $\cdot$ l $\cdot$ s^{-1}.

Substrates

For characterization purpose, all the samples were deposited on several substrate materials. First, silicon (100) wafers (unetched, i.e. with native oxide) were used. The low roughness of these substrates make them convenient for the X-ray (in particular XRR) and mechanical characterization of the coatings. Silicon wafers moreover can be used for profilometry measurements and the calculation of residual stress in the coating, deduced from the substrate (Si) bending. Al-Si-N films were also deposited on polished tungsten carbide substrates (WC-Co). These substrates enable the preparation of high quality TEM samples, thanks to their mechanical properties that are comparable to those of Al-Si-N, as well as similar sputter rate under ion milling. Glass (standard microscope slides) and polished fused silica (SiO_2 - UV-VIS grade) were used as transparent substrates for the optical characterization of the coatings.

5.1.2 Sample series

Three series of Al-Si-N samples were prepared, using two different constant power values on the Al target (100 W and 200 W – i.e. 4.9 W/cm^2 and 9.8 W/cm^2 respectively) and two different deposition temperatures (200°C and 500°C). The composition[5] of the coatings was varied from pure AlN to Al-Si-N with 30 at.% of Si by keeping the power on the Al target constant and progressively increasing the power on the Si target. The deposition parameters are listed in Table 5.1. For sake of simplicity, the conditions coding A, B and C of Table 5.1 are used throughout this manuscript. The film thickness is in the range 1–2 µm for all Al-Si-N nanocomposite samples, as determined by mechanical profilometry.

Table 5.1: Deposition conditions for three series of Al-Si-N samples.

Series	Substrate temperature (°C)	Power on Al (W)	Power on Si (W)	Deposition rate (nm/h)
A (○)	200	100	0–100	95–190
B (■)	200	200	0–150	245–595
C (▲)	500	200	0–170	265–680

---

[5] The composition of the films is expressed in atomic percentages, defined as the concentration of a given element over the total amount of Al, Si, N and residual O in the coatings. For further details, see Subsections 4.1 and 5.2.1.

5.1.3 Post-deposition annealing

Post-deposition annealing experiments on Al-Si-N films deposited on silicon were performed in a Nabertherm (RHT 08/17) tube oven. Prior to heating, the oven chamber was evacuated and backfilled several times with argon. An argon flow (equivalent to a constant pressure of 1 atmosphere in the pumped oven chamber) was then established and the heating procedure was started, as indicated in Figure 5.2. Annealing of the samples at 1000°C during 2h was performed in this way.

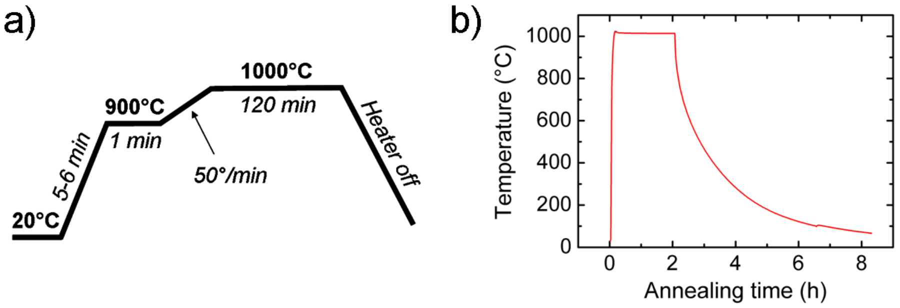

Figure 5.2: Annealing procedure used in this work: (a) programmed heater control sequence, and (b) measured evolution of the annealing temperature. The temperature increase was performed as fast as possible from room temperature to 900°C, and then slowed down before reaching 1000°C. The annealing temperature of 1000°C was then kept constant during 2h. The heater was then turned off and the samples were allowed to cool down without any external cooling. The whole procedure was performed in Ar (1 atmosphere).

5.2 Experimental results

The chemical, structural, mechanical and optical properties of Al-Si-N thin films, as well as their thermal stability and oxidation resistance, were extensively investigated by XPS, XRD, electron microscopy (SEM, TEM), nanoindentation, mechanical profilometry and optical transmission spectroscopy, as reported in the following sections.

5.2.1 Chemical properties

X-ray Photoelectron Spectroscopy (XPS) is a powerful technique that enables not only the determination of the atomic concentrations of elements but also the identification of chemical states and their evolution upon change e.g. in the deposition conditions of Al-Si-N thin film. The main results of

XPS investigations on Al-Si-N thin films are presented here. Details on the analysis conditions are given in Chapter 4, section 4.1.

a) Chemical composition of Al-Si-N films

The elemental composition of the films was determined with respect to their main constituents (N, Al, Si) and their main impurity (O). Films with a composition ranging from pure AlN to Al-Si-N up to 23 at.% of Si were investigated. The Al content decreases as the Si content is increased; the nitrogen content was found to be constant and equal to 50 ± 2 at.% for all Al-Si-N films except pure SiN_y (as specified below). The deposition conditions were set to provide a sufficient amount of nitrogen resulting in fully nitrided layers, i.e layers that do not contain free (unreacted) metal atoms, all the Al and Si atoms being covalently bonded to nitrogen. This is necessary for optical transparency in the whole visible range[6].

Over six films of pure SiN_y deposited and investigated by XPS, the mean N/Si ratio was determined as 1.15 ± 0.08, instead of 1.33 for stoichiometric Si_3N_4. This measured stoichiometry, however, probably does not correspond to a significant intrinsic nitrogen deficiency in the as-deposited coating. It is well known that the use of argon sputter cleaning prior to XPS analysis can lead to small nitrogen depletion due to nitrogen preferential sputtering in SiN_y [Pavl 93] [Dise 00]. This nitrogen depletion had an evident consequence on the Si2p peak shape in pure SiN_y, which was found to be slightly asymmetric - larger on the low BE side - and better fitted by at least two components[7]. The minor component at low binding energy represented about 15% of the total area and was attributed to Si atoms bonded to less than four nitrogen atoms, based on the work of Ingo *et al.* [Ingo 90]. These authors developed a model that explains the Si2p line shape in amorphous SiN_y in term of the superposition of five chemically-shifted components corresponding to the five Si tetrahedral bonding configurations $\mathrm{Si{-}Si}_{4-n}\mathrm{N}_n$ (with $n = 0,...4$). In this model, nitrogen atoms remain bonded to three Si atoms at all compositions. From curve fitting[8], Ingo *et al.* obtained a value

---

[6] Non-fully nitrided Al-Si-N films could be easily recognized from their brownish color (in transmission).

[7] No reliable fit could be performed with three components or more. For such a high number of peak components, a physically meaningful fit requires to make founded assumption on fit constraints to be fixed during the fitting procedure (see e.g. [Ingo 90]). In the present case I considered that the uncertainty on the constraints to be set was too high, so that I restrained myself to a fit with a minimum number of components, i.e. two.

[8] including assumptions on the line shape and the use of fixed increments of binding energy position and full width at half maximum (FWHM) from one component to the

of 0.6 eV for the chemical shift induced by each additional bonded nitrogen atom. Comparing this value to the chemical shift observed using two peak components, namely $\sim$ 0.9 eV, it is assumed that more than two bonding configurations for Si atoms are present in the sputtered region analyzed by XPS. From the analysis of the Si2p photoelectron peak it was moreover concluded that no free Si was present in the films.

⇒ *As the exact stoichiometry of the silicon nitride deposited in this work remains unknown, it is referred to as* SiN_y *throughout this thesis, instead of using the notation for a stoichiometric composition,* Si_3N_4.

As mentioned above, the coatings are also contaminated with oxygen. The mean oxygen concentration determined by XPS after argon pre-sputtering of the surface was about 4 at.%. Such a high concentration could be partially related to an incomplete removal of the surface native oxide during argon sputter-cleaning prior to XPS analysis. This was demonstrated by XPS sputter depth profiles (see section 5.2.5) that also revealed that a few atomic percents of oxygen (0.5–2 at.%) were incorporated in the coatings during reactive sputter deposition process, despite an excellent base pressure of the deposition chamber ($< 10^{-6}$ Pa). This may arise from the incorporation of residual water and oxygen desorbed from the chamber walls during sputter deposition and to the high reactivity of aluminum with oxygen.

b) Al-Si-N chemical states analysis

Chemical states in a material can be evidenced through the binding energy (BE) position of photoelectron (PE) lines in XPS measurements. Large ($>$ 1 eV) variations in peak positions can be used to distinguish different bonding state(s) of an element by comparison to literature data[9] reported for pure materials. Small energy shifts ($<$ 1 eV) can evidence minor changes in the chemical environment of atoms. The detection of small energy shifts requires, however, that binding energies are accurately determined before they can be compared from one sample to the other[10], or even from one lab to the other[11]. This is achieved by the use of a charge reference. As mentioned in section 4.1.3 (p. 55), charge referencing

---

other (corresponding to the different bonding configurations)

[9] directly taken from original publications, or from the NIST database [NIST 03] - or any other XPS data-bank. A critical review of the specific content and structure of several XPS data-banks was recently published [Cris 07].

[10] same experimenter, same XPS apparatus and same analysis conditions

[11] different experimenter, different apparatus and different analysis conditions

is necessary in the case of insulating materials such as Al-Si-N thin films but it remains a delicate issue. A way around the problem is to study ΔBE values, the energy difference of two photoelectron lines of two distinct elements recorded on the same specimen during the same measurement run. The energy shift due to static charging is assumed to be the same for all photoelectron lines, so that this shift cancels out when the energy difference between two lines is calculated. Additional information on chemical effects can be deduced from photoelectron line widths and line shapes, which can be studied independently on the knowledge of absolute BEs. Last but not least, further information can be obtained from the combination of PE and Auger line positions in the form of the so-called Auger parameter (cf. section 4.1.1, p. 53) that is not affected by charge referencing procedures.

In this section, an extensive XPS study of the chemical states in Al-Si-N thin films is presented. The reason for this study is that the local chemistry in Al-Si-N systems containing more than a few atomic percents of silicon is not well understood, as reviewed in section 2.2.3 p. 26. According to the existing Al-Si-N ternary phase diagram (Fig. 2.4, p. 21), AlN and Si_3N_4 are predicted to be immiscible. The formation of an $Al_{1-x}Si_xN$ solid solution was nevertheless reported by Kasu *et al.* in films deposited at 900°C by MOVPE [Kasu 01]. To date, no study on the local chemistry of Al-Si-N samples sputter deposited at low deposition temperature is available. The present study is therefore aimed at determining if a solid solution of Al-Si-N or a mixture of AlN and Si_3N_4 (or both) is formed in the deposited Al-Si-N samples[12]. For this purpose, XPS data (BEs, ΔBEs, line widths, Auger parameter etc.) were carefully examined. The section is organized as follows:

- First, strong indications of the evolution of chemical states in Al-Si-N films with increasing the Si content are given in the form of ΔBE values between the main PE peaks of Al, Si and N, as well as the line widths of these PE peaks. These data do not require any correction for static charging and are hence the most reliable data that can be obtained by XPS on Al-Si-N thin films.

---

[12] It must be born in mind that for all low temperature PVD deposition processes of carbide, nitride and boride coatings, the formation of metastable phases is to be expected [Spen 90] [Spen 01]. This is explained by kinetic limitations that prevent the growing films to reach a thermodynamic equilibrium during the deposition process. One must hence refrain from extracting a phase diagram from the data reported in this work. It must also be emphasized that the term "phase" will be used extensively throughout this manuscript, however not to be associated to a thermodynamical meaning. The kinetically-limited material phases discussed in this work did not necessarily reach a thermodynamical equilibrium.

- As a more detailed understanding of the chemical environment of the atoms can only be deduced from absolute BE positions, the issue of charge referencing of Al-Si-N thin films is discussed. An evaluation of several charge references (namely the C1s, Ar2p$_{3/2}$ and Au4f$_{7/2}$ PE line positions) is provided.
- Gold-referenced BE values are then reported and their evolution is discussed.
- Finally, complementary information is sought in the evolution of the nitrogen N(KLL) Auger peak, nitrogen Auger parameter and chemical state plot.

All these data are confronted to the strong indications of a solubility limit of 6 at.% of Si in aluminum nitride found by XRD characterization and reported in section 5.2.2, p. 108. At the end of this section on XPS, a conclusion is given on the information that can be gained by XPS on Al-Si-N films. It will be seen that these information are complementary to the structural information obtained from XRD or TEM characterization techniques.

Indications of the evolution of chemical states The evolution of ΔBE values between the main core level photoelectron lines of the three constituting elements Al, N and Si as a function of the Si content are shown in Figure 5.3. In Figure 5.3a, the binding energy difference between N1s and Al2p, ΔBE(N1s–Al2p), is constant and equals 323.2 eV over the whole composition range. This corresponds to the average value reported for pure AlN in literature (cf. Appendix B). In contrast the binding energy difference between N1s and Si2p lines, ΔBE(N1s–Si2p), increases by 0.6 eV from 295.3 eV in Al-Si-N with 1.5 at.% of Si to 295.9 eV in Al-Si-N with about 15 at.% of Si (Fig. 5.3b). Beyond 15 at.% of Si, ΔBE(N1s–Si2p) remains constant. The ΔBE equals 295.9 eV in pure SiN_y, which corresponds to the average value reported for Si_3N_4 in literature (cf. Appendix B). The same shift of 0.6 eV is observed for ΔBE(Si2p–Al2p) (Fig. 5.3c). At 1.5 at.% of Si and 15 at.% of Si, ΔBE(Si2p–Al2p) values of 27.9 eV and 27.3 eV were found, respectively. Again the binding energy difference remains constant at 27.3 eV beyond 15 at.% of Si. Note that the values reported here agree with those reported in previous XPS studies of Al-Si-N thin films, namely 27.5 eV at 11 at.% of Si [Perr 97] and 27.2 eV at about 25 at.% of Si [Maen 90].

The behavior shown in Figure 5.3 suggests that the Al–N bonding remains unaffected by the incorporation of Si in hexagonal wurtzite AlN (w-AlN), while the core electrons of silicon encounter a clear chemical shift, seemingly to lower binding energies, as the Si content is increased. Above 15 at.% of Si, all the ΔBE values remain constant. This suggests that there is no more change in the chemical environment of atoms in Al-Si-N films. In particular the chemical environment of Si atoms may be then similar to that in pure silicon nitride. However energy difference values can only inform on relative chemical shifts, not on absolute chemical shifts. Here charge referenced binding energies are needed; these are reported later.

Complementary information on the evolution of chemical states is gained by the study of line shapes and line widths. In insulators with a sufficiently large bandgap (as it is the case for AlN) the line shape of core level photoelectrons is symmetric. Any deviation from the symmetrical line shape, in the form of a shoulder or of a small asymmetry, indicates that several lines associated to distinct chemical states overlap. When no effect on the overall line shape is observed, further information can be obtained from line broadening effects. The line width of a given photoelectron line is related, among other parameters, to the core-hole lifetime and depends on the chemical environment of the emitting atom. The full width at half maximum (FWHM) of a photoelectron line is therefore a valuable indicator of the chemical state of elements. In particular, local variations in the atomic arrangement may cause a redistribution of local potentials, leading to a "disorder broadening" of the core photoelectron lines [Brig 03]. Line broadening may also be attributed to the coexistence of distinct chemical states that give rise to overlapping photoelectron lines so close to each other that they cannot be resolved. It is commonly agreed that when the FWHM ratio of a given peak – measured e.g. in Al-Si-N films – to a reference line – measured e.g. in pure AlN or SiN_y – equals ca. 1.15 or more, then two lines may be assigned to fit the measured peak.

The full widths at half maximum (FWHM) of the main photoelectron peaks, namely Al2p, Si2p and N1s are reported in Figure 5.4, together with critical FWHM values that correspond to the above criterion. Stacking plots of these photoelectron peaks are reported in Figure 5.10 (p. 101): it can be seen that the Al2p, Si2p and N1s PE peaks are symmetrical over the whole composition range explored in this work, i.e. they show neither a shoulder nor any significant asymmetry. This justifies the use of the above "1.15 criterion".

In Figure 5.4a, the FWHM of Al2p is constant ($\sim$ 1.6 eV) over the whole composition range. The Al2p line remains moreover symmetrical. In

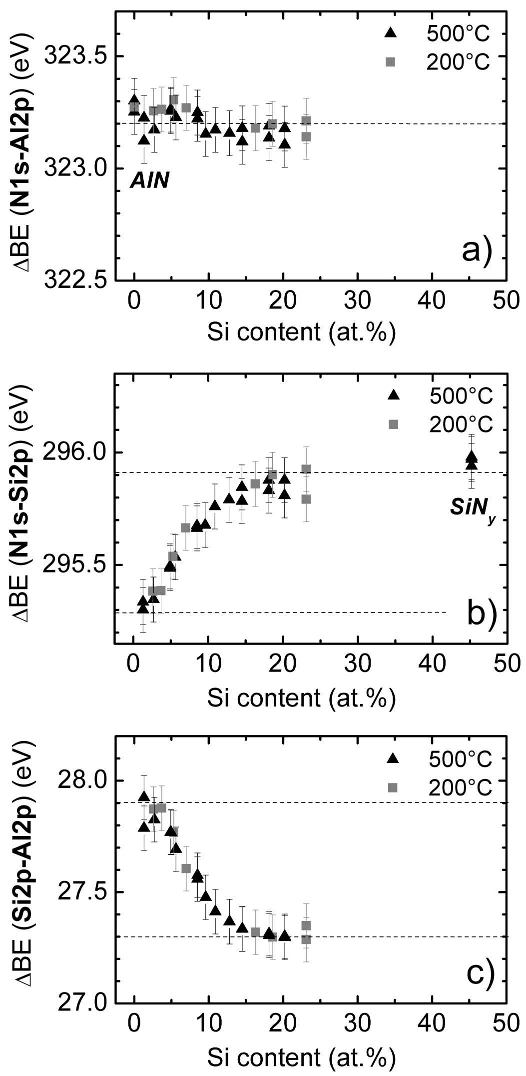

Figure 5.3: Evolution of the binding energy difference ΔBE between the N1s and Al2p, N1s and Si2p, and Si2p and Al2p photoelectron peaks, as a function of the silicon content in Al-Si-N films. Note that some samples were measured several times (i.e. several data points for one film composition) in completely independent measurements (new sample mounting, new position on the sample) under identical measurement conditions to improve the statistics of XPS data.

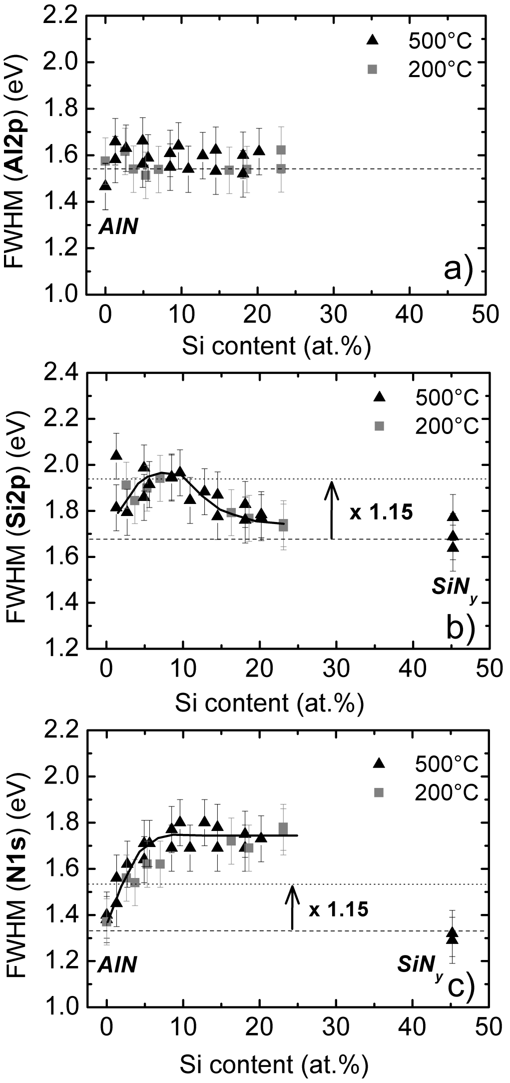

Figure 5.4: Evolution of the FWHM of Al2p, Si2p and N1s core level photoelectron (PE) lines as a function of the composition of Al-Si-N films. Solid lines are added as a guide to the eye. Dashed lines correspond to the criterion of critical line broadening indicating the existence of several chemical states of an element in Al-Si-N composite films when the FWHM of a PE line exceeds 1.15 × the FWHM of the same PE line taken in a reference material, here reactively sputter deposited AlN and SiN_y.

contrast, the FWHM of Si2p and N1s peak encounter line broadening effects as compared to the pure materials (sputter deposited AlN and SiN_y) when the Si content in Al-Si-N films is varied. This suggests that not only the silicon bonding but also the nitrogen bonding is affected by the formation of a composite material. Since the Al–N bonds are seemingly not affected (Fig. 5.3a), this change in the nitrogen bonding must be associated with the Si–N bonds [13]. The Si2p line is found to be symmetrical at all compositions with the exception of pure SiN_y, as already mentioned p. 85. For a Si content between 1 and 5 at.% (Fig. 5.4b), the Si2p line width is found to increase[14] from 1.8 eV to about 1.95 eV. It is there right at the limit defined as 1.15 times the line width (1.7 eV) in pure SiN_y. Between 5 and 10 at.%, the line width remains constant. Beyond 10 at.% the line width decreases to about 1.75 eV, close to the value of pure SiN_y. The "1.15 criterion" value is not exceeded, so that the broadening of the Si2p line cannot be unambiguously attributed to the existence of distinct chemical states or to a disordered chemical state. An interpretation for this broadening is given below. As for nitrogen (Fig. 5.4c), the N1s line width quickly increases from 1.4 eV in pure AlN to 1.7 eV in Al-Si-N with 10 at.% of Si, clearly surpassing 1.15 times the reference line width taken in AlN (1.4 eV) and SiN_y (1.3 eV). The line width remains unchanged upon further addition of silicon up to the highest content explored in this study, 23 at.%. Below about 5 at.% of Si, the N1s line broadening is small and cannot be unambiguously attributed to distinct chemical states or to a disordered chemical state, as for the Si2p line. Above 10 at.% of Si, however, the N1s peak probably results from the overlap of several lines associated to distinct chemical states in a phase-separated composite. This is further supported by the appearance, above about 4 at.% of Si, of a slight asymmetry of the N1s peak: the low BE tail of the peak becomes progressively narrower as the Si content is increased, as shown in Figure 5.5. Yet attempts to fit this peak with a base set of lines taken from pure AlN and SiN_y[15] remained unsuccessful; the relative areas under the fitted component lines could not be correlated to the amount of silicon in Al-Si-N. This is probably due to a line broadening and/or a change of line shape of individual component lines related to a non-uniform chemical environment of N atoms in Al-Si-N films.

---

[13] No elemental Al or Si was identified in the fully nitrided films. Moreover, no Al-Si compound is known to exist, neither is such a compound identified in the present work. The bonds formed in Al-Si-N films should therefore be exclusively Al–N and Si–N bonds.

[14] The FWHM values of the Si2p line are scattered at low Si contents, due to the small intensity of the Si2p signal at such concentrations.

[15] i.e. a set of two lines with fixed line shapes, corresponding to best fits of the N1s line in pure AlN and in pure SiN_y, respectively.

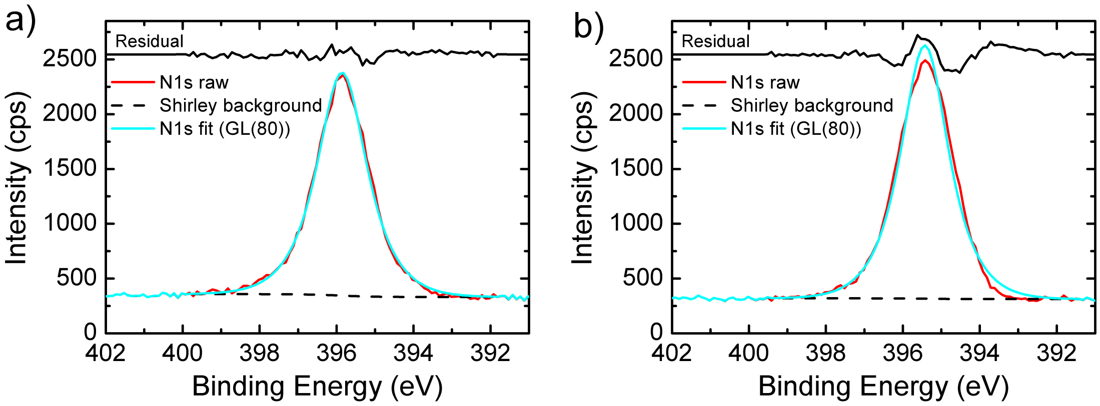

Figure 5.5: N1s line fitting in Al-Si-N films containing (a) 2.5 at.% and (b) 15 at.% of Si. As described in section 4.1.4 p. 57, an iterative Shirley background was removed before line fitting with a Gaussian/Lorentzian product of type GL(80). An asymmetry on the low binding energy tail of the N1s line is clearly seen in (b).

The ΔBE(N1s–Al2p) and the width of the Al2p peaks are found to remain constant for all Si contents (Fig. 5.3a and 5.4a). This suggests that the chemical environment of the Al atoms does not change when the Si content is increased from 0 to 23 at.%. In contrast, the binding energy difference between N1s and Si2p (ΔBE(N1s–Si2p)) and Si2p and Al2p (ΔBE(Si2p–Al2p)) change considerably with increasing Si content. Similarly, the line widths of the Si2p and N1s peaks increases up to and beyond the 1.15 times reference line width criteria, respectively. This suggests variations in the chemical environment of silicon and nitrogen atoms with increasing the Si content in Al-Si-N; variations associated to the Si–N bonds. However, it cannot be concluded if Si atoms are incorporated in the films as a separate silicon nitride phase or as an Al-Si-N solid solution (or both) and for which Si contents. From Figure 5.4c, it can only be stated that several chemical states of nitrogen atoms coexist between about 10 and (at least) 23 at.% of Si in Al-Si-N. This is compatible with both a complete phase separation into pure AlN and $\mathrm{SiN_y}$, and a phase separation into an Al-Si-N solid solution and $\mathrm{SiN_y}$ from a Si content that cannot be identified here.

Considering now that a solubility limit of 6 at.% of Si in wurtzite AlN is found from XRD data (section 5.2.2), the evolution of the PE line widths reported in Figure 5.4 is interpreted as follows:

- *Al atoms*: The local chemical environment of Al atoms in pure AlN and $Al_{1-x}Si_xN$ is the same, i.e. a four-fold (tetrahedral) coordination to N atoms (see Appendix A), so that the formation of an Al-Si-N solid solution has no visible influence on the Al2p line width (Fig. 5.4a).

- *Si atoms*: In pure and also amorphous Si_3N_4, Si atoms are four-fold coordinated to N atoms (see Appendix A). Si atoms incorporated in an $Al_{1-x}Si_xN$ solid solution are expected to retain a four-fold coordination to N atoms. However, geometrical distortions can be expected in the form of variations of the Si–N bond length (see section 5.2.2) or of the formation of defects which compensate for the extra electron brought by Si in the AlN lattice [Bogu 97] [Goen 01] [Tani 02] [Herm 05]. In particular, the formation of Si DX[16] centers can cause a large local lattice distortion with the deviation of the position of Si atoms from the exact substitutional lattice sites. From 0 to 6 at.% of Si, Si atoms may feel a chemical environment different from that in pure silicon nitride: this corresponds to a disorder broadening of the Si2p line, in agreement with small broadening observed in Figure 5.4b. Above 6 at.% of Si, a separate SiN_y phase is formed and two distinct chemical states coexist. However, the local environment of Si atoms is identical in both existing phases, so that the "1.15 criterion" value for the line width is not exceeded. When the Si content is increased far above 6 at.%, the Si2p line width decreases to the value of pure silicon nitride, as the SiN_y phase becomes the phase that contains the majority of the Si atoms present in the films.

- *N atoms*: N atoms have a four-fold (tetrahedral) coordination to Al atoms in w-AlN and a three-fold (trigonal planar) coordination to Si atoms in Si_3N_4 (see Appendix A). The coexistence of AlN (or $Al_{1-x}Si_xN$) and SiN_y distinct phases therefore leads to a significant line broadening of the N1s PE peak. In addition, N atoms in $Al_{1-x}Si_xN$ can be simultaneously bonded to Al and Si atoms, resulting in a disorder broadening of the N1s line. This explains the evolution shown in Figure 5.4c and the impossibility to fit the N1s peak with a base set of lines taken from pure AlN and pure SiN_y.

From the evolution described in Figures 5.3 and 5.4, it is remarkable that no particular effect is observed at 6 at.% of Si, as a separate SiN_y phase starts

---

[16] A DX center is a deep energy level (impurity level close to the Fermi energy in the band gap of a semiconductor) generated by the association of a substitutional donor impurity atom coupled to a point defect (e.g. a displacement of the donor atom from the ideal substitutional position, or a vacancy on a neighbor site) found in III-V and II-VI compound semiconductors [Moon 90].

to form at the grain boundaries of the Al-Si-N solid solution nanocrystalline phase (from structural data). Instead, two regions of distinct chemical evolutions with the Si concentration can be distinguished at Si contents below and above 10–15 at.%. This "critical" Si concentration of 10–15 at.% can be attributed to the appearance of a "thick" SiN_y phase, where the term "thick" means a SiN_y interlayer thicker than 1–2 monolayers. Above this thickness, the local chemical environment of Si and N atoms may be similar to what is found in bulk silicon nitride. In the composition region between 6 and 10–15 at.% of Si, the thin SiN_y interlayer that progressively forms and covers the entire surface of Al-Si-N crystallites may have a local environment considerably influenced by the presence of the majority phase, so that the Si2p and the N1s photoelectron lines can be shifted and/or broadened. This explains in turn why the chemical state of Si and N atoms cannot be unambiguously associated to the existence of a separate SiN_y phase with bulk properties[17] below 10–15 at.% of Si in the Al-Si-N films.

Charge referencing procedure Careful charge referencing is essential to produce reliable XPS data when insulating materials, such as Al-Si-N[18], are studied. Charge referencing methods rely on the use of a reference element supposed to be insensitive to the chemical environment of the studied specimen. The chemical state of this element must be known, so that the binding energy position of a main photoelectron line can be used as energy reference and assigned a tabulated BE position. The C1s line of adventitious carbon is often used for this purpose. However, if the XPS specimen samples are sputter-cleaned prior to chemical analysis – e.g. to remove a native oxide layer as it is the case here – the carbon contamination will be removed. In this work, two alternative methods of charge referencing were evaluated and compared with respect to their ability to induce the least artifacts during charge referencing. Both methods rely on the Ar^+ pre-sputtering (3 kV for 90 s) of the Al-Si-N samples. The first method makes use of the $Ar2p_{3/2}$ photoelectron line of implanted Ar atoms. The second uses the $Au4f_{7/2}$ line of gold atoms re-deposited to the analyzed area from the Au-coated masks used to clamp the samples and to avoid excessive charging of the surface during analysis (Fig. 5.6). As a small C1s signal could nevertheless be recorded for a few samples, among which "pure" AlN and SiN_y, it was used as test reference for comparison with literature data and with the two charge referencing

---

[17] In this respect, the term "phase" may not be the appropriate description for interlayers of one or two monolayers in nanocomposite coatings.

[18] The issue of accurate charge referencing is addressed in section 4.1.3 p. 55.

methods described above. The binding energies recommended by the NIST[19] were assigned to the C1s, Ar2p$_{3/2}$ and Au4f$_{7/2}$ lines, i.e. 284.8 eV, 241.82 eV and 84.0 eV respectively [NIST 03].

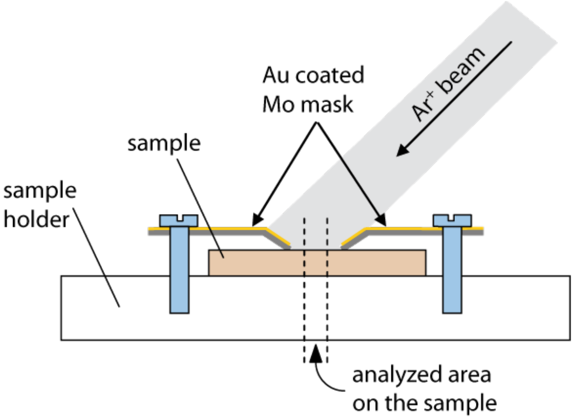

Figure 5.6: Experimental setup used for XPS analysis of Al-Si-N samples, in particular static charge referencing. The sample is clamped on a sample holder using a molybdenum mask coated with a thin layer of gold (a few 100 nm). The $100\times 100\,\mu m^2$ analyzed area is situated in the middle of the Ø 1 mm circular aperture of the mask. As the surface contamination is removed by Ar^+ sputtering of a 2×2 mm^2 area, argon atoms are implanted in the sample and a small quantity of gold sputtered from the mask is re-deposited on the sample surface.

The reason for the use of gold referencing in addition to argon referencing is that preliminary experiments – using implanted argon only – led to doubts concerning the validity[20] of this referencing method when comparing charge-referenced data to literature data. A second referencing method was hence considered. The validity of both methods was carefully assessed, looking for indications for possible chemical shifts of the Ar2p$_{3/2}$ and Au4f$_{7/2}$ photoelectron lines. These shifts unfortunately cannot be separated from static charge effects in absence of an additional "super" charge reference. Indications for the existence or the absence of chemical effects must therefore be obtained indirectly, as described below.

---

[19] National Institute of Standards and Technology

[20] Validity refers to the accuracy of the method, i.e. the extent to which the charge referencing method actually provides referenced binding energies for the studied specimen that are free from artifacts. Such artifacts can be either caused by a chemical interaction between the reference element and the specimen, or by any other phenomenon that results in an uncertainty on the chemical state of the reference element, i.e. on the BE value to assign to the photoelectron line position taken as an energy reference.

A first indication of the validity of the charge referencing method used here is simply given by the amount of reference atoms present in the analysis volume. Indeed, a dependence of this amount on the specimen chemistry or microstructure, or a too small amount of reference atoms may reveal a possible "sensitivity" of the reference element to its chemical environment. In the present case, the amount of implanted argon in Al-Si-N films due to Ar sputter cleaning prior to XPS analysis is of the order of 2–3 at.%. As shown in Figure 5.7, it is lowest for pure AlN (∼2 at.%). When incorporating silicon in the films, the amount of implanted Ar atoms increases slowly first (0–4 at.% of Si) and quicker at higher Si contents (4–10 at.%). It saturates to about 3–3.5 at.% in the range 15–25 at.% of Si. Note that in pure $\mathrm{SiN_y}$ only 2.5 at.% of Ar is found. The higher Ar content found in the Al-Si-N composite may arise from a facilitated implantation of Ar atoms at the grain boundaries. The increase of the Ar content with increasing Si content in Al-Si-N coincides with the increase of grain boundaries in the films, as the grain size is found to decrease (see section 5.2.2). This microstructure-dependent implantation sites may in turn have a noticeable influence on the chemical state of implanted argon atoms. For the other investigated method, i.e. gold decoration, the amount of gold deposited on the specimen surface was found between 0.3 at.% and 1.5 at.%. This is small, so that a sub-monolayer coverage of the Al-Si-N surface is expected. This may have a consequence on the chemical state of gold atoms, as presented in section 4.1.3 p. 55 and discussed in the following. Note that the large variations in Au content are related to the use of the same Au-coated mask for several successive XPS analyses before the gold layer was renewed.

The evolution of binding energy differences between the $\mathrm{Ar2p_{3/2}}$ and the $\mathrm{Au4f_{7/2}}$ photoelectron lines (Fig. 5.8), as well as the evolution of line widths (Fig. 5.9) are expected to give further insight into the chemical state of gold and implanted argon atoms.

Figure 5.8 shows a decrease from 157.5 eV (AlN) to 156.3 eV ($\mathrm{SiN_y}$) of the binding energy difference between the $\mathrm{Ar2p_{3/2}}$ and the $\mathrm{Au4f_{7/2}}$ line positions $\Delta\mathrm{BE}(\mathrm{Ar2p_{3/2}}\text{–}\mathrm{Au4f_{7/2}})$. This corresponds to a total chemical shift of -1.2 eV, which is clearly not acceptable for a charge referencing technique. The reported ΔBE values are moreover smaller than the value calculated from the Ar and Au line positions recommended by the NIST: $\Delta\mathrm{BE}(\mathrm{Ar2p_{3/2}}\text{–}\mathrm{Au4f_{7/2}}) = 241.8 - 84.0 = 157.8$ eV. Assuming that the Au line remains fixed at 84.0 eV, the Ar line position varies from 241.5 eV in AlN to 240.3 eV in $\mathrm{SiN_y}$ (see right axis of Fig. 5.8). This is far away from the Ar line position without chemical effects (241.8 eV). Furthermore the evolution

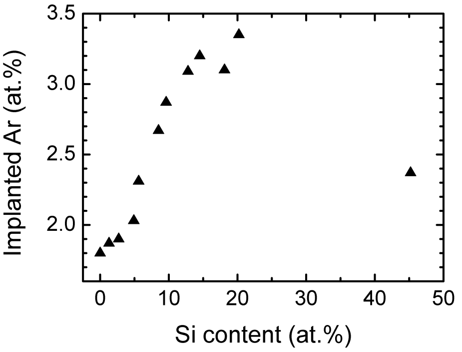

Figure 5.7: Amount of implanted Ar in Al-Si-N during Ar$^+$ sputter cleaning of the film surface, as a function of the Si content (series C).

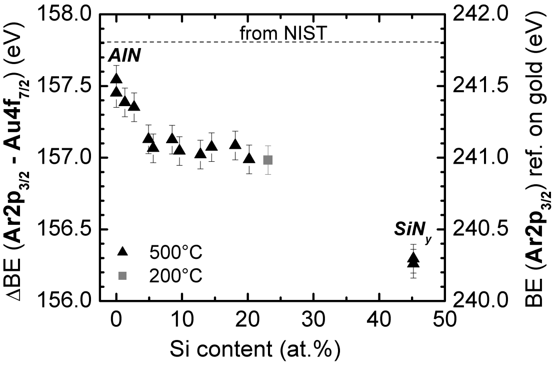

Figure 5.8: Left axis: Evolution of the binding energy difference between Ar2p$_{3/2}$ and Au4f$_{7/2}$ photoelectron lines measured on Al-Si-N specimens with variable Si content. Right axis: BE of the Ar2p$_{3/2}$ line as reference on Au4f$_{7/2}$ taken at 84.0 eV.

of the line position is remarkable: an initial decrease of the values between 0 ant 4 at.% of Si is observed, followed by a plateau between 4 and 23 at.% of Si, and a final decrease to the value in pure SiN$_y$. These three composition regions actually correspond to those found from a structural analysis of the films (see section 5.2.2). First an Al-Si-N solid solution is formed at low Si content. Above the solubility limit identified at about 6 at.% of Si, excess Si atoms are segregated and form a SiN$_y$ interlayer surrounding Al-Si-N crystallites. At a Si content of the order of 20–30 at.%, the coatings become fully amorphous. This dependence of ΔBE(Ar2p$_{3/2}$–Au4f$_{7/2}$) on the microstructure of the Al-Si-N specimens recalls that of the Ar content on the microstructure (Fig. 5.7). Ar atoms are therefore presumably responsible for the observed shift in Figure 5.8.

Further information can be gained from the evolution of the photoelectron line widths of the elements intended for charge referencing (Fig. 5.9). The FWHM of the Ar2p$_{3/2}$ line decreases by 0.6 eV from AlN to SiN$_y$ (Fig. 5.9a). It remains at 1.8 eV for a Si content between 0 to 4 at.%. For higher Si contents, it decreases to ∼ 1.3 eV and is constant above 10 at.%. It is about 1.2 eV in pure SiN$_y$. In contrast, the Au4f$_{7/2}$ line width is roughly constant (1.7 eV) over the whole composition range (Fig. 5.9b).

From Figures 5.7, 5.8 and 5.9a, it can be concluded that the Ar atoms

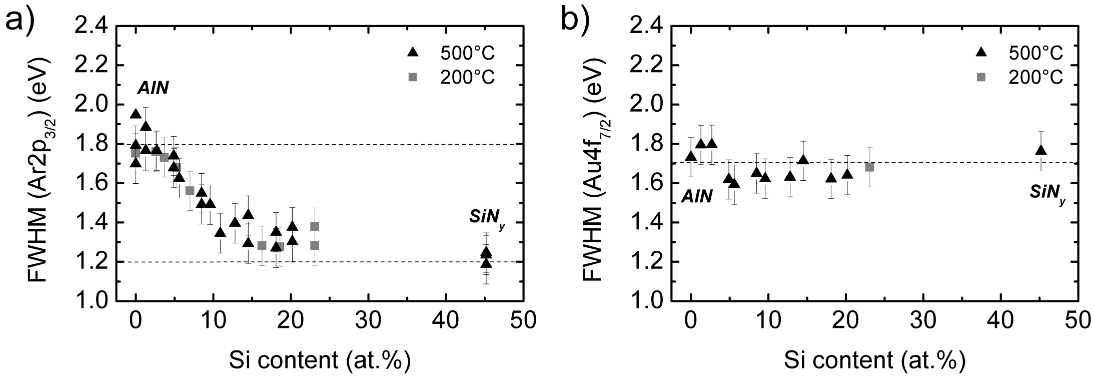

Figure 5.9: Evolution of the FWHM of Ar2p$_{3/2}$ *(a) and Au4f*$_{7/2}$ *(b) photoelectron lines as a function of the Si content in Al-Si-N. Multiple data points for a given composition and deposition temperature correspond to fully independent XPS measurements (new region on the sample, new mounting etc.).*

implanted in Al-Si-N are subject to pronounced chemical effects that coincide with microstructural changes of the films. Consequently, it must be stated that implanted Ar atoms are not suitable for charge referencing of Al-Si-N thin films.

Contrary to Ar atoms, gold atoms are expected to be located on the film surface so that they are not influenced by the microstructure of the Al-Si-N films; this is supported by the constant Au4f$_{7/2}$ line width shown in Figure 5.9b. However, a known limitation of the gold decoration technique is related to the surface coverage achieved. In the present case, the amount of redeposited gold is small ($\leq$ 1.5 at.%). Thus a formation of gold particles (clusters) can be expected. This can lead to a constant chemical shift of the Au4f$_{7/2}$ line that is however independent on the composition and the microstructure of the films. As reported in section 4.1.3, this shift may be as large as +1 eV, as compared to the line position in bulk gold (84.0 eV). Moreover a differential charging effect of gold particles on the Al-Si-N insulating surface may explain the broadening of the Au4f$_{7/2}$ line i.e. 1.7 eV (Fig. 5.9b) compared to the 0.7 eV measured under the same conditions in bulk gold. This effect was found to be related to the resistivity of XPS specimens[21]. It was anyway found to be independent on the exact composition of the Al-Si-N films, from pure AlN to pure SiN$_y$.

The data presented in Table 5.2 illustrate the issue of the reliable charge

---

[21] Tests conducted on AlN, SiN$_y$ (reactively sputtered films), Si (wafer), α-Al$_2$O$_3$ (single crystalline, bulk) and SiO$_2$ (fused silica, bulk).

referencing of Al-Si-N specimens. Here, the binding energies of the Al2p, Si2p and N1s photoelectrons in pure AlN and SiN_y reactively sputtered films are reported, as referenced on three different photoelectron lines: the C1s line of adventitious carbon measured after Ar pre-sputtering (fixed at 284.8 eV), the $Ar2p_{3/2}$ line of implanted argon atoms (fixed at 241.82 eV) and the $Au4f_{7/2}$ line of re-deposited gold atoms (fixed at 84.0 eV). The uncertainty is ±0.1 eV for the referenced BE and ΔBE values, as deduced from the measurements step size. For comparison, mean values are provided that were calculated from C1s referenced data taken from the literature[22] (see Appendix B). The uncertainty of these literature values, defined this time as the standard deviation of the original published data, amounts to ±0.3 eV in the best case.

Table 5.2: Referenced binding energies in pure AlN and SiN_y films (see text).

Compound	BE (eV)		ΔBE (eV)	Charge reference
	N1s	Al2p	(N1s–Al2p)	
AlN (literature)	396.8	73.7	323.2	Adventitious carbon
AlN	396.9	73.6		Adventitious carbon
AlN	396.0	72.8	323.3	Implanted argon
AlN	395.8	72.5		Gold
	N1s	Si2p	(N1s–Si2p)	
Si_3N_4 (literature)	397.8	101.7	295.8	Adventitious carbon
SiN_y	397.6	101.7		Adventitious carbon
SiN_y	397.8	101.9	295.9	Implanted argon
SiN_y	396.3	100.3		Gold

The experimental data obtained in this work and referenced on the C1s line agrees well with literature data. Large apparent energy shifts are however associated to the argon and gold referencing techniques. BE values referenced on implanted argon are hence shifted by −0.9 eV in AlN and +0.2 eV in SiN_y, as compared to C1s referenced BEs. This chemical shift is clearly material-dependent – and obviously microstructure-dependent as well – so that implanted argon atoms cannot be used as charge reference for XPS on Al-Si-N thin films. This is an important finding since argon referencing is usually considered as a reliable alternative to C1s referencing in the case Ar^+ sputter cleaning is used prior to surface analysis [Bert 02]. It must

---

[22] Note that literature mean ΔBE values were determined here as the mean values of literature ΔBEs, and not as the energy differences between the mean BE values given in the Table - hence the apparent discrepancy between the BE and ΔBE literature values.

be emphasized that, similarly to Al-Si-N thin films, many other nanocomposite hard coatings encounter considerable microstructural changes upon variations of their chemical composition and/or deposition conditions. As a consequence, the validity of a charge referencing relying on implanted argon atoms should always be check in such coatings before it can be used. As for BE values referenced on re-deposited gold atoms on Al-Si-N, they are -1.1 eV (in AlN) and -1.3 eV (in SiN_y) lower than those referenced on C1s. This can be explained by a positive shift by ~ 1 eV of the $Au4f_{7/2}$ line that is expected to arise from the presence of Au clusters (or islands, anyway not a continuous film) on the surface of the samples. This shift is nevertheless independent on the Al-Si-N composition and microstructure. Charge referencing on re-deposited gold during argon sputtering enables hence a reliable evaluation of the relative chemical alterations of elements in Al-Si-N thin films when the preparation conditions are changed. Absolute binding energies, however, cannot be derived from the Al-Si-N insulating specimens studied here; they are presumably underestimated by ~ 1 eV. Despite this limitation, the gold decoration technique described in this work constitutes the best charge referencing methods for the Al-Si-N system.

Au charge referenced binding energies The evolution of Au referenced BE positions of the Al2p, Si2p and N1s photoelectron lines in Al-Si-N as a function of the Si content is shown in Figure 5.11. With increasing silicon content, the BE of Al2p photoelectrons remains constant up to about 13 at.% of Si (Fig. 5.11a). It increases then by 0.3 eV between 13 and 23 at.% of Si. The binding energy of the N1s line shows a similar evolution (Fig. 5.11c): it is first constant at low Si contents and then increases by 0.5 eV between 13 at.% of Si and pure SiN_y. In contrast, the binding energy of Si2p photoelectrons (Fig. 5.11b) first decreases by 0.5 eV between 1.5 and 13 at.% of Si. Above 13 %, it progressively increases by 0.3 eV up to the value reported for pure SiN_y. From these data, two composition regions, below and above about 13 at.% of Si in Al-Si-N, can be distinguished.

The *point charge model* that relates the binding energy of a photoelectron to atomic charges inside and outside the ionized atom can be used to formulate hypotheses on the origin of the observed chemical shifts. This model is described in section 4.1.1 p. 53. In short, the measured binding energy of a core electron is the result of several physical phenomena divided into *initial state effects*, acting before the photoionization, and *final state effects*, corresponding to the relaxation of the ionized system after photoionization. These groups are divided in turn into intra-atomic and extra-atomic

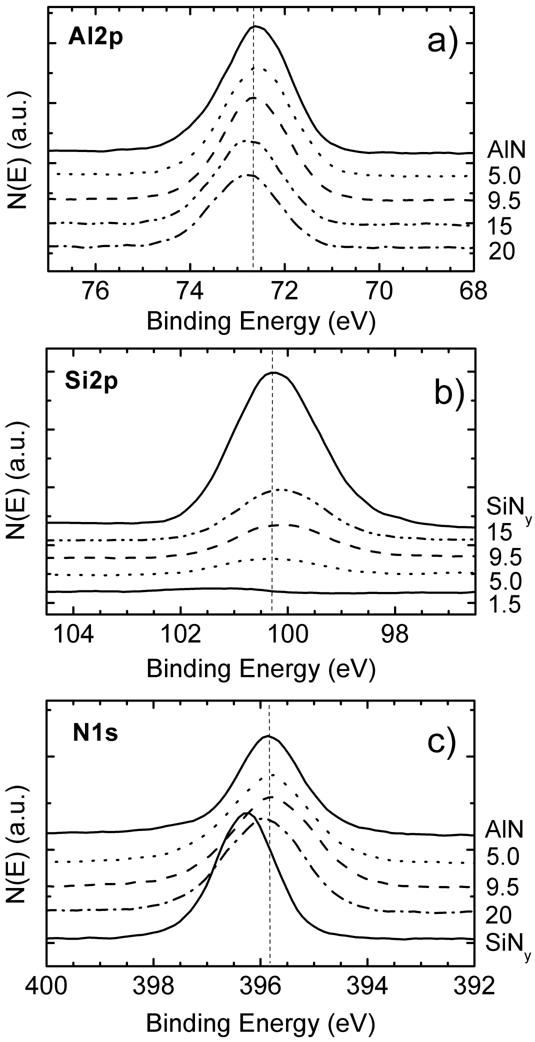

Figure 5.10: Evolution of the Al2p, Si2p and N1s line shapes for selected Al-Si-N compositions – films of series C. The numbers on the right-hand side of the curves represent the Si atomic contents (in percentage) of each film. Vertical dotted lines are added as a guide to the eye.

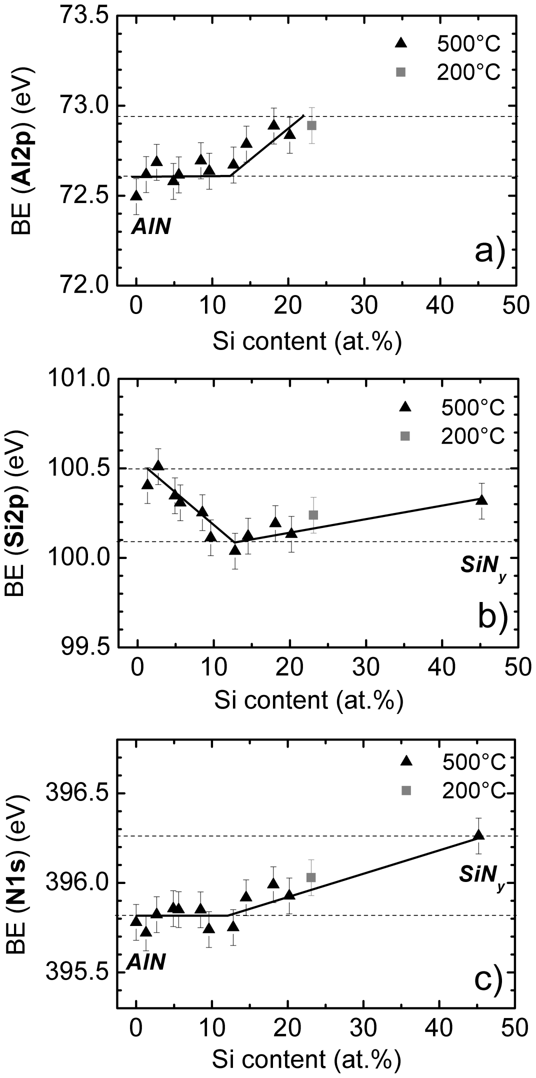

Figure 5.11: Binding energy evolution of Al2p, Si2p and N1s photoelectrons as a function of the Si content in Al-Si-N. The charge referencing is based on the Au4f$_{7/2}$ photoelectron line set at 84.0 eV. Solid lines are added as a guide to the eye.

terms, as visible from Equations 4.2 and 4.3 p. 53. The binding energy shift of the photoelectron line of an element taken in two different chemical environments corresponds to the variation of one or several of these effects.

Al–N and Si–N bonds are of mixed covalent and ionic nature. These bonds are therefore polarized. As the composition of Al-Si-N films is changed, the polarization of the bonds is expected to vary due to a redistribution of charges in the material. This effect can induce binding energy shifts. Indeed, neglecting Madelung and relaxation effects in equations 4.2 and 4.3 p. 53, it appears that an increase of the ionic character of a bond (i.e. an increase of charge transfer), leading to an increase of the atomic charge, would cause an increase in the photoelectron binding energy for cations and a decrease in the photoelectron binding energy for anions. From the Pauling electronegativity of Al (1.61), Si (1.90) and N (3.04) atoms, a continuous increase of the absolute value of both the positive partial charge on Al and Si atoms, and of the negative partial charge on N atoms is predicted as the Si content is increased [Crug 03]. This will lead to a continuous increase of the Al2p, Si2p and N1s photoelectron binding energies (i.e. a decrease of the photoelectron kinetic energies respectively) upon addition of silicon in AlN.

This simplified model may explain the chemical shifts to higher binding energies of the Al2p, Si2p and N1s peaks observed above 13 at.% of Si in Figure 5.11. However, it fails to explain the decrease of the Si2p binding energy and the constant values of Al2p and N1s binding energies between 0 and 13 at.% of Si. Seemingly another contribution than pure polarization effects must play a significant role in the low silicon concentration region. The nature of this contribution is, however, difficult to delineate. These shifts may be closely related to the additional electron brought in the AlN lattice by Si atoms in substitutional position on Al sites, acting as donor atoms. A partial localization of this electronic charge on Si atoms may explain the shift of the Si2p line to lower binding energies, whereas a partial delocalization of this charge over the lattice, in particular Al and N atoms, may explain the constant binding energy position of Al2p and N1s photoelectrons. However, the exact distribution of this additional negative charge in the Al-Si-N lattice remains unknown. The literature on Si-doped AlN suggests the existence of lattice compensation defects such as aluminum vacancies, Si DX centers and oxygen impurity atoms [Bogu 97] [Goen 01] [Tani 02] [Herm 05] that may greatly influence both initial and final state effects in the XPS photoionization process. *Ab initio* calculations are in progress[23] that should allow a better understanding of this issue.

Finally, it is noteworthy that, as in the case of BE differences and photoelectron line widths (Figs. 5.3 and 5.4), no specific effect is observed in Figure 5.11 at 6 at.% of Si, as Si atoms start to segregate at the grain boundaries and form there a $\mathrm{SiN_y}$ layer. Instead, a composition between 10 and 15 at.% of Si (here, 13 at.% of Si) is once again identified as a critical composition that separates concentration regions with distinct chemical evolutions. The interpretation for this apparent discrepancy between XPS and structural (XRD) data remains unchanged (see p. 93).

Nitrogen Auger peak, Auger parameter and chemical state plot The shape and position of Auger electron lines can give further information on the evolution of chemical states. Chemical shifts encountered by these lines can be significantly larger that those measured on photoelectron of the same element. This is due to the fact that Auger transitions involve valence electrons that are more sensitive to the local chemical environment than core electrons.

A stacking plot of N(KLL) Auger lines taken for different Al-Si-N film compositions is given in Figure 5.12. The lines are presented in derivative mode so as to highlight their fine structure. The position of the Auger peak maximum ($dN(E)/d(E) = 0$) is indicated on each line, that reveals a clear chemical shift of the Auger signal from pure AlN to pure $\mathrm{SiN_y}$. The chemical shift is about 1.5 eV, which is three times larger than the energy shift of the N1s photoelectron lines shown in Figure 5.11c.

Soto *et al.* [Soto 04] showed that the N(KLL) Auger peak structure in metal nitrides consists of a central peak surrounded by satellite peaks on the low and high energy sides, with a total width being as large as ~ 50 eV. The restricted energy window presented in Figure 5.12 corresponds to the central and major peak of the nitrogen Auger transition. The shape of the N(KLL) derivative curves in pure AlN and pure $\mathrm{SiN_y}$ is in excellent agreement with the shapes reported by Soto. The fine structure of the nitrogen Auger line in metal nitride can be related to the electronic population of different bonding, non-bonding and anti-bonding orbitals [Soto 04]. However the high energy dispersion of s-p hybrid orbitals (expected in the Al-Si-N system) gives rise to broad features as observed in Figure 5.12, characteristic of covalent

---

[23] as an intern Empa collaboration with Dr. Carlo Pignedoli and Dr. Daniele Passerone, from the "Theory and atomistic simulation of materials" group, "nanotech@surfaces" Lab.

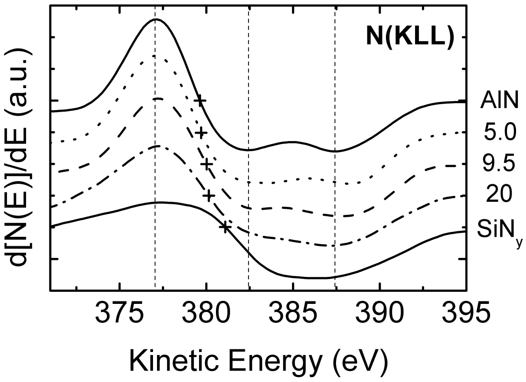

Figure 5.12: Shape of the N(KLL) Auger transition (in derivative mode) for selected Al-Si-N compositions (series C). The Si content (at.%) of each film is indicated on the right-hand side of the curves. Vertical dotted lines are added as a guide to the eye to highlight the fine structure of the transition. (+) symbols indicate the position of the peak maximum ($dN(E)/d(E) = 0$) on each N(KLL) line.

bonds. As a consequence, orbital contributions cannot be resolved to give direct information on the electronic structure of nitrogen bonds. A regular transition from the line shape associated to AlN to the line shape associated to SiN$_y$ is observed in Figure 5.12. The change of Auger line shape is apparently related to the progressive replacement of N–Al bonds by N–Si bonds. The line shape is moreover expected to be affected by the change in nitrogen coordination number from four to three between wurtzite AlN and SiN$_y$, as a two-phase nanocomposite is deposited (i.e. above 6 at.% of Si). However the transition from the pure AlN to the pure SiN$_y$ line shape is so progressive that it does not give any indication of a sudden microstructural change in the Al-Si-N films. Unfortunately, neither a silicon nor an aluminum Auger transition could be recorded in this study[24]. The Si(KLL) line in particular would have been of interest, so as to better understand the chemical effects encountered by the Si atoms in Al-Si-N, since the most striking effects are seen on the Si2p line (see Figs. 5.3 and 5.11, in particular[25]).

By making use of the energies of an Auger and a photoelectron peak of an

---

[24] The excitation energy (1486.6 eV) of the monochromatic Al Kα X-ray source used in this work is indeed too low to excite the Si(KLL) Auger line (KL$_{23}$L$_{23}$ at ca. 1610 eV). As for the Al(KLL) Auger line (ca. 1390 eV), it was found to overlap with an Al plasmon line, precluding its evaluation.

[25] See also Ref. [Henr 97], where some data are reported on the Si(KLL) transition in Al-Si-N coatings. This publication is reviewed in Chapter 2 p. 27.

element, the so-called Auger parameter can be calculated that is independent of static charge effect and therefore does not require any charge referencing. The evolution of the nitrogen Auger parameter, defined as:

$$\alpha' = E_k(\mathrm{NKLL}) + E_b(\mathrm{N1s}) \tag{5.1}$$

i.e. the sum of the kinetic energy of the N(KLL) line and the binding energy of the N1s line, is reported in Figure 5.13. α' is found to increase with increasing silicon content in Al-Si-N, with a total chemical shift of $\sim$ 2 eV between AlN ($\alpha' = 775.4$ eV) and $\mathrm{SiN_y}$ ($\alpha' = 777.5$ eV). This shift is four times larger than the shift identified on the N1s line using gold charge referencing. With such a large shift, it could be expected that changes in the evolution of the chemical state of the nitrogen atoms with the Si content in Al-Si-N (e.g. associated to the appearance of a separate $\mathrm{SiN_y}$ phase) would be clearly seen, and that composition regions could be defined, as previously seen e.g. for the binding energy of the N1s line. This is not the case. This is at least partly due to the scattering of the experimental values of α' that can be seen in Figure 5.13. This scattering is related to the extremely large width of the N(KLL) line (FWHM $\sim$ 8–10 eV) that limits the accuracy in the determination of the line position. Despite its great advantage of being independent on the charge referencing procedure, the nitrogen Auger parameter is therefore obviously not an appropriate parameter to study changes in the local chemistry of Al-Si-N thin films as a function of the Si content.

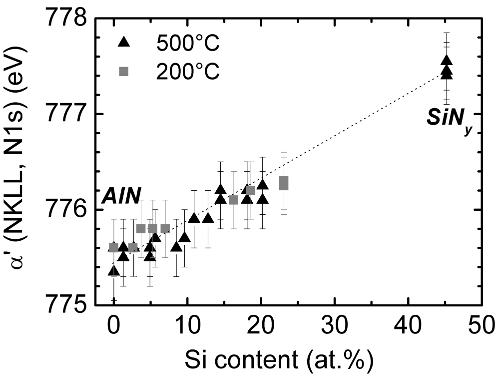

Figure 5.13: Evolution of the nitrogen Auger parameter α' (defined in Equation 5.1) as a function of the Si content in Al-Si-N.

A chemical state plot of nitrogen is presented in Figure 5.14. This two-dimensional representation of the Auger line position as a function of the photoelectron line position gives information on respective contributions of initial state and final state effects[26]. In such a plot data points corre-

---

[26] see Section 4.1.1, starting p. 53 for a introduction about the construction of a chemical state plot, also called Wagner plot. Equations 4.5 and 4.7 are particularly important for the physical interpretation of a chemical state plot.

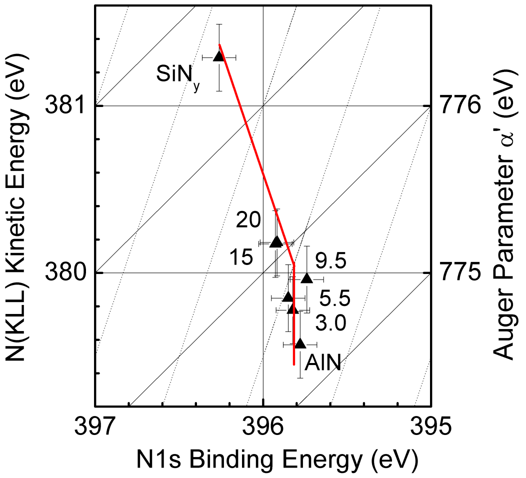

Figure 5.14: Chemical state plot (Wagner plot) of nitrogen for selected Al-Si-N compositions. Film compositions (at.% of Si) are indicated in the plot. Black lines with slope -1 and -3 (appearing $+1$ and $+3$ due to the negative direction of the BE axis) correspond to compounds with similar final state and initial state effects, respectively (see text). Lines of slope -1 are intercepts of constant Auger parameter (right axis). A red line is added as a guide to the eye.

sponding to similar final state effects (relaxation effects) are found on lines of slope -1 (appearing $+1$ on the plot due to the negative direction of the abscissa), which are also lines of constant Auger parameter (solid lines in Fig. 5.14). Chemical states with similar initial state effect appear on lines of slope -3 (dotted lines in Fig. 5.14). Using Equations 4.5 and 4.7 (p. 53 and following), it appears that the chemical shift of nitrogen photoelectrons results from a large change in initial state effects (about $3/2 = 1.5$ eV, as deduced from Fig. 5.14) and final state effects (about 1 eV, as deduced from Figs. 5.13 and 5.14). These shifts act in opposite directions (see Eq. 4.3, p. 53) so that the total binding energy difference of N1s photoelectrons from pure AlN to pure SiN$_y$ does not surmount 0.5 eV (Fig. 5.11). Moreover both variations of initial and final state effects seem to be smaller from 0 to $\sim$ 10 at.% of Si, and then larger for higher Si contents. Once again, the evolution of the nitrogen chemical state can be divided into two distinct composition regions, here below and above $\sim$10 at.% of Si.

As a conclusion of the study of the N(KLL) Auger line, Auger parameter and chemical state plot, a change in the chemical state of nitrogen atoms is clearly seen as a function of the Si content in Al-Si-N. In particular, the Auger parameter shift (Fig. 5.13) is much larger than shifts in the photoelectron binding energies (Fig. 5.11). However, detailed information on the evolution of the chemical environment of N atoms (e.g. change of coordination number, bonding to Al or to Si atoms) cannot be deduced from these data, probably because several chemical states coexist in the films at all Si contents.

Conclusion on the XPS analysis of Al-Si-N thin films The present XPS study of Al-Si-N thin films was aimed at identifying the local chemical environment of Al, Si and N atoms, to find out whereas a two-phase AlN/SiN_y composite was formed, a single-phase ternary Al-Si-N solid solution, or a mixture of Al-Si-N and SiN_y above a given solubility limit of Si in AlN. The chemical states of atoms in AlN, Al-Si-N and SiN_y are similar, in particular Al–N and Si–N bonds only are expected to form. It is nevertheless shown that changes in the distribution of atomic charges, in the bonding coordination and the coexistence of several chemical states for a given element have noticeable effects e.g. on photoelectron binding energies and line widths. Two regions of distinct chemical evolution as a function of the Si content were thus outlined – below and above 10–15 at.% of Si – in the description of ΔBEs (Fig. 5.3), photoelectron line widths (Fig. 5.4) and BE positions (Fig. 5.11). The evolution of the N1s photoelectron line width (Fig. 5.4c), in particular, suggests that the region at high Si contents corresponds to a multi-phase structure. With increasing Si concentration above 10 at.%, the Si2p line width (Fig. 5.4b) was found to evolve to that of pure SiN_y. This is strong indication for the existence of a separate SiN_y phase. The constant binding energy difference between the N1s and Al2p lines (Fig. 5.3a) and the constant Al2p line width (Fig. 5.4a) moreover show that the Al–N bonds remain unaffected by the introduction of Si in the films; changes in ΔBEs and in the N1s line width are therefore attributed to the Si–N bonds. In addition, the chemical effects revealed by the analysis of implanted argon atoms (initially intended for charge referencing) suggest a sudden change in the Al-Si-N matrix at 4 at.% of Si (Fig. 5.7, 5.8 and 5.9). Structural effects induced by a phase separation may explain this behavior.

These observations alone are however not sufficient to draw reliable conclusions on the evolution of the Al-Si-N film local chemistry, in particular on its phase composition. Complementary characterization techniques such as XRD, TEM etc. are required. From XRD data in particular (Section 5.2.2), the formation of an $Al_{1-x}Si_xN$ solid solution with a solubility limit at 6 at.% of Si ($x = 0.12$) is clearly identified. Above this Si concentration, excess Si atoms are segregated outside the Al-Si-N solid solution and form a separate SiN_y phase at the grain boundaries. With this knowledge from a structural analysis, the critical concentration of about 4 at.% of Si found in XPS data can be identified as the onset of a Si segregation, accompanied with structural changes. As already discussed, the "critical" Si concentration of 10–15 at.% is identified as the onset of a SiN_y grain boundary layer that is thick enough so that the local chemical environment of Si and N atoms is similar to that of bulk silicon nitride. The chemical changes observed between ~ 6

and 10–15 at.% of Si (line positions, line widths, etc.) clearly show that the chemical states associated to a minor phase (e.g. SiN_y) can be greatly influenced by the presence of a majority phase (e.g. Al-Si-N) and hence show properties different than that of bulk. A further example is reported by Diserens [Dise 00], who identified the existence of a charge transfer between neighboring phases in the TiN/SiN_y system, when the SiN_y grain boundary layer surrounding TiN grains was thinner than ~ 0.5 nm. In the present case, the influence of the majority Al-Si-N crystalline phase results in an atomic ordering of the SiN_y grain boundary layer, otherwise expected to be disordered (amorphous) at low deposition temperatures (here $< 500°C$). This is deduced from the XRD and TEM investigations of the coatings presented in the next section (5.2.2), and discussed again section 5.3. Noteworthy, the "critical" concentrations of 4 and 10–15 at.% of Si identified in XPS data are also identified in the evolution of the optical properties of Al-Si-N coatings, reported in section 5.2.4 (see Fig. 5.34 p. 138).

5.2.2 Structural properties

The structural properties of Al-Si-N thin films were extensively investigated using X-ray diffraction in various geometries (θ-2θ, rocking curves, Pole Figures)[27], as well as electron microscopy techniques (SEM and TEM).

a) X-ray investigations

The X-ray θ-2θ diffractograms measured on the samples of series B, being representative for all three series of Al-Si-N nanocomposite coatings fabricated here (see Table 5.1, p. 83), are given in Figure 5.15. Only a restricted 2θ angular range is presented here, as no other signal coming from the films was observed elsewhere in the range $30° < 2\theta < 75°$.

Texture The samples are crystalline up to about 12 at.% of Si with the crystallographic structure of hexagonal (wurtzite) AlN (w-AlN) and a pronounced (002) texture in the growth direction. Above 12 at.% of Si the (002) diffraction peak vanishes and the films become progressively X-ray amorphous. The X-ray (002) diffraction peak disappears at about 16 at.% of Si, concentration at which small crystallites (2–5 nm) could nevertheless still be observed on high-resolution TEM pictures (see Fig. 5.23 p. 121). It should moreover be mentioned here that a weak diffraction signal close to

---

[27] A short introduction to these different measurement geometries is given Chapter 4, section 4.2.1, starting p. 59.

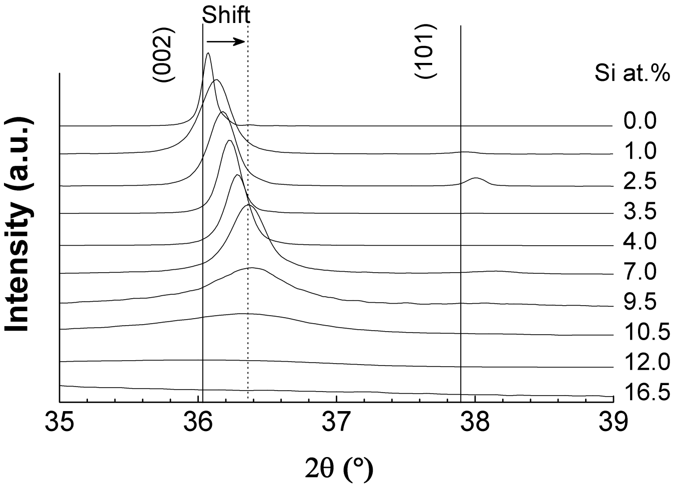

Figure 5.15: XRD patterns in θ-2θ geometry for Al-Si-N films of series B, representative for all three series. The solid vertical lines represent the peak positions in pure wurtzite AlN. The intensities of diffractograms corresponding to Si contents from 0 to 7.0 at.% are normalized each to 1, so that the shift of the (002)-peak position can be better visualized. For Si contents from 9.5 to 16.5 at.%, diffracted intensities are normalized to the maximum intensity of the 7.0 at.% curve times 5, so as to show the quick decrease of the (002)-peak intensity with increasing the Si content.

the (002) peak was still recorded up to a Si content of about 20 at.%, as reported and discussed later in this section (see Fig. 5.20 p. 116).

The (002) texture is a consequence of the growth conditions. It is independent on the substrate material used, namely Si, WC-Co, fused silica and glass. Diffractograms measured on samples deposited at 200°C (series A and B) and 500°C (series C) are identical. The deposition temperature has obviously no influence on the texture for the deposition pressure ($\sim$ 0.3 Pa), Ar:N_2 gas mixture (2:1), Al target power (100–200 W) and for substrates at floating potential used in this work. The film composition was varied by increasing the power applied to the silicon target. This corresponds to an increase of incoming silicon atoms, i.e. of the total amount of impinging atoms on the growing Al-Si-N films. The resulting increase of the deposition rate was found to have no influence on the texture, since the (002) texture was retained with increasing the Si content, as shown in Figure 5.15 above. According to Ishihara *et al.* the (002) texture is favored over the (100) texture at lower total deposition pressure, shorter target to substrate distance and higher sputter power [Ishi 98]. This was attributed to the nature of the growth unit, being rather Al and N atoms than Al–N dimers under such conditions. The nature of the growth unit can be deduced from the relationship between the mean free path (λ) of the sputtered particles and the distance (L) between target and substrate. When $\lambda > L$, only a small amount of sputtered particles will undergo collisions with gas molecules on their way to the substrate. This means that only a negligible amount of Al–N dimers (or AlN clusters) are formed in the gas phase. The conditions of low pressure and small L leading to $\lambda > L$ is fulfilled for the present work, with[28] $P = 0.3$ Pa and $L \sim 12$ cm. The (002) texture of Al-Si-N films reported here is hence in agreement with Ishihara's predictions. Moreover, as the condition $\lambda > L$ is fulfilled, the sputtered particles incoming on the substrate should be more energetic (as compared to particles that have encountered collisions). According to Xu *et al.*, a higher energy of the sputtered particles corresponds to a higher growth rate of the (002) planes over the (100) planes [Xu 01], which is also in agreement with Ishihara's observations of texture development. In wurtzite AlN, each Al atom is surrounded by four N atoms forming a distorted tetrahedron with three B_1-type bonds and one B_2-type bond in the direction of the *c*-axis (see Appendix A p. 198). Both Al and N atoms are sp^3 hybridized. The coupling between semi-full orbits of Al and N atoms gives rise to B_1 bonds, while the coupling between the remaining Al empty orbit and the N full orbit gives rise to a B_2 bond. As a consequence, B_2 bonds have a more ionic character and a lower bond energy than B_1 bonds. According to Xu, growth along the *c*-axis direction therefore requires particles of higher energy [Xu 01]. Further effects must be considered when no substrate bias is used[29], as it is the case in this work. These are the minimization of the surface energy and the adatom mobility on the sample surface [Medj 06]. The planes of minimum surface energy in w-AlN are (002) planes. During a sputtering process, crystallites will nucleate with (100) and (002) planes parallel to the surface. Depending on the mobility of adatoms on each surface, (100) or (002), one direction will grow faster than the other. Medjani *et al.* showed that by increasing the substrate temperature, a [001] growth direction can be favored [Medj 06]. In the present work, the change of adatom mobility obviously does not play a significant role at a temperature ≤ 500°C, since a transition from a (002) to a (100) texture is not observed. Another parameter can influence the texture, namely the N_2 concentration

---

[28] Considering a N_2 atmosphere at 200°C and $P = 0.3$ Pa (i.e. molecular regime), the mean free path of the gas particles equals $\lambda = 36$ cm. In this work, an Ar to N_2 ratio of 2:1 was used. Therefore λ shall be 3 times larger due to smaller N_2 partial pressure. Even if the real mean free path during magnetron sputtering, especially close to the target, is probably smaller, the relation $\lambda > L$ should be verified here.

[29] In case of substrate bias, the resulting increase of adatom mobility and re-sputtering effects will be the dominant effects that control the film texture [Medj 06].

in the gas mixture, as reported e.g. by Musil *et al.* [Musi 08a]. Ishihara *et al.* observed the development of a (002) texture in the region of high N_2 concentrations and small L values. The effect of the N_2 concentration on the texture development was found to be negligible as compared to other parameters, such as the distance L from target to substrate [Ishi 98]. In the present work, the N_2 concentration was chosen so as to achieve full nitridation of the films. This concentration favors (or at least does not hinder) the (002)-plane growth, as no other planes were observed in growth direction.

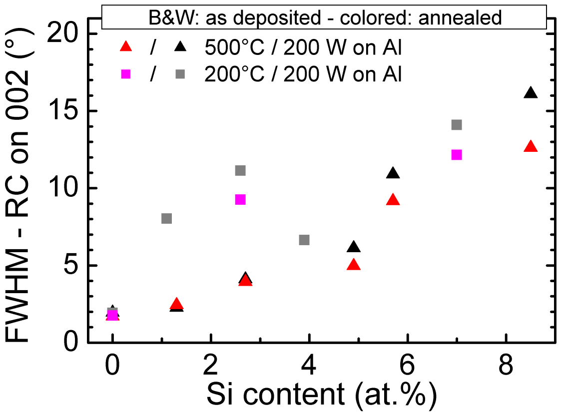

Figure 5.16: Full width at half maximum (FWHM) of rocking curves (RC) measured on the (002) diffraction peak of Al-Si-N films, as a function of the Si content. Results for the sample series B (200° C, symbol: ■) and C (500° C, symbol: ▲) as-deposited (black and white symbols) and after annealing (colored symbols) are reported.

Additional information on the texture of Al-Si-N films can be deduced from rocking curves (RC). The angular distribution of the (002) planes increases with increasing Si content, as shown in Figure 5.16. This increase is more pronounced above about 4–6 at.% of Si. The deposition temperature has little influence except at low silicon contents. At Si contents below 4–6 at.%, the angular distribution of (002) planes in Al-Si-N samples of series B is higher and more scattered compared to samples of Series C, which suggests that a higher substrate temperature may favor a better alignment of crystallites during the film growth. After annealing at 1000°C during 2h, the (002) texture of Al-Si-N films is retained. As shown in Figure 5.16, annealing leads to an only small decrease of the FWHM of the rocking curves. However, this decrease is not associated to a grain growth (coarsening), as shown later, but rather to possible re-arrangements at the grain boundaries. Above 9 at.% of silicon, the rocking curves are too broad to enable a quantification of their FWHM.

The pole figures measurements reported in Figure 5.17 reveal an uniaxial texture of Al-Si-N films. This is shown by the isotropic distribution of the 002 and 101 poles by a φ rotation about the normal to the surface ([002] direction). Similar to RC data, an increase of the angular distribution of the texture upon addition of Si in AlN is observed in the pole figures. This corresponds to an increase of the radial distribution of diffracted intensities from pure AlN ((a) and (b)) to Al-Si-N with 4 at.% of Si ((c) and (d)).

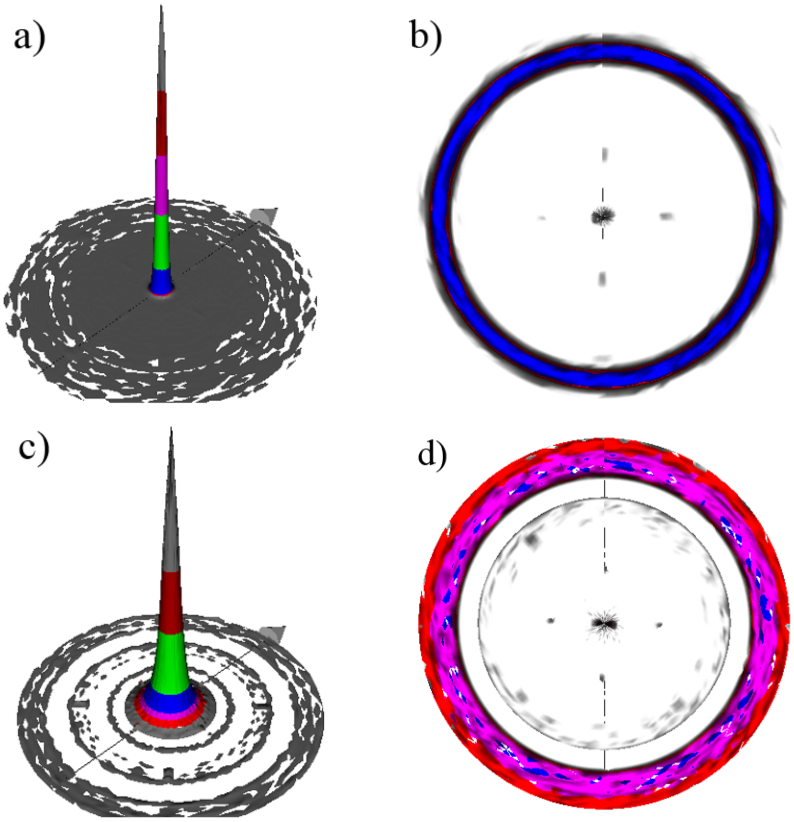

Figure 5.17: Pole figures (PF) of Al-Si-N films. (a) 002-PF (side view) and (b) 101-PF (top view) of pure AlN. (c) 002-PF (side view) and (d) 101-PF (top view) of Al-Si-N with 4.0 at.% of Si. Samples from series B.

Bond length A remarkable feature of the diffractograms shown in Figure 5.15 is the progressive shift to higher diffraction angle of the (002) diffraction peak as the Si content is increased. It corresponds to a shrinking of both the c-axis lattice parameter and the bond length d between Al and N atoms in the w-AlN lattice, related to each other by $d = 3/8c$. The bond length deduced from the evolution of the (002) diffraction peak position in all sample series was calculated and is reported in Figure 5.18. It decreases linearly with increasing Si content up to 6 at.% and then remains constant for higher Si contents. This evolution is moreover neither dependent on the Al-Si-N film deposition conditions, nor it is influenced by the post-deposition annealing of the films.

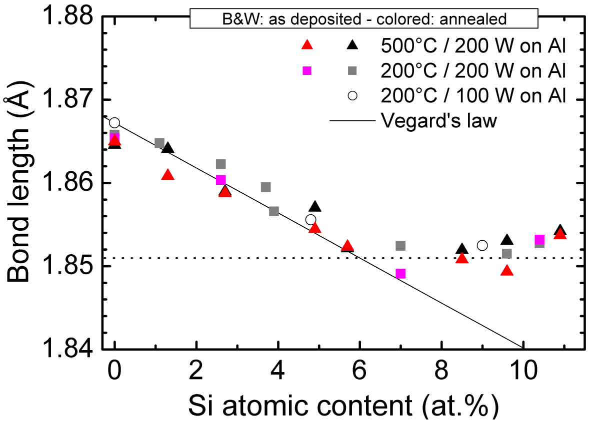

Figure 5.18: Evolution of the bond length in Al-Si-N films as a function of the Si content as calculated from the (002) XRD peak position. The solid line represents the calculated bond length of an $Al_{1-x}Si_xN$ *solid solution using Vegard's law; the horizontal dotted line corresponds to the calculated bond length at 6 at.% of silicon (i.e.* $x = 0.12$*).*

The bond length decrease at low Si contents can be explained by an incorporation of Si atoms in the w-AlN lattice. Among the possible bonds formed by Si atoms in an Al-Si-N ternary alloy, namely Si–Si, Si–Al and Si–N, only the Si–N bond is shorter than the Al–N bond. Moreover, no indication for Si–Si and Al–Si bonds was found by XPS. This suggests the formation of an $\mathrm{Al_{1-x}Si_xN}$ substitutional solid solution, with Si atoms sitting on Al tetrahedral sites in the hexagonal wurtzite lattice of AlN. An estimation of the corresponding bond length can be made by a linear interpolation (Vegard's law[30]) between Al–N (1.8672 Å, JCPDS-ICDD card # 25-1133) and Si–N (1.732 Å in average in β-$\mathrm{Si_3N_4}$ [Grun 79]) bond lengths, giving:

$$d = 1.8672 - 0.1352\mathrm{x} \quad (\text{Å}) \tag{5.2}$$

---

[30] Vegard's law is an empirical approximation that is only valid for ideal solutions with sufficiently small atomic size disparities - see e.g. [Dent 91] [Jaco 07]. The atomic radii of Al and Si atoms equal respectively 1.25 and 1.10 Å [Slat 64]. Si atoms have an atomic radius slightly smaller than Al atoms. This supports the formation of an $\mathrm{Al_{1-x}Si_xN}$ solid solution and justifies the use of Vegard's law to estimate the average Al(Si)–N bond length.

This relation, plotted as a solid line in Figure 5.18, agrees well with the experimental data up to about 6 at.% of Si for all samples. For silicon concentrations exceeding 6 at.%, the bond length remains constant, which suggests that more than 6 at.% of Si cannot be incorporated in the crystalline lattice. Instead, the silicon atoms in "excess" segregate and form a – presumably amorphous – SiN_y layer around the $Al_{0.44}Si_{0.06}N_{0.5}$ crystallites. From the good agreement between experimental data and Vegard's rule, it is assumed that below 6 at.% of Si no SiN_y is formed. A solubility limit of 6 at.% of Si atoms in w-AlN is hence identified, that does not depend on the Al-Si-N film deposition conditions. The bond length is moreover stable upon post-deposition annealing of the samples at 1000°C during 2h, which means that Si atoms are not further segregated during annealing.

Grain size Effective crystallite sizes D in the direction normal to (002) planes were determined from the integral width of the (002) diffraction peak using the Scherrer equation (Equation 4.11 p. 62). They are plotted in Figure 5.19a.

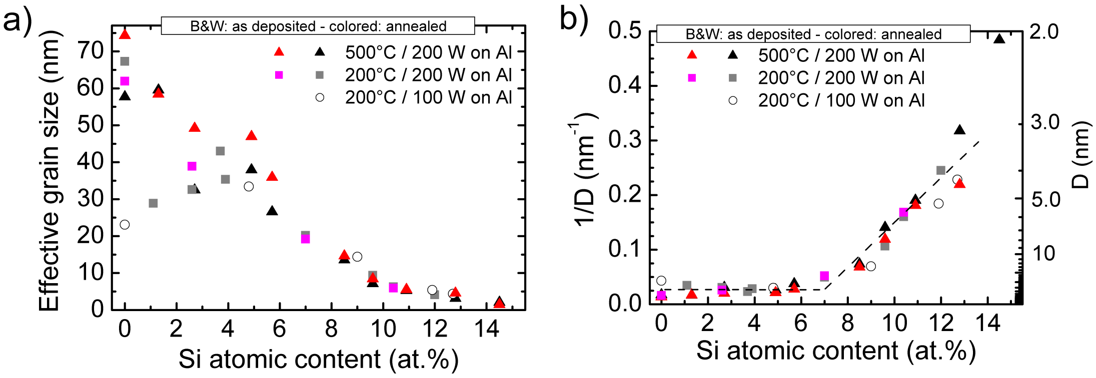

Figure 5.19: Dependence (a) of the crystallite size (D) and (b) of the inverse crystallite size (1/D) on the Si content, for Al-Si-N films deposited on silicon.

At low Si concentrations (≤ 4 at.%) a crystallite size between 25 and 65 nm is found for all preparation conditions. In this composition range, the data are quite scattered and there is no correlation between the deposition conditions and the crystallite size. This large distribution of the crystallite size may be due to a partial coherency of small crystallites having only a negligible mutual misorientation between each other [Rafa 06]. This is supported by the TEM observations presented in the next section. Random micro-stress could also cause some uncertainty in the determination of large crystallite size, as shown in [Nied 99]. For Si contents higher than about

4 at.%, the crystallite size steadily decreases to about 5 nm; the sub–10 nm range is reached at [Si] $\approx$ 9 at.%. This evolution is consistent with the formation of a $\mathrm{SiN_y}$ second phase that stops the growth of Al-Si-N crystallites and forces the renucleation of new crystallites, thereby decreasing the mean crystallite size. The appearance of a second phase is further supported by an abrupt change of the growth behavior above the solubility limit of Si in AlN. This is nicely visible when plotting the inverse crystallite size $1/D$ against the silicon concentration, as shown in Figure 5.19b. Above about 7 at.% of Si, the crystallite size D is inverse proportional to the Si concentration in the film. By analogy with the Ti-Ge-N, Nb-Si-N and Zr-Si-N systems investigated by Sandu *et al.* [Sand 06a] [Sand 06b] [Sand 06c] [Sanj 05] [Sand 08], a film formation model is proposed here; this model is divided into three Si composition regions. The first region, at low Si content ($\lesssim$ 6 at.%), corresponds to the solubility of Si atoms in the AlN lattice. Once the solubility limit is exceeded ($\sim$ 6 at.% of Si), a $\mathrm{SiN_y}$ layer starts to form at the grain boundaries and the surface coverage of Al-Si-N crystallites by that layer increases. This transition regime, corresponds to the second (narrow) region. In the third region ($\gtrsim$ 6 at.% of Si), an increasing amount of silicon is incorporated as $\mathrm{SiN_y}$ in the Al-Si-N films by increasing the surface/volume ratio of the crystallites, i.e. by decreasing their size, and maintaining the $\mathrm{SiN_y}$ film thickness constant, as shown by the [Si]$\sim 1/D$ dependence. This structural model is further developed in the discussion section of this Chapter, together with estimations of both the Si coverage and the $\mathrm{SiN_y}$ thickness on top of the Al-Si-N crystallites (Section 5.3, starting p. 143). A fourth region at [Si] $\gtrsim$ 10–15 at.% will be introduced then.

Grain boundaries As mentioned above, the Al-Si-N films progressively become X-ray amorphous as the silicon content exceeds about 12 at.%. This is deduced from the decrease of the (002) diffraction peak intensity shown in Figure 5.15. However, a second broad and very weak peak appears at the same time at the low 2θ-angle side of the (002) diffraction peak. This is shown in Figure 5.20. The existence of this second peak was revealed by the increasing asymmetry of the diffracted signal at $2\theta \approx 36°$, together with a progressive shift to lower 2θ values. This feature was fitted by two individual Lorentz (Cauchy) lines[31] after suppression of a linear background and without using any weighting of the fit components. Interestingly the

---

[31] From [Klug 74], line profiles generated by a distribution of crystallite sizes are better described by Cauchy profiles than by Gaussian ones. In contrast strain broadening is best fitted by a Gaussian line. Since the main contribution to line broadening comes obviously from a grain refinement to crystallites smaller than 10 nm, the choice of a Lorentz (Cauchy) shape is justified.

major component, at Si concentrations lower than about 12 at.%, stays at the fix position of the (002) diffraction peak in $Al_{0.44}Si_{0.06}N_{0.5}$ (i.e. Al-Si-N at the solubility limit). It is hence attributed to the Al-Si-N crystalline phase. The intensity of this first component decreases with increasing the Si content, but actually only completely vanishes for silicon concentrations of the order of 20 at.%. The second component already appears for a Si concentration of about 9 at.%. Its intensity increases, reaching a maximum at about 16–20 at.% of Si. In parallel, a shift of the line position is observed from about 35.5° to 34° between 9 and 16–20 at.% of Si respectively. The area under this component represents about 10% of the total peak area at 9 at.% of Si, 50% at about 14 at.% of Si and more than 90% at 20 at.% of Si. The diffractograms are fully flat for Si concentrations exceeding about 25–30 at.% of Si.

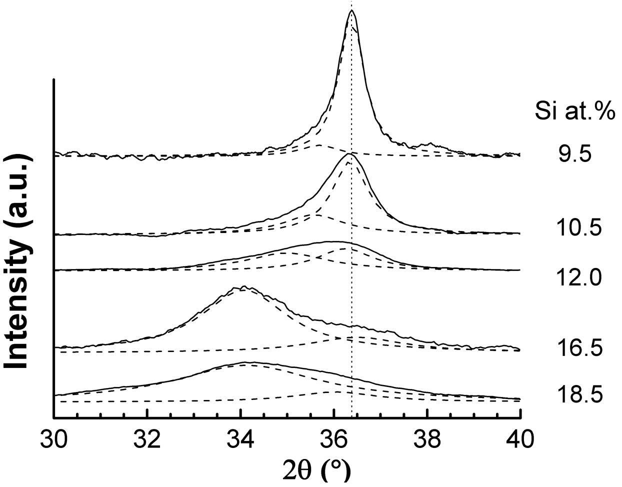

Figure 5.20: XRD patterns for Al-Si-N films with Si contents ≥ 9.5 at.% (series B, representative for all three series). The dotted vertical line represents the (002) peak position in an $Al_{1-x}Si_xN$ solid solution with 6 at.% of Si (i.e. $x = 0.12$). Each XRD peak is decomposed into two overlapping Lorentz lines. The same intensity scale was used for all diffractograms.

The appearance of this second component in XRD diffractograms is seemingly related to the formation of a SiN_y phase surrounding Al-Si-N crystallites, and to the resulting increasing amount of grain boundaries in the nanocomposite coatings as the grain size decreases. The SiN_y phase starts to form already in Al-Si-N films containing about 6 at.% of Si, but the XRD second component only appears for Si concentrations [Si] $\geq$ 9 at.%. This can be explained in terms of minimum amount and minimum thickness of the SiN_y on top of the Al-Si-N crystallites, necessary to give rise to a XRD signal. As it will be shown at the end of this chapter, section 5.3.2 (starting p. 145), a monolayer coverage of the Al-Si-N crystallites is first achieved for [Si] $\gtrsim$ 7 at.% and the volume percentage of $\mathrm{SiN_y}$ in Al-Si-N films is of the order of 15% for a silicon concentration of 9 at.%. Note, however, that the peak position of this second XRD signal cannot be attributed to a diffraction peak of a known crystalline form of silicon nitride, all the more as the signal is not found at a fix position but encounters a large (1.5°) shift as the Si content is increased. Instead, an explanation taking two mechanisms into account is proposed, both mechanisms corresponding to a grain boundary effect.

First, the shoulder in the X-ray diffraction pattern can correspond to a dilatation of the (002) lattice spacing at the grain boundaries in nanocrystalline Al-Si-N films. Remember that the crystallite size is in the sub–10 nm range for [Si] $\geq$ 9 at.%, when the shoulder appears in the XRD signal. The total shift between $2\theta \approx 36°$ (crystallite core) and 34° (crystallite surface) would correspond to a bond dilatation of about 6%. This bond dilatation phenomenon was proposed by Vepřek *et al.* to explain a shoulder in the (111) diffraction peak of nanocrystalline silicon (*nc*-Si) that was correlated to an enhancement of the intensity of a Raman active mode [Vepr 87] [Vepr 81]. Vepřek and co-workers later used this argument to explain a lattice strain phenomenon observed in *nc*-MeN/*a*-$\mathrm{Si_3N_4}$ nanocomposite coatings (Me = Ti, W, V) with a crystallite size $D \leq 7$ nm [Proc 04]. Sandu *et al.* recently used this argument of Vepřek to explain a clear increase of the lattice parameter in Zr-Si-N nanocomposite films for small grain size ($D \lesssim 10$ nm)[32] [Sand 06b]. However, such an explanation does not take into account the formation of a $\mathrm{SiN_y}$ layer at the Al-Si-N crystallites surface, based on strong indications for a solubility limit of Si in w-AlN (Fig. 5.18 and 5.19b). The second "scenario" proposed here is hence that the XRD signal at lower diffraction angle comes from a partially ordered $\mathrm{SiN_y}$ layer, the short range order of which is governed by the crystallographic structure of the neighboring Al-Si-N grains and depends on the amount (coverage, thickness) of $\mathrm{SiN_y}$ at the grain boundaries. The position of the XRD second signal would then be determined by the short range order in the $\mathrm{SiN_y}$ grain boundary layer. In contrast to crystalline materials that show a long range order, materials with only a short range order are characterized by a distribution of interatomic distances, as well as a distribution of bond

---

[32] Unfortunately, both in [Proc 04] and in [Sand 06b], it is unclear wether the reported lattice dilatation was concomitant to the appearance of a shoulder under a diffraction peak, as it is the case in this work, or not.

orientations [Birk 06]. The position of the resulting diffracted signal in a θ-2θ diffractogram is thus not trivial [Birk 06]; in particular Bragg's law cannot be used to estimate a characteristic length within the short-range ordered material. For this reason the peak shift observed in Figure 5.20 cannot easily be more specifically attributed to a given modification of the bond length and/or of the bond angle in the SiN_y grain boundary layer.

Both a bond dilatation phenomenon in Al-Si-N crystallites in the vicinity of grain boundary regions and a partial ordering phenomenon of the SiN_y layer may actually coexist and be correlated. Note that the present situation of a nanocrystalline material with partially ordered grain boundaries is similar to what was reported for nanocrystalline materials such as Si or SiC [Kebl 97] [Szlu 05]. With decreasing the grain size, these materials show an increasing volume of disordered intergranular phase that can be treated as a distinct quasi-amorphous phase surrounding the ordered crystalline phase in the grain interiors. A progressive loss of atomic ordering (atomic distances and bong angles) at the interface between these two phases was reported [Kebl 97]. Thus the structure of grain boundary regions in nanocomposite coatings that show only a small amount of grain boundary phase, the ordering of which is governed by the nanocrystalline phase, shall be very similar to the one of single-phase nanocrystalline materials. In the case of Al-Si-N/SiN_y nanocomposite coatings, the existence of a partially crystalline SiN_y grain boundary phase, possibly forming semi-coherent interfaces with Al-Si-N crystallites, is further supported by the work reported in Chapter 6, where it is shown that a crystalline form of silicon nitride can be stabilized on top of AlN and Al-Si-N in multilayer structures deposited at low temperature (200°C).

b) Electron microscopy investigations

SEM Cross-sections of Al-Si-N thin films deposited on silicon were observed by scanning electron microcopy (SEM) after cleavage of the substrate (see p. 67 for preparation details). Cross-sectional SEM micrographs of Al-Si-N films with two different compositions (0 and 12 at.% of Si) are given in Figure 5.21. A columnar growth is revealed for pure AlN (a). The columns go through the entire coating thickness and have a diameter in the range 50–80 nm. As silicon is added, the diameter of the columns progressively decreases. Above the solubility limit (6 at.% of Si), the films consist of elongated grains in the growth direction (not shown here). At 12 at.% of Si (b), the columnar structure is not visible anymore. Instead a glass-like fracture surface is seen, that corresponds either to a material structured at the nanometer scale, or to an amorphous material. The microstructure of single-phase Al-Si-N films corresponds to the columnar structure of zone T in the structure zone model developed by Thornton (see Chapter 3 section 3.2 p. 44) [Thor 77]. The homologous temperature considered here, defined as T_s/T_m with T_s the substrate temperature and T_m the melting temperature of the film, is of the order of 0.1–0.2. The densification of the structure and the loss of columnar feature when a second phase is introduced may be attributed to grain refinement due to the condensation of a SiN_y tissue phase that blocks the growth of Al-Si-N crystallites and forces repeated nucleation of new crystallites [Barn 98] [Petr 03].

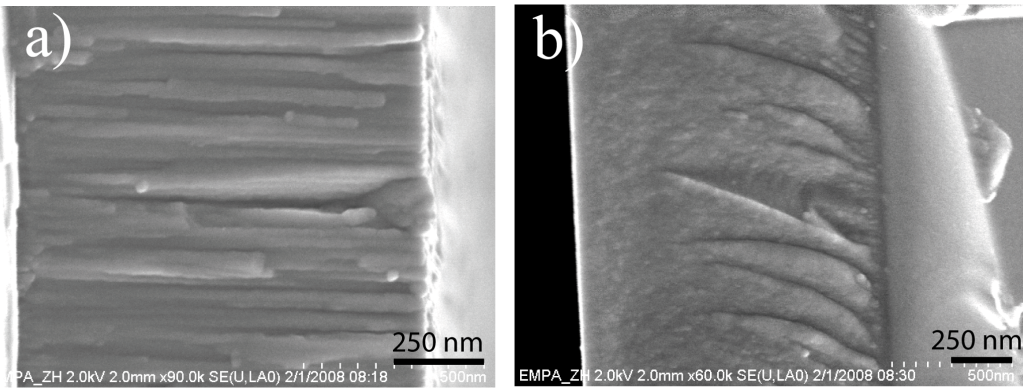

Figure 5.21: Cross-sectional SEM micrographs taken from Al-Si-N films of series B deposited on silicon substrates with (a) 0 at.% of Si (i.e. pure AlN) and (b) 12 at.% of Si.

TEM Cross-sections of Al-Si-N films were prepared for transmission electron microscopy (TEM). Typical bright field (BF) micrographs of an Al-Si-N film with low Si content (here 4 at.%) are shown in Figure 5.22. The columnar growth already seen in SEM is confirmed here. A majority of columns seems to propagate through the entire coating thickness. Their diameter is smaller at the bottom of the coating, close to the substrate, which can correspond to a competitive growth mode over the first ∼ 100–200 nm. This structure is characteristic of the zone T of the Thornton structure zone model (see Fig. 3.7 p. 45). The column diameter in Al-Si-N with 4 at.% of Si is of the order of 20–30 nm, smaller than in pure AlN in which the columns have a diameter of 30–60 nm, as revealed by similar TEM pictures. This is in agreement with the SEM results. All Al-Si-N coatings are found to be dense, i.e. have no grain boundary porosity. Only pure AlN films have a more open structure, with few long and narrow voids seen on TEM images (not shown here).

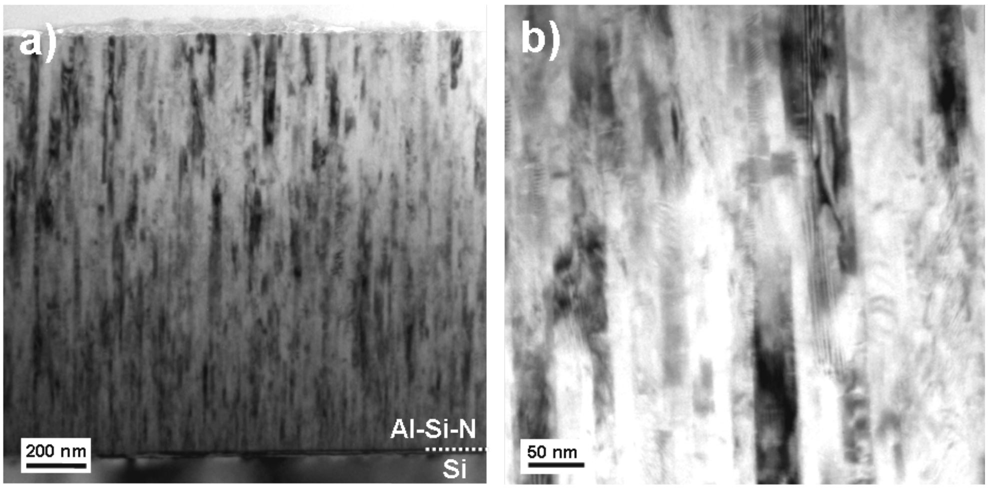

Figure 5.22: Cross sectional TEM micrograph (bright field) of an Al-Si-N film with 4 at.% of Si deposited on Si (100). (a) General view over the total film thickness; (b) higher magnification on the columnar substructure.

The evolution of the film microstructure with the addition of silicon is illustrated by cross-sectional micrographs shown in Figure 5.23. Al-Si-N films of series B at 0 at.% of Si (pure AlN), 4 at.% of Si and 16 at.% of Si are presented. For each sample, a high-resolution (HR) micrograph, a lower resolution (002) dark field (DF) image and an electron diffraction pattern are given.

The diffraction patterns are those of wurtzite AlN. No other phase is identified. In pure AlN, the diffraction pattern consists of a periodic array of well defined spots, indicating a high crystalline quality of the film with a (002) texture. The columnar structure is clearly visible on DF pictures, each column being composed of several contrast zones with similar crystallographic orientation. The contour of these zones is diffuse, probably due to the superposition of several crystallites over the thickness of the TEM specimen, typically a few tens of nanometer for electron transparency. For this reason, only zones of similar crystallographic orientation can be distinguished on BF and DF pictures, but not individual crystallites with specific shape and size. Thus a mean crystallite size value cannot be estimated to be compared with XRD data. The high-resolution imaging mode of the TEM enables to zoom in on one of these zone. In Figure 5.23a, a fraction of a crystallite fills the whole field of view and shows (002) planes parallel to the film surface.

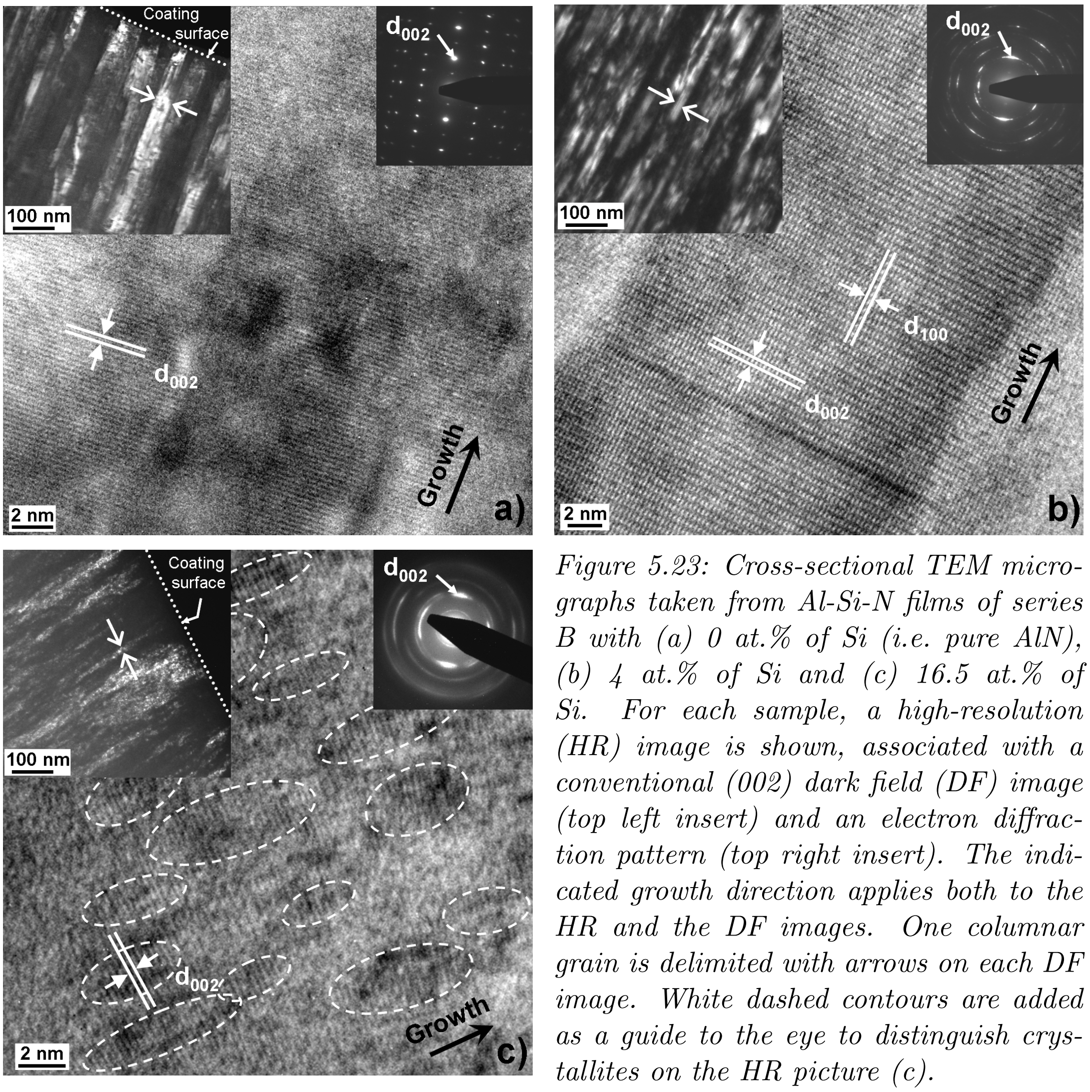

Figure 5.23: Cross-sectional TEM micrographs taken from Al-Si-N films of series B with (a) 0 at.% of Si (i.e. pure AlN), (b) 4 at.% of Si and (c) 16.5 at.% of Si. For each sample, a high-resolution (HR) image is shown, associated with a conventional (002) dark field (DF) image (top left insert) and an electron diffraction pattern (top right insert). The indicated growth direction applies both to the HR and the DF images. One columnar grain is delimited with arrows on each DF image. White dashed contours are added as a guide to the eye to distinguish crystallites on the HR picture (c).

When adding 4 at.% of Si in AlN (Fig. 5.23b), the column width decreases, as visible on the DF images. This corresponds to a narrower crystallites (as seen in HR mode) and to an increasing misorientation between neighboring crystallites (smaller contrast zones in the columns). The appearance of circular arcs with an increasing width instead of dots in the diffraction pattern confirms the increasing misorientation of crystallographic planes as well as the decreasing crystallite size. The (002) texture is however retained. One crystallite, elongated in the growth direction and with (002) planes parallel to the surface, is shown on the HR picture (Fig. 5.23b). The crystallite width is about 20 nm and its length, much larger than the field of view, is estimated to be larger than 50 nm from further HR pictures not shown here.

As for the Al-Si-N film with 16 at.% of Si (Fig. 5.23c), the angular spread around the [002] growth direction is even larger, as revealed by the diffraction pattern and also apparent on the HR picture. A columnar growth mode is still apparent on the DF picture, but the columns are not well defined anymore. Regions of similar crystallographic orientations are much smaller than for lower Si concentrations. On the HR picture, elongated crystallites with an average length of 5 nm in the growth direction are visible. On this picture, dotted lines are given as a guide to the eye. The exact delimitation of the crystallite boundaries is however hard to define. This is attributed to the low mutual misorientation of the Al-Si-N nanocrystallites, to the only small thickness of the SiN_y grain boundary phase (of the order of 1–2 monolayers, as reported in section 5.3.2), and to the thickness of the TEM specimen that is larger than the size of one crystallite.

Note that according to the design rules for hard nanocomposite coatings (see Chapter 2, section 2.1.4 p. 16), sharp interfaces should be achieved between the two constitutive phases of nanocomposite coatings. In the present case, HRTEM cannot identify sharp or smooth interfaces since grain boundaries cannot be recognized very well. The low mutual misorientation between crystallites observed even at high Si contents (e.g. here at 16 at.%), when a two-phase nanocomposite structure is formed, suggests that the [002] preferred orientation of Al-Si-N crystallites transfers through the SiN_y grain boundary phase, i.e. these two phases are – at least partially – coherent. This implies a partial ordering of the SiN_y layer during the film growth, as the result of the segregation of Si atoms outside the Al-Si-N lattice. This ordering of the SiN_y phase is further supported by the XRD data reported above. Note that Rafaja *et al.* reported a similar micro- and nano-structure in Zr-Al-N, Cr-Al-(Si-)N and Ti-Al-(Si-)N hard nanocomposite coatings, also attributed to coherency effects as a result of phase segregation during film growth. A detailed XRD and (HR)TEM study of these coatings is reported in [Rafa 08].

5.2.3 Mechanical properties

The mechanical properties of the Al-Si-N coatings were evaluated by nanoindentation and profilometry measurements, to determine the nanohardness H, the elastic modulus E and the internal residual stress σ. Films deposited on silicon substrates were studied here. The experimental procedures for nanoindentation testing (measurement and data processing) are reported

Chapter 4, section 4.3.1 (pp. 71–72).

a) Critical evaluation of nanoindentation experimental parameters

In general, a large coating thickness (ideally of a few micrometers) and a large indentation depth (say a few 100 nanometers, but less than 10% of the coating thickness) are favorable in nanoindentation testing to obtain hardness values free from artifacts such as the so-called indentation size effect (ISE), as reported in Chapter 4, section 4.3.1 (p. 72). In this work, Al-Si-N coatings were deposited with a thickness in the range of 1–2 μm. The minimum thickness of 1 μm was chosen as a compromise between the minimum thickness required for nanoindentation testing and an acceptable deposition time of the coatings. The latter suffers from the low deposition rate[33] attainable with DC reactive magnetron sputtering with targets in the so-called poisoned state, limiting the maximum power applied to the Al and the Si targets. A maximum indentation load of 2 mN was chosen to keep the indentation depth below 10% of the thickness of the thinner films. Typical indentation depths obtained were of the order of 60 nm. Unless explicitly otherwise indicated (Figs. 5.24 and 5.27), all measurements reported here were done with loads of 2 mN to ensure comparable measurement conditions. In this section, it is shown that these conditions were not fully optimal and led to a small ISE effect. As a result, the hardness values reported in this work for 2 mN loads are typically overestimated by about 2.5 GPa. However the reported trends on the evolution of hardness and E modulus are correct.

At 2 mN maximum load, the recorded load-depth curves were often noisy, presumably because of the small indentation depth. This led to a scattering of calculated H and E values of ± 15% (± 10% in the best cases). On account of this and motivated by the recent literature about nanoindentation testing of thin films [Bull 05] [Fisc 06a], several "thicker" samples (2–4 μm) were deposited in order to investigate the dependence of H and E on the indentation depth. The results obtained on two of these samples deposited on silicon substrates are reported in Figure 5.24. Note that the hardness and the E modulus of uncoated silicon wafers were measured and found equal to 10.5 GPa and 165 GPa respectively. These values are smaller than those corresponding to Al-Si-N. An influence of the Si substrate during nanoindentation testing of Al-Si-N thin films will hence cause artificially smaller H and E values, calculated without taking the substrate into account as shown in section 4.3.1 (p. 68).

---

[33] See Table 5.1 p. 83.

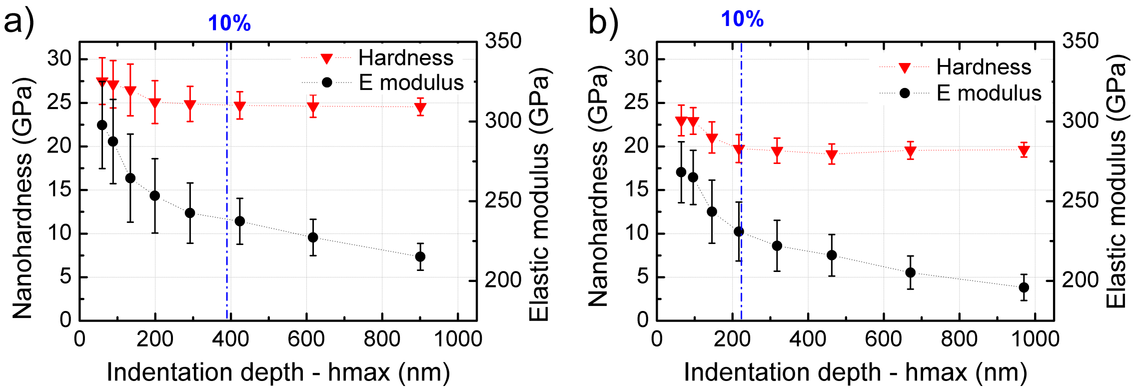

Figure 5.24: Dependence of hardness and E modulus on the indentation depth for nanoindentation tests performed on (a) Al-Si-N with 15 at.% of Si (3.9 µm) and (b) SiN_y (2.2 µm) thin films deposited on silicon. The substrate temperature during film deposition was 200°C. The deposition rates achieved were similar to those of samples of series B and C. Indentation tests with increasing load were performed using the load series 2–4–8–16–32–64–128–256 mN, that is 8 successive load cycles on each test point. The 10% rule for recommended maximal indentation depth is indicated on the graphs. This rule only applies to the hardness values.

In Figures 5.24a and 5.24b, E moduli values steadily decrease as the indentation depth is increased. This illustrates that the calculated values of E modulus are always influenced by the substrate, even at the lowest indentation depths. A comparison of the E-moduli of different samples requires therefore that all samples are deposited on the same substrate and have the same thickness. For the calculated hardness values reported in Figures 5.24a and 5.24b, a clear indentation size effect is visible for indentation depths smaller than ∼ 200 nm, corresponding in both cases to less than 10% of the film thickness. Above 200 nm and up to 1 µm, hardness values are constant and seemingly not influenced by the substrate.

The hardness values reported for the smallest load (2 mN) and an indentation depth of ∼ 60 nm are overestimated by about 10%, as compared to the indentation-depth-independent hardness. This hardness increase at low indentation depths may be related to several effects, namely a strain gradient plasticity effect at the tip apex, a non-fully developed plastic zone within the film material[34] (elastic contact), or an invalid tip calibration for

---

[34] Whether this should cause an increase or a decrease of the hardness as the indentation depth is decreased is unclear. There are divergences on this matter between S. J. Bull (hardness increase, cf. Fig. 4 from [Bull 03] - measurements on PVD deposited TiN films with blunt and sharp indenter tips) and A.C. Fischer-Cripps (hardness decrease, cf. Fig. 11

low indentation depths[35]. The absence of fall-off in hardness values at large penetration depth is surprising considering what is reported in [Fisc 06a] and the common knowledge that lead to the "10% rule" mentioned in Chapter 4 to avoid an influence of the substrate on the measured hardness values. I have no explanation for this phenomenon at the moment. Finally, note that the amplitude of the error bars shown in Figure 5.24 quickly decreases as the indentation depth is increased. This indicates that a better measurement quality is achieved at higher loads, due to a reduced noise and scattering of the data.

Clearly a balance must be found between film thickness and indentation depth, so that a good quality and reliability of the measurement is ensured. In the case of Al-Si-N thin films, a minimum coating thickness of ∼ 2 µm and a minimum indentation depth of ∼ 250 nm would have been optimum conditions that were however not fulfilled here because of the low deposition rate of the films, as said before.

b) Hardness and E modulus

As-deposited coatings The evolution of the nanohardness and elastic modulus of Al-Si-N coatings of series A (○), B (■) and C (▲) as a function of their Si content is shown in Figure 5.25.

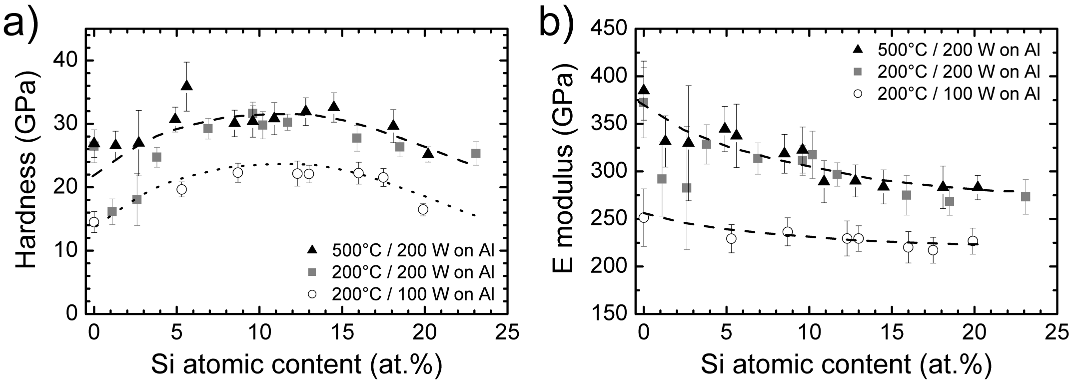

Figure 5.25: Hardness (a) and Young's modulus E (b) of Al-Si-N films deposited on silicon, as determined from nanoindentation tests at 2 mN load - series A (○), B (■) and C (▲).

---

from [Fisc 06a] - measurements on a super-hard *nc*-TiN/*a*-BN nanocomposite coating).

[35] The tip area function of the nanoindenter used in this work was actually not calibrated for indentation depths lower than 100 nm.

The data corresponding to series B and C show a hardness maximum of about 32 GPa around 10 at.% of Si. For comparison, the hardness of single-crystalline sapphire (α-Al_2O_3) was found to be 27 GPa, as determined by nanoindentation testing at 6 mN maximum load of a commercial sapphire substrate[36]. The maximum hardness reported here for Al-Si-N coatings thus exceeds the hardness of sapphire. However the maximum hardness of Al-Si-N coatings remain smaller than 40 GPa, which means that Al-Si-N films are hard, but not superhard. The elastic modulus is found to monotonously decrease from 370 GPa for pure AlN to 270 GPa in Al-Si-N films with a silicon concentration exceeding about 15 at.%. In the case of series A, the qualitative evolution is the same but the hardness maximum equals only 22 GPa. The E modulus of samples of series A decreases from about 250 GPa for pure AlN to 220 GPa in Al-Si-N films with [Si] $\geq$ 15 at.%.

The higher power applied on the Al target (200 W) for the deposition of the samples of series B and C compared to series A (100 W) leads to a considerably increased hardness and E modulus. Measurements of plasma electron currents were performed in the sputter deposition unit used in this work. They revealed that an increase of the power applied on the Al target when the target is in a poisoned state (i.e. AlN surface) leads to an increase of the secondary electron emission, in agreement with what is reported in [Depl 09]. This corresponds to a higher plasma density and in turn probably to denser coatings. It is therefore assumed that the difference in H and E modulus reported here is related to a higher density of coatings fabricated at 200 W power on the Al target. In contrast, the deposition temperature shows no visible influence on the mechanical properties of coatings deposited at 200°C and 500°C (series B–C). An interpretation of the evolution of the hardness of Al-Si-N films with increasing Si content is provided at the end of the present section, after results on the residual stress of the films are reported.

For sake of clarity, the values reported in Figure 5.25 correspond to the composition range of 0–25 at.% of Si in Al-Si-N, therefore excluding pure silicon nitride. A hardness value of $\sim$ 20 GPa for SiN_y can is plotted in Figure 5.24b. This value is close to the 22 GPa reported independently by Diserens *et al.* [Dise 99] and Benkahoul *et al.* [Benk 04] for amorphous Si_3N_4.

The hardness values reported in Figure 5.25 for 2 mN load on pure AlN samples of series B and C agree reasonably well with values published by

---

[36] α-Al_2O_3 (0001) substrate from CrysTec GmbH, Berlin (D).

Mortet *et al.* who reported 22 GPa for deep indentation measurements (indentation depth up to ∼ 1 µm) on 10 µm thick magnetron sputtered AlN films [Mort 04]. However, the hardness values determined here for pure AlN were found to depend strongly on the measurement position on the samples. This is illustrated in Figure 5.26, where selected indentation curves and average curves are shown for a pure AlN film, to be compared to an Al-Si-N composite film with 7 at.% of Si. This large variation of the hardness may arise from the relatively open columnar structure of the AlN films, but may also be caused by a native oxide layer on top of these films. Note that the native oxide was found to be thicker on pure AlN than on Al-Si-N coatings, as revealed by XPS composition depth profiles shown in section 5.2.5 (p. 139). Thicker AlN coatings (1.7–3.5 µm) were also deposited and lower hardness values (15–20 GPa) were obtained from nanoindentation load series similar to those reported in Figure 5.24. However a large variation in the initial shape of indentation load curves was always observed, even a larger indentation depths.

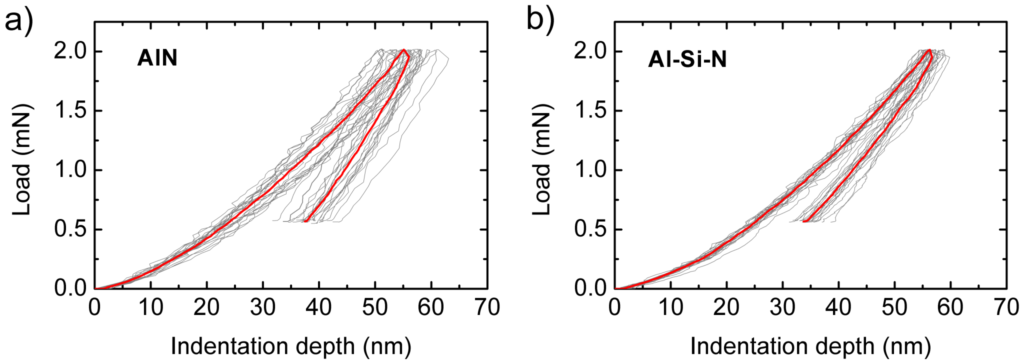

Figure 5.26: Load-displacement nanoindentation curves measured on (a) pure AlN and (b) Al-Si-N with 7.0 at.% of Si, deposited on silicon (series B). The grey curves correspond to the 20 selected and corrected curves (see section 4.3.1) which are averaged (red curve) before the data are fitted to calculate H and E values. Maximum indentation load: 2 mN.

Nanoindentation tests also proved to be difficult on all Al-Si-N films containing less than 4 at.% of Si. Large surface detection errors were typically obtained on load curves (not shown here), which could not entirely be corrected during data processing. It resulted in large errors on the calculated values of hardness and E modulus (see Fig. 5.25). These difficulties were related to major damages of the as-deposited coatings: a high density of cracks was observed at the sample surface. These cracks indicate the relaxation of a large tensile stress in the coatings. The density of cracks was found to be almost independent of the substrate material; it was higher at lower Si contents, progressively decreasing upon further addition of silicon and eventually disappearing for Si concentrations larger than 4 at.%. Using the optical microscope of the nanoindenter, nanoindentation test points were defined as far as possible from the cracks. The large surface detection errors in the load curves however indicates that the individual domains between cracks were probably partially free standing on the substrate, although still attached to it since the films were not pealing off.

Annealed coatings Hardness values and E moduli of Al-Si-N coatings annealed at 1000°C in Ar (1 atm) during 2h are reported in Figure 5.27. Here, indentation tests were performed at 2 mN, 4 mN and 6 mN maximal loading forces that caused indentation depths of 55, 85 and 110 nm respectively, never exceeding 10% of the film thickness. Since elastic modulus values are always influenced by the substrate (i.e. they are depth-dependent), only the values determined at 2 mN of maximum load, which can be compared to the values reported for as-deposited sample (Fig. 5.25), are reported here.

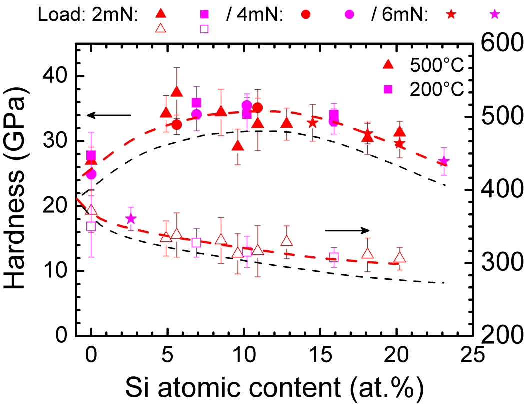

Figure 5.27: Hardness and E modulus of Al-Si-N films annealed at 1000°C in Ar (1 atm) during 2h (series B and C). As indicated above the graph, nanoindentation tests were repeated using several maximum loads (2-4-6 mN). The black trend lines correspond to the measurements on as-deposited films reported Figure 5.25a and 5.25b.

Both hardness and E modulus were found to slightly increase upon annealing. In particular hardness values measured on annealed samples are about 2 GPa larger than those measured on as-deposited coatings, which is not a significant increase considering the accuracy of the measurements (typically ±10% of the calculated values). This change is nevertheless apparently related to an increase of the residual compressive stress measured in the annealed films, as shown and discussed later.

H/E ratio Hardness is commonly regarded as the most important property for protective coatings. A high hardness if often found to be accompanied by a high elastic modulus. However a high hardness alone is not sufficient for good wear resistance; the coating elasticity and toughness in particular can be equally important. Several indicators for wear resistance are proposed in literature. Among them, the H/E ratio is seemingly a good indicator of coating durability; it describes the "elastic strain to failure" or "resilience" of a material [Leyl 04]. A large H/E ratio is in particular associated to a high fracture toughness [Leyl 00] and a high elastic recovery [Musi 02a]. To achieve a good wear resistance of a protective coating, it is favorable to simultaneously increase the hardness and decrease the E modulus of this coating. This rule-of-thumb is related to the low elastic modulus of the materials usually used as substrates. As the low-modulus substrate is deformed, there is an inherent tendency to place the high-modulus coating in tension, which is detrimental to the durability of the protective coating. To avoid or at least moderate this effect, it is recommended to match as much as possible the coating elastic modulus to that of the substrate [Leyl 00] [Leyl 04]. Besides the H/E ratio, the H^3/E^2 ratio can also be used, that is proportional to the yield pressure (i.e. resistance to plastic deformation) of a material [Leyl 00] [Musi 02a].

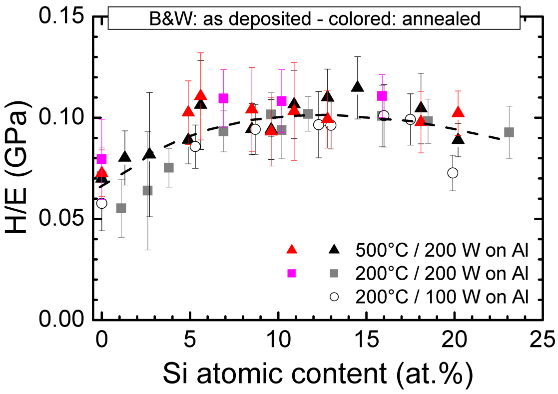

Figure 5.28: Hardness to E modulus ratio (H/E) of Al-Si-N films as-deposited (on silicon) and after annealing at 1000°C in Ar (1 atm) during 2h.

The evolution of the H/E value as a function of the silicon content in Al-Si-N films is reported in Figure 5.28. An increase by 50% of the resilience of the coatings is observed upon addition of about 6 at.% of silicon in AlN; this improved resilience is retained for higher Si contents. The H/E ratio measured on Al-Si-N coatings is found to be independent on the deposition conditions. Moreover annealing of the samples at 1000°C in Ar (1 atmosphere) during 2h does not cause any significant variations of the H/E values.

The good wear resistance of Al-Si-N coatings is illustrated through the results of a simple scratch test, presented in Figure 5.29.

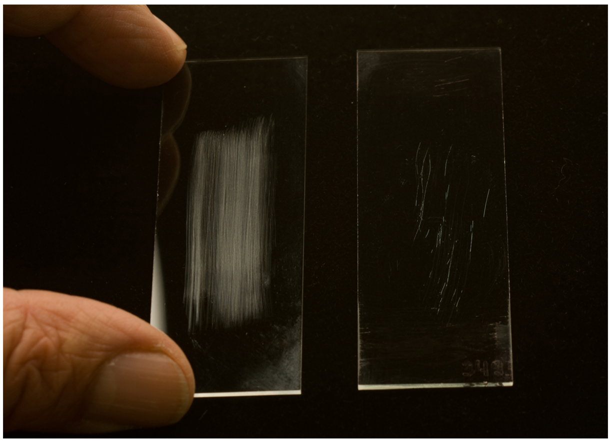

Figure 5.29: Scratch test of glass plates with sand paper. Left*: uncoated glass is readily scratched,* right*: coated glass shows only few scratches after prolonged scratching (here, for an Al-Si-N film containing* $\sim$ *8 at.% of Si).*

c) Stress

It is well known that a hardness increase in sputtered hard coatings may be due to high compressive residual stresses caused by energetic ion bombardment during film deposition (see Chapter 2, section 2.1.2, p. 14). Therefore, the biaxial macroscopic residual stress σ in Al-Si-N coatings was deduced from the Si substrate bending for as-deposited coatings and annealed ones. The obtained stress values are plotted in Figure 5.30 as a function of the Si content.

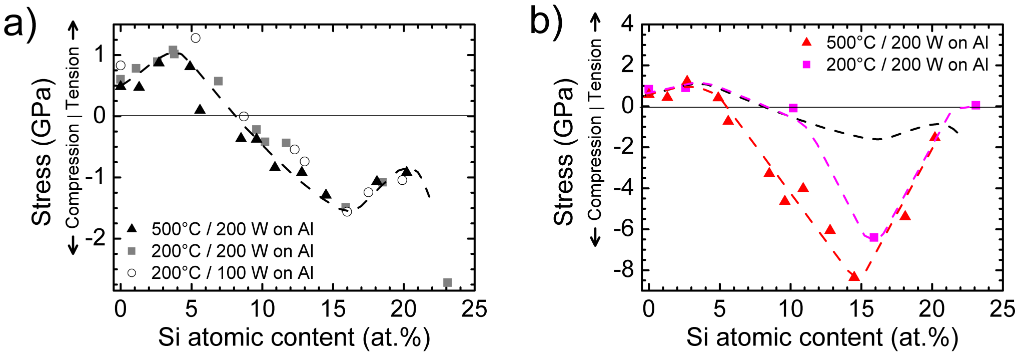

Figure 5.30: Residual stress in Al-Si-N films deposited on silicon. (a) Residual stress of as-deposited samples – series A (○), B (■) and C (▲). (b) Residual stress after annealing: the black doted line corresponds to the doted line in (a) for as-deposited samples and is given for comparison purpose – Mind the different y-axis scales used in (a) and (b).

In contrast to what was observed for the hardness and E modulus of Al-Si-N films, the stress values are not influenced by a change in power applied on the Al target (comparing series A and B). They are also not significantly influenced by a change in deposition temperature (comparing series B and C), although annealed coatings of series B and C seemingly show distinct quantitative behaviors for Si contents between 5 and 15 at.%. The latter quantitative difference would nevertheless require to dispose of more data points (i.e. further annealed coatings from series B) to be ascertained. Comparing now the overall shape of the evolution of H and E values (Fig. 5.25, p. 125) and of the evolution of stress values (Fig. 5.30a above) with the Si content in Al-Si-N films, no correlation can be found between the H and E values and the stress values. In particular, the hardness maximum found at about 10 at.% of Si (Fig. 5.25a) cannot be explained by a large compressive stress in the as-deposited films. Therefore a hardening effect of the films due to energetic ion bombardment during growth is excluded. Moreover, the hardness values of the films are only slightly increased (by $\sim$ 2 GPa) after annealing at 1000°C in Ar during 2h (Fig. 5.27), while a large increase of the compressive stress in annealed films above 4 at.% of Si is shown Figure 5.30b (up to -8 GPa at 15 at.% of Si). Again, no correlation is found between hardness and stress values in Al-Si-N films.

In the following, the evolution of the residual stress of as-grown and annealed Al-Si-N films is described in details.

As-deposited coatings In Figure 5.30a, from pure AlN to Al-Si-N with about 4 at.% of Si (i.e. below the solubility limit of 6 at.% of Si), the coatings show an increasing tensile stress varying from 0.5 to 1.0 GPa. This is attributed to the relatively open anisotropic columnar microstructure of the coatings, where crystalline grains tend to attract each other, building a tensile stress in single-phase crystalline films. This *grain boundary (GB) relaxation model* is reviewed e.g. in [Wind 92]. When silicon atoms are introduced in low concentrations in AlN, the stress is probably dramatically increased, as suggested by the high density of cracks observed in the films[37]. These cracks develop to partially relax a high tensile stress, so that the stress reported in Figure 5.30a "only" corresponds to the residual stress after relaxation by crack formation. If no stress relaxation would have occurred, the stress curve would have shown an even larger initial increase of the tensile stress at low Si concentrations. This would have been followed by a progressive decrease of the tensile stress, supported by the observed

---

[37] No cracks were observed in pure AlN films. A high density of cracks was formed in the coatings with the lowest Si content, i.e. about 1 at.%. The density of cracks was then found to decrease with increasing the Si content. No more cracks are seen in coatings with a Si content equal to or exceeding 4 at.%.

decreasing density of cracks. For a silicon content [Si] $\geq$ 4 at.%, no cracks occur. Hence the stress values plotted in Figure 5.30a are reliable. This dramatic influence of the addition of only $\sim$ 1–2 at.% of Si remains currently unexplained but may be related to the formation of structural defects in AlN (e.g. dislocations, generation of misaligned AlN seed crystals due to incoming $\mathrm{SiN_y}$ clusters on the growing film surface [Herm 06]). The assumed decrease of the tensile stress when the Si content is increased from 1 to 4 at.% may be due to smaller columnar widths and grain sizes, revealed by TEM observations (see e.g. Fig. 5.23). This agrees with the GB relaxation model mentioned above, that predicts a stress inversely proportional to the grain size and proportional to the Young modulus of the material. This is further supported by the decrease of the E modulus[38] with increasing Si content in Al-Si-N films, as reported in Figure 5.25b.

By increasing the silicon concentration above 4 at.%, the stress state changes from tensile to compressive with a transition ($\sigma = 0$) at about 8 at.% of Si. The maximum compressive stress determined in as-deposited nanocomposite films amounts to -1.5 GPa at 16 at.% of Si. This transition from tensile to compressive stress coincides with the appearance of the $\mathrm{SiN_y}$ grain boundary phase. The $\mathrm{SiN_y}$ phase progressively relaxes the tensile stress built up between the crystalline grains by filling the space between them. The increasingly compressive stress is probably built up as a result of the increasing atomic bombardment on the growing films during sputter deposition (”atomic peening” mechanism [Wind 92]). Indeed the Si content of Al-Si-N films was increased by increasing the power applied on the silicon target, i.e. by increasing the total power and so the deposition rate.

Above 15 at.% of Si, a decrease of the compressive stress is observed. This is attributed to an increase of the thickness of the amorphous $\mathrm{SiN_y}$ tissue phase that separates the tiny (< 5 nm) Al-Si-N crystallites and decreases the overall compressive stress. In this composition range, the amount of grain boundaries is predominant in the films (compared to the number of atoms situated in the grain interior), as revealed by XRD data; the Al-Si-N structure becomes progressively amorphous.

The stress values reported in this work are in agreement with data recently

---

[38] Note that the decrease of the E modulus with increasing Si content reported in Figure 5.25b corresponds to nanoindentation measurements done in the same conditions, on films of similar thickness and deposited on the same substrate material (silicon). Although the absolute value of the E modulus is certainly influenced by the substrate, the observed decrease corresponds to an intrinsic property of the Al-Si-N films.

reported by Musil *et al.* on Al-Si-N films with a low ($\sim$ 5 at.%) and high ($\sim$ 40 at.%) Si content. These films were deposited at 500°C by close field ac pulsed dual magnetron sputtering from two identical Si targets fixed by an Al ring [Musi 08a]. Musil reported a small amount of tensile stress for films with a low Si content ($\sigma < 0.5$ GPa) and a moderate compressive stress ($\sigma = -1.8$ GPa) at high Si content.

Annealed coatings After annealing of the Al-Si-N films for 2h at 1000°C in Ar, the overall shape of the stress curve is retained, as shown in Figure 5.30b. The residual stress remains unchanged from 0 to about 4 at.% of Si. Above 4 at.%, however, the transition from tensile to compressive stress is intensified and the compressive stress of the coatings is much increased as compared to as-deposited coatings. The maximum compressive stress is measured at 15 at.% of Si for an annealed coating of series C and amounts to -8 GPa, that is more than five times larger than the -1.5 GPa measured in the as-deposited film. The same phenomenon is observed for coatings of series B, but apparently in smaller proportions. Above 15 at.% of Si, the compressive stress is progressively released. It is less than -1.5 GPa for Si contents larger than 20 at.%.

The annealing of sputtered hard coatings usually leads to a relaxation (”recovery”) of the compressive stress built-in as a result of energetic ion bombardment. This corresponds to an annihilation of the defects created during sputter deposition (see p. 14). In contrast to what is expected, the compressive stress reported in Figure 5.30b is enhanced by annealing for 2h at 1000°C in Ar. This is a striking behavior considering that up to this point, coatings of series B and C always showed the same properties.

To investigate the possible effect of a surface oxide layer grown during annealing [39] on the residual stress, XPS composition depth profiles were measured on as-grown and annealed Al-Si-N samples of series C containing 0 at.% (pure AlN), 8.5 at.% and 15 at.% of Si. These depth profiles are reported and discussed in section 5.2.5 p. 139. They reveal that the thickness of the surface oxide layer is the same for samples containing 8.5 and 15 at.% of Si. The thickness of the oxide layer grown on the Al-Si-N films (with 8.5 at.% and 15 at.% of Si) was moreover found to be smaller than in the case of pure AlN, while the measured stress of the AlN coating remains unchanged

---

[39] Remember that annealing was performed under argon and not in air. However a limited amount of oxygen coming from the desorption of residual oxygen and water adsorbed on the walls of the annealing chamber caused a surface oxidation of the annealed films.

upon annealing. The evolution of the stress with Si content is thus obviously not affected by the surface oxide layer.

An alternative explanation is based on the evolution of the structural properties of the films. It is important to note that the increase of compressive stress with annealing occurs only after the material has formed its second phase (above 6 at.% of Si), i.e. in two-phase Al-Si-N/$\mathrm{SiN_y}$ films. In addition the stress progressively disappears as – at $\sim$ 15 at.% of Si – the grain size reaches a minimum size (maximum amount of grain boundaries) and the $\mathrm{SiN_y}$ layer thickness is assumed to increase. XRD data revealed that neither the Si solubility limit in w-AlN (deduced from the evolution of the c lattice parameter), nor the mean grain size are changed upon annealing of the samples. Since the (002) texture of as-deposited samples is retained even in the two-phase composites, a rearrangement at the grain boundaries upon annealing is proposed. This would consist in the realignment of Al-Si-N crystallites toward each other along the [002] crystallographic direction. Above 15 at.%, an increase of the $\mathrm{SiN_y}$ layer thickness would hinder such a reorganization by efficiently separating the Al-Si-N crystallites from each the other by an amorphous (i.e. no longer ordered) grain boundary layer, so that the trend would be inverted. This scenario corresponds to the evolution of the residual stress shown in Figure 5.30b. The hypothesis of a grain realignment is supported by the evolution of the FWHM of XRD rocking curves (RC) (Fig. 5.16, p. 111) that was found to decrease for annealed films containing more than 4 at.% of Si. However no RC data is available for silicon concentrations exceeding 9 at.% of Si, so that this hypothesis cannot be unambiguously confirmed. Unfortunately, no further information could be deduced from the study of the XRD low-angle "grain boundary" peak (Fig. 5.20, p. 116). The question remains hence open.

d) Relationship between hardness and microstructure

As shown in Figure 5.25a (p. 125), the hardness evolution of Al-Si-N films with increasing Si content consists in a progressive increase of the hardness values from about 20 GPa (pure AlN) up to a moderate hardness maximum of 32 GPa at $\sim$ 10 at.% of Si, followed by a similarly progressive decrease of hardness down to about 24 GPa at the highest Si content studied here, namely 25 at.% of Si. Considering the clear indications brought by XRD of a phase segregation above 6 at.% of Si and of a rapid decrease of the grain size above this silicon concentration, the hardness behavior seems to result from the competition between various phenomena:

- At very low silicon content ([Si] $\leq$ 1 at.%), the crystallite size in growth direction is larger than about 50 nm. In crystals of this size, dislocations may be active but blocked at the grain boundaries, leading to an enhancement of the hardness by a Hall-Petch effect (grain boundary hardening) [Arzt 98].

- As the Si content is increased ($1 < [\mathrm{Si}] \leq 6$ at.%), the crystallite size decreases down to about 35 nm and the Hall-Petch effect reaches its limits as the generation of new dislocations in the crystallite interior becomes impossible, as described Chapter 2, section 2.1.2 (from p. 10). The hardness increase observed in this composition region may result from the competition between grain boundary sliding in the single-phase nanocrystalline materials and solid solution hardening of the Al-Si-N crystallites.

- Above 6 at.% of Si ($6 < [\mathrm{Si}] \leq 15$ at.%), a $\mathrm{SiN_y}$ layer is formed at the grain boundaries between $\mathrm{Al_{0.44}Si_{0.06}N_{0.5}}$ crystallites, and the crystallite size is forced to decrease rapidly, reaching the sub-10 nm range at about 9 at.% of Si (Fig. 5.19, p. 114). As-deposited films moreover show a negligible residual macroscopic stress with $|\sigma| \leq 0.5$ GPa up to a silicon content of 10 at.%. The hardness enhancement observed in this region hence corresponds to a nanostructure hardening phenomenon, related to the small grain size and to the hindering of grain boundary sliding thanks to the $\mathrm{SiN_y}$ interlayer that surrounds the Al-Si-N crystallites. This hardness enhancement is, however, moderate compared to the superhardness ($H > 40$ GPa) often achieved in conventional transition metal based nanocomposite systems such as $\mathrm{TiN/SiN_x}$. This can be related e.g. to the presence of defects at the grain boundaries (vacancies, impurities) [Vepr 05], and therefore to weak cohesive forces at the grain boundaries (see Section 5.3), which facilitate grain boundary sliding. Further reasons will be discussed in section 5.3.3.

- For Si concentrations larger than 15 at.%, an increasing effect of grain boundary sliding on the hardness is expected, as a consequence of grain refinement (i.e. higher density of grain boundaries) and of the assumed increase of the $\mathrm{SiN_y}$ layer thickness between the crystallites. The compressive residual stress is then larger than 0.5 GPa, so that compressive strain hardening may counteract the expected hardness decrease. The hardness value of pure $\mathrm{SiN_y}$ (~ 20 GPa) is thus only reached for Si contents larger than 25 at.% of Si.

5.2.4 Optical properties

In contrast to traditional hard nanocomposite coating systems, the Al-Si-N system does not contain any transition metal nitrides or carbides. Because of the wide bandgap of AlN, Al-Si-N thin films can be used as protective coatings in application requiring transparency in the visible range of light. In addition, these coatings can be used as decorative coatings on reflecting surfaces, where the thickness of Al-Si-N coatings is the primary parameter to control their color, as shown in the next section. In this section, the visual aspect of the coatings in transmission and in reflection conditions is first described. Results of transmission measurements in the visible range of light are then presented. In particular the evolution of the refractive index of Al-Si-N films as a function of the wavelength and of the Si content is shown.

Visual aspect

Figure 5.31: Al-Si-N coatings on glass show a good transparency, as seen from the printed text in the background. The slight shades of color are caused by interference effects which are related to small variations in the thickness of the coatings (about 1 µm). The silicon content in at.% is indicated on the picture. It has however no influence on the colors seen here.

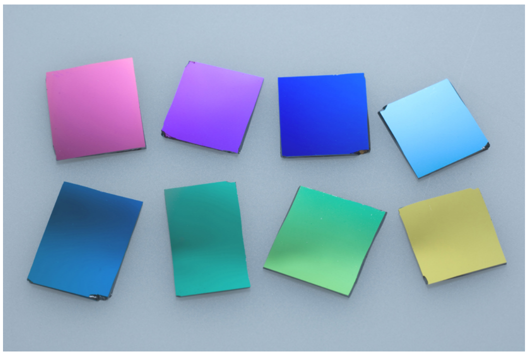

Figure 5.32: Al-Si-N coatings on pieces of silicon wafers. The colors are related to the thickness of the coatings, except for the yellow, that is a result of nitrogen deficiency during deposition. It was found that violet corresponds to 50 nm film thickness, blue to ∼ 200 nm, green to ∼ 500 nm and pink to ∼ 800 nm, seemingly independent on the exact Al-Si-N film composition.

Figure 5.31, Al-Si-N coatings with a total thickness of ∼ 1 µm deposited on glass show a good transparency. When the coatings are deposited on a substrate such as silicon, as shown in Figure 5.32, the color resulting from interferences at the coating interfaces are dependent on the coating thickness. A wide color palette from pink to deep violet can be tuned by varying the thickness of the films. The quasi-periodicity of this color variation can be reported in so-called chromaticity diagrams as described e.g. in [Legr 94] and [Birn 04]. Note that non-fully nitrided films show a yellowish color in reflection (on a Si substrate) and a brownish color in transmission (on a glass substrate).

Refractive index

Optical transmission measurements were performed on Al-Si-N coatings deposited on UV-VIS grade[40] fused silica (SiO_2) substrates in the range 190–1100 nm (6.5–1.1 eV). The optical properties of the Al-Si-N films could be decoupled from the substrate properties using the envelope method described in section 4.4.1 (p. 74). Examples of transmission curves measured on the Al-Si-N/fused silica system are reported in Figure 4.8, p. 75.

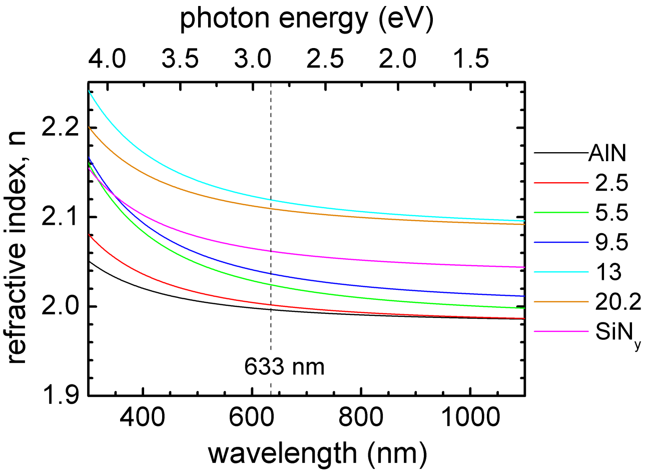

Figure 5.33: Refractive index spectra of Al-Si-N thin films of various compositions. The numbers given on the right hand side of the graph represents the Si concentrations in at.%. These properties of the coatings alone (i.e. decoupled from the substrate) are deduced from optical transmission measurements of coatings of series C deposited on fused silica substrates.

Figure 5.33 shows the dispersion curves of the refractive index n for various film compositions. All films have in common that the refractive index decreases by about 5% in the wavelength range 200–1100 nm. The evolution

---

[40] Transmittance > 0.96 in the range 200–1100 nm and refractive index at 633 nm $n_{633} = 1.46$ (from MaTecK GmbH).

of the refractive index n_{633} and of the extinction coefficient κ_{633} at 633 nm of Al-Si-N films with the Si content is summarized in Figure 5.34.

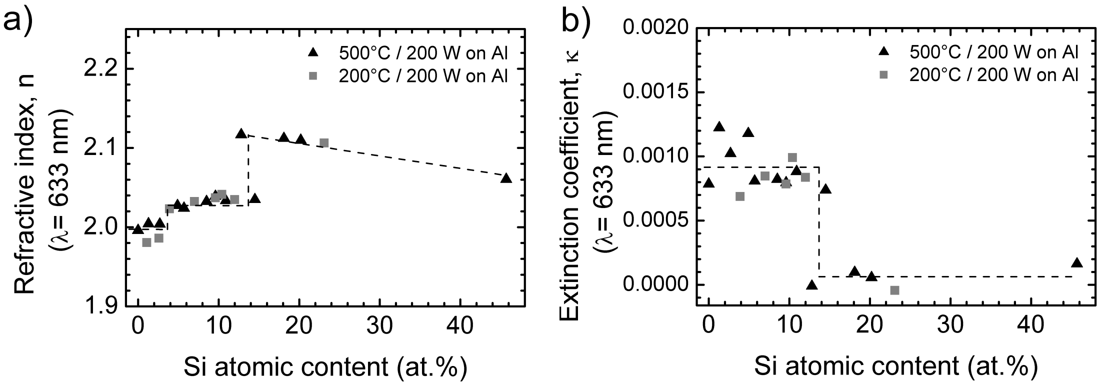

Figure 5.34: Evolution of the refractive index n (a) and of the extinction coefficient κ (b) of Al-Si-N films at 633 nm wavelength, as a function of the Si content.

As described below, the dependence of the optical properties (refractive index and extinction coefficient) on the Si content shows three distinct regions that agree with those discussed before (sections 5.2.2 p. 115 and 5.2.3 p. 134). However, n_{633} only varies from 2.00 to 2.12 over the whole composition range. This corresponds to a transmittance T_c of the coatings alone (i.e. isolated from the substrate) of 77–81%, with $T_c = 2n/(n^2+1)$. The extinction coefficient is small, $\kappa_{633} \sim 10^{-4} - 10^{-3}$, and is found for each sample to be nearly constant in the low energy region ($\lesssim$ 3 eV) (not shown here). In pure AlN, values of $n_{633} = 2.00$ and $\kappa = 8 \times 10^{-4}$ are found. This corresponds well to values reported in the literature for sputtered AlN thin films [Joo 99] [Easw 05] [Brud 05]. Al-Si-N films have slightly higher values of refractive index than pure AlN coatings, which agrees with what is reported in [Asan 87] and [Bend 02]. Bendavid *et al.* reported a high refractive index of $n_{670} = 2.20$ for Al-Si-N with about 10 at.% of Si. This value was found to decrease in $\mathrm{AlSiO_xN_y}$ composite films with increasing oxygen content down to $n_{670} = 1.65$ in $\mathrm{AlSiO_x}$ [Bend 02]. The incorporation of a few atomic percents of oxygen in the films deposited in this work (see section 5.2.1, p. 86) can therefore probably explain the comparatively low values ($n < 2.20$) reported in Figure 5.34a.

The three distinct composition regions that can be distinguished in Figures 5.34a and 5.34b are the following ones:

- Below 4 at.% of Si, the optical properties of the Al-Si-N films are those of pure AlN.

- At 4 at.% of Si, (Fig. 5.34a only), a small increase of the refractive index from 2.00 to 2.03 indicates a structural change of the Al-Si-N films. The values of the refractive index remain then constant up to a Si content of about 13 at.%. This change at 4 at.% of Si is probably related to the segregation of Si atoms outside Al-Si-N crystallites above the solubility limit of Si in w-AlN. The solubility limit was clearly identified at 6 at.% of Si from XRD data. The present results suggest that the segregation of Si atoms may begin already at 4 at.% of Si. Note that a similar change at 4% of Si is not observed in the evolution of the extinction coefficient (Fig. 5.34b). Instead, κ values are scattered for $0 < [Si] < 4$ at.%, probably as a consequence of the cracks observed in the coatings in this composition range.

- At 13 at.% of Si, a large increase of n_{633} from 2.03 to 2.12 (Fig. 5.34a) and a simultaneous decrease of κ_{633} from 10^{-3} to 10^{-4} (Fig. 5.34b) are seen. As for the interpretation of chemical state (XPS) and stress data, this is attributed to the appearance of a few monolayer-thick and probably amorphous $\mathrm{SiN_y}$ grain boundary layer around the Al-Si-N crystallites, that separates the crystallites from each other.

Note that a similar decomposition of the optical properties into composition regions is reported by Sanjinés *et al.* in the case of Nb-Si-N [Sanj 05] and Zr-Si-N [Sand 07].

5.2.5 Thermal stability and oxidation resistance

As mentioned in Chapter 2, section 2.2.2 (p. 23), Al-Si-N thin films were identified already 15 years ago as potential anti-oxidation coatings [Henr 93] [Perr 97]. In pure AlN films, the oxidation of the surface is limited by the low oxygen diffusion rate through the dense oxide layer [Perr 97]. The thermal stability and the oxidation resistance improve by the addition of silicon, as is the case for transition metal nitrides and Ti-Al-N based hard coatings [Mann 01] [Vepr 04a] [Parl 04a] [Rave 07] [Musi 08a]. The $\mathrm{SiN_y}$ tissue phase formed upon addition of silicon is expected to hinder the recrystallization and growth of the nanocrystalline phase. It also suppresses the diffusion of oxygen at the grain boundaries.

Thermal stability The thermal stability of the physical properties, such as the microstructural, optical and mechanical properties, is of key importance for applications like air-plane windows (e.g. for space shuttles), furnace windows, solar devices (e.g. solar cells or water-heating devices), glass-ceramic cooktops, but also for architectural window glasses. For the latter, a post-fabrication annealing treatment may be used to relieve internal stresses in the glass and improve its durability (toughened or tempered glass). To investigate the thermal stability of Al-Si-N coatings, selected samples [41] deposited on silicon were annealed at $T_a = 1000°\text{C}$ in Ar (1 atmosphere) during 2h (see section 5.1.3 p. 84 for experimental details). Note that the melting temperature of AlN is $T_m \approx 2523$ K and the decomposition temperature[42] of Si_3N_4 equals $T_d \approx 2173$ K [Holl 86]. A ratio $T_a/T_{m,d}$ larger than 0.5 is hence used in this study.

As already reported in section 5.2.2 together with the microstructural properties of as-deposited coatings, the phase composition and the grain size of Al-Si-N films were found to be independent on the deposition temperature in the range 200–500°C and unchanged upon annealing. This stability of the microstructure agrees with the recent results reported by Musil *et al.* in [Musi 08a]. These authors studied the thermal stability and the oxidation resistance of Al-Si-N films with a low ($\sim$ 5 at.% - $Al_{54}Si_5N_{41}$, containing elemental Al atoms, i.e. not bonded to N atoms) and high ($\sim$ 40 at.% - $Al_7Si_{33}N_{60}$) Si content. They found no change in the amorphous structure of the film with high Si content after annealing at $1000°\text{C} < T_a < 1200°\text{C}$ about 30 min in air. The hardness of this film was moreover unchanged after 4h annealing at 1100°C in air. Upon annealing at 1200°C, the hardness was found to decrease with annealing time, which was related to the progressive growth of an oxide layer with lower hardness on top of the film. The film with low Si content was found to remain crystalline with the same [002] w-AlN preferred orientation as as-deposited films. No data was reported by Musil on the residual stress of annealed films.

In the present study, the hardness and the E modulus of Al-Si-N films with $0 < [\text{Si}] < 23$ at.% was found almost unchanged after annealing during 2h at 1000°C in Ar. This agrees with the high thermal stability of the mechanical properties reported by Musil. However annealed films showed an unexpected increase of compressive stress in two-phase Al-Si-N/SiN_y coatings ($[\text{Si}] \geq 6$ at.%). A similar behavior could not be found in literature. Instead of that, annealing is usually associated to the release of the compressive stress generated by ion bombardment during film deposition, as mentioned before. A possible explanation for this unexpected stress behavior of annealed Al-Si-

---

[41] All samples of series C, some of series B, none of series A.

[42] Si_3N_4 is found to decompose before it even can melt, so that its meting temperature is not known.

N coatings is a realignment of crystallites along the [002] direction through coherent grain boundaries.

Oxidation resistance The study of the oxidation resistance of a material requires to perform annealing experiments in air. In the present case, however, annealing was not performed in air but in argon. However, the presence of a small amount of residual oxygen in the oxidation chamber enabled the study of the oxidation resistance of Al-Si-N films as compared to pure AlN and pure SiN_y.

Composition depth profiles were measured by XPS on as-deposited and annealed Al-Si-N samples with 0 at.% (pure AlN), 8.5 at.%, 15 at.% and 46 at.% (SiN_y) of Si. These depth profiles are shown in Figure 5.35. The samples were alternatively sputtered with Ar^+ during 12 s at 3 keV and analyzed by recording detailed spectra of the Al2p, Si2p, N1s, O1s and C1s photoelectron lines. The total sputtering time was fixed at 6 min.

As seen in Figure 5.35, all as-deposited samples have a thin native oxide layer. This layer is thicker in pure AlN than in Al-Si-N and SiN_y. It is almost entirely removed upon Ar^+ sputtering at 3 keV during 90 s, which corresponds to the pre-sputtering conditions used for the routine XPS composition analysis of Al-Si-N films. A constant level of oxygen concentration is reached after about 4 min of sputtering time[43]. This concentration amounts to 0.5-2 at.% and corresponds to the residual oxygen incorporated in the layers during their reactive sputter deposition. The oxygen content is seemingly determined by the history of the sputter deposition chamber; the longer Al was sputtered for depositions and hence the chamber remained under vacuum, the lower were the oxygen contaminations. Carbon is only present as a surface contamination and is easily sputtered away after only a few seconds.

During annealing at 1000°C in Ar, a thermal oxide is grown on all the samples by reaction with the residual oxygen of the annealing chamber. A thin layer of stoichiometric Al_2O_3 is built on top of pure AlN. Although aluminum shows a higher reactivity with oxygen than silicon does, a thicker oxide layer (of stoichiometric SiO_2) is formed on SiN_y. This illustrates that the oxide layer growing on pure AlN is so dense that its growth is quickly limited by the diffusion of oxygen atoms through the oxide layer. As for annealed Al-Si-N films with 8.5 and 15 at.% of Si, an oxynitride layer is

---

[43] This was deduced from a close study of the numerical data (O content) and cannot be distinguished on Figure 5.35.

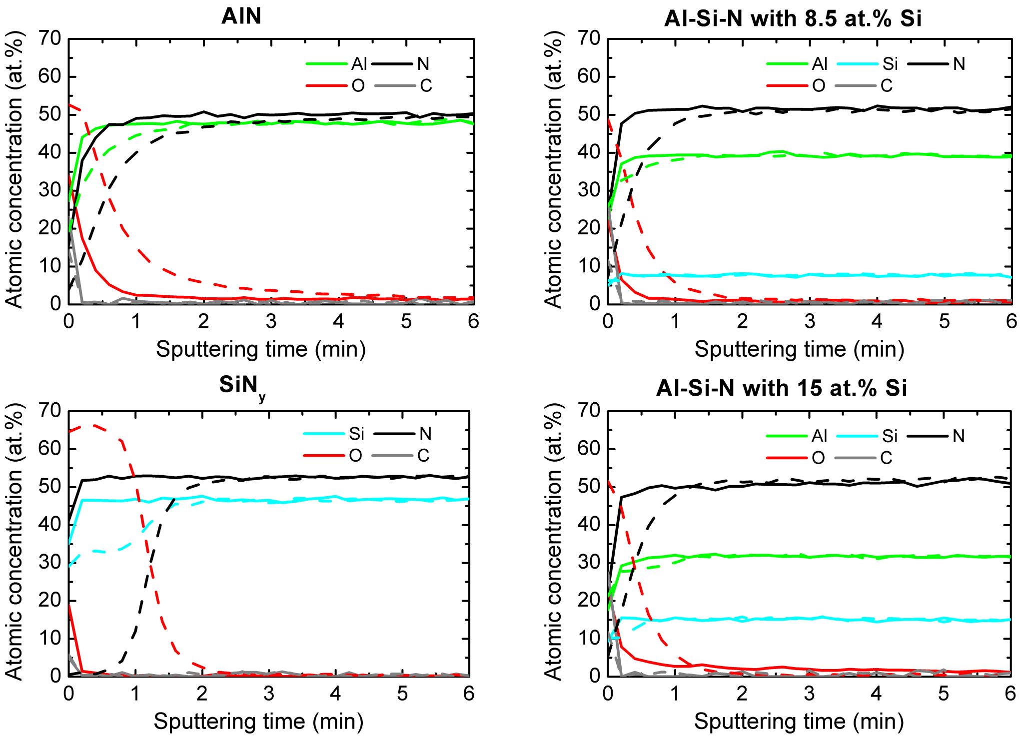

Figure 5.35: XPS depth profiles on as-deposited (solid lines) and annealed (dashed lines) Al-Si-N films of series C. The atomic concentrations of Al, Si and N main elements, as well as O and C contaminations were determined. The XPS sputter rate equals ∼ 8 nm/min, as estimated from height profiles through the XPS sputtered areas in Al-Si-N films with a mechanical profilometer.

formed, whose oxygen distribution over depth is independent on the silicon content. On these coatings, the concentration of oxygen at the surface as well as the oxide layer thickness are found to be smaller than for pure AlN and SiN$_y$. Perrem *et al.* compared the oxidation resistance of pure AlN with that of Al-Si-N with 11 at.% of Si deposited by CVD at 1150°C [Perr 97]. They found that the oxidation of pure AlN progresses far quicker than that of Al-Si-N, which agrees with the results reported here. Musil *et al.* explored the oxidation resistance of Al-Si-N films, defined as the temperature at which the coatings start to oxidize[44] [Musi 08a]. They found that crystalline Al-Si-N with a low (∼ 5 at.%) Si content exhibits a high oxidation resistance up to ∼ 1000°C and that amorphous Al-Si-N with a high (∼ 40 at.%) Si content exhibits even higher oxidation resistance up to ∼ 1150°C.

---

[44] As revealed e.g. by a significant increase of mass of the samples upon oxidation in thermogravimetric studies.

Recently an oxidation resistance exceeding 1000°C was reported by Musil and co-workers in transition metal (TM) silicon nitride systems, TM-Si-N (with TM = Mo, Ti, Zr), containing more than $\sim$ 25 at.% of silicon [Musi 08a]. This was attributed to the high thermal stability of the amorphous structure of these films, the thermal stability of coatings with low Si concentration being limited by the low ($<$ 1000°C) recrystallization temperature of the TM-N dominant phase. As reported by Musil and supported by the results reported in this work, Al-Si-N coatings with a high Si content show an equivalent good thermal stability and oxidation resistance as compared to the TM-Si-N amorphous systems cited above. Al-Si-N films are hence promising for advanced high temperature applications.

5.3 Discussion

To put into perspective the most important results of Chapter 5, several issues are again highlighted here. First, the solubility limit of silicon in aluminum nitride is discussed. The main features of the structural evolution of Al-Si-N nanocomposite films with increasing silicon content are then summarized, and an estimation of the silicon nitride coverage on top of the Al-Si-N crystallites is given. To finish, the evolution of the hardness with the structural properties of the films fabricated in this work is compared to the widely accepted design rules for nanocomposite hard coatings.

5.3.1 Solubility limit of Si in AlN

Based on thermodynamical data, it was believed at the beginning of this thesis work that AlN and Si_3N_4 were fully immiscible materials so that a two-phase nanocomposite structure would be formed for all Si contents. Literature on Si-doped AlN nevertheless suggested that silicon donor impurities could be incorporated in the AlN wurtzite lattice in substitution of Al atoms [Bogu 97]. A solubility limit as high as a few atomic percents of Si (4–6 at.%) was even suggested by the work of Taniyasu *et al.* [Tani 01] [Kasu 01] and the work of Hermann *et al.* [Herm 05] [Herm 06] (see the literature review provided in Section 2.2.3, pp. 26–31). Yet these works dealt with Al-Si-N films deposited at high substrate temperatures ($\geq$ 850°C) by CVD techniques. Although few studies were already published on low temperature sputtered Al-Si-N coatings [Mart 01] [Bend 02] [Musi 02b] [Li 05], this is the first time that a systematic investigation of the Al-Si-N system over a wide composition range is presented. This is also the first time that the formation of an $Al_{1-x}Si_xN$ solid solution is demonstrated for low temperature sputtered films.

The most significant implication of the substitutional incorporation of silicon in the AlN wurtzite lattice is the linear shrinking of the c-lattice parameter, and therefore of the average Al(Si)–N bond length, as the Si content is increased from 0 to 6 at.% (Fig. 5.18 p. 113). This behavior is similar to what was found by Taniyasu *et al.* [Tani 01]. Above 6 at.%, the c-lattice parameter does no longer decrease and remains constant. This coincides with an abrupt change of the crystallite growth behavior, as revealed by the linear increase of the inverse crystallite size ($1/D$) with the silicon concentration for [Si] $\gtrsim$ 7 at.% (Fig. 5.19 p. 114). In addition to the direct characterization of the film microstructure by XRD, structural changes are also supported by the evolution of the chemical, mechanical and optical properties of Al-Si-N films. At a silicon concentration of 4 at.% in Al-Si-N films, XPS studies revealed a distinct change in the evolution of the chemical state of argon atoms implanted in the films during sputter-cleaning of the surface prior to XPS analysis (Figs. 5.7, 5.8 and 5.9 pp. 97–98). This suggests a structural change of the Al-Si-N implantation matrix at 4 at.% of Si. At the same concentration, the refractive index n of the Al-Si-N films slightly increases (Fig. 5.34a p. 138). A noticeable change in the film stress was also observed: cracks were formed in Al-Si-N films containing less than 4 at.% of Si. Above this concentration, no cracks are visible anymore and the residual stress rapidly evolves into a small compressive stress (Fig. 5.30 p. 130).

In summary, the film properties were found to change considerably within a Si concentration range between 4 and 7 at.%. Since the strongest indication for the formation of an $Al_{1-x}Si_xN$ solid solution is given by the evolution of the c-lattice parameter that abruptly changes at 6 at.% of Si, a solubility limit of 6 at.% is defined. Note that this solubility limit is independent on the substrate temperature for sputter-deposited films at 200°C and 500°C, in contrast to what was reported by Sandu and co-workers for the Zr-Si-N system [Sand 06b] [Sand 07] [Sand 08]. These authors found the Si solubility limit in ZrN to decrease with increasing deposition temperature. Here, no such decrease is observed, i.e. the solubility limit of Si in AlN remains stable. This is a strong evidence that the incorporation of Si in AlN results from thermodynamics, i.e. a solid solution thermodynamic phase is formed. Moreover, the sharp kink in the lattice parameter evolution at 6 at.% of Si indicates a strong thermodynamic driving force for phase separation above this silicon concentration. From about 4 at.% of Si, however, silicon atoms start to segregate to the grain boundaries of Al-Si-N crystallites, presumably as a result of the kinetic limitations of the deposition method (i.e. non-equilibrium process), and a SiN_y tissue layer starts to form. Above about 7 at.% of Si, a sufficiently thick SiN_y grain boundary layer is formed around the Al-Si-N crystallites, forcing the crystallite size to rapidly decrease (see section 5.3.2).

5.3.2 Two-phase structural model

By analyzing the chemical composition and comparing the evolution of the chemical, structural, mechanical and optical properties of reactive sputtered Al-Si-N films, a model for the film formation mechanism is proposed. This model was developed in analogy to the structural model introduced by Sandu, Sanjinés *et al.* for the Ti-Ge-N, Nb-Si-N and Zr-Si-N coating systems (mainly) [Sand 06a] [Sand 06b] [Sand 06c] [Sanj 05].

- In Region I ($0 \leq$ [Si] ≤ 4 at.%) the majority of the Si atoms substitute Al atoms in the hexagonal wurtzite AlN lattice, forming an $Al_{1-x}Si_xN$ solid solution, i.e. a single-phase material. The films are uniaxially (002) textured. They show an open columnar microstructure with large columns running through the entire film thickness and composed of crystalline regions with similar crystalline orientation. This open microstructure is responsible for a residual tensile stress of the films, partially released through cracks formation. With increasing the Si content the hardness is increased due to solid solution hardening effect.

- In Region II ($4 \leq$ [Si] $\lesssim 7$ at.%), the solubility limit is exceeded and Si atoms segregate to the grain boundaries of Al-Si-N crystallites. A SiN_y grain boundary phase is formed and progressively envelops the Al-Si-N crystalline grains. This releases the tensile stress and finally leads to a compressive stress, typical for sputter deposited films, as the Si content is increased. A dense two-phase microstructure appears. Region II hence can be defined as a transition region between a single-phase solid solution and a fully developed two-phase nanocomposite structure.

- In Region III ($7 \lesssim$ [Si] $\lesssim 12$ at.%)[45], a SiN_y grain boundary phase has formed that leads to an inversely proportional decrease of the crystallite

---

[45] The upper Si concentration limit of region III is not well defined. Based on the evolution of the chemical, structural, mechanical and optical properties of Al-Si-N films, changes are observed between 10 and 15 at.% of Si. For sake of clarity, the transition between Region III and Region IV is defined at 12 at.% of Si.

size with increasing the Si content. In all films, the Al-Si-N crystallites are of an elongated shape in the growth direction; their aspect ratio is found to decrease with increasing the Si content. In Region III, the thickness of the SiN_y layer remains constant. It is estimated to about one monolayer (see end of this section), such that the chemical state evolution of Si and N atoms is governed by the majority Al-Si-N crystalline phase. Above about 9 at.% of Si, the XRD signal coming from the (002) textured Al-Si-N phase progressively vanishes and a weak additional XRD peak, attributed to an ordered grain boundary phase, appears. Nevertheless the initial (002) texture of the films survives the formation of the two-phase structure and remains detectable even in Region III when the crystallite size drops below 10 nm. This infers that the Al-Si-N crystallites must be coherent: their preferred crystalline orientation is transferred through the ordered SiN_y grain boundary phase. The mutual misorientation of Al-Si-N crystallites nevertheless increases when the Si content is increased, as revealed by XRD and TEM studies. At 9 at.% of Si, the crystallite size is decreases below 10 nm, preventing the nucleation of dislocations. Thus a nanostructure hardening effect[46] conspires with the solid solution hardening effect of Region I, such that the hardness further increases to reach a maximum of 32 GPa at about 10 at.% of Si.

- In Region IV ([Si] $\geq$ 12 at.%), the crystallite size is smaller than 5 nm. The Al-Si-N films are X-ray amorphous for a silicon concentration larger than about 25 at.% of Si. Within a concentration range of 10–15 at.% of Si, XPS data reveals a SiN_y grain boundary phase with similar chemical properties to those of bulk SiN_y. The chemical state of nitrogen atoms then arises from the superposition of two distinct chemical states associated to the two phases present in the Al-Si-N films as the SiN_y phase achieves a sufficient volume to be seen: at 15 at.% of Si, the SiN_y phase represents about 30% of the volume in Al-Si-N composite coatings[47]. This change in the chemical state of Si and N atoms is attributed to an increase of the SiN_y layer thickness. This is supported by the sudden decrease of the residual compressive stress in Al-Si-N films containing more than 15 at.% of Si. At about

---

[46] i.e. absence of dislocation activity due to the small grain size, plus hindering of grain boundary sliding thanks to the SiN_y tissue phase surrounding the Al-Si-N crystallites.

[47] As estimated from the volume ratio R_2 between the Al-Si-N crystalline phase and the SiN_y amorphous phase, expressed in Equation C.2 p. 205 (Appendix C) and used for the calculations presented below in this section. The volume percentage of the SiN_y phase is given by: $R_2/(1+R_2)$.

13 at.% of Si, an abrupt increase of the coating refractive index and a large decrease of the extinction coefficient further indicate this last structural change. Grain boundary sliding may then be the reason for the gradual decrease of the film hardness that approaches that of pure $\mathrm{SiN_y}$ ($\sim$ 20 GPa).

Based on the above proposed evolution model, the surface coverage of Al-Si-N crystallites and the interlayer thickness are estimated.

Si surface coverage The Si surface coverage is estimated in analogy to the model proposed by Sandu *et al.* in [Sand 06c]. This model was initially derived in the case of cubic-shaped crystallites of rock-salt cubic structure for various M-X-N systems (M stands for an early transition metal and X = Si, Ge, Sn), in particular for the Ti-Ge-N, Nb-Si-N and Zr-Si-N systems. Here the model is modified to account for elongated crystallites of w-AlN structure, with an hexagonal section parallel to (002) crystallographic planes (see Fig. C.1, p. 203). In this calculation, the Si coverage is defined as the ratio between the number of Si atoms at the crystallite surface and the number of available substitutional Al sites on top of the crystallites. The Si surface coverage is given by[48]:

$$\text{Si surface coverage} = \frac{C_{\mathrm{Si}} - \alpha}{C_{\mathrm{Al}} + \alpha} \times \frac{3h}{(4ra + 2c)} \tag{5.3}$$

where C_{Si} and C_{Al} are the silicon and the aluminum atomic concentrations, respectively, α is a parameter that corresponds to the silicon atomic concentration at which the first Si atoms segregate outside the Al-Si-N crystallites, r is the aspect ratio of the elongated crystallites of height h (in the [002] crystallographic direction) and width w, with $r = h/w$, a and c are the lattice parameters of w-AlN.

$\mathbf{SiN_y}$ interlayer thickness The $\mathrm{SiN_y}$ interlayer thickness t is calculated from the estimated volume ratio of the Al-Si-N and $\mathrm{SiN_y}$ phases, using the same crystallite shape as in the previous calculation. The following expression is obtained[48]:

$$t = \frac{\sqrt{3}h}{(\sqrt{3} + 4r)} \times \frac{C_{\mathrm{Si}} - \alpha}{C_{\mathrm{Al}} + \alpha} \times \frac{(3M_{\mathrm{Si}} + 4M_{\mathrm{N}})}{3(M_{\mathrm{Al}} + M_{\mathrm{N}})} \times \frac{d_{\mathrm{AlN}}}{d_{\mathrm{SiNy}}} \tag{5.4}$$

where M_{Si}, M_{Al} and M_{N} are the relative atomic masses of Si, Al and N atoms, d_{AlN} and d_{SiNy} are the densities of the AlN (respectively Al-Si-N) and

---

[48] The detail of this calculation is given in Appendix C (p. 203).

SiN_y phases.

For the onset of the second phase formation[49], the parameter α is taken in both calculations equal to $\sim$ 4 at.% of Si. The aspect ratio r of the elongated crystallites is however difficult to determine. As mentioned before, r is not constant but decreases with increasing the Si content in Region III. From XRD data, only the crystallite length (height) h is accessible. The crystallite width w and hence the aspect ratio r can only be evaluated from TEM high-resolution images. r is estimated to equal about 3 in the lower Si concentration range of Region III, progressively decreasing to a value of about 1 going into region IV. For the calculations of Si coverage and SiN_y interlayer thickness, a linear decrease of the aspect ratio r from 3 to 1 in Region III is arbitrarily chosen. r is taken as a constant value of 3 in Region II and 1 in Region IV. The results of these calculations are plotted in Figure 5.36.

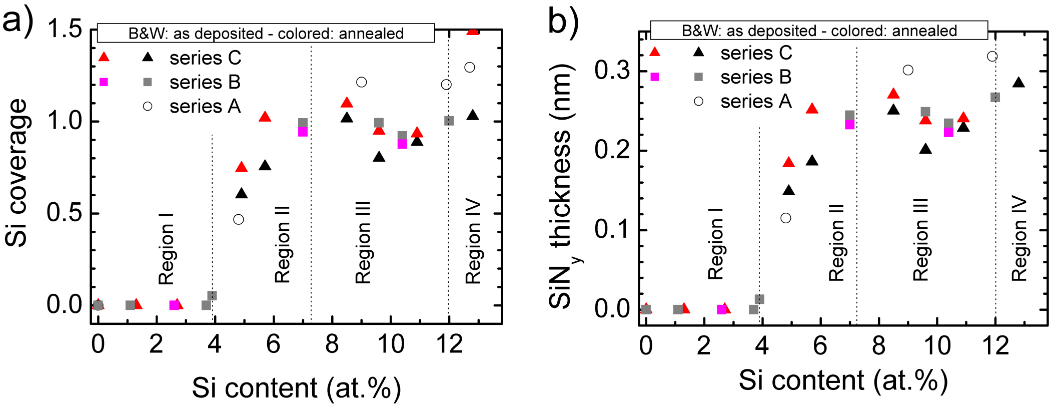

Figure 5.36: Estimation of (a) the Si surface coverage at the surface of Al-Si-N crystallites and (b) the SiN_y layer thickness between the Al-Si-N crystallites, as a function of the silicon content in the films. XRD data from all samples series (as-deposited and annealed) were used here (see Table 5.1 p. 83). The four composition regions defined in the text are shown.

The qualitative evolution of the Si coverage (Fig. 5.36a) and of the SiN_y interlayer thickness (Fig. 5.36b) with an increasing content of Si in the Al-Si-N films is the same. This is related to the crystallite size model (crystallite shape, h and r values) used for both calculations. Both the Si coverage and

---

[49] i.e. when the first Si atoms segregate at the grain boundaries, which occurs for a Si content smaller than the solubility limit (6 at.%) due to the kinetic limitations of the deposition process.

the $\mathrm{SiN_y}$ layer thickness start to increase in Region II and reach a constant value in Region III. The Si coverage is found to amount to unity in Region III, which means that all the Al sites on the surface of Al-Si-N crystallites are filled by substitutional Si atoms. This corresponds to a $\mathrm{SiN_y}$ layer thickness of about 0.25 nm. For comparison, note that the Si–N, the N–N and the Si–Si interatomic distances in β-$\mathrm{Si_3N_4}$ equal – in average – 1.73 Å, 2.83 Å and 3.00 Å respectively [Grun 79]. One monolayer (ML) of $\mathrm{SiN_y}$ growing on top of an Al-Si-N crystallite is here arbitrarily defined as the N–N distance, i.e. the length of one edge of a Si–$\mathrm{N_4}$ tetrahedron, which is the basic building block of silicon nitride. The 0.25 nm interlayer thickness seen in Figure 5.36b corresponds therefore roughly to a $\mathrm{SiN_y}$ thickness of 1 ML. The [Si]$\sim 1/D$ dependence shown in Figure 5.19 p. 114 (or $C_{Si} \sim 1/h$ dependence, using the notation of Equations 5.3 and 5.4) was interpreted as an increasing amount of $\mathrm{SiN_y}$ in the films achieved by increasing the surface/volume ratio of the Al-Si-N crystallites while maintaining a constant $\mathrm{SiN_y}$ thickness on top of them. This is confirmed by the plateau observed in Region III in Figure 5.36. A closer look at Figure 5.36 however reveals that the values of Si coverage and $\mathrm{SiN_y}$ thickness may actually not be constant in Region III. This ambiguity may arise from the assumed linear evolution (decrease) of the aspect ratio r in this region and to uncertainties on the exact values of r. Above ∼12 at.% of Si, the Al-Si-N crystallite size reaches a minimum (∼2–3 nm, see Fig. 5.19 p. 114). The amount of $\mathrm{SiN_y}$ is thereafter probably increased by increasing the $\mathrm{SiN_y}$ interlayer thickness. The crystallites are then completely surrounded by a $\mathrm{SiN_y}$ interlayer, the thickness of which quickly increases as the Si content is increased, isolating the crystallites the one from the other. This has a direct influence on the mechanical (biaxial stress) and optical (transmission, absorption) properties of Al-Si-N films. A similar behavior was reported by Diserens in TiN/$\mathrm{SiN_y}$ nanocomposite hard coatings that showed a constant grain boundary thickness ($\sim$ 0.5 nm) between 0 and 10 at.% of Si, that was found to increased above 10 at.% of Si [Dise 00] [Pats 01].

In summary, the experimental data presented in this thesis clearly support the proposed four region model to explain the evolution of the morphological, structural, chemical, mechanical and optical properties of the Al-Si-N films with different Si content.

5.3.3 Comparison to the traditional design rules for hard nanocomposite coatings

The design rules for superhard ($H > 40$ GPa) nanocomposite coatings proposed by Vepřek include the self-organization of a stable nanostructure by thermodynamically driven spinodal phase segregation [Vepr 95] [Vepr 99] [Vepr 05], as a required but nevertheless not sufficient condition. In the case of nanocomposite coatings made of transition metal nitrides and silicon nitride, this necessary but not sufficient condition implies the use of a sufficient nitrogen partial pressure, to avoid the formation of a silicide phase i.e. to provide a thermodynamic driving force for phase segregation and the use of a sufficiently high deposition temperature ($T \gtrsim 500°C$), so that the diffusion-rate limited phase segregation can then occur during deposition. As a result, the obtained materials generally show an isotropic morphology for the optimum deposition conditions and maximum hardness. TEM images revealed a (sometimes incomplete) suppression of the columnar microstructure. For the TiN/SiN_y system, Vepřek and co-workers showed that the crystallite size may vary quite differently with the Si content according to the deposition conditions used. For instance the crystallite size may initially decrease with increasing the Si content, show a minimum at hardness maximum, and then increase again by further increasing the Si content (HF-PACVD, Fig. 5 in [Vepr 95], Fig. 1 in [Nied 01]). In contrast, the crystallite size may only slightly decrease with the first few added Si at.% and remain then constant (DC-PACVD with a high or low discharge current density, Fig. 2 in [Nied 01] and Fig. 3 in [Vepr 00]). At maximum hardness, the crystallite size is extremely small (only a few nm). Vepřek showed that neither the crystallite size nor the volume content of each phases alone determines the hardness maximum, but the effective coverage of the crystallites: the maximum hardness is achieved when about one monolayer of Si_3N_4 covers the surface of the transition metal nitride nanocrystals [Proc 04] [Vepr 05]. The Si content that corresponds to a coverage of one monolayer of SiN_y depends on the crystallite size and shape, that depend in turn on the exact deposition conditions of the films [Vepr 05]. Strong and atomically sharp interfaces with a low defect concentration between the two phases are then believed to be formed as a result of spinodal phase separation of (at least) two immiscible materials. The improvement of the mechanical properties (essentially of the hardness) results from the suppression of dislocation activity in crystallites smaller than about 10 nm in diameter and from the hindering of grain boundary sliding thanks to the presence of a thin grain boundary phase, that is however no thick enough so that initiation and propagation of nanocracks could occur in this phase.

The work presented in this thesis was initially guided by these design rules. However here a lower nitrogen partial pressure could be used to simply achieve a sufficient nitridation of Al and Si. The formation of a metal-silicide did not occur, because an Al-silicide does simply not exist. Having in mind later applications of the coatings, lower deposition temperatures were used, namely 200°C and 500°C. As a result *a*) the formation of a two-phase composite coating was achieved – despite the formation of an $Al_{1-x}Si_xN$ solid solution for $x < 0.12$ (i.e. $[Si] < 6$ at.%), with *b*) sufficiently small grain size ($D < 10\,\mathrm{nm}$ for $[Si] > 9$ at.%) and *c*) a monolayer SiN_y coverage of Al-Si-N crystallites (for $6 < [Si] \leq 12$–15 at.%). Thus three of the structural and morphological requirements for hardness enhancement are clearly met. However the maximum hardness of about 32 GPa remains moderate. Despite the loss of a macroscopic columnar morphology, the Al-Si-N coatings were found to retain a (002) texture at all Si contents. This suggests that the condition *d*) of strong and sharp interfaces between two phases with distinct mechanical properties may not be fulfilled in the Al-Si-N system. Thus the nucleation of dislocations within the crystalline phase and the successive dislocation motion at the grain boundaries may not be fully hindered.

Three explanations are proposed for the formation of ”weak” interfaces:

- The first one is based on the nature of the involved materials. Both AlN and Si_3N_4 are covalently bonded nitrides with same metalloid coordination numbers and similar mechanical properties, in particular similar E modulus, which is not the case for transition metal nitride–silicon nitride nanocomposites [Holl 86]. Moreover, the AlN (resp. $Al_{1-x}Si_xN$) crystalline phase in the composite has a hexagonal crystallographic structure; this also differs from widely used transition metallic nitrides (such as TiN, CrN, ZrN, etc.) that have a cubic NaCl structure and hence a different set of slip systems. The similarities between AlN and SiN_y may result in interfaces that are not ”sharp” in term of structural properties but show a gradual transition between the two phases present in the nanocomposite films. This is further supported by the evidences found by XRD and TEM of the ordering of the SiN_y grain boundary layer and of the coherency between Al-Si-N crystallites that is retained in the two-phase nanostructured coatings. This ordered structure is self-organized during the film growth as a consequence of the segregation of Si atoms when the silicon concentration exceeds the solubility limit of Si in w-AlN.
- The second explanation is based on the origin of the formation of a

nanostructure in the Al-Si-N system, that can be of thermodynamic and/or of kinetic nature. As mentioned in section 5.3.1, XRD data gives a strong indication of a thermodynamically stable $\mathrm{Al_{1-x}Si_xN}$ solid solution up to 6 at.% of silicon (x = 0.12) and of a thermodynamically driven phase segregation above this concentration limit. Nevertheless, Si atoms start to segregate already at about 4 at.% of Si. This may arise from deposition conditions that are away from a thermodynamic equilibrium process. The constant $\mathrm{SiN_y}$ coverage of Al-Si-N crystallites found in region III of the proposed film formation model and the inverse proportional decrease of the crystallite size with the Si content strongly indicate that the nanostructure achieved is not the result of spinodal phase segregation. Instead the increasing amount of incoming Si atoms or Si-N clusters, as the power applied on the Si target is increased (to increase the Si content in Al-Si-N films), may cause the limitation of crystalline grain growth and force the nucleation of new grains on the growing surface. Thus kinetic effects may be dominant effects in the formation of the film microstructure. As a result, the interfaces are presumably diffuse (i.e. gradual composition). In addition a high concentration of defects may be present at the interfaces, which degrade the mechanical properties of the coatings.

- A third cause for the limited hardness enhancement may be the oxygen content of the layers, here less within 0.5–2 at.% as determined from XPS depth profiles. Previous studies have shown a fast decrease of hardness in $\mathrm{AlSiON_x}$ coatings with increasing the oxygen content [Bend 02]. Already 0.2–0.3 at.% of oxygen were even identified by Veprek and co-workers as being sufficient to cause significant hardness reduction to values smaller than 40 GPa [Vepr 04b] [Vepr 05]. Also, according to recent density-functional theory calculations, oxygen impurities present at grain boundaries can weaken the interface strength [Hao 06b].

All three explanations may play a role here, in which interface properties clearly appear to be a key parameter. The critical role of interfaces is further supported by recent findings concerning the structure of the $\mathrm{SiN_y}$ interfacial layer: this layer may not be amorphous as initially thought but epitaxially stabilized by the crystalline phase, as shown e.g. for the TiN-$\mathrm{SiN_y}$ system [Hu 05] [Sode 05] [Vepr 07a] [Hult 07]. However the complicated three-dimensional nanocrystalline morphology of the films prevents a more elaborated study of the properties of the intergranular phase. In order to gain additional insight, two-dimensional multilayers were prepared as model systems (Chapter 6).

Chapter 6

Al-Si-N/SiN$_y$ multilayers as an interface model

6.1 Indication of epitaxial stabilization in nanocomposites

Nanocomposite thin films are defined by a complex three-dimensional network of phases and interfaces between different constituents. The exact nature and the properties of these interfaces remain, however, difficult to access. Current efforts in the field of hard and superhard coatings include multilayer structure models to understand the properties of the interfaces and of the thin tissue "phase" or interlayer that is formed in nanocomposite structures. *Ab initio* calculations are used [Hao 06a] [Hao 06b] [Zhan 07a] [Zhan 07b] [Hult 07] [Zhan 08b] as well as model experiments on the growth of thin TiN/SiN$_x$ superlattice systems [Hu 05] [Sode 05] [Sode 06] [Hult 07] [Sode 07b].

Nanoscale multilayer structures composed of materials having different crystalline structures (under thermodynamic equilibrium conditions) often reduce their interfacial energy by forming coherent interfaces, stabilizing one layer material in the lattice structure of the other one. The most prominent example is the one of AlN/TiN superlattices. In this material system the epitaxial stabilization of a metastable cubic AlN phase due to a "template effect" was reported already 10 years ago by Setoyama *et al.* [Seto 96] and Madan *et al.* [Mada 97], as shown in Figure 6.1b. Above a critical thickness of the AlN layer, however, the stabilization effect is lost and the AlN transforms into the stable hexagonal phase. The critical thickness is determined by the balance between the gain in interfacial (surface) energy, obtained by the formation of a coherent interface, and the loss in AlN lattice (volume) energy due to the stabilization of a metastable phase [Mada 97] [Kim 01] [Mei 04]. In the case of AlN/TiN superlattices, the critical AlN thickness is about 2–3 nm. Several other systems show a similar epitaxial stabilization effect, such as cubic AlN, NbN, $CrN_{0.6}$ and TaN that can form in AlN/VN, TiN/NbN, TiN/$CrN_{0.6}$ and TiN/TaN superlattice structures ([Mei 04] and further references therein). In the same way, the crystallization of normally amorphous layers (under the deposition conditions used) was reported for CN_x, SiC, SiO_2 and TiB_2 in TiN/CN_x, ZrN/CN_x, TiN/SiC, TiN/SiO_2 and TiN/TiB_2 multilayer systems ([Mei 05] and references therein). In all cases, the critical thickness is of the order of a few nanometers, never exceeding $\sim$ 9 nm. This stabilization effect is usually associated with a pronounced hardening effect ("superlattice effect"). The latter is commonly ascribed to a difference in shear moduli between the alternating layer materials (Koehler's mechanism), as described in Chapter 2, Section 2.1.2 (starting p. 10). An influence of alternating strain fields (related to the formation of coherent interfaces and the existence of a lattice mismatch) is also mentioned, that should block the dislocation motion [Shin 92] [Mei 04]. In addition, experimental results have shown that the E modulus of AlN increases when the material is stabilized in the cubic form, which also corresponds to a densification of the material. Mei *et al.* suggested that this may contribute to the strengthening of multilayers [Mei 04]. However Zhang *et al.* recently reported that in spite of the large difference in elastic modulus between the hexagonal (hcp) and cubic (fcc) forms of AlN, the difference in shear strength was small and could not explain the hardness enhancement of AlN/TiN superlattices when the cubic form of AlN is epitaxially stabilized [Zhan 07a]. Finally, Karimi *et al.* reported that the relative crystalline orientation in adjacent layers influences the degree of coherency of the interface and therefore the extent of hardness enhancement [Kari 06].

Only recently, it was suggested that a similar stabilization effect may play a role in hard three-dimensional nanocomposite systems such as the TiN/SiN_x system, explaining the importance of forming a thin (1–2 monolayers) SiN_x tissue phase in TiN/SiN_x nanocomposite coatings [Hu 05] [Sode 05]. Hu *et al.* and Söderberg, Hultman *et al.* reported the successful stabilization of cubic SiN on top of low index (typically (001)) TiN surfaces, as shown in Figure 6.1a [Hu 05] [Sode 05] [Sode 06] [Hult 07] [Sode 07b] [Sode 07a]. The epitaxial breakdown thickness of the silicon nitride layer is about 0.7 nm only, that is much smaller than the one reported for cubic AlN in AlN/TiN superlattices. Hultman *et al.* explained it based on two major differences between the AlN/TiN and the SiN/TiN systems [Hult 07].

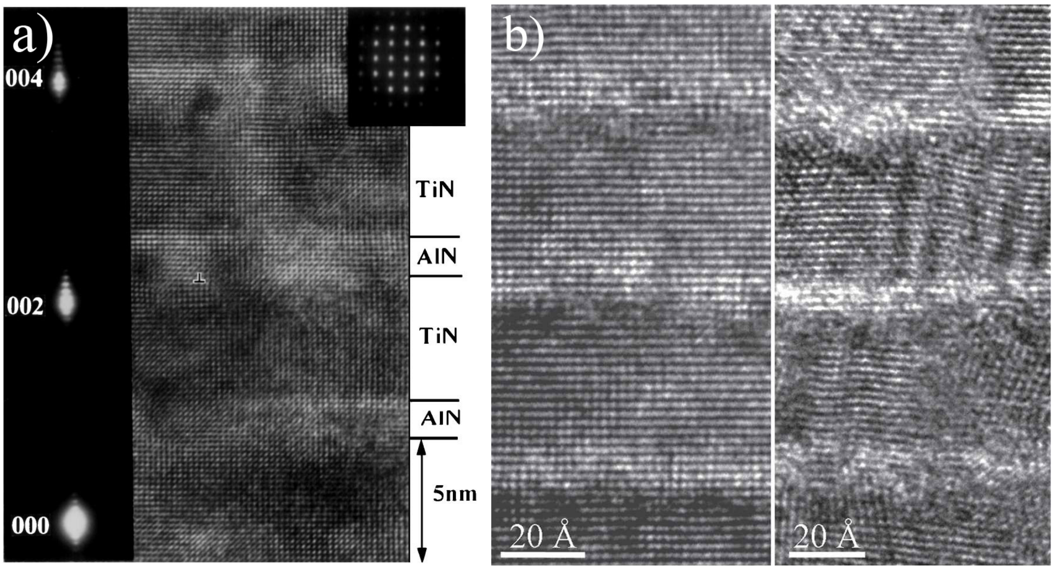

Figure 6.1: (a) Cross-sectional high-resolution TEM micrograph of a [AlN(1.7 nm)/TiN(5.1 nm)]$_{40}$ superlattice [Mada 97]. A selected area diffraction (SAD) pattern is shown in the top-right inset. A magnified portion of the SAD picture is given on the left side of the HR picture, where superlattice reflections are seen around the (000), (002) and (004) Bragg reflections. (b) Cross-sectional HRTEM micrographs from TiN/SiN$_x$ multilayers containing (left) 5.5 Å SiN(001) and (right) 13 Å SiN$_x$ layers respectively. TiN layers are $\sim$ 40 Å thick [Sode 07b].

First the Si/N stoichiometric ratio varies from 1 in cubic SiN to $\sim$ 1.33 in amorphous SiN$_x$, corresponding to a change in Si bond coordination from octahedral (6-fold coordination with N) to tetrahedral (4-fold coordination with N). Secondly, while both the cubic and the hexagonal forms of AlN show a lattice mismatch with (cubic) TiN – i.e. a non-zero associated coherence strain energy –, there is no strain energy associated with amorphous silicon nitride. The critical thickness of 0.7 nm corresponds to 2–3 monolayers of silicon nitride. From this finding of an epitaxial stabilization of cubic SiN, Hultman *et al.* developed an updated schematic diagram for TiN-SiN$_x$ nanocomposite structures shown in Figure 6.2. Figure 6.2a, the traditional two-phase model of TiN nanocrystals surrounded by an amorphous Si$_3$N$_4$ tissue phase is shown. The authors proposed instead a three-phase model, where the silicon nitride tissue phase can be divided into epitaxially stabilized cubic SiN on low-index TiN facets, and amorphous SiN$_x$ in triple junctions and on higher index facets.

To explain the unexpected low hardness enhancement observed in Al-Si-N

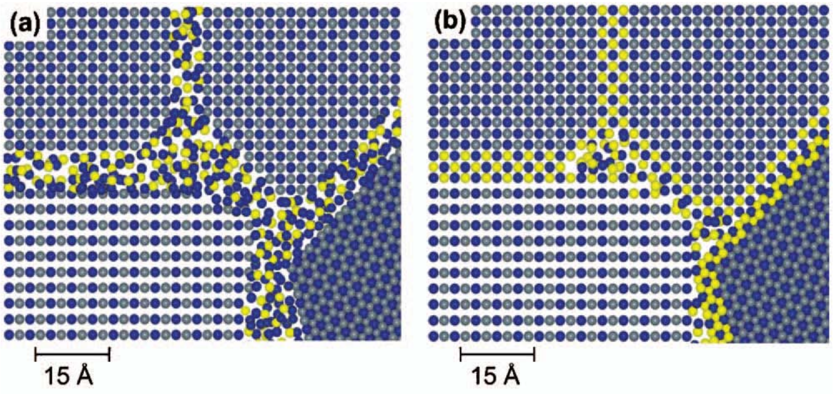

Figure 6.2: Cross-sectional schematic diagrams of superhard TiN-SiN$_y$ nanocomposite coatings were TiN crystallites are encapsulated by a SiN$_y$ tissue phase. (a) Two-phase model in which SiN$_y$ is amorphous; (b) Three-phase model in which SiN$_y$ grows either epitaxial cubic (for a thickness t of SiN$_y$ < 2–3 monolayers) or consists of a bilayer of cubic SiN and amorphous SiN$_y$ (t < 3 monolayers). Ti: gray; N: blue and Si: yellow. From [Hult 07].

nanocomposite coatings, despite the formation of two distinct phases and the grain refinement to crystallites smaller than 10 nm, a similar approach to the one described above was adopted. Multilayer structures of type Al(Si)N/SiN$_y$ were deposited on various substrates and with variable SiN$_y$ layer thicknesses to establish a growth model for SiN$_y$ on top of wurtzite AlN (w-AlN).

6.2 Sample preparation

Al-Si-N/SiN$_y$ multilayer samples were deposited in the same deposition machine and with the same general deposition conditions as those described for Al-Si-N nanocomposite coatings in section 5.1.1 p. 81. The substrate temperature was fixed at 200°C for all the samples. Three series of multilayers were deposited on Si, WC-Co, fused silica and glass substrates[1]. The deposition conditions and their corresponding coding letters (D, E and F) are listed in Table 6.1. The Al-Si-N layer composition was chosen as pure AlN (series D), Al-Si-N with about 6.5 at.% of Si (series E) and Al-Si-N with about 13 at.% of Si (series E). The Si concentration in Al-Si-N for the samples of series E and F were chosen so as to be at the solubility limit of Si in AlN (grain size in Al-Si-N films ∼ 40 nm) and above the solubility limit (grain size ∼ 4 nm) respectively. The purpose was to study the influence of

---

[1] Transparent substrates were used here to check the transparency in visible light of the deposited samples as an indication of full nitridation of the Al and Si atoms in the coatings

the composition and of the microstructure of the Al-Si-N layer on the growth behavior and on the mechanical properties of the multilayer coatings, and to gain insight into the issue of coherent interfaces Al-Si-N/SiN$_y$. For each series, the Al-Si-N layer thickness was kept constant at 5 nm and the SiN$_y$ layer thickness was varied from 0.25 to 2 nm (namely 0.25, 0.35, 0.5, 0.7, 1.2 and 2 nm). The total thickness of the coatings of series D, E and F is in the range 0.9 – 1.4 µm.

Table 6.1: Deposition conditions for Al(Si)N/SiN$_y$ multilayer series deposited on Si and WC-Co.

Series	[Si] in Al(Si)N (at.%)	Al(Si)N thickness (nm)	SiN$_y$ thickness (nm)	Bilayer #	P on Al(/Si) in Al(Si)N (W)	P on Si in SiN$_y$ (W)
D (●)	0	5	0.25–2	150–250	200	40–200
E (▼)	6.5	5	0.25–2	190–250	200/40–50	40–200
F (□)	13	5	0.25–2	190–250	200/80	40–150

Further experiments on multilayers involved the use of α-Al$_2$O$_3$ (0001) (sapphire) single-crystalline substrates, in addition to silicon and glass substrates. Sapphire substrates were used to promote the growth of heteroepitaxial layers of w-AlN (0001) type. This will be further explained in Section 6.3.2. The corresponding deposition conditions and coding letters (G, H) are summarized in Table 6.2. For samples of series H, in particular, the Al-Si-N layer thickness was kept constant at 10 nm and the SiN$_y$ layer thickness was varied from 0.4 to 2 nm (namely 0.4, 0.7, 1.2 and 2 nm). The total thickness of coatings deposited on α-Al$_2$O$_3$ was 200 nm for the samples of series G and around 40 nm for the samples of series H.

Table 6.2: Deposition conditions for Al(Si)N/SiN$_y$ multilayer series deposited on α-Al$_2$O$_3$ (001).

Series	[Si] in Al(Si)N (at.%)	Al(Si)N thickness (nm)	SiN$_y$ thickness (nm)	Bilayer #	P on Al(/Si) in Al(Si)N (W)	P on Si in SiN$_y$ (W)
G	0	20, 50	20, 50	5, 2	200	150
H	0, 6.5	10	0.4–2	4	200, 200/40	40

6.3 Experimental results

In the present section, the experimental results obtained on samples of series D, E and F, deposited on silicon and WC-Co substrates, are presented first. The structural and mechanical properties of these coatings were studied by XRD, XRR, (HR)TEM, nanoindentation testing and mechanical profilometry. In a second subsection, results on the samples deposited on sapphire substrates (principally AlN/SiN$_y$ samples of series H) are reported. Emphasis is placed on the study of interfacial properties in multilayer structures using high-resolution transmission electron microscopy.

6.3.1 Multilayers on silicon and WC-Co

a) Investigations of the multilayer ordering (XRR, XRD, TEM)

Low angle XRD (XRR) The multilayer coatings of series D, E and F deposited on silicon were characterized using X-ray reflectometry (XRR), also called low angle XRD[2]. The technique gives an insight into the interface quality (sharpness, roughness) and enables, for instance, to check the individual layer thickness in a multilayer structure. This, however, requires the fitting of experimental XRR curves to simulated ones. In the case of multilayers, the fitting procedure involves many parameters such as the thickness, the interfacial roughness and the density of each layer, as well as a possible aperiodicity in thickness and/or roughness. It is therefore difficult to obtain accurate and reliable values for each parameter. From experience only the thickness can be determined reliably independent of small variations of the measurement set-up and of the data processing procedure.

An example of XRR curve measured on an AlN/SiN$_y$ multilayer coating of series D is shown in Figure 4.6b, p. 65. The total thickness of the coating was of the order of 1 µm, i.e. too thick so that Kiessig Fringes could be observed[3]. Superlattice peaks associated to the bilayer period of the multilayer stack were nevertheless clearly seen, proving the existence of a layered structure with well-defined interfaces. Such superlattice peaks were observed for all the multilayers, including those having the smallest SiN$_y$ layer thickness, namely 0.25 nm, which corresponds to only one monolayer of silicon nitride.

---

[2] A short introduction to low angle and high angle XRD on multilayer structures is given in Chapter 4, section 4.2.1 (p. 63).

[3] The periodicity (distance between two maxima) of Kiessig fringes is inversely proportional to the total thickness of the film.

From the fit of experimental to simulated curves, it appeared that the bilayer thickness was equal to the targeted one within 5%. Note that the bilayer thickness obtained from fitting was seemingly more reliable than the thicknesses of individual Al-Si-N and $\mathrm{SiN_y}$ layers. Nevertheless, the largest uncertainty could be associated to the thin $\mathrm{SiN_y}$ layers. The deposition times (shutter open in front of the target(s)[4]) corresponding to the specific thicknesses of individual layers were calculated using deposition rates calibrated on 50 nm-thick Al-Si-N and $\mathrm{SiN_y}$ layers. The 5 nm-thick Al-Si-N layers were deposited within about 60 s. As for the $\mathrm{SiN_y}$ layers deposited with a thickness from 0.25 nm up to 2 nm, the shortest deposition time used (corresponding to 0.25 nm) was about 17 s. For such a small deposition time, the mean deposition rate was obviously slightly smaller than the calibrated one. This may be related to a non-negligible influence of the opening and closing time of the shutters between each new layer and to the transient changes induced each time in the plasma. As a consequence, the thickness uncertainty of the thinnest layer (0.25 nm of $\mathrm{SiN_y}$) was estimated here to about 10% of the targeted layer thickness. This uncertainty however quickly decreases to a few percents ($< 5\%$) when the $\mathrm{SiN_y}$ layer thickness exceeds about 1 nm. The knowledge of this uncertainty is important for the interpretation of high-resolution TEM images, as reported later in Chapter 6.

High angle XRD Further X-ray investigations on the multilayer samples deposited on silicon were performed in the "high angle" configuration, that is a θ-2θ configuration with $2\theta \geq 15°$. Similar to the case of nanocomposite coatings reported in the previous chapter, the samples were found to be 002-textured with the crystalline structure of w-AlN. Only the 002 diffraction peak was observed in the measured diffractograms, except those originating from the substrate. In addition, satellite peaks surrounding the 002 diffraction peak were observed that arise from the multilayer structure, as shown in Figure 6.3. The existence of these peaks, called Laue oscillations, reveals that interfaces are well-defined. This was the case for all the multilayer coatings, including those deposited with the smallest $\mathrm{SiN_y}$ layer thickness, in agreement with the XRR observations reported above.

The position of the m^{th} order satellite peak is given by the following

---

[4] Note that the plasma was always "on" on both Al and Si targets during the deposition of multilayers, no matter if the shutters were closed or opened. In the case of Al-Si-N/$\mathrm{SiN_y}$ coatings – in contrast to AlN/$\mathrm{SiN_y}$ coatings – the power applied to the Si target was varied, shutter closed, between the deposition of two successive layers of Al-Si-N and $\mathrm{SiN_y}$.

modified Bragg's law [Yash 99]:

$$\Lambda = \pm \frac{m\lambda}{2(\sin\theta_{\pm} - \sin\theta_B)} \tag{6.1}$$

with Λ being the bilayer period, $\theta_{\pm}$ and θ_B the angular position of the satellite peak and the Bragg diffraction peak respectively, and λ the X-ray wavelength.

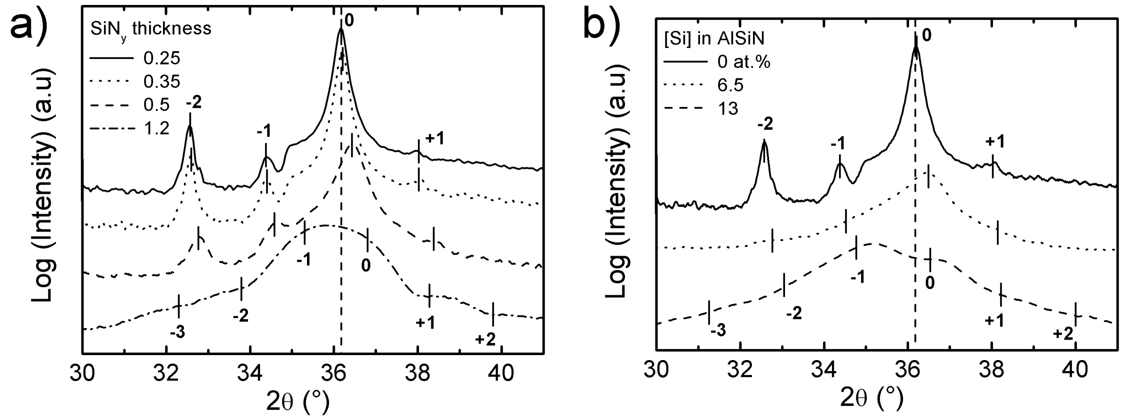

Figure 6.3: High angle XRD curves measured on multilayers of series D, E and F - zoom on the AlN (002) diffraction peak region. (a) AlN/SiN$_y$ series (series D) for different SiN$_y$ layer thickness. (b) Al-Si-N/SiN$_y$ series (series D, E and F) for a constant SiN$_y$ layer thickness of 0.35 nm. For each curve, the estimated position of the satellite peaks is indicated.

In Figure 6.3, the position of each satellite was first guessed by a visual inspection of the curves and then refined using the above equation and the bilayer thickness determined from XRR measurements. No simulations of a model system were performed to be compared to the measured diffraction pattern. The reason for this is that the measurements were done using a non-monochromatic X-ray beam. Moreover the studied samples were polycrystalline, i.e. far away from the ideal epitaxially grown single-crystalline structure assumed in simulations. As a result, the intensity of the 002 (zero order) Bragg peak quickly decreases[5] and the peak broadens with increasing thickness of the SiN$_y$ layer at constant Al-Si-N layer composition (Fig. 6.3a), and with increasing Si content in Al-Si-N at constant SiN$_y$ layer thickness (Fig. 6.3b). Hence only few satellites can be observed before they are hidden in the background.

---

[5] Note the logarithmic scale for the intensity in Fig. 6.3.

In AlN/SiN$_y$ multilayer coatings (Fig. 6.3a), the remarkable broadening of the the 002 diffraction peak observed above 0.5 nm SiN$_y$ layer thickness may be related to a progressive loss of crystalline order in the AlN layers, i.e. a significant decrease of the crystallite size in the direction normal to the film plane and an increase of the misorientation of crystallites (as revealed by rocking curve measurements, not shown here). A limited amount of satellite broadening, expected to be more or less constant for all samples, can also arise from small thickness fluctuations (i.e. interfacial roughness) of individual layers [Yash 98]. The first hypothesis of a loss of crystalline order in AlN layers is in agreement with the results reported later here on the mean crystallite size and on the residual stress measured in the films. These results suggest an epitaxial stabilization of SiN$_y$ layers thinner than 0.5 nm. Such an epitaxial growth in AlN/SiN$_y$ multilayers implies that crystallites can space over several bilayers, exceeding the thickness of a single AlN layer. The progressive broadening and disappearance of the satellite peaks seen in Figure 6.3a may thus indicate a transition in the SiN$_y$ layer from a crystalline to an amorphous structure above 0.5 nm SiN$_y$ layer thickness, that induces a loss of mutual orientation between successive AlN layers. This phenomenon was mentioned by Kim *et al.* [Kim 01] and Söderberg *et al.* [Sode 07b] in the case of AlN/TiN and TiN/SiN$_x$ superlattices respectively.

As mentioned before, no simulation was performed, so that the origin of the shift toward higher diffraction angles of the zero order Bragg peak, seen in Figure 6.3a, could not be identified. It is *a priori* not associated to the existence of alternative strain fields at the interfaces since the SiN$_y$ layer is expected to grow amorphous at 200°C deposition temperature. However, the indications of a partial epitaxial stabilization of the SiN$_y$ layers mentioned above suggest that coherency strains may actually be present in AlN layers, which could correspond to a contraction of the interatomic distances and hence explain the shift observed in Figure 6.3a.

Figure 6.3b presents three diffractograms measured on Al-Si-N/SiN$_y$ multilayer coatings with a constant SiN$_y$ thickness and an increasing Si content in Al-Si-N. The broadening and decrease in intensity of all the peaks (Bragg peak and satellites) can be explained by a loss of crystalline order in the Al-Si-N layers with increasing Si content. This means a decrease of the mean crystallite size and an increase of the misorientation between crystallites, as known from three-dimensional nanocomposite coatings. The constant shift of the zero-order peak toward higher diffraction angles in Al-Si-N/SiN$_y$ multilayers with Si content of 6.5 at.% and 13 at.% in Al-Si-N is related to the decrease of the average bond length in the $Al_{0.44}Si_{0.06}N_{0.5}$ solid solution expected to form. As for the Al-Si-N/SiN$_y$ multilayers with 13 at.% of Si in Al-Si-N, the existence of an additional XRD peak a low diffraction angle (around 34–35°), as found in Al-Si-N two-phase nanocomposite coatings and associated to the grain boundaries (Fig. 5.20, p. 116), may explain the relative increase of the -1 order satellite peak as compared to the zero-order one.

X-ray investigations on the multilayer samples of series D, E and F show that the multilayer structure is well enough defined (i.e. limited interface roughness and no material mixing at the interface) so that superlattice peaks can be observed in both XRR and high-angle XRD diffractograms. The multilayers are 002-textured, with a crystalline quality (crystallite size and mutual orientation) decreasing with increasing the Si content in the Al-Si-N layers and/or increasing the SiN$_y$ layer thickness.

TEM investigations To obtain further insight into the microstructure of these polycrystalline multilayer coatings, cross-section specimens were observed by TEM. The coatings studied here were deposited on tungsten carbide which is much easier to prepare TEM lamellae from than if silicon was used as substrate material. X-ray investigations on nanocomposite coatings deposited on WC-Co and Si (001) showed that the obtained microstructure was the same, except for a slightly larger angular distribution of the 002-oriented crystallites in the case of WC-Co, related to the larger surface roughness of these substrates. The crystalline quality of multilayers deposited on WC-Co should be hence identical to the one of multilayers deposited on Si, except for a rougher interface between the layers.

TEM micrographs taken on four different multilayer coatings are presented in Figure 6.4. In (a) and (b) pictures of AlN/SiN$_y$ multilayer coatings (series D) with 0.35 and 1.2 nm SiN$_y$ layer thickness respectively are shown. In (c) and (d) similar pictures (same SiN$_y$ thicknesses) of Al-Si-N/SiN$_y$ multilayer coatings with 6.5 at.% of Si in Al-Si-N (series E) are presented. For each sample, bright-field (BF) and dark-field (DF) views of (different) regions of 150 nm × 150 nm size are shown, together with an electron diffraction pattern. The most striking feature of these TEM pictures is the apparent absence of multilayer structure for coatings with a 0.35 nm SiN$_y$ layer thickness. Instead, the growth is clearly columnar and the narrow columns propagate through the multilayer structure. In the AlN/SiN$_y$ multilayer shown in (a), the columns have a diameter of 20–40 nm, that is slightly smaller than in pure AlN, where the diameter of columns was found to be 30–60 nm, as reported in the previous chapter. From the DF image, it appears that the columns

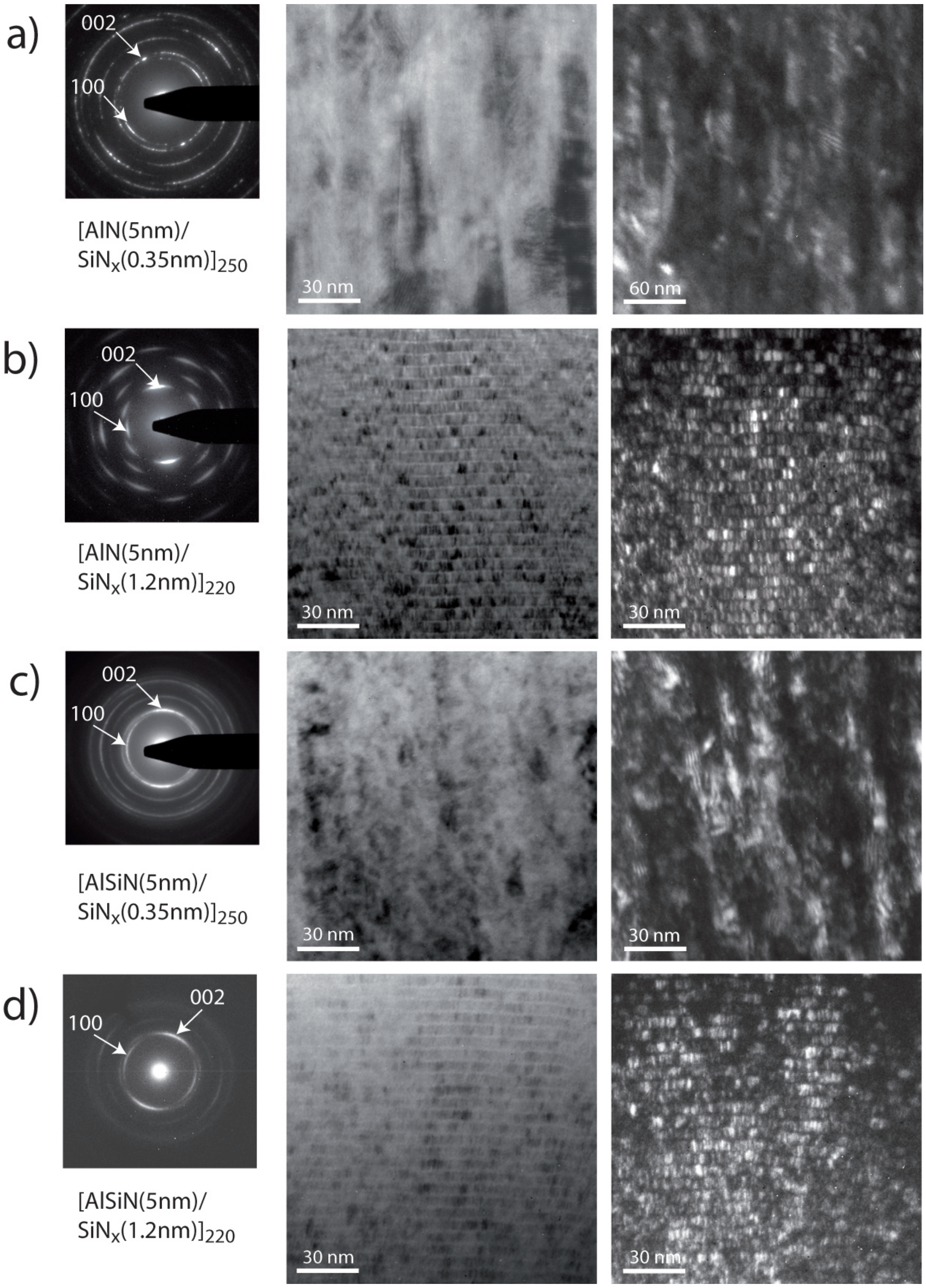

Figure 6.4: Cross-sectional TEM micrographs taken on AlN/SiN$_y$ *(a,b) and Al-Si-N/SiN*$_y$ *(c,d) multilayer coatings of series D and E, respectively, deposited on WC-Co substrates. For each sample, a bright field (BF) image (center), a (002) dark field (DF) image (right) and an electron diffraction (ED) pattern (left) are shown. The growth direction is from bottom to top. In (a), note the different scales used for BF and DF pictures. Miller indices are used in ED ring patterns.*

are composed of regions of similar crystallographic orientation with only little misorientation between each other, as revealed by the overall weak contrast of the picture. The structure is moreover dense. The electron diffraction pattern nevertheless indicates that the observed region is nanocrystalline, with not only a strong 002-texture, but also many crystallites oriented quite randomly in the film. In XRD θ-2θ diffractograms, no diffraction peak was observed in addition to the strong 002 and 004-peaks of w-AlN. These small crystallites are probably so small and randomly oriented that the corresponding X-ray diffraction signal was hidden by the background of the 002 diffraction peak. As the SiN$_y$ layer thickness is increased to 1.2 nm, the multilayer structure is then clearly seen in both the DF and BF pictures in (b). The growth of AlN crystallites is interrupted by the SiN$_y$ layer so that re-nucleation is forced after each silicon nitride layer and the columnar structure is no longer observed. The 002-texture is nevertheless retained. In each AlN layer, elongated zones of similar crystallographic orientation are seen on the DF image, with a lateral (in sample plane) extension of about 2–3 nm only, and a length equal to the layer thickness, that is 5 nm. The Al-Si-N/SiN$_y$ coating with 0.35 nm SiN$_y$ layer thickness presented in (c) shows a structure quite similar to its AlN/SiN$_y$ counterpart in (a). The multilayer structure is not apparent. The DF image in (c) shows small coherent areas elongated in the growth direction, but the columnar microstructure is essentially removed. The domains of similar crystallographic orientation are much smaller, in particular in the growth direction, than what is seen in (a), and column boundaries cannot be defined anymore. This is a consequence of the lower crystalline quality of the Al-Si-N layers with a silicon concentration at the solubility limit of Si in w-AlN. The observed microstructure recalls that of Al-Si-N nanocomposite layers with a silicon concentration above the solubility limit. The associated electron diffraction pattern is a ring pattern, indicating a nanocrystalline structure with quasi-randomly oriented grains. As in (a), a 002-texture is observed, with however a larger angular distribution. As the SiN$_y$ layer thickness is increased to 1.2 nm, the multilayer stacking becomes apparent, as shown in (d). The length of crystalline domains is limited to the layer thickness, as for the AlN/SiN$_y$ multilayer coating shown in (b). A similar decrease of crystalline quality is observed between the samples presented in (b) and (d), as the one described above for the samples shown in (a) and (c).

Mean crystallite size Additional information on the growth behavior in Al-Si-N/SiN$_y$ multilayer coatings was deduced from the evolution of the mean crystallite size (XRD, TEM), and from the close observation of interfaces using high-resolution TEM.

The mean crystallite size, or coherency length of domains of similar crystallographic orientation, was calculated using the Scherrer formula with the integral breadth of the 002 Al-Si-N diffraction peak and K=1. This calculation was done whenever the breadth of the zero order peak alone could be determined without any contribution from a Laue oscillation. For a SiN_y layer thickness exceeding 0.5 nm, this was not possible. However, from TEM observations the mean crystallite size in growth direction is found to be equal to the Al-Si-N layer thickness, i.e. 5 nm, for multilayer coatings with a SiN_y layer thickness larger than $\sim$ 1 nm. The obtained values of mean crystallite size are reported in Figure 6.5.

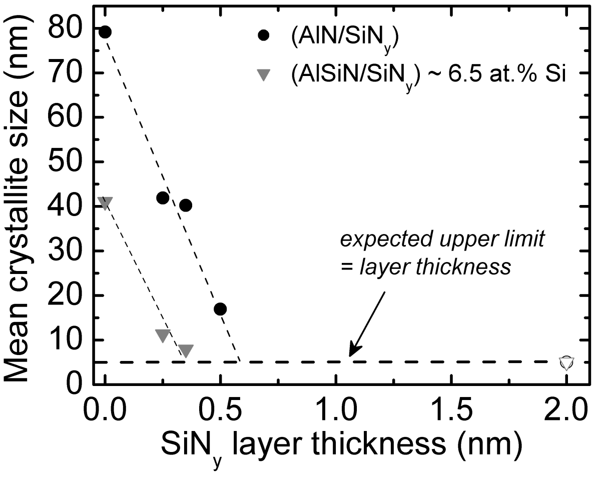

Figure 6.5: Evolution of the mean crystallite size in AlN/SiN_y and Al-Si-N/SiN_y multilayer coatings of series D and E, respectively. The data given with solid symbols corresponds to the coherency length calculated as described in the text. The open symbols, at a SiN_y of 2 nm, correspond to values deduced from TEM observations. Lines are a guide to the eye only.

It appears that the crystallite size largely exceeds the expected upper limit of 5 nm, which corresponds to the Al-Si-N layer thickness. In AlN/SiN_y multilayers with 0.25 and 0.35 nm SiN_y layer thickness, the mean crystallite size amounts to as much as 40 nm, which is less than in pure AlN (80 nm), but eight times larger than the AlN layer thickness. In Al-Si-N/SiN_y multilayers with 0.25 nm SiN_y layer thickness, the crystallite size is also found to be larger than expected, however "only" by a factor of two (i.e. 10 nm), as a consequence of the lower crystallinity of the Al-Si-N layer as compared to pure AlN. Moreover the mean crystallite rapidly decreases as the SiN_y layer thickness is increased. The threshold of 5 nm is reached at about 0.6 nm of SiN_y in AlN/SiN_y multilayers (series D) and 0.3 nm in Al-Si-N/SiN_y multilayers (series E). Note here that the multilayer coatings were deposited at a substrate temperature of only 200°C, temperature at which the silicon nitride layers are expected to be amorphous. However, the strong coherency in the crystalline orientation of AlN and Al-Si-N layers separated by a silicon nitride layer in nanometer-sized multilayer structures suggests the existence of an – at least partial – epitaxial ordering of the silicon nitride layer induced by the underlaying crystalline Al-Si-N material.

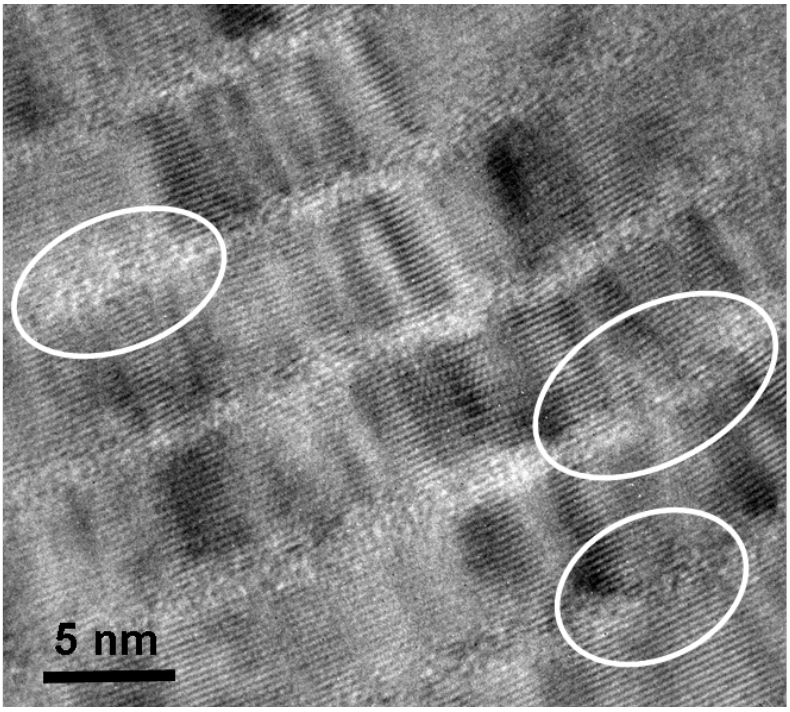

Figure 6.6: HRTEM image of a [AlN(2 nm)/ SiN$_y$(1.2 nm)]$_{220}$ multilayer coating of series D deposited on WC-Co. Several zones are encircled where partial ordering between two AlN layers all the way across the SiN$_y$ layer is seen. The growth direction is here from the bottom right to the top left of the picture. The corrugation of interfaces is caused by the roughness of the WC-Co substrate.

In order to check the existence of such a stabilization of the silicon nitride layer in a crystalline form, the coatings were observed by high-resolution TEM. For coatings with a small (≤ 0.35 nm) SiN$_y$ layer thickness[6], the multilayer structure could not be observed. This is easily understandable considering that the chemical contrast between Al and Si atoms in TEM images is weak. In contrast, the existence of a local disorder in thicker silicon nitride layers easily reveal the position of the layers and thus the multilayer structure. A high-resolutionTEM picture taken on an AlN/SiN$_y$ multilayer

---

[6] No TEM investigations were performed on multilayer structures with a silicon nitride layer thickness of 0.5 and 0.7 nm.

coating with a SiN_y thickness of 1.2 nm is shown in Figure 6.6. In this picture, the atomic arrangement in silicon nitride layers appears quite disordered. Several zones of partial ordering across the silicon nitride layers can nevertheless be identified[7], thereby supporting the previous guess of an epitaxial stabilization phenomenon. However since the observed interfaces are rough and the samples polycrystalline, these interfaces could not be aligned with the electron beam to be investigated in more details. As a consequence the thickness of amorphous SiN_y cannot be measured accurately enough to be compared to the total SiN_y layer thickness, so as to conclude on a possible mixed crystalline/amorphous growth mode of the silicon nitride, as reported for TiN/SiN_x superlattices by Hultman *et al.* [Hult 07]. Due to the substrate roughness and the possible misorientation of the observed TEM specimen, regions of crystalline Al-Si-N layers may superimpose with regions of pure silicon nitride over the total specimen thickness, potentially inducing errors of interpretation of the pictures. To overcome this difficulty, well ordered structured are needed in which the first AlN layer is epitaxially grown on a single crystalline substrate with a smooth surface. The growth of a multilayer structure on such an epitaxial AlN layer should result in the formation of flat interfaces. These interfaces could then be oriented in the TEM instrument by aligning a well chosen crystallographic direction (*zone axis*[8]) of the substrate with the direction of the electron beam. Such an experiment is presented in subsection 6.3.2 below.

b) Mechanical properties

The hardness of Al-Si-N/SiN_y multilayer films deposited on silicon was studied by nanoindentation testing. The results of these investigations are reported in Figure 6.7a. In this figure, a weak hardness maximum is observed for series D (AlN/SiN_y multilayers) and E (Al-Si-N/SiN_y multilayers with 6.5 at.% of Si in Al-Si-N) at 0.35 nm SiN_y layer thickness, which corresponds to about 1.25 monolayers of silicon nitride. This hardness maximum amounts

---

[7] Note that when a TEM instrument equipped with a field emission gun (FEG) is used, edges effects can produce interference lines, in HRTEM pictures, that are not related to crystallographic planes. This is a result of the coherency of the electron beam. However, the TEM instrument used in this work was a Philips CM30 instrument equipped with a LaB_6 source, for which such a problem cannot be encountered. Interference lines in all the HRTEM pictures presented here therefore correspond to crystallographic planes.

[8] A prism of $(h_i\ k_i\ l_i)$ planes that intersect in a common $[u\ v\ w]$ direction is known as a *zone of planes*. The common axis is called the *zone axis*. All the $(h_i\ k_i\ l_i)$ planes that verify the equation $hu + ku + lw = 0$ are parallel to this axis, i.e. belong to the $[u\ v\ w]$ zone. Single crystalline specimens observed by TEM are aligned along a zone axis, i.e. a direction of high symmetry of the crystal, to facilitate their study.

to 29 GPa for series D and 33 GPa for series E. The latter coatings have a mean crystallite size of 7–8 nm in the growth direction, according to Figure 6.5. In the case of Al-Si-N nanocomposite coatings, a hardness maximum of 32 GPa (Fig. 5.19 p. 114) is observed at about 10 at.% of Si. At this composition, the coatings are nanocrystalline and consist of two distinct material phases. Al-Si-N crystalline grains of about 10 nm in the growth direction (Fig. 5.25 p. 125) are surrounded by a thin silicon nitride interlayer of about one monolayer (Fig. 5.36 p. 148). Hence the hardness enhancement achieved in 3D nanocomposite is reproduced in multilayer structures for similar structural dimensions, that is grain size and silicon nitride thickness. In the case of series F (Al-Si-N/SiN_y multilayers with 13 at.% of Si in Al-Si-N), no hardness enhancement is observed when varying the SiN_y layer thickness. This is related to the two-phase structure of the Al-Si-N layers, the microstructure of which is not influenced by the introduction of silicon nitride interlayers. The obtained hardness seems to follow a rule of mixture and decreases continuously towards the hardness of pure SiN_y ($\sim$ 20 GPa) with increasing the SiN_y thickness.

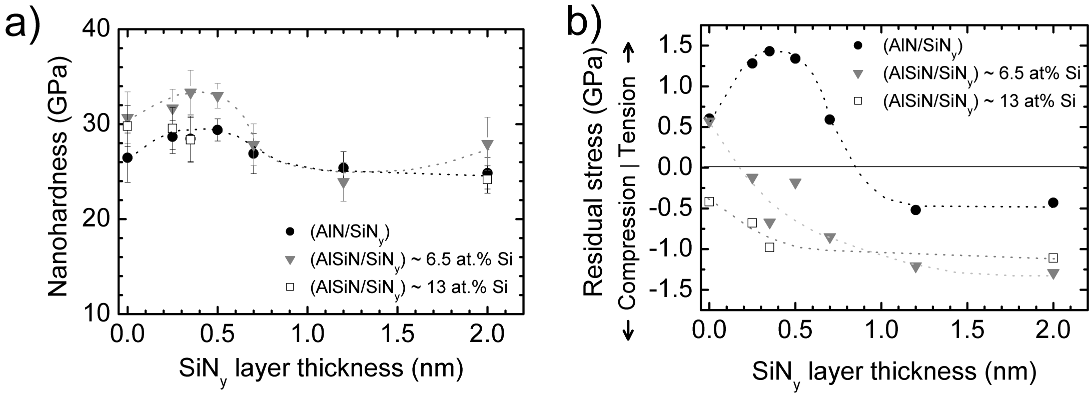

Figure 6.7: Evolution of (a) the hardness and (b) the biaxial residual stress of Al-Si-N/SiN_y multilayer films deposited on silicon (series D, E and F), as a function of the SiN_y layer thickness. Hardness values were determined from nanoindentation tests at 2 mN load. The residual stress in the films was deduced from the bending of the Si substrate, measured by mechanical profilometry. Dotted lines are given as a guide to the eye.

To better understand the evolution of the hardness of multilayer coatings, their residual biaxial stress was calculated from the bending of Si substrates. Two distinct behaviors are seen in Figure 6.7b. AlN/SiN_y multilayer films are first in tension for the smallest SiN_y layer thickness ($\leq$ 0.5 nm) and cracks were observed in these coatings. The maximum tensile stress amounts to 1.5 GPa – this is however a value of residual stress after relaxation of part of the stress by a coating failure (cracks). Above 0.5 nm of SiN_y layer thickness, no cracks are anymore observed in the coatings, the tensile stress quickly decreases and changes to a compressive stress. It levels off at −0.5 GPa for a SiN_y layer thickness larger than about 1 nm. In contrast, the Al-Si-N/SiN_y multilayer coatings of series E and F show a continuous evolution. From a small tensile stress (0.5 GPa) for series E and a small compressive stress (−0.5 GPa) for series F at zero silicon nitride layer thickness, the stress evolves into a larger but still moderate compressive stress of about −1 GPa, being roughly constant above 1 nm silicon nitride thickness. No cracks were observed in any of the coatings of series E and F.

The high tensile stress built in the AlN/SiN_y may be accounted for by the contribution of coherency strains due to a lattice mismatch between AlN and SiN_y when the silicon nitride is epitaxially stabilized in a crystalline form. Since the Si–N bond length (1.732 Å in average in β-Si_3N_4 [Grun 79]) is shorter than the Al–N bond length (1.8672 Å, JCPDS-ICDD card # 25-1133), the AlN layers are presumably forced to contract at the interfaces with silicon nitride. Since AlN accounts for more than 90% of the material, (5 nm AlN vs. 0.5 nm SiN_y), this leads to a global tensile stress of the multilayer structure. As the silicon nitride layer thickness is increased, the ordering forced in SiN_y by the interface with AlN collapses when the distance (thickness) from the stabilizing interface exceeds 0.6 nm (2 ML). Since there is no coherency strain at the interface formed by AlN growing on amorphous SiN_y, the total amount of coherency strains is decreased. The compressive stress state found in multilayer structures with a SiN_y layer thickness larger than 1 nm reflects the compressive state commonly found in sputtered dense thin films. In the case of Al-Si-N/SiN_y multilayer coatings, the mean crystallite size is of the order of the Al-Si-N layer thickness. Moreover the angular distribution of the crystalline orientations is much larger than in pure AlN, which means that the Al-Si-N layers show some disorder. As a consequence, the introduction of a silicon nitride layer every 5 nm does not influence much the global stress state. The increase of the compressive stress as the silicon nitride layer thickness is increased can be explained in the same way as in the case of AlN/SiN_y multilayer coatings.

When comparing the evolution of the hardness and of the residual biaxial stress state of the multilayers, it first appears that the hardness maximum cannot be explained by a large compressive stress in the layers (e.g. due to ion bombardment). Instead, the hardness evolution is related to size effects in the films: for small SiN_y thicknesses (say < 0.5 nm), the length of the crystallites largely exceeds the individual layer thickness and a dislocation activity may exist in such large crystalline domains. In contrast, at larger SiN$_y$ thicknesses the crystallite size is small enough so that the dislocation activity within each crystallite is suppressed. However, the crystalline order of the "thick" SiN$_y$ layers is simultaneously lost. This may result e.g in a lower interface cohesion energy and in turn in a lower resistance to plastic deformation. The hardness maximum observed at 0.35 nm of SiN$_y$ may hence results from the balance of these two deformation mechanisms at lower and higher silicon nitride thicknesses. In addition, the larger hardness values achieved in Al-Si-N/SiN$_y$ multilayer coatings of series E may be due to a better balance of the stress state.

6.3.2 Multilayers on sapphire

The necessity of carrying out experiments on well ordered multilayer structures was mentioned before. These structures should have flat interfaces that could be aligned in the TEM to be observed along an in-plane direction, thereby avoiding artifacts related to the thickness of the TEM specimen. For this purpose, AlN/SiN$_y$ multilayer structures were grown on α-Al$_2$O$_3$ (0001) (sapphire) substrates. In this section, the epitaxial growth of the aluminum nitride on sapphire is presented first. The observation of AlN/SiN$_y$ multilayer structures by high-resolution TEM is then reported. The emphasis is on the study of the growth mode of a thin silicon nitride layer ($\leq$ 2 nm) on top of a single crystalline aluminum nitride surface, as well as on the evolution of the film microstructure as several bilayer periods are deposited on each other.

a) AlN growth on sapphire

Both aluminum nitride and sapphire have an hexagonal structure. They belong to the P6$_3$mc and the R-3c space groups, respectively. The lattice parameters of AlN are a = 3.111 Å and c = 4.979 Å (JCPDS-ICDD card #25-1133), those of sapphire are a = 4.759 Å and c = 12.993 Å (JCPDS-ICDD card #46-1212). In this work, AlN was reactively sputter deposited on sapphire at a substrate temperature of 200°C. From XRD (θ-2θ scans, φ scans and pole figures) and TEM (electron diffraction) observations, a single-crystalline epitaxial AlN (0001) layer was obtained[9]. The epitaxial

---

[9] In the following section and when dealing with TEM data, crystallographic notations are given using the Miller-Bravais notation (i.e. four-axis hexagonal indexing) since this is the notation used by the scientific community in the field of transmission electron microscopy. This notation differs from the Miller notation (three-axis indexing) commonly used in X-ray techniques, in particular for the indexing of crystallographic directions. A brief comparison of the Miller and the Miller-Bravais axial systems is reported in Appendix

relationship with sapphire is: $(0001)_{\mathrm{AlN}} \| (0001)_{\mathrm{sap}}$, $[10\bar{1}0]_{\mathrm{AlN}} \| [11\bar{2}0]_{\mathrm{sap}}$. This corresponds to a 30° rotation of the AlN unit lattice with respect to the substrate in the basal plane (i.e the plane perpendicular to the c axis); the c-axes of AlN and sapphire coincide. This can be visualized in Figure 6.8, where XRD φ scans on (101) planes of AlN and (104) planes of Al_2O_3 are shown. If the unit lattices of the two crystals were aligned, the diffraction peaks should be recorded at the same angular position. Here, a shift of 30° is observed. The occurrence of six peaks for AlN and three for Al_2O_3 is explained by the three-fold symmetry of both crystals along the [001] direction, and by the frequent twinning[10] in the thick ~ 1 µm AlN layer studied here.

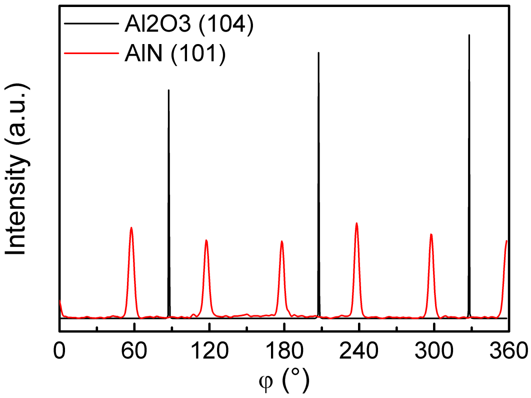

Figure 6.8: XRD φ scans measured on a AlN/α-Al_2O_3 (0001) sample. The ~ 1 µm thick AlN layer was grown in conditions similar to the samples of series G and H, and showed a strong 002 texture. The φ scans reported here correspond hence to rotations about the c-axis both in AlN and Al_2O_3. The curves were recorded on AlN (101) planes at $\chi = 61.6°$ and Al_2O_3 (104) planes at $\chi = 38.24°$. A 30° in-plane rotation of the AlN unit lattice with respect to the substrate is observed.

The orientation relationship between the AlN layer and the α-Al_2O_3 (0001) surface is controlled by matching Al and O sublattices at the interface, as illustrated in Figure 6.9. In this configuration, the lattice mismatch[11] between AlN and sapphire along a direction perpendicular to the c-axis is about 13.2%. As a consequence, geometrical misfit dislocation are formed to accommodate the mismatch. For the present epitaxial relationship, a full relaxation is obtained for an average number of planes between two dislocations of 8.1 [Venn 06]. A HRTEM cross-section image of the interface between AlN and Al_2O_3 is shown in Figure 6.10a. Figure 6.10c is a Fourier filtered image corresponding to planes perpendicular to the interface. The position of geometrical misfit dislocations is indicated with red arrows. The distance between additional planes is around 8 AlN planes, which corresponds to the predicted number of planes for full relaxation of the lattice mismatch.

D. An introduction to the interpretation of transmission electron micrographs of materials

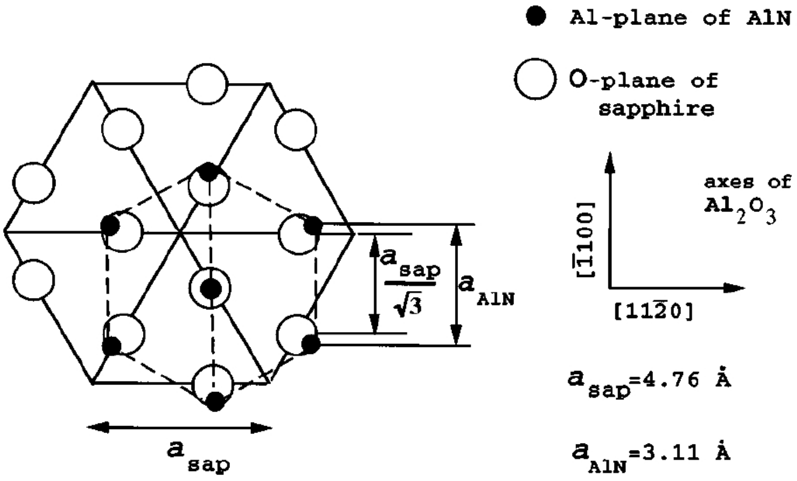

Figure 6.9: Schematic representation of the in-plane atomic arrangement of the Al and O sublattices of AlN and Al_2O_3 respectively, in the case of AlN (0001) grown on sapphire (0001) [Dovi 96].

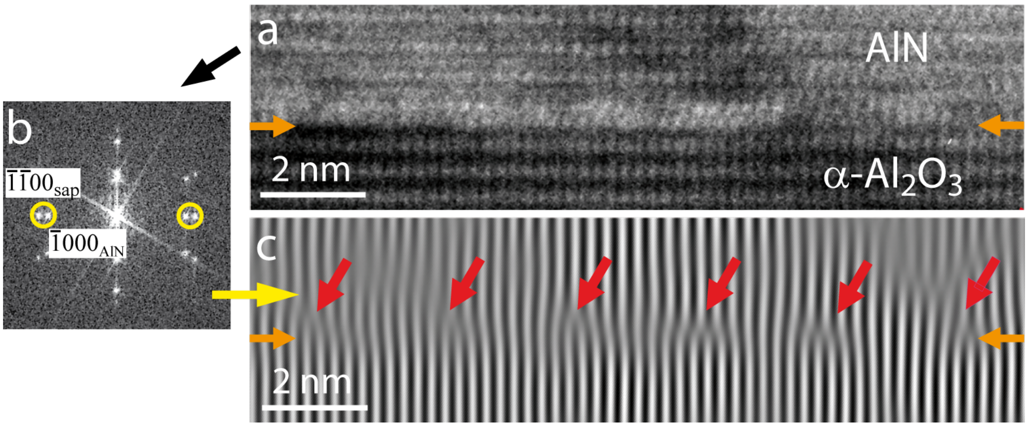

Figure 6.10: TEM investigations of the AlN (0001)/Al_2O_3 (0001) interface region. A high-resolution image along the $[1\bar{1}00]_{sap}$ zone axis is given in (a), together with a FFT diagram of the region. (c) is an inverse Fourier transform image of the image in (a) using $(\bar{1}000)_{AlN}$ and $(\bar{1}\bar{1}00)_{sap}$ diffraction spots (yellow). Orange arrows indicate the position of the interface. Red arrows point at geometrical misfit dislocations.

---

with hexagonal crystal structure is given in [Edin 75].

[10] i.e. stacking faults in the growth directions corresponding to a rotation of the crystal by 180° about the c axis.

[11] defined as $(d_{\mathrm{AlN}} - d_{\mathrm{sapphire}})/d_{\mathrm{sapphire}}$

b) AlN/SiN$_y$ multilayers grown on sapphire

AlN/SiN$_y$ multilayers were grown on the single crystalline AlN (0001) layer described above and investigated by HR-TEM. First, the cross-section of a multilayer structure composed of "thick" (20 nm) layers of AlN and SiN$_y$ was investigated, as shown in Figure 6.11.

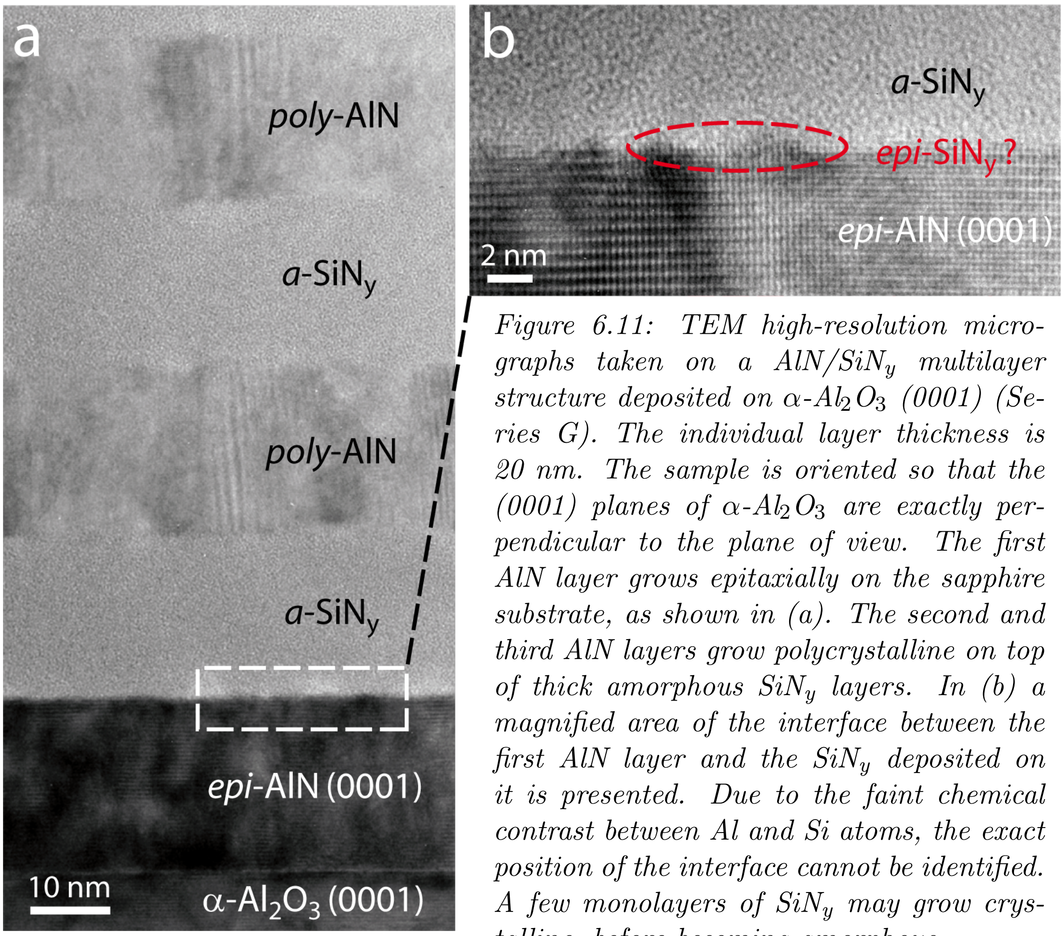

Figure 6.11: TEM high-resolution micrographs taken on a AlN/SiN$_y$ multilayer structure deposited on α-Al$_2$O$_3$ (0001) (Series G). The individual layer thickness is 20 nm. The sample is oriented so that the (0001) planes of α-Al$_2$O$_3$ are exactly perpendicular to the plane of view. The first AlN layer grows epitaxially on the sapphire substrate, as shown in (a). The second and third AlN layers grow polycrystalline on top of thick amorphous SiN$_y$ layers. In (b) a magnified area of the interface between the first AlN layer and the SiN$_y$ deposited on it is presented. Due to the faint chemical contrast between Al and Si atoms, the exact position of the interface cannot be identified. A few monolayers of SiN$_y$ may grow crystalline, before becoming amorphous.

In (a), an overview the first three bilayer periods is presented. It turns out that the first AlN layer grows epitaxially on sapphire, whereas the next AlN layers grow polycrystalline on top of amorphous silicon nitride. A closer view on the first AlN(0001)/SiN$_y$ interface is shown in (b). The transition from the crystalline AlN layer, in which single crystallographic planes can be seen, to the amorphous SiN$_y$, in which no crystalline order is observed, appears to be gradual. However, in absence of a sufficient Z contrast (atomic number) in TEM images, the exact position of the interface cannot be identified. Hence there is no conclusive evidence whether the first few monolayers of silicon nitride show a crystalline order or not.

With the information that AlN grown on amorphous silicon nitride is clearly polycrystalline, multilayers with a smaller bilayer period were deposited. The AlN thickness was fixed at 10 nm so that large enough regions where available to study separately the crystallinity of each AlN layer. Multilayer films with four different SiN$_y$ layer thicknesses, namely 0.4 nm, 0.7 nm, 1.2 nm and 2 nm, were deposited. Cross-section TEM samples were prepared. They were aligned in the TEM so that the [0001] crystallographic direction of the sapphire substrate lies in the plane of view.

A first indication of an epitaxial stabilization of the silicon nitride layer is given in Figure 6.12. Two 0002 dark field images of AlN/SiN$_y$ are reported here for a silicon nitride thickness of (a) 0.4 nm and (b) 1.2 nm. For a thin SiN$_y$ interlayer (a) the growth of AlN layer is coherent over several bilayer units, as revealed by continuous variations of the contrast across the entire structure. For a thicker SiN$_y$ interlayer, abrupt variations of contrast are seen at the interfaces. The SiN$_y$ layers appear as black horizontal lines between AlN layers. The growth is stopped and nucleation is forced at the beginning of each new AlN layer. In addition the in-plane dimension of domains of similar crystallographic orientation is dramatically decreased from the first AlN layer grown on a silicon nitride layer.

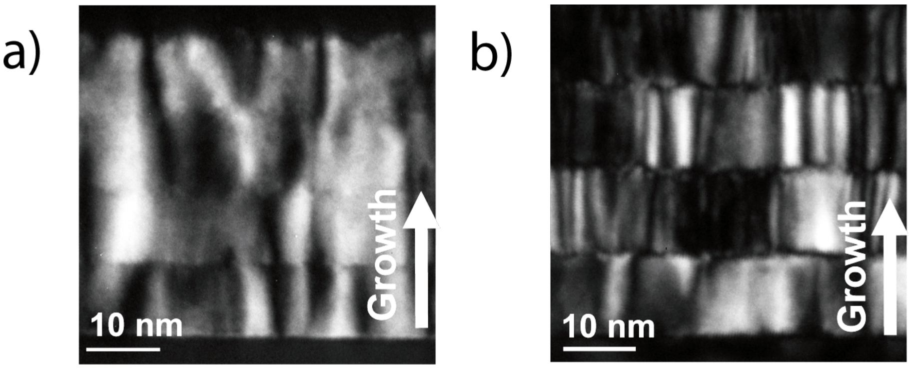

Figure 6.12: Cross-sectional TEM (0002) dark field images taken on four AlN/SiN$_y$ bilayers deposited on α-Al$_2$O$_3$ (0001) (series H – cf. Table 6.2, p. 157), with a SiN$_y$ thickness of (a) 0.4 nm and (b) 1.2 nm.

Cross-section high-resolution TEM micrographs on multilayers with 0.4 nm, 0.7 nm and 1.2 nm SiN$_y$ thickness are presented in Figure 6.13, together with indexed spot electron diffraction (ED) patterns. The orientation

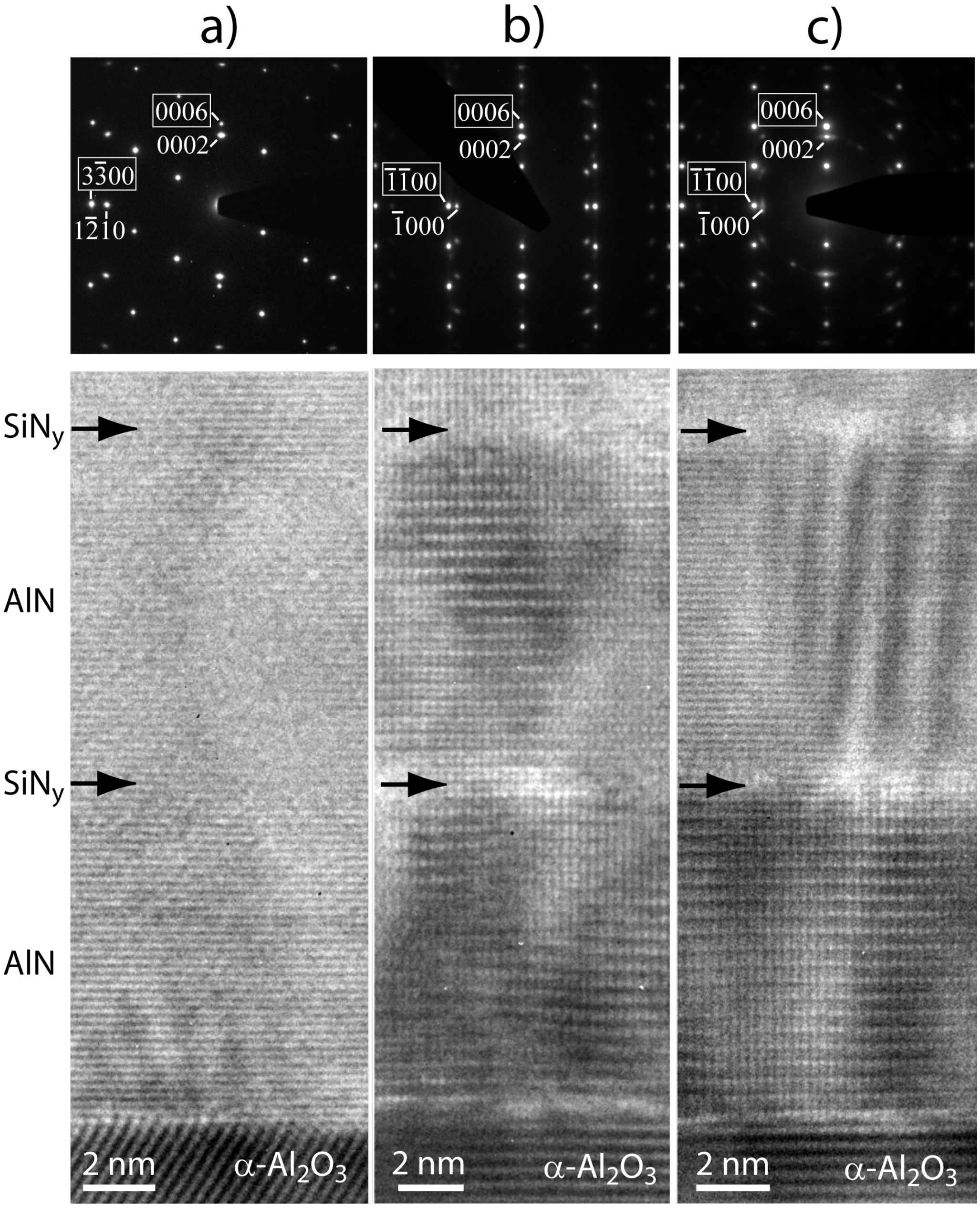

Figure 6.13: Cross-sectional HRTEM micrographs taken on AlN/SiN$_y$ multilayers deposited on α-Al$_2$O$_3$ (0001) (series H), with (a) 0.4 nm , (b) 0.7 nm and (c) 1.2 nm SiN$_y$ thicknesses. For each sample, a high-resolution picture and an electron diffraction pattern is presented. The AlN layer thickness equals 10 nm. In the diffraction images, spots coming from AlN and from the Al$_2$O$_3$ substrate are seen; framed indices correspond to sapphire. The specimens were oriented in the TEM so that the electron beam coincides with (a) the $[11\bar{2}0]_{sap}$ zone axis, (b) and (c) the $[1\bar{1}00]_{sap}$ zone axis. (These two directions of observation are perpendicular to each other, as a result of the TEM sample preparation: the samples were cut along perpendicular directions.)

relationship between each high-resolution (HR) picture and the corresponding ED pattern is preserved in this figure. For the sample with a 0.4 nm SiN_y layer thickness in (a), the multilayer structure cannot be resolved on the HR picture. Continuous lattice fringes across the successive AlN and SiN_y layers are observed, with no indication of any atomic disorder in the SiN_y layers. The spot pattern indicates that the epitaxial relationship between AlN and the sapphire substrate is retained over the entire structure. As the SiN_y layer thickness is increased, the position of the silicon nitride layers become apparent first by a small change in contrast (i.e. brighter lines) in (b) and then by a change in the crystalline orientation of the second AlN layer in (c). As for the the diffraction patterns, a small elongation of the spots is seen in (b), but the crystalline quality of the structure is not significantly altered, as confirmed by the HR picture. For the sample shown in (c), however, the spots are clearly elongated and a transition to a ring pattern for w-AlN is started. This is related to an increasing misorientation between crystallites, together with a decrease of the mean crystallite size. In the corresponding HR picture, the crystalline ordering through the silicon nitride layer is only partial. In particular the second AlN layer does not have exactly the same orientation toward the electron beam as the first epitaxial AlN layer: the lattice interference fringes are seen in only one direction instead of two. In addition, Moiré interference fringes are seen in this second AlN layer. These fringes are indicative of the superposition of several crystalline domains that have the same structure but different orientations within the thickness of the TEM specimen.

The progressive loss of crystalline ordering in the silicon nitride layers by increasing their thickness is further illustrated in Figure 6.14. In this figure, 23 nm × 8 nm cross-section HR images centered each on the first silicon nitride layer surrounded by two AlN layers are shown. The SiN_y layer thickness is (a) 0.7 nm, (b) 1.2 nm and (c) 2.0 nm. In (a) the entire SiN_y layer seemingly grows in a crystalline form (c-SiN_y), while in (c) the SiN_y grows initially crystalline (exhibiting local epitaxy with the underlying AlN layer) to a thickness of ~ 0.7 nm before it becomes amorphous (a-SiN_y)[12]. In (b), the crystalline growth is almost continuous through the 1.2 nm thick SiN_y interlayer (left side). However, partial disorder is also seen at the interface (right side). This results in a misorientation of the crystalline planes in the top AlN layer.

---

[12] The top of the SiN_y layer is defined by the first lattice fringes – i.e. atomic planes – that can be seen in the upper AlN layer.

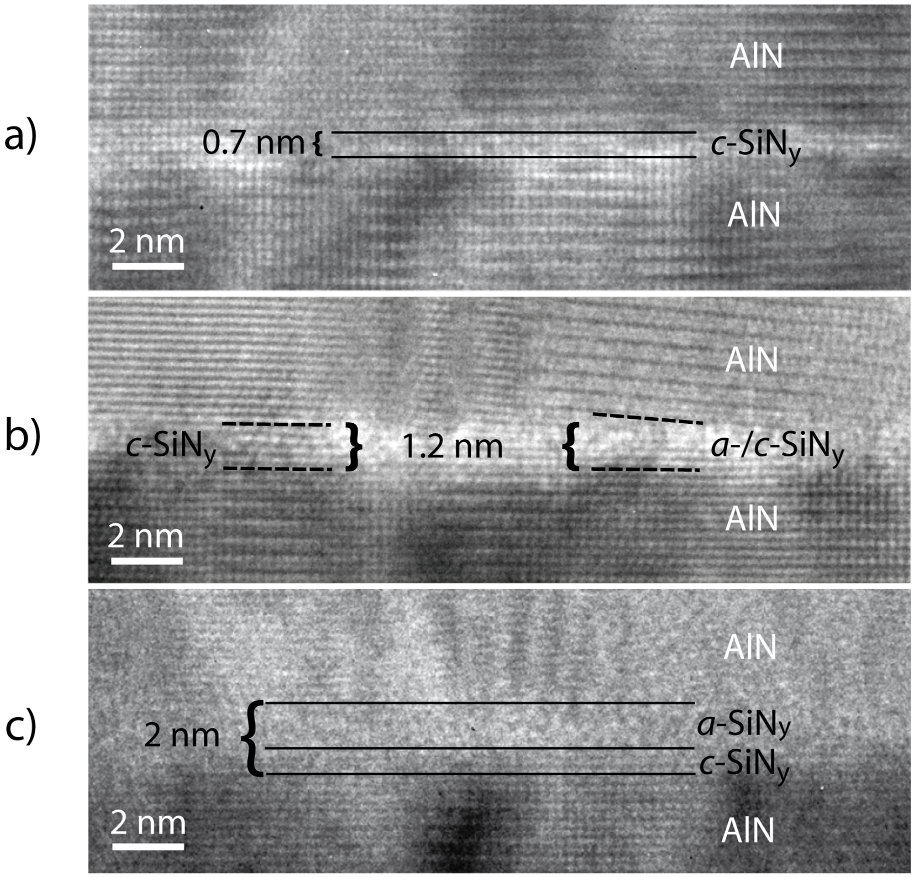

Figure 6.14: Cross-sectional HRTEM images from AlN/SiN_y multilayers grown on α-Al_2O_3 (0001) (series H), with (a) 0.7 nm, (b) 1.2 nm and (c) 2.0 nm SiN_y thickness. c- and a-SiN_y refer to crystalline and amorphous silicon nitride respectively. In each picture, the bottom layer corresponds to the epitaxial AlN (0001) layer grown on α-Al_2O_3.

6.4 Discussion on the epitaxial stabilization of $\mathrm{SiN_y}$ in Al-Si-N/$\mathrm{SiN_y}$ multilayers

6.4.1 Growth model

The study of AlN/$\mathrm{SiN_y}$ multilayers deposited on a template single-crystalline AlN (0001) layer grown on sapphire reveals that silicon nitride can be epitaxially stabilized in a crystalline form up to an epitaxial breakdown thickness $l^{\mathrm{sg}}_{\mathrm{SiN_y}}$ of about 0.7–1.0 nm ($\sim$ 2.5–3.5 ML[13]), anyway smaller

---

[13] In this work, one monolayer (ML) of silicon nitride is arbitrarily defined p. 149 as one edge of a Si-N_4 tetrahedron, that is a N–N atomic distance, i.e 2.83 Å.

than 1.2 nm (∼ 4 ML) (Figs. 6.12, 6.13, 6.14). For $l_{\mathrm{SiN_y}} > l^{\mathrm{sg}}_{\mathrm{SiN_y}}$, amorphous SiN$_\mathrm{y}$ is grown on top of crystalline SiN$_\mathrm{y}$ in a mixed growth mode (Fig. 6.14c). A similar growth behavior was reported by Söderberg *et al.* [Sode 07b] in the case of TiN/SiN$_\mathrm{x}$ superlattice structures: the stabilization of a cubic SiN phase was demonstrated up to a thickness of about 0.7 nm. In the Al-Si-N/SiN$_\mathrm{y}$ multilayers grown on Si and WC-Co presented at the beginning of this chapter, the maximum stabilization thickness of crystalline silicon nitride on top of polycrystalline Al-Si-N layers, $l^{\mathrm{pc}}_{\mathrm{SiN_y}}$, is smaller than for multilayers grown on sapphire. This is a consequence of the lower crystalline quality of the "template" first AlN layer. $l^{\mathrm{pc}}_{\mathrm{SiN_y}}$ is of the order of 0.5–0.7 nm (Figs. 6.4, 6.5, 6.6 and 6.7b).

The formation of amorphous silicon nitride above a critical layer thickness results in a loss of epitaxial orientation relationship between the first single crystalline AlN layer and the layers deposited later on silicon nitride, as seen in Figures 6.13 and 6.14. This explains that the mean crystallite size, or coherency length, deduced from XRD measurements in a direction perpendicular to the sample surface largely exceeds the thickness of the AlN layer, as shown in Fig. 6.5 p. 165. This phenomenon is illustrated in Figure 6.15 below. This figure schematically shows how the apparent AlN crystallite size ("d$_\mathrm{app}$") can be much larger than the actual size ("d$_\mathrm{real}$") of the AlN layers, due to the epitaxial stabilization of crystalline silicon nitride.

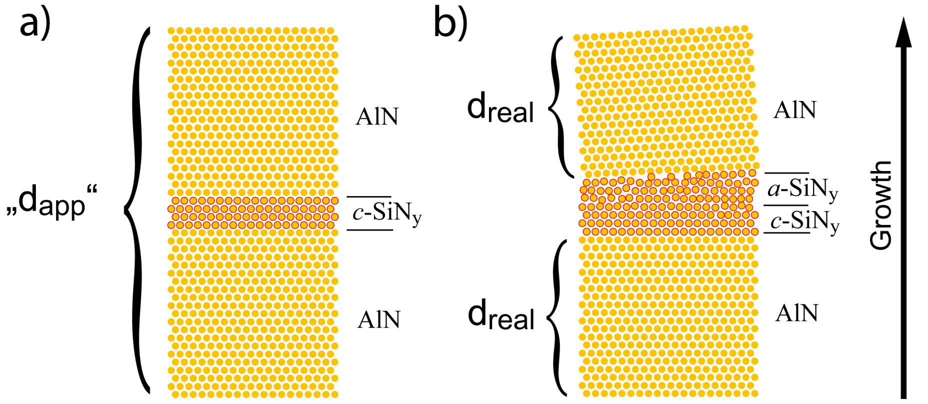

Figure 6.15: Cross-sectional schematic representation of an AlN-SiN$_y$-AlN multilayer structure. (a) Growth of crystalline SiN$_y$ (c-SiN$_y$) for a layer thickness smaller than ∼ 0.7 nm; (b) Mixed growth of a "thick" SiN$_y$ layer: a transition from crystalline to amorphous (a-SiN$_y$) growth occurs when the critical thickness of 0.7 nm is exceeded.

6.4.2 The SiN_y/AlN(0001) interface

TEM experiments reveal continuous lattice fringes across the SiN_y layers deposited on top of AlN (0001). However, the volume of the stabilized crystalline silicon nitride phase is so small that its crystallographic structure cannot be resolved experimentally neither by XRD nor by high-resolution TEM[14]. Yet hypotheses can be formulated that are based on the observation of the crystalline lattices of AlN and SiN_y stable forms at atmospheric pressure and ambient temperature, i.e. wurtzite AlN and β-Si_3N_4. Additional insight into the atomic structure of the SiN_y/AlN(0001) interface can be provided by *ab initio* DFT calculations to determine minimum energy configurations as a function of the SiN_y layer thickness.

Wurtzite AlN and β-Si_3N_4 both have an hexagonal structure. They belong however to different space groups, namely $P6_3mc$ and $P6_3$ respectively. Perspective views of their unit cells along the [0001] direction are shown in Figure 6.16. Further crystallographic data and lattice representations can be found in Appendix A.

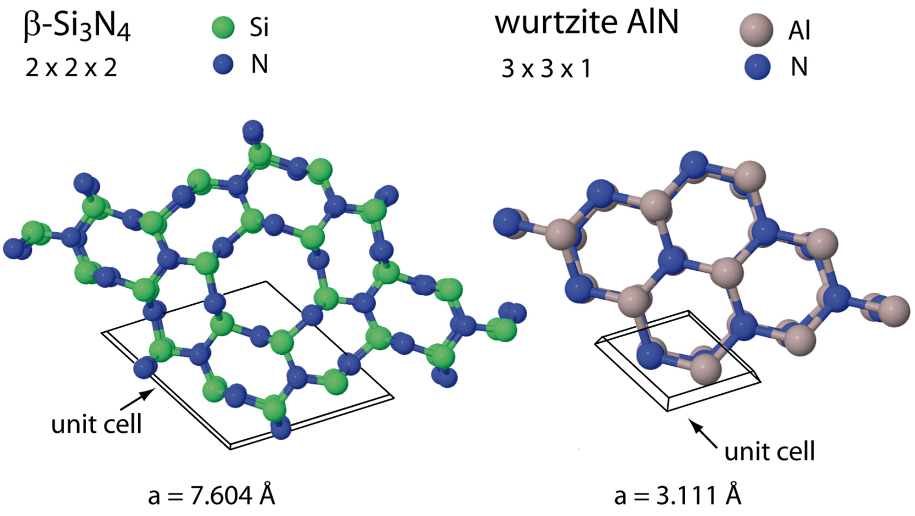

Figure 6.16: Perspective top views (along the c axis) of the β-Si_3N_4 and the wurtzite AlN lattices. Note that the atomic rings forming (0001) surfaces in both crystals are non-planar. This can be seen from a careful observation of the perspective representation of the chemical bonds. (Lattice views from [FIZ 07].)

From Figure 6.16, the unit cells of AlN and β-Si_3N_4 seems to be so different that no epitaxial relationship can be possibly established between

---

[14] at least with the Philips CM30 instrument used in this study.

these materials. In particular, there is a factor of two between the in-plane dimensions (i.e. *a* lattice parameter) of the unit cells. Nevertheless, a growth of crystalline SiN_y on top of AlN (0001) is experimentally observed. Considering the structural differences between the stable forms of aluminum nitride and silicon nitride, it is expected that if a β-form of silicon nitride is stabilized on wurtzite AlN, the silicon nitride layer would be considerably strained, resulting in large deviations of the average bond lengths and bond angles from equilibrium values.

A speculative epitaxial orientation relationship between β-Si_3N_4 (0001) and wurtzite AlN (0001) is shown in Figure 6.17. In this figure, the unit cells of AlN and β-Si_3N_4 are shifted by an in-plane rotation of 90°. Al-N and Si-N bonds are likely to be formed at the interface along the hexagonal (non planar) rings of the underlying AlN (0001) surface, so that this interface configuration may be favored. However, the theoretical in-plain strain that corresponds to this configuration amounts to about 30% (in compression) for the β-Si_3N_4 layer. In particular, the N-Si_3 units in rings labeled "2" show a trigonal planar symmetry and lay in the (0001) plane (i.e. in the plane of view here). The ideal (i.e. bulk) Si–N bond length would correspond to Si atoms situated just above the underlying Al-N bond in AlN, and not inside the ring, as seen in the picture. This may be partially accommodated e.g. by a rotation of the Si-N_4 tetrahedrons at each corner of these planar N-Si_3 units. Additional information is needed to determine whether this configuration is likely to be adopted in reality and to which cost (i.e. lattice reconstruction). However it would be surprising if such a heavily strained configuration could be effectively stabilized.

Another possible epitaxial relationship between aluminum nitride and silicon nitride could be obtained in a β-$Si_3N_4(10\bar{1}0)$/AlN(0001) configuration, in which the N (or Al) terminated AlN (0001) surface would be matched with a Si (or N) terminated surface[15] in β-Si_3N_4. A similar orientation relationship was studied by Hao *et al.* [Hao 06a] [Hao 06b]. These authors identified the β-like $Si_2N_3(10\bar{1}0)$/TiN(111) interface geometry[16] as the energetically most favorable interface configuration in the TiN/SiN_x system.

If the stable crystalline form of silicon nitride, β-Si_3N_4, is not likely to be epitaxially stabilized on AlN (0001), other non-equilibrium forms of

---

[15] The alternating Si and N $(10\bar{1}0)$ planes in β-Si_3N_4 can be seen in Fig. 6.16.

[16] Here, the Si_2N_3 stoichiometry of the silicon nitride is related to the small thickness (2.24 Å) of the layer considered, smaller than the minimum stacking sequence of successive Si and N atomic planes in the β-Si_xN_y $(10\bar{1}0)$ slab needed to keep the Si_3N_4 stoichiometry.

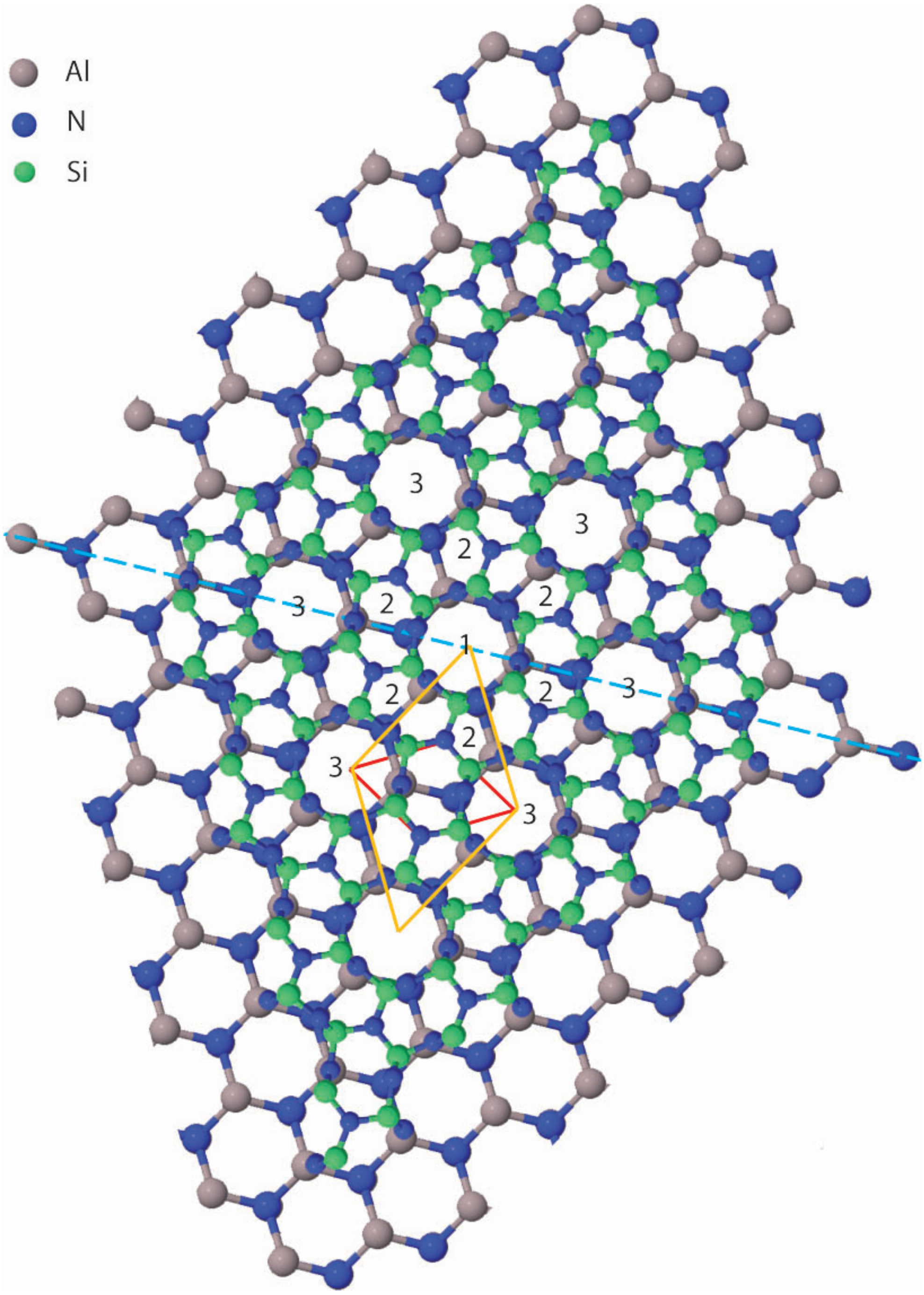

Figure 6.17: Hypothetical epitaxial orientation relationship between strained β-Si_3N_4 *(0001) and w-AlN (0001). Here a 4× 4× 1 slab of β-*Si_3N_4 *was put on top of wurtzite AlN. The unit cells of the two crystals are shown in yellow (β-*Si_3N_4*) and red (AlN). They are shifted by an in-plane rotation of 90°. In this configuration,* $\sqrt{3}a_0(AlN) = a(Si_3N_4)$*, where* a_0 *and a denote bulk and strained lattice parameters respectively. This corresponds to a strain of 29.1% in compression of the β-*Si_3N_4 *lattice. (Lattice views taken from [FIZ 07].)*

silicon nitride should be considered. In the case of TiN/SiN$_x$ superlattice films, the epitaxial stabilization of a metastable cubic SiN phase of NaCl type was reported [Sode 06] [Hult 07]. In this configuration, the silicon nitride layer is stabilized in the crystallographic structure of TiN. *Ab initio* DFT calculations predicted a lattice mismatch of 0.5% between NaCl-SiN and NaCl-TiN [Sode 06], as well as a Si-N bond length (0.2131 nm) much longer than that of bulk β-Si_3N_4 (0.1732 nm) [Zhan 07b]. By analogy to this system, an epitaxial stabilization of an isostructural wurtzite form of silicon nitride (w-SiN) on top of wurtzite AlN in AlN/SiN$_y$ multilayers should be considered. Such a configuration could provide a better match to the AlN surface, corresponding to a fully coherent interface, as compared to the complex structure of β-Si_3N_4, for which the interface with AlN (0001) is non-coherent or at best semi-coherent for most crystallographic orientations of the silicon nitride. However, this would be at the cost of a lower stoichiometric ratio of only 1 (SiN) instead of 1.33 (Si_3N_4) in silicon nitride. This is one of the reasons given by Hultman *et al.* to explain why a cubic SiN layer could only be stabilized up to about 0.7 nm in TiN/SiN$_x$ superlattices, i.e. up to a much smaller thickness than the maximum 2–3 nm of cubic AlN stabilized in AlN/TiN superlattices [Hult 07] [Sode 07b]. In contrast to the formation of NaCl-SiN, the formation of w-SiN would not imply a large change in bonding coordination, since Si atoms would keep a tetrahedral bond geometry (four-fold with N), while the bonding coordination of N atoms will change from planar trigonal (three-fold with Si) in β-Si_3N_4 to tetrahedral (four-fold with Si) in w-SiN. This should favor a larger epitaxial breakdown thickness in the AlN/SiN$_y$ system as compared to the TiN/SiN$_x$ system. However the lattice mismatch between w-SiN and w-AlN is presently unknown; it may have a large influence on the maximum stabilization thickness of a w-SiN layer, as a high interfacial strain energy would be in favor of the formation of amorphous silicon nitride (or another crystalline structure of silicon nitride) instead of w-SiN.

Finally, it should be pointed out that crystallites in Al-Si-N nanocomposite coatings were found to be elongated in the growth direction, that is in the [0001] crystallographic direction of the wurtzite Al-Si-N solid solution. This means that (0001) facets – as studied in the multilayer structures presented here – can only be found at the top and at the bottom of the crystallites, while the side facets would consist of (1000) or $(10\bar{1}0)$ planes. Further experiments on multilayers structures are hence needed to study the possibility of an epitaxial stabilization of silicon nitride on these surfaces.

Interface configurations involving w-SiN, as well as other configurations based on the β-Si_3N_4 lattice structure (including but not limited to those mentioned above) are currently studied by *ab initio* DFT calculations[17]. First results suggest a stable reconstruction of the β-Si_3N_4 lattice in a wurtzite-like structure on AlN (0001). However these calculations are at an intermediate stage only, so that no further detail is reported here.

6.5 Conclusions on multilayers as interface model for nanocomposite systems

As discussed in Chapter 5, the composition and the structure of interfaces in nanocomposite systems play a key role for the enhancement of their hardness. However, due to the small size of the nanocrystallites, these interfacial properties remain difficult to access by present experimental methods. For this reason Chapter 6 is devoted to the study of multilayer systems that make the interface accessible. Similar to the previously studied AlN/TiN and TiN/SiN_x multilayer systems, an epitaxial stabilization of crystalline silicon nitride by aluminum nitride is found in the AlN/SiN_y system discussed here. In a first section, the present understanding of the hardening mechanisms arising from epitaxially stabilized interfaces is critically reviewed. In the final section the predictive power of multilayer structures on nanocomposite structures is discussed.

6.5.1 Hardening mechanisms in epitaxial multilayer systems

According to Hultman, Söderberg and co-workers, the epitaxial stabilization of up to 2.5 ML of crystalline silicon nitride in TiN/SiN_x multilayer structures suggests that the 1–2 ML-thick SiN_x grain boundary layer found at maximum hardness in TiN/SiN_x nanocomposite coatings may not be fully amorphous, as previously thought, but partially ordered, as schematically depicted in Figure 6.2 p. 156 [Hult 07] [Sode 07b]. Based on these results Hultman suggested new design strategies for hard nanostructured coatings: The material system and the processing conditions must be chosen such that the tissue phase is epitaxially stabilized on the surface of crystalline grains of the majority phase. This stabilization is believed to generate stronger interfaces that hinder grain boundary sliding and thus enhance the hardness of the structure [Hult 07]. However, other works (see below) on the TiN/AlN

---

[17] as a collaboration with Dr. Denis Music and Prof. Dr. Jochen Schneider, from the RWTH Aachen University (D).

and TiN/SiN_x multilayer systems revealed that the relationship between epitaxial stabilization and hardness enhancement remains unclear!

For the hardness enhancement observed in epitaxially stabilized multilayer systems, three distinct hardening mechanisms have been proposed [Koeh 70] [Shin 92] [Chu 95] [Seto 96] [Yash 99] [Mei 04] [Mei 05]:

1. *The enhancement of the interfacial bond strength, associated to a stronger cohesive energy at the interface that reduces grain boundary sliding and thus yields a stronger material.*
   For the the TiN/SiN_y system, Hao *et al.* reported that the Si2p-state in the β-like Si_2N_3/TiN(111) system was found at a higher energy (i.e. Si atoms in a more negative electronic environment) than in bulk β-Si_3N_4, and that the Si–N bond length at the interface was shorter [Hao 06a]. This suggests a stronger Si–N bond for the β-like Si_2N_3 interface system than in bulk β-Si_3N_4 [Kisl 86] [Gao 03] [Simu 06]. This argument is supported by calculations that showed a higher cohesive energy for the β-like Si_2N_3 system. In contrast, the stabilization of cubic NaCl-SiN_x ($x \sim 1$) on TiN(001), reported by Hultman *et al.*, corresponds to an increase of the Si–N bond length by about 20% [Sode 06]. This should clearly lead to the opposite effect, i.e. weaker bonds. Based on *ab initio* DFT calculations, Zhang *et al.* reported that NaCl-SiN is mechanically much weaker (i.e. smaller shear strengths) than β-Si_3N_4 [Zhan 07b]. Thus epitaxial stabilization of a crystalline form of SiN_y can lead either to stronger or weaker bonds in multilayer heterostructures, depending on the details of the epitaxial relationship at the interfaces.

2. *Pinning of dislocations at the interfaces of materials with different shear moduli (Koehler's mechanism)* [Koeh 70].
   An enhancement of the difference in shear moduli in the TiN/AlN system due to the epitaxial stabilization of cubic AlN was postulated to explain the superlattice effect (hardness maximum) observed in this system. From first principle studies, however, Zhang *et al.* [Zhan 07a] reported that fcc(NaCl)-AlN and hcp(wurtzite)-AlN had similar shear strengths and bonding nature. Thus the enhanced hardness of fcc-TiN/fcc-AlN structures compared to fcc-TiN/hcp-AlN cannot be explained by an increased difference of the shear moduli.

3. *Periodic coherent strain fields caused by lattice mismatch* [Shin 92].
   In the TiN/AlN structure, the mismatch between cubic AlN and TiN is 4.8% [Mada 97]; an effect of periodic strain fields is plausible. However,

the lattice mismatch between fcc-TiN and fcc-SiN is only 0.5%: thus at least for this system this mechanism cannot explain the increased hardness.

In summary, the above discussion reveals that for each hardening mechanism of multilayer structures reviewed here, experimental examples that support or exclude the proposed model were found. Nevertheless, systems that are epitaxially stabilized show a high hardness. Yet the epitaxial stabilization is not a physical parameter that can be given as an explanation for the increased hardness. Instead, the increased hardness is caused by one or several physical or material properties that appear at the same time as the epitaxial growth of a metastable phase. However, the property or set of properties that prevail(s) is presumably not universal but dependent on the interface system. Since the origin(s) of hardness enhancement in epitaxially stabilized multilayer systems is not well understood, it seems too speculative to propose the epitaxial stabilization of an intergranular phase in nanocomposite coatings as a new design strategy to produce hard materials, as suggested by Hultman et al. [Hult 07].

6.5.2 Extrapolation of the interface properties of multilayer structures to those of nanocomposites

Let us now point out that interfaces in nanocomposite structures may greatly differ from those formed in 2D heterostructures.

Nanocrystalline grains in nanocomposite coatings are expected to have numerous facetted surfaces. The crystalline orientation of these surfaces can be different from the orientations studied in multilayer systems, so that the epitaxial relationship shown experimentally or predicted from *ab initio* calculations may or may not exist.

Moreover the surface area of these facets will remain a few square nanometers only. Thus a high density of triple junctions is expected that is predicted to hinder an ordering of the intergranular phase in nanocomposite coatings. This issue was recently raised by Zhang and Veprek in [Zhan 08b], and was previously mentioned by Söderberg in [Sode 07b]. In TiN/SiN_x multilayer structures, the latter reported that the "growth front" should be as flat as possible so that the SiN_y layer grow evenly on TiN and a thicker crystalline layer can be stabilized. This is in agreement with the present work that showed that rougher interfaces or interfaces with polycrystalline

Al-Si-N restrains the epitaxial growth of the $\mathrm{SiN_y}$ to smaller thicknesses.

In addition, multilayer structures show abrupt (sharp) interfaces as a consequence of the alternative deposition of distinct materials. For the Al-Si-N/$\mathrm{SiN_y}$ multilayer structures deposited in this work, superlattice peaks were observed in XRR spectra even for a $\mathrm{SiN_y}$ layer thickness of only 0.25 nm (i.e. one monolayer of $\mathrm{SiN_y}$). In contrast, interfaces in nanocomposite structures may be "rough" or "diffuse" (i.e. show a composition gradient), unless complete phase segregation occurs by spinodal decomposition of immiscible materials, which leads to the formation of sharp and flaw-free interfaces, as postulated by Veprek *et al.* [Vepr 07a].

In conclusion, multilayer systems allow the control of various interface properties (e.g. interface chemistry, chemical gradients, interface roughness etc.) and the study of the influence of these properties on the hardness. However, properties observed in multilayer systems, e.g. an epitaxial stabilization of a metastable phase, cannot necessarily be extrapolated to the corresponding nanocomposite system. For the Al-Si-N/$\mathrm{SiN_y}$ multilayer system studied here, an epitaxial stabilization of a crystalline form of $\mathrm{SiN_y}$ is found. Despite the restrictions notified above, this supports the hypothesis formulated in Chapter 5 that, in the Al-Si-N nanocomposite system, the preferred orientation of the Al-Si-N crystallites is due to a transfer of orientational order through a $\mathrm{SiN_y}$ intergranular phase that shows some degree of crystallinity, as deduced from XRD data (see Fig. 5.20, p. 116).

Part IV

Conclusion

Chapter 7

Conclusions and outlook

7.1 Al-Si-N coatings – Take-home message

In this work, hard nanocomposite coatings made of Al-Si-N were successfully fabricated with a maximum hardness (32 GPa) exceeding that of sapphire (α-Al_2O_3) and a transmittance of about 80% in the visible range of light. The coatings were deposited by reactive unbalanced magnetron sputtering at a deposition temperature as low as 200°C. Such a deposition process can be scaled up for industrial applications.

The properties of the deposits and the underlying growth behavior depend on the silicon content, varied from 0 to 23 at.%. These properties can be divided into three main composition regions, plus a narrow transition region. At low Si concentrations ($<$ 6 at.%), a solid solution of $Al_{1-x}Si_xN$ is formed with the crystalline structure of hexagonal wurtzite AlN (w-AlN), as showed by a linear decrease of the c lattice parameter with the silicon content. The thermodynamically stable solubility limit of silicon in w-AlN is identified at 6 at.% of Si. Around 6 at.% of Si (transition region), silicon atoms segregate at the grain boundaries and build a thin silicon nitride layer. Above 6 at.% of Si, the films consist of a mixture of $Al_{0.44}Si_{0.06}N_{0.5}$ crystallites embedded in a one-monolayer thick ($\sim$ 0.25 nm) silicon nitride layer: a nanocomposite structure is formed. As the Si content is further increased, the SiN_y layer thickness remains constant while the crystallite size is forced to decrease inversely proportional to the silicon concentration. The average grain size was determined to be about 40 nm at 6 at.% of Si and less than 5 nm at 12 at.% of Si. As the composite structure is formed and the crystallite size dramatically decreases, the columnar morphology observed at low Si content ($<$ 6 at.%) progressively vanishes, however still retaining a (002) texture. Evidence is found of a transfer of preferred orientation between neighboring Al-Si-N crystallites through an ordered $\mathrm{SiN_y}$ grain boundary layer. The formation of structural coherent interfaces between wurtzite Al-Si-N and an ordered ("crystalline") form of silicon nitride is supported by the results of model experiments conducted on Al-Si-N/$\mathrm{SiN_y}$ multilayer heterostructures, reactively sputter deposited at 200°C. These experiments demonstrate the epitaxial stabilization of up to 0.7–1.0 nm ($\sim$ 2.5–3.5 monolayers) of crystalline $\mathrm{SiN_y}$ – otherwise expected to grow amorphous at 200°C – between AlN (0001) layers. Above a Si content limit of 10–15 at.%, the Al-Si-N nanocomposite films encounter a last structural change as the thickness of the $\mathrm{SiN_y}$ layer increases. This has a noticeable effect e.g. on the chemical state of the $\mathrm{SiN_y}$ layer, that approaches that of bulk silicon nitride.

A hardness maximum of 32 GPa is gradually reached as the silicon content is increased from 0 to about 10 at.% of Si. The hardness values then slowly decrease as the Si content is further increased. This evolution results from the interplay of different hardening mechanisms such as solid solution hardening of the Al-Si-N crystalline phase, and nanostructure hardening as the nanocomposite structure is formed, consisting of small crystallites ($<$ 10 nm) surrounded by a monolayer-thick grain boundary layer. The achieved maximum hardness of 32 GPa is moderate as compared to the superhardness (H $>$ 40 GPa) which is often achieved in conventional transition metal-based nanocomposite systems such as TiN/$\mathrm{SiN_x}$. This lower hardness is first attributed to structural similarities between the materials present in the Al-Si-N nanocomposite coatings, secondly to a possible small composition gradient at the grain boundaries due to the finite solubility of Si in w-AlN and to kinetic limitations during low temperature sputter deposition, and third to the 0.5–2.0 at.% of oxygen impurities present in the films. It must be noted that, at maximum hardness, the biaxial residual stress state of the films is close to zero ($|\sigma| \leq 0.5$ GPa) so that hardening due to a high compressive stress in the coatings can be excluded. This low-stress state is favorable for a good adherence of the coatings on the substrate.

The coatings are transparent in the visible range of light with a refractive index slightly increasing from 2.00 to 2.12 as the Si content is increased. This corresponds to about 80% visible light transmission.

The microstructure, phase composition, hardness of Al-Si-N films were found to be stable upon annealing for 2 h in argon at 1000°C.

This combination of hardness, optical transparency and thermal stability makes Al-Si-N coatings good candidates for applications as protective coatings e.g. for architectural glass, furnace windows, ceramic cooktops or solar devices (solar cells, water-heating devices).

7.2 A broader perspective on hardening mechanisms in nanocomposite coatings

The basic design rules for the fabrication of hard nanocomposite coatings were first introduced by Vepřek in 1995 [Vepr 95] and hardly changed since then [Vepr 99] [Vepr 05]. Vepřek stated that hard and superhard coatings may consist in an isotropic nanocomposite system made of two phases: a nanocrystalline phase of a hard material, surrounded by a grain boundary (GB) phase made of a distinct, immiscible, material (either crystalline or amorphous). For the fabrication of such coatings, it is strongly advised that the conditions for spinodal phase separation are fulfilled, as thoroughly discussed by Vepřek. It was postulated that the increased hardness of such composite material results from the suppression – or strong reduction – of dislocation activity (thanks to a small grain size), of grain boundary sliding (associated to strong and sharp interfaces) and of crack propagation (by minimizing the thickness of the GB phase). This design strategy was particularly successful in the case of transition metal-containing systems of type *nc*-MeN/*a*-SiN_x.

Today, these design rules still prevail to a large extent but are too restrictive. Despite several refinements, they still focus on the spinodal decomposition of fully immiscible materials. The prototype remains the *nc*-TiN/*a*-SiN_x system. In the future, basic design considerations should be enlarged e.g. to include non-spinodal phase separation (i.e. phase separation by segregation and re-nucleation), partially-miscible systems (such as the Al-Si-N system), and metastable systems whose microstructural features can be tailored by post-deposition annealing (such as Ti-Al-N-related systems). At present, most of the research work on hard nanocomposite coatings is devoted to the systematic investigation of the properties of specific coating systems. Beside this experimental work, *ab initio* calculations are now performed to study the decomposition thermodynamics and phase stabilities of given material systems. For the future development of advanced coatings, however, it appears increasingly necessary to adopt a more fundamental and global approach. This should enable to better evaluate the implications of specific features (e.g. epitaxial stabilization of the GB phase, texture, partial miscibility) of the nanocomposite systems on their mechanical properties (especially hardness, but also toughness etc.), and lead to the definition of new research priorities.

In the following, a list of answers to the question: "how to make a hard material?" is compiled. To each proposed answer (1,2,3...), a sub-list of necessary – but not sufficient – conditions (a,b,c...) for the formation of a hard material is given. The aim is to provide scientists with a large panel of physical properties that promote hardness. In the list below, each condition is independent on the others and is proposed free from any practical consideration on the way to implement it in a real system (i.e. choice of a material system, of fabrication conditions etc.).

How to make a hard material?

1. *Suppress dislocations activity within crystalline grains, by:*
    - *(a) small grains, isolated from each other (i.e. no cooperation between different grains)*
    - *(b) defects in the grains (e.g. solute atoms)*
2. *Ensure efficient dislocation pinning at grain boundaries, through:*
    - *(a) high-angle grain boundaries (in single-phase materials)*
    - *(b) different slip systems (in multi-phase materials)*
    - *(c) a large lattice mismatch (in multi-phase materials)*
    - *(d) a large difference in shear moduli (in multi-phase materials)*

    + sharp interfaces, both geometrically (e.g. no disclinations) and atomically (i.e. no composition gradient)

    ⇒ Leads to a large energy difference of the dislocation line over a short distance at the interfaces, generating a strong image force that acts against the dislocation movement.
3. *Prevent grain boundary sliding, through:*
    - *(a) large, non deformable grains with well defined edges (e.g. rectangular or hexagonal shape)*
    - *(b) a narrow grain size distribution*

    (c) *a high interface cohesion energy (high bond strength; absence of defects such as dangling bonds and impurities; solute coverage etc.)*

4. *Hinder crack nucleation, by:*
    (a) *a high bond strength*
    (b) *an amorphous material*
5. *Impede or stop crack propagation, by:*
    (a) *a network of materials with different mechanical properties to force meandering of cracks*
    (b) *the inclusion of macro- or micro-voids*

The above list is incomplete and should be further developed. In its present form, however, it already points out the competition between deformation mechanisms and the interrelation between specific conditions (e.g. *if* small grains **(1a)** *then* grain boundary sliding may become the dominant deformation mechanism **(3a)** *unless* the GB strength is increased **(3c)** *in which case* ...). The present list can be used to define sets of conditions to build a hard material. Nanocomposite coatings, in their traditional picture given at the beginning of this section and proposed by Veprek, only constitute one option to form a strong and hard material, well adapted to a class of immiscible materials and for which a fabrication process is known. Other options, adapted to other material systems and (or) different fabrication routes can be found.

To illustrate how such a list is helpful in the understanding of current issues in the field of hard nanocomposite coatings, several examples are given below:

- *Coherency at grain boundaries.*
  Some physical properties can be either beneficial or detrimental to the formation of a hard material. This is the case of a structural coherency at grain boundaries: it has a beneficial effect insofar GBs present less defects and have therefore a higher cohesive energy **(3c)** i.e. GB sliding is more efficiently blocked. However, coherent interfaces may also be found between materials of same (or similar) crystallographic structure **(2b-c)**, orientation **(2a)** and mechanical properties **(2d)**, in which case efficient dislocation pinning at GBs is not anymore ensured (e.g. (002)-textured Al-Si-N films).

- *Material systems with a finite solubility.*
  Looking at the above list, the condition of "sharp" interfaces postulated by Vepřek can be better understood as a necessary condition for efficient pinning of dislocations (or any other deformation strain field) at grain boundaries **(2+)**, and for efficient reduction of dislocation activity within grains that are well separated from each other **(1a)**. In this respect, nanocomposite coatings based on partially miscible materials, such as the Al-Si-N system, are expected to have a lower maximum hardness than coatings based on fully immiscible materials. Systems with a finite solubility have a smaller driving force for phase separation. They are hence "more prone" to incomplete phase separation when non-equilibrium deposition processes are used, as it is often the case. This is expected to result in a composition gradient between the phases, i.e. diffuse (penetrable) interfaces that only slow down the deformation movement without stopping it **(2⇒)**.

- *Thickness of the grain boundary layer.*
  The maximum hardness in nanocomposite coatings is often found for an average thickness of the grain boundary layer (typically $\mathrm{SiN_y}$) of the order of 1–2 monolayers only, as in the case of the Al-Si-N system. Several effects can be mentioned to explain this finding:
  i) The GB layer must be thin enough so that crack propagation is hindered due to frequent deviations at grain boundaries **(5a)**. This, however, does not explain why the optimum thickness shall be restricted to one monolayer only.
  ii) As recently proposed by Vepřek, the thickness of 1–2 monolayers may correspond to the critical thickness of a pseudomorphic layer before the strain energy must be release by the creation of misfit dislocations, i.e. by the creation of defects that lower the interface strength **(3c, 4a)** [Vepr 07a] [Vepr 07b].
  iii) Specific physical properties that are found only in very thin GB layers may have an effect on hardness and shall be considered. For instance, an enhancement of the negative charge on Si atoms in $\mathrm{SiN_x}$ thin GB layers was reported in [Vepr 07a] [Hao 06a] for $\mathrm{TiN/SiN_x}$ nanostructures. Quite similarly, Diserens evidenced by XPS a charge transfer between the TiN and the $\mathrm{SiN_x}$ phases associated to an increase of the covalent character of both Ti–N and Si–N bonds [Dise 00]. Interestingly, this effect was found for nanocomposite coatings in which the $\mathrm{SiN_y}$ grain boundary phase had a thickness of about 0.5 nm (i.e. ~ 2 monolayers), corresponding to a Si content below 10 at.%, and disappeared when the grain boundary thickness was increased above 0.5 nm.

iv) A GB thickness of one monolayer corresponds to the minimum thickness needed to achieve full coverage of the crystallites (e.g. **3c**). Keeping this thickness to its minimum enables to achieve the highest density of grain boundaries for a given grain size. To increase the GB layer thickness would correspond to a loss of pinning volume **(2)** for the deformation strain field (larger grain size). Considering now that hardening is mostly ensured by the suppression of dislocation nucleation within grains of nanometer size **(1a)**, one monolayer of GB layer may represent the minimum thickness to efficiently isolate grains from each other (impenetrable GB) and maximize the volume of the hard nanocrystalline phase.

As can be seen, an enlightened evaluation of the physical origin and of the implications of specific material properties requires approaching the problem from different points of view. It is important to realize that there is a huge amount of knowledge available in the literature on basic principles to obtain hardness and on basic mechanisms responsible for the deformation of materials, especially for nanostructured materials. However, this knowledge is widely distributed over distinct research fields (e.g. nanocrystalline metals, polymeric nanostructured materials etc.) and only a small part is commonly used by scientists working in the field of hard nanocomposite coatings. A broader view of size effects, deformation and hardening mechanisms can be gained e.g. from Arzt [Arzt 98], Gleiter [Glei 00], Van Swygenhoven [Van 06]. It is noteworthy that such a fundamental and global approach as praised here was recently adopted in publications such as [Cava 06] and [Vepr 07b]. This task should be carried on.

7.3 Future directions

Future research work in the field of hard nanocomposite coatings should aim at a better understanding of deformation mechanisms in nanocrystalline multi-phase ceramics and at a better control of interface states (sharpness, purity, strength) in nanostructured materials. *Ab initio* calculations on model systems (interfaces, multilayers) and atomic scale simulations (such as those conducted on nanocrystalline metals) should provide a working scheme for experimentalists i.e. help them to identify interesting physical properties that could be used to improve the mechanical properties of nanostructured materials. The control of interface states can be achieved through a better control and understanding of non-equilibrium processes such as low temperature reactive sputtering and cathodic arc deposition, which are widely used techniques in the industry. Such processes could be modified by the simultaneous use of ”soft” surface chemistry, e.g. the addition of a chemical element (He, chloride, etc.) whose only function is to enhance the surface diffusion during film growth and hence improve the kinetics of phase separation. Other process routes can also be explored, including multi-step processes in which a post-treatment procedure (e.g. annealing) is implemented to adjust the properties of deposited thin films.

Appendixes

Appendix A

Crystalline structures of AlN and β-Si_3N_4

This appendix gives an overview of the wurtzite AlN and β-Si_3N_4 crystalline structures. The main parameters defining the crystallographic lattices of aluminum nitride and silicon nitride are reported in Table A.1. Three-dimensional views of the AlN and β-Si_3N_4 lattices are shown in Figures A.1, A.2 and A.3.

Table A.1: Structural characteristics of aluminum nitride and silicon nitride

Material	w-AlN	β-Si_3N_4
System	hexagonal	hexagonal
Space group	$P6_3mc$ (186)	$P6_3/m$ (176) or $P6_3$ (173)
Lattice parameter (Å)	a = 3.1114 c = 4.9297	a = 7.6044 c = 2.9075
Density	3.261	3.200
Bond lengths (Å)	Al–N 1.885 and 1.917	Si–N between 1.704 and 1.767 mean value: 1.732
Bond angles	N–Al–N 107.7° and 110.5°	N–Si–N between 106.6° and 113.5° mean value: 109.45° Si–N–Si between 113.5° and 125.1° mean value: 119.97°

Source: JCPDS-ICDD card # 25-1133 and [Xu 01] for AlN, JCPDS-ICDD card # 33-1160, [Grun 79] and [Wang 96] for β-Si_3N_4.

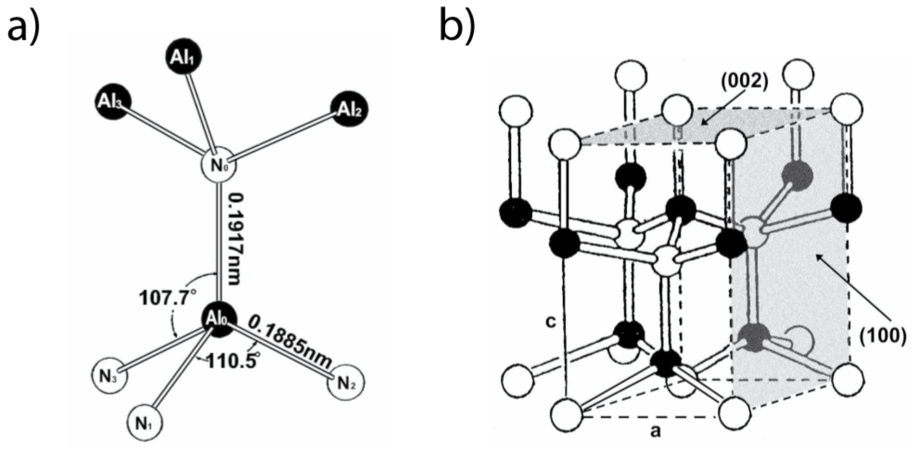

Figure A.1: The AlN wurtzite crystalline structure: (a) the double AlN_3–NAl_3 tetrahedral building unit; (b) the AlN crystallographic unit lattice. From [Xu 01]. Note that Al atoms are surrounded by four N atoms in a distorted tetrahedra geometry, with three B_1-type bonds, and one B_2-type bond in the direction of the c-axis.

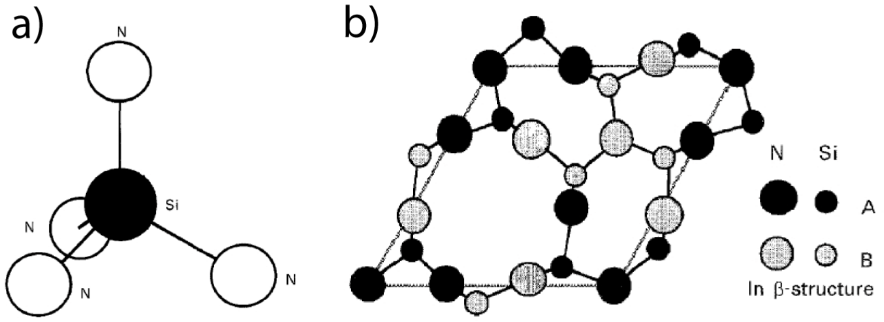

Figure A.2: (a) The tetrahedral SiN_4 building unit in silicon nitride. (b) Visualization of the crystal structure in β-Si_3N_4 as an arrangement of puckered Si-N layers stacked in an ...ABAB... way. From [Wang 96]

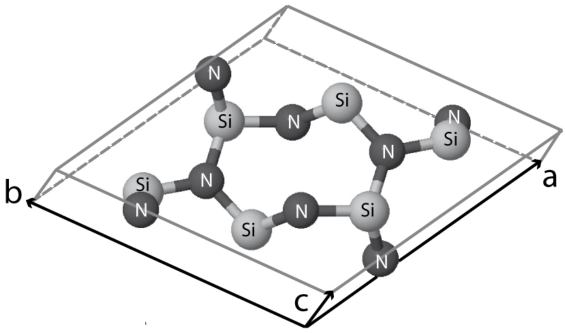

Figure A.3: Side view of the β-Si_3N_4 crystalline unit lattice. Original lattice view from [FIZ 07]

In AlN and β-Si_3N_4 crystals, the basic building units are aluminum-nitrogen and silicon-nitrogen tetrahedra respectively (Figs. A.1 and A.2). In AlN, Al atoms are bonded to four N atoms, with Al being situated at the center of a tetrahedron with four N atoms at the corners. The situation is the same for N atoms, forming a Si–Al_4 tetrahedron. In β-Si_3N_4, the tetrahedral units (with one Si atom at the center and four N atoms at the corners) are joined by sharing corners in such a way that each nitrogen is common to three tetrahedra. As a result, Si atoms are four-fold bonded to nitrogen (tetrahedral geometry), while N atoms are bonded to "only" three Si atoms (in a planar trigonal geometry). In both crystalline structures, the tetrahedral unit is slightly distorted, as revealed by the distribution of bond length and bond angles reported in the literature (Table A.1, [Grun 79], [Wang 96], [Xu 01]).

Appendix B

XPS on AlN and Si_3N_4 – a literature review

In the frame of X-ray photoelectron spectroscopy investigations on Al-Si-N coatings, a literature review of XPS data on pure AlN and Si_3N_4 films was done. The results of this review are reported in Table B.2. From these data, mean photoelectron binding energy (BE) values and standard deviations were calculated using, first, C1s-referenced data only and, secondly, all data from Table B.2 independent on the charge referencing method. This is reported in Table B.1.

Table B.1: Mean binding energies and standard deviations calculated using the data listed in Table B.2.

Compound	BE (eV)		ΔBE (eV)	Charge ref.
	N1s	Al2p	(N1s–Al2p)	
AlN	396.8 ± 0.3	73.7 ± 0.7	323.10	C1s only
AlN	396.9 ± 0.3	73.8 ± 0.6	323.10	All data
	N1s	Si2p	(N1s–Si2p)	
Si_3N_4	397.8 ± 0.4	101.7 ± 0.6	296.10	C1s only
Si_3N_4	397.9 ± 0.4	101.8 ± 0.5	296.10	All data

Table B.2: N1s, Al2p and Si2p photoelectron binding energies (BE) for AlN and Si_3N_4, as found in the literature.

Compound	BE (eV)			ΔBE (eV)		Charge referencing	Specimen information	Reference
	N1s	Al2p	Si2p	(N1s–Al2p)	(N1s–Si2p)	method		
AlN	397.3	73.9		323.4		N1s at 397.3 eV	powder	[Tayl 81b]
AlN	397.3	74.1		323.2		metallic Al2p at 72.8 eV	reaction by ion bombardment	[Tayl 81b]
AlN	–	74.4		–		Adv. carbon	oxidized surface ?	[McGu 73]
$AlN_{1.5}$	397.0	74.2		322.8		not specified	PLD - in situ XPS	[Soto 04]
AlN	396.8	73.6		323.2		Adv. carbon	sputtered thin film	[Bert 02]
AlN	396.9	73.8		323.1		Adv. carbon	reaction by ion bombardment	[Sang 99]
AlN	396.3	72.4		323.8		Adv. carbon	sputtered film	[Witt 00]
AlN	396.7	74.0		322.7		Adv. carbon	sputtered - large amount of O	[Kova 84]
AlN	397.1	73.8		323.3		Adv. carbon	LPCVD	[Perr 97]
Si_3N_4	397.4		101.8		295.6	Adv. carbon	CVD	[Tayl 78b]
Si_3N_4	398.0		101.9		296.1	Conductor	reaction by ion bombardment	[Tayl 81a]
Si_3N_4	397.6		102.0		295.6	Gold	thin film	[Tayl 78a]
Si_3N_4	398.5		102.4		296.1	Conductor	reaction by ion bombardment	[Donl 88]
Si_3N_4	398.3		102.0		296.3	C1s at 284.5 eV and $Ar2p_{3/2}$ at 242.2 eV (unclear which one)	reaction bonded	[Ingo 90]
Si_3N_4	398.3		102.0		296.3		amorphous - CVD	[Ingo 90]
Si_3N_4	398.3		102.0		296.3		amorphous - DIBS	[Ingo 90]
Si_3N_4	398.3		102.0		296.3	Conductor	amorphous, CVD, thin film	[Ingo 89]
Si_3N_4	397.5		101.8		295.7	Adv. carbon	amorphous	[Goto 88]
Si_3N_4	–		100.6		–	Adv. carbon	α-phase, CVD	[Du 89]
Si_3N_4	–		101.5		–	Adv. carbon	CVD	[Witt 78]
Si_3N_4	397.4		101.8		295.6	not specified	IBAD	[Zhan 04]
Si_3N_4	397.9		102.2		295.7	Adv. carbon	PACVD	[Bert 02]
$SiN_{1.4}$	397.7		101.5		296.2	not specified	PLD - in situ XPS	[Soto 04]

Unless else specified, the C1s peak is set at 284.8 eV for charge referencing using adventitious carbon (Adv. carbon) and the $Au4f_{7/2}$ peak is set at 84.0 eV for vapor deposited gold references (Gold). "Conductor" means that the specimen was judged sufficiently conductor and no charge referencing was needed.

Appendix C

Structural model calculations

C.1 Si coverage calculation

Let us consider Al-Si-N grains (crystallites) of height h with an hexagonal section of side length L and diameter (width) $w = 2L$, as shown in Figure C.1. These grains are elongated in the [002] direction. The aspect ratio r of the grains is defined as $r = h/w$.

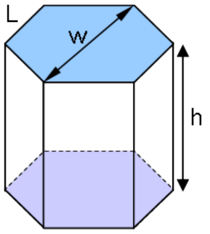

Figure C.1: Model of Al-Si-N crystallite shape. The height h and the width w are defined on the picture.

The volume of one grain is $\mathrm{V}_{\mathrm{grain}} = \frac{3\sqrt{3}}{2}L^2h = \frac{3\sqrt{3}}{8}rw^3$. The volume of a unit cell of wurtzite Al-Si-N is $\mathrm{V}_{\mathrm{cell}} = \frac{\sqrt{3}}{2}a^2c$ (with a and c the lattice constants).

The surface of one grain is divided into $\mathrm{S}_{\mathrm{grain}} = 2 \times \mathrm{S}_{\mathrm{top,\ grain}} + 6 \times \mathrm{S}_{\mathrm{side,\ grain}}$ with $\mathrm{S}_{\mathrm{top,\ grain}} = \frac{3\sqrt{3}}{2}L^2 = \frac{3\sqrt{3}}{8}w^2$ and $\mathrm{S}_{\mathrm{side,\ grain}} = Lh = \frac{rw^2}{2}$. Similarly, the surface of one Al-Si-N wurtzite unit cell is divided into $\mathrm{S}_{\mathrm{top,\ cell}} = \frac{\sqrt{3}}{2}a^2$ and $\mathrm{S}_{\mathrm{side,\ cell}} = ac$.

From there, the number of unit cells per Al-Si-N grain is $\mathrm{N}_{\mathrm{cell/grain}} = \frac{\frac{3\sqrt{3}}{8}rw^3}{\frac{\sqrt{3}}{2}a^2c} = \frac{3}{4}\frac{rw^3}{a^2c}$. The number of unit cell top faces per Al-Si-N grain top surface is $\mathrm{N}_{\mathrm{cell/top}} = \frac{\frac{3\sqrt{3}}{8}w^2}{\frac{\sqrt{3}}{2}a^2} = \frac{3}{4}\frac{w^2}{a^2}$ and the number of unit cell side faces per

Al-Si-N grain side surface is $\mathrm{N}_{\text{cell/side}} = \frac{rw^2}{2ac}$.

For the wurtzite AlN (w-AlN) structure, the number of Al atoms in each unit cell is $4 \times \frac{1}{6} + 4 \times \frac{1}{3} + 1 = 3$ atoms. On each top face of the unit cell, there is $2 \times \frac{1}{6} + 2 \times \frac{1}{3} = 1$ atom, and on each side face of the unit cell, there is $4 \times \frac{1}{4} = 1$ atom as well.

The number of Al(Si) atoms in one Al-Si-N grain is hence $\mathrm{N}_{\text{Al-sites/Vgrain}} = 3 \times \mathrm{N}_{\text{cell/grain}} = \frac{9}{4}\frac{rw^3}{a^2c}$. The number of Al sites on the surface of one Al-Si-N grain is $\mathrm{N}_{\text{Al-sites/ Sgrain}} = 1 \times (2 \times \frac{3}{4}\frac{w^2}{a^2} + 6 \times \frac{rw^2}{2ac}) = \frac{3}{2}\frac{w^2}{a^2c}(2ra + c)$. The ratio between the number of Al sites on the grain surface and inside the grain is $R_1 = \frac{\mathrm{N}_{\text{Al-sites/Sgrain}}}{\mathrm{N}_{\text{Al-sites/Vgrain}}} = \frac{2}{3}\frac{(2ra+c)}{h}$.

Under the assumption that the segregated Si atoms occupy the sites of Al atoms at the grain (crystallite) surface, the Si coverage can be expressed as the ratio between the number of Si atoms at the grain surface and the total number of available Al sites at the grain surface:

$$\text{Si surface coverage} = \frac{\mathrm{N}_{\text{Si-atoms/Sgrain}}}{\mathrm{N}_{\text{Al-sites/Sgrain}}}$$

By multiplying the numerator and the denominator by $\mathrm{N}_{\text{Al-sites/Vgrain}}$, it follows:

$$\text{Si surface coverage} = \frac{\mathrm{N}_{\text{Si-atoms/Sgrain}}}{\mathrm{N}_{\text{Al-sites/Vgrain}}} \times \frac{1}{R_1}$$

The number of Si atoms at the surface of the grains equals the total number of Si atoms in the coating minus those incorporated in the Al-Si-N crystalline phase, i.e. $\mathrm{N}_{\text{Si-atoms/Sgrain}} = C_{\text{Si}} - \alpha$ with α a parameter that corresponds to the silicon atomic concentration at which the first Si atoms segregate outside the Al-Si-N crystallites. The number of Al sites in the Al-Si-N grains equals the total number of Al atoms in the system, plus the incorporated Si atoms in the w-AlN lattice, i.e. $\mathrm{N}_{\text{Al-sites/Vgrain}} = C_{\text{Al}} + \alpha$. It follows:

$$\text{Si surface coverage} = \frac{C_{\text{Si}} - \alpha}{C_{\text{Al}} + \alpha} \times \frac{3h}{(4ra + 2c)} \tag{C.1}$$

C.2 SiN$_\mathrm{y}$ thickness calculation

The same crystallite shape introduced for the previous model is again used here. The thickness t of the SiN$_\mathrm{y}$ layer on top of the grains (crystallites) is now estimated, based on volume ratios of the two phases.

Assuming that the $\mathrm{SiN_y}$ interlayer shows the $\mathrm{Si_3N_4}$ stoichiometry (i.e. y = 1.33), the volume percentage of the silicon nitride phase is:

$$\mathrm{V_{SiNy}} = \frac{C_{\mathrm{Si}} - \alpha}{N_A} \times \left(\frac{3M_{\mathrm{Si}} + 4M_{\mathrm{N}}}{3}\right) \times \frac{1}{d_{\mathrm{SiNy}}}$$

with C_{Si} the silicon concentration (in at.%), α the Si concentration at which the first Si atoms segregate at the grain boundaries and form a $\mathrm{SiN_y}$ interlayer, M_{Si} and M_{N} the relative atomic mass of Si and N atoms, N_A Avogadro's number and d_{SiNy} the density of the silicon nitride phase.

In the same way, the volume of the Al-Si-N crystalline phase can be expressed as:

$$\mathrm{V_{AlN}} = \frac{C_{\mathrm{Al}} + \alpha}{N_A} \times (M_{\mathrm{Al}} + M_{\mathrm{N}}) \times \frac{1}{d_{\mathrm{AlN}}}$$

The ratio between the volumes of these two phases is:

$$R_2 = \frac{\mathrm{V_{SiNy}}}{\mathrm{V_{AlN}}} = \frac{C_{\mathrm{Si}} - \alpha}{C_{\mathrm{Al}} + \alpha} \times \frac{(3M_{\mathrm{Si}} + 4M_{\mathrm{N}})}{3(M_{\mathrm{Al}} + M_{\mathrm{N}})} \times \frac{d_{\mathrm{AlN}}}{d_{\mathrm{SiNy}}} \tag{C.2}$$

In the present model, the grains are arranged in a compact way with a spacing t between them that corresponds to the thickness of the $\mathrm{SiN_y}$ interlayer. The volume of one grain is $\mathrm{V_{grain}} = \frac{3\sqrt{3}}{8}rw^3$. The surface of one grain is $\mathrm{S_{grain}} = 2 \times \frac{3\sqrt{3}}{8}w^2 + 6 \times \frac{rw^2}{2} = \frac{3}{4}w^2(\sqrt{3} + 4r)$. The volume of $\mathrm{SiN_y}$ per grain is hence $\mathrm{V_{SiNy/grain}} = \mathrm{S_{grain}} \times \frac{t}{2} = \frac{3}{8}tw^2(\sqrt{3} + 4r)$.

The ratio R_2 can also be expressed as:

$$R_2 = \frac{\mathrm{V_{SiNy/grain}}}{\mathrm{V_{grain}}}$$

The $\mathrm{SiN_y}$ interlayer thickness t can be deduced from there. It follows:

$$t = \frac{\sqrt{3}h}{(\sqrt{3} + 4r)} \times \frac{C_{\mathrm{Si}} - \alpha}{C_{\mathrm{Al}} + \alpha} \times \frac{(3M_{\mathrm{Si}} + 4M_{\mathrm{N}})}{3(M_{\mathrm{Al}} + M_{\mathrm{N}})} \times \frac{d_{\mathrm{AlN}}}{d_{\mathrm{SiNy}}} \tag{C.3}$$

with: $M_{\mathrm{Si}} = 28.09$ u, $M_{\mathrm{Al}} = 26.98$ u, $M_{\mathrm{N}} = 14.01$ u, $d_{\mathrm{AlN}} = 3.26$ (from JCPDS-ICDD card # 25-1133) and $d_{\mathrm{SiNy}} \approx 3$ (from XRR experiments).

Appendix D

Crystallographic formulae for hexagonal lattices

For structures with hexagonal symmetry, several axial systems can be used, among which two different hexagonal sets of axis, as shown in Figure D.1 [Otte 65]. The indices of directions and planes may be referred to either a three-axis or a four-axis reference basis. The former corresponds to "Miller indices", traditionally used in X-ray techniques, the latter to "Miller-Bravais indices", used in transmission electron microscopy. In the Miller-Bravais four-axis system, directions are labeled $[u\ v\ t\ w]$, chosen so that $t = -(u+v)$, as shown in Figure D.2.

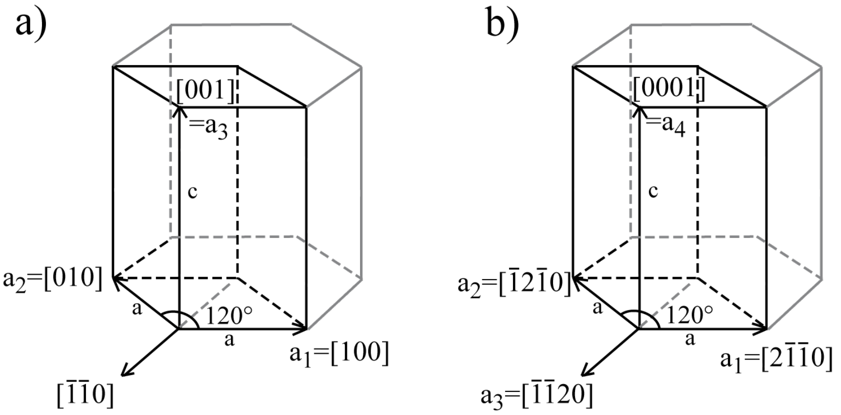

Figure D.1: Directions in the hexagonal lattice using (a) a three-axis basis (Miller notation) and (b) a four-axis basis (Miller-Bravais notation).

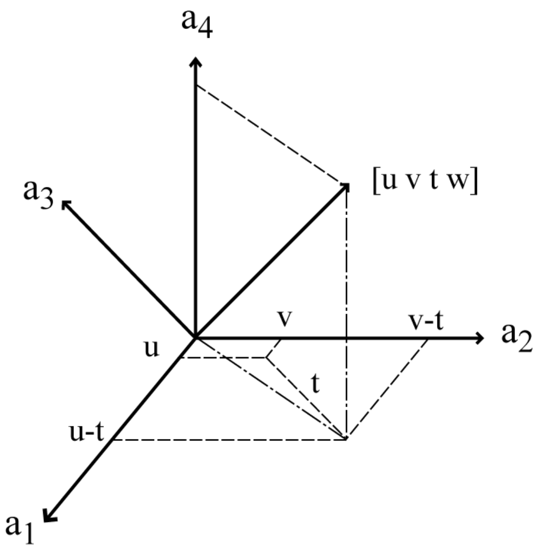

Figure D.2: Miller-Bravais notation for directions. [Rare 66]

The conversion between the two systems can be made the following way:

- A direction with Miller-Bravais indices $[u\ v\ t\ w]$ (also written[1] $[u\ v\ .\ w]$) has Miller indices $[U\ V\ W] = [2u+v,\ u+2v,\ w]$
- A plane with Miller-Bravais indices $(h\ k\ i\ l)$ or $(h\ k\ .\ l)$ has Miller indices $[U\ V\ W] = (h\ k\ l)$, i.e. no change of indices is necessary in this case.

Distinct sets of crystallographic formulae arise for these two indexing systems, as shown in Table D.1. Further formulae can be found e.g. in [Otte 65], [Nich 66] and [Nich 70].

---

[1] In the Miller-Bravais notation, the third indice is redundant, so that it is often omitted. Indeed for a vector $[u\ v\ t\ w]$, the condition $t = -(u+v)$ is imposed. In the same way for a plane $(h\ k\ i\ l)$, $i = -(h+k)$.

Table D.1: Crystallographic formulae for hexagonal lattices

	Miller (3-axis hexagonal)	Miller-Bravais (4-axis hexagonal)
D	$[U\ V\ W]$	$[u\ v\ t\ w]$
P	$(H\ K\ L)$	$(h\ k\ i\ l)$
$d =$	$\left[\frac{3}{4}\frac{H^2+HK+K^2}{a^2}+\frac{L^2}{c^2}\right]^{-\frac{1}{2}}$	$\left[\frac{3}{4}\frac{h^2+hk+k^2}{a^2}+\frac{l^2}{c^2}\right]^{-\frac{1}{2}}$
$\cos\phi =$	$\frac{H_1H_2+K_1K_2+\frac{1}{2}(H_1K_2+K_1H_2)+\frac{3}{4}\frac{a^2}{c^2}L_1L_2}{\left[\left(H_1^2+K_1^2+H_1K_1+\frac{3}{4}\frac{a^2}{c^2}L_1^2\right)\left(H_2^2+K_2^2+H_2K_2+\frac{3}{4}\frac{a^2}{c^2}L_2^2\right)\right]^{\frac{1}{2}}}$	$\frac{h_1h_2+k_1k_2+\frac{1}{2}(h_1k_2+k_1h_2)+\frac{3}{4}\frac{a^2}{c^2}l_1l_2}{\left[\left(h_1^2+k_1^2+h_1k_1+\frac{3}{4}\frac{a^2}{c^2}l_1^2\right)\left(h_2^2+k_2^2+h_2k_2+\frac{3}{4}\frac{a^2}{c^2}l_2^2\right)\right]^{\frac{1}{2}}}$
$\cos\varrho =$	$\frac{U_1U_2+V_1V_2-\frac{1}{2}(U_1V_2+V_1U_2)+\frac{c^2}{a^2}W_1W_2}{\left[\left(U_1^2+V_1^2-U_1V_1+\frac{c^2}{a^2}W_1^2\right)\left(U_2^2+V_2^2-U_2V_2+\frac{c^2}{a^2}W_2^2\right)\right]^{\frac{1}{2}}}$	$\frac{u_1u_2+v_1v_2+\frac{1}{2}(u_1v_2+v_1u_2)+\frac{1}{3}\frac{c^2}{a^2}w_1w_2}{\left[\left(u_1^2+v_1^2+u_1v_1+\frac{1}{3}\frac{c^2}{a^2}w_1^2\right)\left(u_2^2+v_2^2+u_2v_2+\frac{1}{3}\frac{c^2}{a^2}w_2^2\right)\right]^{\frac{1}{2}}}$
(1)	$\left[2H+K,\, H+2K,\, \frac{3}{2}L\left(\frac{a}{c}\right)^2\right]$	$\left[h,\, k,\, i,\, \frac{3}{2}l\left(\frac{a}{c}\right)^2\right]$
(2)	$\left(2U-V,\, -U+2V,\, 2W\left(\frac{a}{c}\right)^2\right)$	$\left(u,\, v,\, t,\, \frac{2}{3}w\left(\frac{c}{a}\right)^2\right)$

D and P represents indices of directions and planes respectively. The quantity d, ϕ and ϱ are the interplanar spacing, the angle between two planes and the angle between two directions respectively. Suffices 1 and 2 have been used to distinguish the two planes and the two directions in the expression for ϕ and ϱ respectively. (1) Equations for finding the indices of the direction perpendicular to a given plane (i.e normal vector). (2) Equations for finding the indices of a plane knowing the indices of its normal vector. [Otte 65] [Nich 66] [Edin 75]

Bibliography

[Alli 07] B. Alling, A. V. Ruban, A. Karimi, O. E. Peil, S. I. Simak, L. Hultman, and I. A. Abrikosov. "Mixing and decomposition thermodynamics of c-$\mathrm{Ti_{1-x}Al_xN}$ from first-principles calculations". *Physical Review B*, Vol. 75, No. 4, p. 45123, 2007.

[Alli 08] B. Alling, E. I. Isaev, A. Flink, L. Hultman, and I. A. Abrikosov. "Metastability of fcc-related Si-N phases". *Physical Review B*, Vol. 78, No. 13, p. 132103, 2008.

[Arzt 98] E. Arzt. "Size effects in materials due to microstructural and dimensional constraints: a comparative review". *Acta Materialia*, Vol. 46, No. 16, pp. 5611–5626, 1998.

[Asan 87] M. Asano, M. Kobayashi, Y. Maeno, K. Oishi, and K. Kawamura. "Magneto-optical recording media with new protective films". *Magnetics, IEEE Transactions on*, Vol. 23, No. 5, pp. 2620–2622, 1987.

[ASM 96] ASM International. "Binary Alloy Phase Diagrams". Software, Copyright 1996.

[ASTM 03] ASTM International. "Standard Guide to Charge Control and Charge Referencing Techniques in X-ray Photoelectron Spectroscopy". ASTM Guide E 1523–03, 2003.

[Barn 98] P. B. Barna and M. Adamik. "Fundamental structure forming phenomena of polycrystalline films and the structure zone models". *Thin Solid Films*, Vol. 317, No. 1-2, pp. 27–33, 1998.

[Beeg 05] D. Beegan and M. T. Laugier. "Application of composite hardness models to copper thin film hardness measurement". *Surface & Coatings Technology*, Vol. 199, No. 1, pp. 32–37, 2005.

[Bend 02] A. Bendavid, P. J. Martin, and H. Takikawa. "The properties of nanocomposite aluminium–silicon based thin films deposited by filtered arc deposition". *Thin Solid Films*, Vol. 420, pp. 83–88, 2002.

[Benk 04] M. Benkahoul, C. S. Sandu, N. Tabet, M. Parlinska-Wojtan, A. Karimi, and F. Lévy. "Effect of Si incorporation on the properties of niobium nitride films deposited by DC reactive magnetron sputtering". *Surface & Coatings Technology*, Vol. 188, pp. 435–439, 2004.

[Berg 05] S. Berg and T. Nyberg. "Fundamental understanding and modeling of reactive sputtering processes". *Thin Solid Films*, Vol. 476, pp. 215–230, 2005.

[Bert 02] I. Bertóti. "Characterization of nitride coatings by XPS". *Surface & Coatings Technology*, Vol. 151–152, pp. 194–203, 2002.

[Birk 06] M. Birkholz. *Thin Film Analysis by X-Ray Scattering.* Wiley-VCH, 2006.

[Birn 04] D. P. Birnie. "Optical video interpretation of interference colors from thin transparent films on silicon". *Materials Letters*, Vol. 58, No. 22-23, pp. 2795–2800, 2004.

[Bogu 97] P. Bogusławski and J. Bernholc. "Doping properties of C, Si, and Ge impurities in GaN and AlN". *Physical Review B*, Vol. 56, No. 15, pp. 9496–9505, 1997.

[Boye 05] H. G. Boyen, A. Ethirajan, G. Kästle, F. Weigl, P. Ziemann, G. Schmid, M. G. Garnier, M. Büttner, and P. Oelhafen. "Alloy Formation of Supported Gold Nanoparticles at Their Transition from Clusters to Solids: Does Size Matter?". *Physical Review Letters*, Vol. 94, No. 1, p. 16804, 2005.

[Bran 03] M. S. Brandt, R. Zeisel, S. T. B. Goennenwein, M. W. Bayerl, and M. Stutzmann. "DX behaviour of Si donors in AlGaN alloys". *Physica Status Solidi B*, Vol. 235, No. 1, pp. 13–19, 2003.

[Bren 89] R. Brener, F. Edelman, and E. Y. Gutmanas. "Formation of an interfacial AlN layer in an Al/Si_3N_4 thin-film system". *Applied Physics Letters*, Vol. 54, pp. 901–903, 1989.

[Brig 03] D. Briggs and J. T. Grant. *Surface Analysis by Auger and X-Ray Photoelectron Spectroscopy.* IM Publications and SurfaceSpectra, UK, 2003.

[Brud 05] A. Brudnik, A. Czapla, and E. Kusior. "AlN thin films prepared by optical emission spectroscopy-controlled reactive sputtering". *Thin Solid Films*, Vol. 478, No. 1-2, pp. 67–71, 2005.

[Bull 03] S. J. Bull. "On the origins and mechanisms of the indentation size effect". *Zeitschrift fuer Metallkunde/Materials Research and Advanced Techniques*, Vol. 94, No. 7, pp. 787–792, 2003.

[Bull 05] S. J. Bull. "Nanoindentation of coatings". *Journal of Physics D: Applied Physics*, Vol. 38, No. 24, pp. R393–R413, 2005.

[Cahn 62] J. W. Cahn. "The Impurity-Drag Effect in Grain Boundary Motion". *Acta Metallurgica*, Vol. 10, pp. 789–798, 1962.

[Cao 91] G. Z. Cao and R. Metselaar. "α-Sialon Ceramics: A Review". *Chem. Mater*, Vol. 3, No. 2, pp. 242–252, 1991.

[Cava 06] A. Cavaleiro and J. T. M. de Hosson, Eds. *Nanostructured Coatings. Nanostructure Science and Technology*, Springer, New York, USA, 2006. ISBN 0387256423, 9780387256429.

[Chad 88] D. J. Chadi and K. J. Chang. "Theory of the Atomic and Electronic Structure of DX Centers in GaAs and $Al_xGa_{1-x}As$ Alloys". *Physical Review Letters*, Vol. 61, No. 7, pp. 873–876, 1988.

[Chen 97] I. W. Chen and A. Rosenflanz. "A Tough SiAlON Ceramic Based on α-Si_3N_4 with a Whisker-like Microstructure". *Nature*, Vol. 389, No. 6652, pp. 701–704, 1997.

[Chib 05] K. Chiba, T. Kageyama, T. Iwata, N. Fujimori, and H. Oda. “Fabrication and Optical Properties of Low-Emissivity Coatings of Indium Tin Oxide or AlSiN and Ag-Alloy Multilayer Films on Glass”. *Japanese Journal of Applied Physics*, Vol. 44, No. 4, pp. 2070–2073, 2005.

[Chib 08] K. Chiba and S. Kaminishi. “Fabrication and Optical Properties of Low-Emissivity Coatings of AlSiN and AgCuNd-Alloy Multilayer Films on Glass”. *Japanese Journal of Applied Physics*, Vol. 47, No. 1, pp. 240–243, 2008.

[Chu 95] X. Chu and S. A. Barnett. “Model of superlattice yield stress and hardness enhancements”. *Journal of Applied Physics*, Vol. 77, No. 9, pp. 4403–4411, 1995.

[Citr 74] P. H. Citrin and D. R. Hamann. “Measurement and calculation of polarization and potential-energy effects on core-electron binding energies in solids: X-ray photoemission of rare gases implanted in noble metals”. *Physical Review B*, Vol. 10, No. 12, pp. 4948–4963, 1974.

[Cons 99] R. Constantin and B. Miremad. “Performance of hard coatings, made by balanced and unbalanced magnetron sputtering, for decorative applications”. *Surface & Coatings Technology*, Vol. 120, pp. 728–733, 1999.

[Cris 07] B. V. Crist. “A Review of XPS Data-Banks”. *XPS Reports*, Vol. 1, pp. 1–52, 2007.

[Crug 03] H. Cruguel, M. J. Guittet, O. Kerjan, F. Bart, and M. Gautier-Soyer. “Bonding and chemical shifts in aluminosilicate glasses: importance of Madelung effects”. *Journal of Electron Spectroscopy and Related Phenomena*, Vol. 128, No. 2-3, pp. 271–278, 2003.

[Csel 05] T. Cselle. “Application of Coatings for Tooling Quo Vadis 2005?”. *Vakuum in Forschung und Praxis*, Vol. 17, pp. 33–39, 2005.

[Csel 07] T. Cselle, M. Morstein, A. Lümkemann, and J. Prochazka. “3 (+1) Kathoden – 30 Schichten – 300 Chargen”. *Schweizer Präzisions-Fertigungstechnik*, pp. 1–4, 2007.

[Dent 91] A. R. Denton and N. W. Ashcroft. “Vegard’s law”. *Phys. Rev. A*, Vol. 43, No. 6, pp. 3161–3164, 1991.

[Depl 09] D. Depla, S. Mahieu, and R. D. Gryse. “Magnetron sputter deposition: Linking discharge voltage with target properties”. *Thin Solid Films*, Vol. 517, No. 9, pp. 2825–2839, 2009.

[DiCe 88] S. B. DiCenzo, S. D. Berry, and E. H. Hartford. “Photoelectron spectroscopy of single-size Au clusters collected on a substrate”. *Phys. Rev. B*, Vol. 38, No. 12, pp. 8465–8468, 1988.

[Dise 00] M. Diserens. *Couches minces nanocomposites de TiN/SiN$_x$ déposées par pulvérisation magnétron réactive: propriétés électroniques, mécaniques et résistance à l’oxydation.* PhD thesis, EPFL, Lausanne (CH), 2000. (in French).

[Dise 98] M. Diserens, J. Patscheider, and F. Levy. “Improving the properties of titanium nitride by incorporation of silicon”. *Surface & coatings technology*, Vol. 108, No. 1-3, pp. 241–246, 1998.

[Dise 99] M. Diserens, J. Patscheider, and F. Lévy. “Mechanical properties and oxidation resistance of nanocomposite TiN–SiN$_x$ physical-vapor-deposited thin films”. *Surface & Coatings Technology*, Vol. 120–121, pp. 158–165, 1999.

[Donl 88] M. S. Donley, D. R. Baer, and T. G. Stoebe. “Nitrogen 1s charge referencing for Si_3N_4 and related compounds”. *Surface and Interface Analysis*, Vol. 11, No. 6-7, pp. 335–340, 1988.

[Dovi 96] K. Dovidenko, S. Oktyabrsky, J. Narayan, and M. Razeghi. “Aluminum nitride films on different orientations of sapphire and silicon”. *Journal of Applied Physics*, Vol. 79, No. 5, pp. 2439–2445, 1996.

[Du 89] H. Du, R. E. Tressler, K. E. Spear, and C. G. Pantano. “Oxidation Studies of Crystalline CVD Silicon Nitride”. *Journal of The Electrochemical Society*, Vol. 136, p. 1527, 1989.

[Easw 05] T. Easwarakhanthan, M. B. Assouar, P. Pigeat, and P. Alnot. “Optical models for radio-frequency-magnetron reactively sputtered AlN films”. *Journal of Applied Physics*, Vol. 98, p. 073531, 2005.

[Edin 75] J. W. Edington. *Electron Diffraction in the Electron Microscope. Monographs in practical electron microscopy in materials science, No. 2.* London, Macmillan, 1975.

[Fan 74] J. C. C. Fan, F. J. Bachner, G. H. Foley, and P. M. Zavracky. “Transparent heat-mirror films of $TiO_2/Ag/TiO_2$ for solar energy collection and radiation insulation”. *Applied Physics Letters*, Vol. 25, pp. 693–695, 1974.

[Fan 85] J. C. C. Fan and F. J. Bachner. “Transparenet Heat-Mirror”. US Patent 4,556,277, Dec. 3 1985.

[Fisc 00] A. C. Fischer-Cripps. “A review of analysis methods for sub-micron indentation testing”. *Vacuum*, Vol. 58, No. 4, pp. 569–585, 2000.

[Fisc 06a] A. C. Fischer-Cripps. “Critical review of analysis and interpretation of nanoindentation test data”. *Surface and Coatings Technology*, Vol. 200, No. 14–15, pp. 4153–4165, 2006.

[Fisc 06b] A. C. Fischer-Cripps, P. Karvánkováb, and S. Veprek. “On the measurement of hardness of super-hard coatings”. *Surface and Coatings Technology*, Vol. 200, No. 18–19, pp. 5645–5654, 2006.

[FIZ 07] FIZ Fachinformationszentrum Karlsruhe. “Inorganic Crystal Structure Database”. `http://icsdweb.fiz-karlsruhe.de`, © 2007.

[Gahl 01] R. Gåhlin, M. Larsson, and P. Hedenqvist. “ME-C: H coatings in motor vehicles”. *Wear*, Vol. 249, No. 3-4, pp. 302–309, 2001.

[Gao 03] F. Gao, J. He, E. Wu, S. Liu, D. Yu, D. Li, S. Zhang, and Y. Tian. “Hardness of covalent crystals.”. *Physical review letters*, Vol. 91, No. 1, p. 015502, 2003.

[Glei 00] H. Gleiter. “Nanostructured materials: basic concepts and microstructure”. *Acta materialia*, Vol. 48, No. 1, pp. 1–29, 2000.

[Goen 01] S. T. B. Goennenwein, R. Zeisel, O. Ambacher, M. S. Brandt, M. Stutzmann, and S. Baldovino. “Generationrecombination noise of DX centers in AlN:Si”. *Applied Physics Letters*, Vol. 79, No. 15, pp. 2396–2398, 2001.

[Goto 88] T. Goto and T. Hirai. "ESCA study of amorphous CVD Si_3N_4-BN composites". *Journal of Materials Science Letters*, Vol. 7, pp. 548–550, 1988.

[Grun 79] R. Grün. "The crystal structure of β-Si_3N_4: structural and stability considerations between α- and β-Si_3N_4". *Acta Crystallographica B*, Vol. 35, No. 4, pp. 800–804, 1979.

[Guo 08] X. Guo, L. Li, Z. Liu, D. Yu, J. He, R. Liu, B. Xu, Y. Tian, and H. T. Wang. "Hardness of covalent compounds: Roles of metallic component and d valence electrons". *Journal of Applied Physics*, Vol. 104, p. 023503, 2008.

[Hall 51] E. O. Hall. "The Deformation and Ageing of Mild Steel: III Discussion of Results". *Proceedings of the Physical Society. Section B*, Vol. 64, pp. 747–753, 1951.

[Hao 06a] S. Hao, B. Delley, and C. Stampfl. "Structure and properties of TiN(111)/Si_xN_y/TiN(111) interfaces in superhard nanocomposites: First-principles investigations". *Physical Review B*, Vol. 74, No. 3, p. 35402, 2006.

[Hao 06b] S. Hao, B. Delley, S. Veprek, and C. Stampfl. "Superhard Nitride-Based Nanocomposites: Role of Interfaces and Effect of Impurities". *Physical Review Letters*, Vol. 97, No. 8, p. 86102, 2006.

[Haue 00] R. Hauert and J. Patscheider. "From alloying to nanocomposites: Improved performance of hard coatings". *Advanced engineering materials*, Vol. 2, No. 5, pp. 247–259, 2000.

[Haue 03] R. Hauert. "A review of modified DLC coatings for biological applications". *Diamond & Related Materials*, Vol. 12, No. 3-7, pp. 583–589, 2003.

[Heid 06] P. A. W. van der Heide. "Photoelectron binding energy shifts observed during oxidation of group IIA, IIIA and IVA elemental surfaces". *Journal of Electron Spectroscopy and Related Phenomena*, Vol. 151, No. 2, pp. 79–91, 2006.

[Helm 06] U. Helmersson, M. Lattemann, J. Bohlmark, A. P. Ehiasarian, and J. T. Gudmundsson. "Ionized physical vapor deposition (IPVD): A review of technology and applications". *Thin Solid Films*, Vol. 513, No. 1-2, pp. 1–24, 2006.

[Henr 93] F. Henry, B. Armas, M. Balat, R. Berjoan, and C. Combescure. "A study of AlN-Si_3N_4 codeposits using the L. P. C. V. D. technique". *Journal de physique IV*, Vol. 3, No. 3, pp. 519–526, 1993.

[Henr 95] F. Henry, B. Armas, C. Combescure, D. Thenegal, and R. Flamand. "Chemical Vapour Deposition of AlN-Si_3N_4 Codeposits". *Journal de Physique IV*, Vol. 5, No. 5, pp. 785–792, 1995.

[Henr 97] F. Henry, B. Armas, R. Berjoan, C. Combescure, and C. Dupuy. "Low pressure chemical vapour deposition of AlN-Si_3N_4 codeposits". *Journal of the European Ceramic Society*, Vol. 17, No. 15-16, pp. 1803–1806, 1997.

[Herm 05] M. Hermann, F. Furtmayr, A. Bergmaier, G. Dollinger, M. Stutzmann, and M. Eickhoff. "Highly Si-doped AlN grown by plasma-assisted molecular-beam epitaxy". *Applied Physics Letters*, Vol. 86, p. 192108, 2005.

[Herm 06] M. Hermann, F. Furtmayr, F. M. Morales, O. Ambacher, M. Stutzmann, and M. Eickhoff. "Impact of silicon incorporation on the formation of structural defects in AlN". *Journal of Applied Physics*, Vol. 100, No. 11, p. 113531, 2006.

[Hill 92] M. Hillert and S. Jonsson. "Prediction of the Al-Si-N system". *Calphad*, Vol. 16, No. 2, pp. 199–205, 1992.

[Holl 86] H. Holleck. "Material selection for hard coatings". *Journal of Vacuum Science & Technology A*, Vol. 4, No. 6, pp. 2661–2669, 1986.

[Holl 88] H. Holleck. "Metastable coatings – Prediction of composition and structure". *Surface and Coatings Technology*, Vol. 36, No. 1–2, pp. 151–159, 1988.

[Holl 95] H. Holleck and V. Schier. "Multilayer PVD coatings for wear protection". *Surface & Coatings Technology*, Vol. 76–77, pp. 328–336, 1995.

[Holl 99] Holleck, H. in. *Surface Engineering: science and Technology I.* The Minerals, Metals and Materials Society, 1999. pp. 207–231.

[Holu 99] P. Holubář, M. Jılek, and M. Šıma. "Nanocomposite nc-TiAlSiN and nc-TiN–BN coatings: their applications on substrates made of cemented carbide and results of cutting tests". *Surface & Coatings Technology*, Vol. 120, pp. 184–188, 1999.

[Hu 05] X. Hu, H. Zhang, J. Dai, G. Li, and M. Gu. "Study on the superhardness mechanism of Ti–Si–N nanocomposite films: Influence of the thickness of the SiN interfacial phase". *Journal of Vacuum Science & Technology A*, Vol. 23, No. 1, p. 114, 2005.

[Hult 00] L. Hultman. "Thermal stability of nitride thin films". *Vacuum*, Vol. 57, No. 1, pp. 1–30, 2000.

[Hult 07] L. Hultman, J. Bareño, A. Flink, H. Söderberg, K. Larsson, V. Petrova, M. Odén, J. E. Greene, and I. Petrov. "Interface structure in superhard TiN-SiN nanolaminates and nanocomposites: Film growth experiments and ab initio calculations". *Physical Review B*, Vol. 75, No. 15, p. 155437, 2007.

[Ingo 89] G. M. Ingo, N. Zacchetti, D. della Sala, and C. Coluzza. "X-ray photoelectron spectroscopy investigation on the chemical structure of amorphous silicon nitride (a-SiN)". *Journal of Vacuum Science & Technology A*, Vol. 7, No. 5, pp. 3048–3055, 1989.

[Ingo 90] G. M. Ingo and N. Zacchetti. "XPS investigation on the growth model of *a*-$\mathrm{SiN_x}$ and silicon and nitrogen chemical bondings". *High Temperature Science*, Vol. 28, pp. 137–151, 1990.

[Ishi 98] M. Ishihara, S. J. Li, H. Yumoto, K. Akashi, and Y. Ide. "Control of preferential orientation of AlN films prepared by the reactive sputtering method". *Thin Solid Films*, Vol. 316, No. 1-2, pp. 152–157, 1998.

[Ive 05] T. Ive, O. Brandt, H. Kostial, K. J. Friedland, L. Däweritz, and K. H. Ploog. "Controlled n-type doping of AlN:Si films grown on 6H-SiC(0001) by plasma-assisted molecular beam epitaxy". *Applied Physics Letters*, Vol. 86, p. 024106, 2005.

[Jaco 07] K. T. Jacob, S. Raj, and L. Rannesh. "Vegard's law: a fundamental relation or an approximation?". *International Journal of Materials Research (formerly Z. Metallkd.)*, Vol. 98, No. 9, pp. 776–779, 2007.

[Joo 99] H. Y. Joo, H. J. Kim, S. J. Kim, and S. Y. Kim. "Spectrophotometric analysis of aluminum nitride thin films". *Journal of Vacuum Science & Technology A: Vacuum, Surfaces, and Films*, Vol. 17, p. 862, 1999.

[Kari 06] A. Karimi, G. Allidi, and R. Sanjines. "Relative orientation of the constituents on the degree of crystallographic coherence in AlN/TiN superlattices". *Surface & Coatings Technology*, Vol. 201, No. 7, pp. 4062–4067, 2006.

[Karv 01] P. Karvánková, H. D. Männling, C. Eggs, and S. Veprek. "Thermal stability of ZrN–Ni and CrN–Ni superhard nanocomposite coatings". *Surface & Coatings Technology*, Vol. 146–147, pp. 280–285, 2001.

[Kasu 00] M. Kasu and N. Kobayashi. "Large and stable field-emission current from heavily Si-doped AlN grown by metalorganic vapor phase epitaxy". *Applied Physics Letters*, Vol. 76, No. 20, pp. 2910–2912, 2000.

[Kasu 01] M. Kasu, Y. Taniyasu, and N. Kobayashi. "Formation of Solid Solution of $\mathrm{Al_{1-x}Si_xN}$ ($0< \mathrm{x} \leq 12\%$) Ternary Alloy". *Japanese Journal of Applied Physics*, Vol. 40, No. 10A, pp. 1048–1050, 2001.

[Kauf 88] L. Kaufman. "Calculation of Multicomponent Ceramic Phase Diagrams". *Physica B*, Vol. 150, No. 12, p. 99114, 1988.

[Kebl 97] P. Keblinski, S. R. Phillpot, D. Wolf, and H. Gleiter. "Amorphous structure of grain boundaries and grain junctions in nanocrystalline silicon by molecular-dynamics simulation". *Acta Materialia*, Vol. 45, No. 3, pp. 987–998, 1997.

[Kell 00] P. J. Kelly and R. D. Arnell. "Magnetron sputtering: a review of recent developments and applications". *Vacuum*, Vol. 56, No. 3, pp. 159–172, 2000.

[Kell 98] P. J. Kelly and R. D. Arnell. "Development of a novel structure zone model relating to the closed-field unbalanced magnetron sputtering system". *Journal of Vacuum Science & Technology A: Vacuum, Surfaces, and Films*, Vol. 16, No. 5, pp. 2858–2869, 1998.

[Khos 05] J. M. Khoshman and M. E. Kordesch. "Spectroscopic ellipsometry characterization of amorphous aluminum nitride and indium nitride thin films". *physica status solidi(c)*, Vol. 2, No. 7, pp. 2821–2827, 2005.

[Kies 31] H. Kiessig. "Interferenz von Röntgenstrahlen an dünnen Schichten". *Annalen der Physik*, Vol. 402, No. 7, pp. 769–788, 1931.

[Kim 01] I. W. Kim, Q. Li, L. D. Marks, and S. A. Barnett. "Critical thickness for transformation of epitaxially stabilized cubic AlN in superlattices". *Applied Physics Letters*, Vol. 78, p. 892, 2001.

[Kisl 86] P. S. Kisly. "The Chemical Bond Strength and the Hardness of High Melting Point Compounds". *Inst. Phys. Conf. Ser.*, Vol. 75, pp. 107–120, 1986.

[Klug 74] H. P. Klug and L. E. Alexander. *X-Ray Diffraction Procedures for Polycrystalline and Amorphous Materials.* John Wiley & Sons, New York, second Ed., 1974. ISBN: 0-471-49369-4.

[Koeh 70] J. S. Koehler. "Attempt to Design a Strong Solid". *Physical Review B*, Vol. 2, No. 2, pp. 547–551, 1970.

[Kohi 84] S. Kohiki. "Problem of evaporated gold as an energy reference in X-ray photoelectron spectroscopy". *Appl. Surf. Sci*, Vol. 17, pp. 497–503, 1984.

[Kohi 85] S. Kohiki and K. Oki. "An appraisal of evaporated gold as an energy reference in X-ray photoelectron spectroscopy". *Journal of electron spectroscopy and related phenomena*, Vol. 36, No. 1, pp. 105–110, 1985.

[Kouz 99] V. Kouznetsov, K. Macák, J. M. Schneider, U. Helmersson, and I. Petrov. "A novel pulsed magnetron sputter technique utilizing very high target power densities". *Surface & Coatings Technology*, Vol. 122, No. 2-3, pp. 290–293, 1999.

[Kova 84] J. A. Kovacich, J. Kasperkiewicz, D. Lichtman, and C. R. Aita. "Auger electron and x-ray photoelectron spectroscopy of sputter deposited aluminum nitride". *Journal of Applied Physics*, Vol. 55, No. 8, pp. 2935–2939, 1984.

[Krok 04] E. Kroke and M. Schwarz. "Novel group 14 nitrides". *Coordination Chemistry Reviews*, Vol. 248, No. 5-6, pp. 493–532, 2004.

[Lebe 06] V. Lebedev, F. M. Morales, H. Romanus, G. Ecke, V. Cimalla, M. Himmerlich, S. Krischok, J. A. Schaefer, and O. Ambacher. "Doping efficiency and segregation of Si in AlN grown by molecular beam epitaxy". *Physica Status Solidi C*, Vol. 3, No. 6, pp. 1420–1424, 2006.

[Legr 94] P. B. Legrand, M. Wautelet, B. Dugnoille, J. P. Dauchot, and M. Hecq. "Optical properties of sputter-deposited aluminum nitride films on silicon". *Thin Solid Films*, Vol. 248, No. 2, pp. 220–223, 1994.

[Leva 07] E. A. Levashov and D. V. Shtansky. "Multifunctional nanostructured films". *Russian Chemical Reviews*, Vol. 76, No. 5, pp. 463–470, 2007.

[Leyl 00] A. Leyland and A. Matthews. "On the significance of the H/E ratio in wear control: a nanocomposite coating approach to optimised tribological behaviour". *Wear*, Vol. 246, No. 1-2, pp. 1–11, 2000.

[Leyl 04] A. Leyland and A. Matthews. "Design criteria for wear-resistant nanostructured and glassy-metal coatings". *Surface & Coatings Technology*, Vol. 177, pp. 317–324, 2004.

[Li 02] X. Li and B. Bhushan. "A review of nanoindentation continuous stiffness measurement technique and its applications". *Materials Characterization*, Vol. 48, No. 1, pp. 11–36, 2002.

[Li 05] M. K. Li, C. B. Li, C. S. Liu, and X. J. Fan. "Preparation of AlN Films and *nc*-AlN/*a*-$\mathrm{SiN_x}$ Nanocomposite Films by Medium Frequency Magnetron Sputtering". *Journal of the Korean Physical Society*, Vol. 46, pp. S83–S87, 2005.

[Li 08] K. Li, X. Wang, F. Zhang, and D. Xue. "Electronegativity identification of novel superhard materials". *Phys. Rev. Lett.*, Vol. 100, p. 235504, 2008.

[Lin 00] C. Lin and W. Loong. "Correlation between the chemical compositions and optical properties of AlSiN embedded layer for attenuated phase-shifting mask in 193 nm and the modification of the R–T method for measuring n and k". *Journal of Vacuum Science & Technology B*, Vol. 18, pp. 3371–3375, 2000.

[Liu 89] A. M. Y. Y. Liu and M. L. Cohen. "Prediction of New Low Compressibility Solids". *Science*, Vol. 245, No. 4920, pp. 841–842, 1989.

[Loff 94] F. H. W. Löffler. "Systematic approach to improve the performance of PVD coatings for tool applications". *Surface & coatings technology*, Vol. 68–69, pp. 729–740, 1994.

[Mada 97] A. Madan, I. W. Kim, S. C. Cheng, P. Yashar, V. P. Dravid, and S. A. Barnett. "Stabilization of Cubic AlN in Epitaxial AlN/TiN Superlattices". *Phys. Rev. Lett.*, Vol. 78, No. 9, pp. 1743–1746, 1997.

[Maen 90] Y. Maeno, M. Kobayashi, K. Oishi, and K. Kawamura. "Properties and Structure of AlSiN and AlSiON Films". *Magnetics in Japan, IEEE Translation Journal on*, Vol. 5, No. 1, pp. 59–67, 1990.

[Mani 76] J. C. Manifacier, J. Gasiot, and J. P. Fillard. "A simple method for the determination of the optical constants n, k and the thickness of a weakly absorbing thin film". *Journal of Physics E: Scientific Instruments*, Vol. 9, pp. 1002–1004, 1976.

[Mann 01] H. D. Männling, D. S. Patil, K. Moto, M. Jilek, and S. Veprek. "Thermal stability of superhard nanocomposite coatings consisting of immiscible nitrides". *Surface & Coatings Technology*, Vol. 146–147, pp. 263–267, 2001.

[Mart 01] P. J. Martin and A. Bendavid. "The filtered arc process and materials deposition". *Surface & Coatings Technology*, Vol. 142–144, pp. 7–10, 2001.

[Mart 05] P. J. Martin, A. Bendavid, J. M. Cairney, and M. Hoffman. "Nanocomposite Ti–Si–N, Zr–Si–N, Ti–Al–Si–N, Ti–Al–V–Si–N thin film coatings deposited by vacuum arc deposition". *Surface & Coatings Technology*, Vol. 200, No. 7, pp. 2228–2235, 2005.

[Mart 95] P. Marti, F. Henry, A. Mazel, B. Armas, and J. Sevely. "Transmission Electron Microscopy Studies of (AlN-Si_3N_4 Codeposits Obtained by LPCVD". *Journal de Physique IV*, Vol. 5, No. 5, pp. 905–912, 1995.

[Matt 89] D. M. Mattox. "Particle bombardment effects on thin-film deposition: A review". *Journal of Vacuum Science & Technology A: Vacuum, Surfaces, and Films*, Vol. 7, No. 3, pp. 1105–1114, 1989.

[Matt 97] T. Mattila and R. M. Nieminen. "Point-defect complexes and broadband luminescence in GaN and AlN". *Physical Review B*, Vol. 55, No. 15, pp. 9571–9576, 1997.

[Mayr 03] P. H. Mayrhofer, A. Hörling, L. Karlsson, J. Sjölén, T. Larsson, C. Mitterer, and L. Hultman. "Self-organized nanostructures in the Ti–Al–N system". *Applied Physics Letters*, Vol. 83, No. 10, pp. 2049–2051, 2003.

[Mayr 05] P. H. Mayrhofer, C. Mitterer, J. G. Wen, J. E. Greene, and I. Petrov. "Self-organized nanocolumnar structure in superhard TiB_2 thin films". *Applied Physics Letters*, Vol. 86, p. 131909, 2005.

[Mayr 06a] P. H. Mayrhofer, C. Mitterer, L. Hultman, and H. Clemens. "Microstructural design of hard coatings". *Progress in Materials Science*, Vol. 51, No. 8, pp. 1032–1114, 2006.

[Mayr 06b] P. H. Mayrhofer, C. Mitterer, J. G. Wen, I. Petrov, and J. E. Greene. “Thermally induced self-hardening of nanocrystalline Ti–B–N thin films”. *Journal of Applied Physics*, Vol. 100, p. 044301, 2006.

[Mayr 06c] P. H. Mayrhofer, D. Music, and J. M. Schneider. “Ab initio calculated binodal and spinodal of cubic TiAlN”. *Applied Physics Letters*, Vol. 88, p. 071922, 2006.

[Mayr 07a] P. H. Mayrhofer, F. D. Fischer, H. J. Böhm, C. Mitterer, and J. M. Schneider. “Energetic balance and kinetics for the decomposition of supersaturated $\mathrm{Ti_{1-x}Al_xN}$”. *Acta Materialia*, Vol. 55, No. 4, pp. 1441–1446, 2007.

[Mayr 07b] P. H. Mayrhofer, D. Music, and J. M. Schneider. “Erratum: Ab initio calculated binodal and spinodal of cubic TiAlN [Appl. Phys. Lett. 88, 071922 (2006)]”. *Applied Physics Letters*, Vol. 90, p. 029902, 2007.

[Maze 97] A. Mazel, P. Marti, F. Henry, B. Armas, R. Bonnet, and M. Loubradou. “Nanostructure and local chemical composition of AlN-Si_3N_4 layers grown by LPCVD”. *Thin Solid Films*, Vol. 304, No. 1-2, pp. 256–266, 1997.

[McGu 73] G. E. McGuire, G. K. Schweitzer, and T. A. Carlson. “Core electron binding energies in some Group IIIA, VB, and VIB compounds”. *Inorganic Chemistry*, Vol. 12, No. 10, pp. 2450–2453, 1973.

[Medj 06] F. Medjani, R. Sanjinés, G. Allidi, and A. Karimi. “Effect of substrate temperature and bias voltage on the crystallite orientation in RF magnetron sputtered AlN thin films”. *Thin Solid Films*, Vol. 515, No. 1, pp. 260–265, 2006.

[Mei 04] F. H. Mei, N. Shao, J. W. Dai, and G. Y. Li. “Coherent growth and superhardness effect of AlN/TiN nanomultilayers”. *Materials Letters*, Vol. 58, No. 27-28, pp. 3477–3480, 2004.

[Mei 05] F. Mei, N. Shao, L. Wei, Y. Dong, and G. Li. “Coherent epitaxial growth and superhardness effects of *c*-TiN/*h*-TiB_2 nanomultilayers”. *Applied Physics Letters*, Vol. 87, p. 011906, 2005.

[Mess 84] R. Messier, A. P. Giri, and R. A. Roy. “Revised structure zone model for thin film physical structure”. *Journal of Vacuum Science & Technology A: Vacuum, Surfaces, and Films*, Vol. 2, No. 2, pp. 500–503, 1984.

[Miao 97] X. S. Miao, Y. C. Chan, and Z. Y. Lee. “Optical Properties and Reactive Sputtering Conditions of AIN and AlSiN Thin Films for Magneto-Optical Applications”. *Journal of Electronic Materials*, Vol. 26, No. 1, pp. 21–24, 1997.

[Mich 99] A. Michels, C. E. Krill, H. Ehrhardt, R. Birringer, and D. T. Wu. “Modelling the influence of grain-size-dependent solute drag on the kinetics of grain growth in nanocrystalline materials”. *Acta Materialia*, Vol. 47, No. 7, pp. 2143–2152, 1999.

[Misk 03] C. R. Miskys, J. A. Garrido, C. E. Nebel, M. Hermann, O. Ambacher, M. Eickhoff, and M. Stutzmann. “AlN/diamond heterojunction diodes”. *Applied Physics Letters*, Vol. 82, pp. 290–292, 2003.

[Monr 06] E. Monroy, J. Zenneck, G. Cherkashinin, O. Ambacher, M. Hermann, M. Stutzmann, and M. Eickhoff. "Luminescence properties of highly Si-doped AlN". *Applied Physics Letters*, Vol. 88, p. 071906, 2006.

[Moon 90] P. M. Mooney. "Deep donor levels (DX centers) in III-V semiconductors". *Journal of Applied Physics*, Vol. 67, No. 3, pp. R1–R26, 1990.

[More 98] G. Moretti. "Auger parameter and Wagner plot in the characterization of chemical states by X-ray photoelectron spectroscopy: a review". *Journal of Electron Spectroscopy and Related Phenomena*, Vol. 95, No. 2-3, pp. 95–144, 1998.

[Mort 04] V. Mortet, M. Nesladek, K. Haenen, A. Moreld, M. D'Olieslaeger, and M. Vanecek. "Physical properties of polycrystalline aluminium nitride films deposited by magnetron sputtering". *Diamond and Related Materials*, Vol. 13, pp. 1120–1124, 2004.

[Musi 00] J. Musil. "Hard and superhard nanocomposite coatings". *Surface and Coatings Technology*, Vol. 125, No. 1-3, pp. 322–330, 2000.

[Musi 01a] J. Musil, H. Hrubỳ, P. Zeman, H. Zeman, R. Čerstvỳ, P. H. Mayrhofer, and C. Mitterer. "Hard and superhard nanocomposite Al–Cu–N films prepared by magnetron sputtering". *Surface & Coatings Technology*, Vol. 142–144, pp. 603–609, 2001.

[Musi 01b] J. Musil, P. Karvánková, and J. Kasl. "Hard and superhard Zr–Ni–N nanocomposite films". *Surface & Coatings Technology*, Vol. 139, No. 1, pp. 101–109, 2001.

[Musi 01c] J. Musil and J. Vlček. "Magnetron sputtering of hard nanocomposite coatings and their properties". *Surface & Coatings Technology*, Vol. 142, pp. 557–566, 2001.

[Musi 02a] J. Musil, F. Kunc, H. Zeman, and H. Poláková. "Relationships between hardness, Young's modulus and elastic recovery in hard nanocomposite coatings". *Surface & Coatings Technology*, Vol. 154, No. 2-3, pp. 304–313, 2002.

[Musi 02b] J. Musil, H. Zeman, and J. Kasl. "Relationship between structure and mechanical properties in hard Al–Si–Cu–N films prepared by magnetron sputtering". *Thin Solid Films*, Vol. 413, No. 1-2, pp. 121–130, 2002.

[Musi 05] J. Musil, P. Baroch, J. Vlček, K. H. Nam, and J. G. Han. "Reactive magnetron sputtering of thin films: present status and trends". *Thin Solid Films*, Vol. 475, No. 1-2, pp. 208–218, 2005.

[Musi 07] J. Musil and P. Zeman. "Hard a-Si_3N_4/MeN_x Nanocomposite Coatings with High Thermal Stability and High Oxidation Resistance". *Solid State Phenomena*, Vol. 127, pp. 31–36, 2007.

[Musi 08a] J. Musil, M. Šašek, P. Zeman, R. Čerstvý, D. Heřman, J. G. Han, and V. Šatava. "Properties of magnetron sputtered AlSiN thin films with a low and high Si content". *Surface & Coatings Technology*, Vol. 202, No. 15, pp. 3485–3493, 2008.

[Musi 08b] J. Musil, J. Vlček, and P. Zeman. "Hard amorphous nanocomposite coatings with oxidation resistance above 1000°C". *Advances in Applied Ceramics*, Vol. 107, No. 3, pp. 148–154, 2008.

[Musi 99] J. Musil, P. Zeman, H. Hrubỳ, and P. H. Mayrhofer. “ZrN/Cu nanocomposite film–a novel superhard material”. *Surface & Coatings Technology*, Vol. 120–121, pp. 179–183, 1999.

[Naka 86] M. Naka, H. Mori, M. Kubo, I. Okamoto, and H. Fujita. “Observation of Al/Si_3N_4 interface”. *Journal of Materials Science Letters*, Vol. 5, pp. 696–698, 1986.

[Nich 66] J. F. Nicholas. “The simplicity of Miller-Bravais indexing”. *Acta Cryst.*, Vol. 21, No. 6, pp. 880–881, 1966.

[Nich 70] J. F. Nicholas. “The indexing of hexagonal crystals”. *physica status solidi (a)*, Vol. 1, No. 3, pp. 563–571, 1970.

[Nied 01] A. Niederhofer, T. Bolom, P. Nesladek, K. Moto, C. Eggs, D. S. Patil, and S. Veprek. “The role of percolation threshold for the control of the hardness and thermal stability of super-and ultrahard nanocomposites”. *Surface & Coatings Technology*, Vol. 146–147, pp. 183–188, 2001.

[Nied 99] A. Niederhofer, P. Nesládek, H. D. Männling, K. Moto, S. Veprek, and M. Jılek. “Structural properties, internal stress and thermal stability of nc-TiN/a-Si_3N_4, nc-TiN/$TiSi_x$ and nc-$(Ti_{1-y}Al_ySi_x)N$ superhard nanocomposite coatings reaching the hardness of diamond”. *Surface & Coatings Technology*, Vol. 120, pp. 173–178, 1999.

[NIST 03] NIST National Institute of Standards and Technology - Gaithersburg. “X-ray Photoelectron Spectroscopy Database”. `http://srdata.nist.gov/xps/`, 2003.

[Nix 98] W. D. Nix and H. Gao. “Indentation size effects in crystalline materials: A law for strain gradient plasticity”. *Journal of the Mechanics and Physics of Solids*, Vol. 46, No. 3, pp. 411–425, 1998.

[Ohri 02] M. Ohring. *Materials science of thin films: deposition and structure.* Academic Press, San Diego, 2nd Ed., 2002. ISBN: 0-12-524975-6.

[Oliv 04] W. C. Oliver and G. M. Pharr. “Measurement of hardness and elastic modulus by instrumented indentation: Advances in understanding and refinements to methodology”. *Journal of Materials Research*, Vol. 19, No. 1, pp. 3–20, 2004.

[Oliv 92] W. C. Oliver and G. M. Pharr. “An improved technique for determining hardness and elastic modulus using load and displacement sensing indentation experiments”. *Journal of Materials Research*, Vol. 7, No. 6, pp. 1564–1583, 1992.

[Otte 65] H. M. Otte and A. G. Crocker. “Crysallographic Formulae for Hexagonal Lattices”. *physica status solidi (b)*, Vol. 9, No. 2, pp. 441–450, 1965.

[Parl 04a] M. Parlinska-Wojtan, A. Karimi, O. Coddet, T. Cselle, and M. Morstein. “Characterization of thermally treated TiAlSiN coatings by TEM and nanoindentation”. *Surface & Coatings Technology*, Vol. 188–189, pp. 344–350, 2004.

[Parl 04b] M. Parlinska-Wojtan, A. Karimi, T. Cselle, and M. Morstein. “Conventional and high resolution TEM investigation of the microstructure of compositionally graded TiAlSiN thin films”. *Surface & Coatings Technology*, Vol. 177–178, pp. 376–381, 2004.

[Pats 01] J. Patscheider, T. Zehnder, and M. Diserens. "Structure–performance relations in nanocomposite coatings". *Surface & Coatings Technology*, Vol. 146–147, pp. 201–208, 2001.

[Pats 03] J. Patscheider. "Nanocomposite hard coatings for wear protection". *MRS bulletin*, Vol. 28, No. 3, pp. 180–183, 2003.

[Pavl 93] F. Pavlyák, I. Bertóti, M. Mohai, I. Biczó, and J. Giber. "AES and XPS characterization of $\mathrm{SiN_x}$ layers". *Surface and Interface Analysis*, Vol. 20, No. 3, pp. 221–227, 1993.

[Pei 05] Y. T. Pei, D. Galvan, and J. T. M. De Hosson. "Nanostructure and properties of TiC/a-C:H composite coatings". *Acta Materialia*, Vol. 53, No. 17, pp. 4505–4521, 2005.

[Peli 07] A. Pélisson, M. Parlinska-Wojtan, H. Hug, and J. Patscheider. "Microstructure and mechanical properties of Al-Si-N transparent hard coatings deposited by magnetron sputtering". *Surface and Coatings Technology*, Vol. 202, No. 4–7, pp. 884–889, 2007.

[Perr 97] R. Perrem, F. Henry, G. Peraudeau, B. Armas, R. Berjoan, and E. Beche. "An XPS and thermogravimetric study of oxidized AlN and AlN-$\mathrm{Si_3N_4}$ layers deposited by liquid-phase chemical vapour deposition". *Journal of Materials Science*, Vol. 32, No. 5, pp. 1305–1312, 1997.

[Petc 53] N. J. Petch. "The cleavage strength of polycrystals". *J. Iron Steel Inst.*, Vol. 174, No. 1, pp. 25–28, 1953.

[Petr 03] I. Petrov, P. B. Barna, L. Hultman, and J. E. Greene. "Microstructural evolution during film growth". *Journal of Vacuum Science & Technology A: Vacuum, Surfaces, and Films*, Vol. 21, p. S117, 2003.

[Powe 95] C. J. Powell. "Elemental binding energies for X-ray photoelectron spectroscopy". *Applied Surface Science*, Vol. 89, No. 2, pp. 141–149, 1995.

[Proc 04] J. Procházka, P. Karvánková, M. G. J. Vepřek-Heijman, and S. Vepřek. "Conditions required for achieving superhardness of $\geq$ 45GPa in nc-TiN/a-$\mathrm{Si_3N_4}$ nanocomposites". *Materials Science & Engineering A*, Vol. 384, No. 1-2, pp. 102–116, 2004.

[Rafa 06] D. Rafaja, A. Poklad, V. Klemm, G. Schreiber, D. Heger, M. Šíma, and M. Dopita. "Some consequences of the partial crystallographic coherence between nanocrystalline domains in Ti–Al–N and Ti–Al–Si–N coatings". *Thin Solid Films*, Vol. 514, No. 1-2, pp. 240–249, 2006.

[Rafa 08] D. Rafaja, C. Wüstefeld, M. Dopita, V. Klemm, D. Heger, G. Schreiber, and M. Šíma. "Formation of defect structures in hard nanocomposites". *Surface & Coatings Technology*, Vol. 203, No. 5-7, pp. 572 – 578, 2008.

[Rare 66] C. R. Rarey, J. Stringer, and J. W. Edington. "Crystallographic Techniques for the Interpretation of Transmission Electron Micrographs of Hexagonal Metals". *Trans. Met. Soc. AIME*, Vol. 236, No. 5, pp. 811–812, 1966.

[Rave 07] A. Raveh, I. Zukerman, R. Shneck, R. Avni, and I. Fried. "Thermal stability of nanostructured superhard coatings: A review". *Surface and Coatings Technology*, Vol. 201, No. 13, pp. 6136–6142, 2007.

[Rein 94] G. Reiners, U. Beck, and H. A. Jehn. “Decorative optical coatings”. *Thin Solid Films*, Vol. 253, No. 1-2, pp. 33–40, 1994.

[Rich 04] B. S. Richards, A. Lambertz, and A. B. Sproul. “Determination of the optical properties of non-uniformly thick non-hydrogenated sputtered silicon thin films on glass”. *Thin Solid Films*, Vol. 460, No. 1-2, pp. 247–255, 2004.

[Rogl 92] P. Rogl and J. C. Schuster. *Phase Diagrams of Ternary Boron Nitride and Silicon Nitride Systems.* ASM Intl, 1992.

[Rose 90] A. Röseler. *Infrared spectroscopic ellipsometry.* Akademie-Verlag Berlin, 1990.

[Rose 99] A. Rosenflanz. “Silicon nitride and sialon ceramics”. *Current Opinion in Solid State & Materials Science*, Vol. 4, No. 5, pp. 453–459, 1999.

[Ross 03] S. M. Rossnagel. “Thin film deposition with physical vapor deposition and related technologies”. *Journal of Vacuum Science & Technology A: Vacuum, Surfaces, and Films*, Vol. 21, No. 5, p. S74, 2003.

[Safi 00] I. Safi. “Recent aspects concerning DC reactive magnetron sputtering of thin films: a review”. *Surface & Coatings Technology*, Vol. 127, No. 2-3, pp. 203–218, 2000.

[Sand 06a] C. S. Sandu, M. Benkahoul, R. Sanjinés, and F. Lévy. “Model for the evolution of Nb–Si–N thin films as a function of Si content relating the nanostructure to electrical and mechanical properties”. *Surface & Coatings Technology*, Vol. 201, No. 6, pp. 2897–2903, 2006.

[Sand 06b] C. S. Sandu, F. Medjani, R. Sanjinés, A. Karimi, and F. Lévy. “Structure, morphology and electrical properties of sputtered Zr–Si–N thin films: From solid solution to nanocomposite”. *Surface & Coatings Technology*, Vol. 201, No. 7, pp. 4219–4223, 2006.

[Sand 06c] C. S. Sandu, R. Sanjinés, M. Benkahoul, F. Medjani, and F. Lévy. “Formation of composite ternary nitride thin films by magnetron sputtering co-deposition”. *Surface & Coatings Technology*, Vol. 201, No. 7, pp. 4083–4089, 2006.

[Sand 07] C. S. Sandu, F. Medjani, and R. Sanjinés. “Optical and electrical properties of sputtered Zr-Si-N thin films: from solid solution to nanocomposite”. *Rev. Adv. Mater. Sci*, Vol. 15, pp. 173–178, 2007.

[Sand 08] C. S. Sandu, R. Sanjinés, and F. Medjani. “Control of morphology (ZrN crystallite size and SiN_x layer thickness) in Zr–Si–N nanocomposite thin films”. *Surface & Coatings Technology*, Vol. 202, No. 11, pp. 2278–2281, 2008.

[Sang 99] H. K. Sanghera and J. L. Sullivan. “Study of Low Energy High Dose Nitrogen Implantation in Aluminium, Iron, Copper and Gold”. *Surf. Interface Anal*, Vol. 27, pp. 678–690, 1999.

[Sanj 05] R. Sanjinés, M. Benkahoul, C. S. Sandu, P. E. Schmid, and F. Lévy. “Relationship between the physical and structural properties of $Nb_zSi_yN_x$ thin films deposited by dc reactive magnetron sputtering”. *Journal of Applied Physics*, Vol. 98, p. 123511, 2005.

[Sanj 06] R. Sanjinés, C. S. Sandu, R. Lamni, and F. Lévy. "Thermal decomposition of $\mathrm{Zr_{1-x}Al_xN}$ thin films deposited by magnetron sputtering". *Surface & Coatings Technology*, Vol. 200, No. 22-23, pp. 6308–6312, 2006.

[Savv 86] N. Savvides and B. Window. "Unbalanced magnetron ion-assisted deposition and property modification of thin films". *Journal of Vacuum Science & Technology A: Vacuum, Surfaces, and Films*, Vol. 4, No. 3, pp. 504–508, 1986.

[Schi 98] J. Schiøtz, F. D. di Tolla, and K. W. Jacobsen. "Softening of nanocrystalline metals at very small grain sizes". *Nature*, Vol. 391, No. 6667, pp. 561–563, 1998.

[Schn 97] M. Schneider, V. A. Gasparov, W. Richter, M. Deckwerth, and C. Russel. "XPS studies on oxynitride glasses in the system Si-Al-O-N". *Journal of non-crystalline solids*, Vol. 215, No. 2-3, pp. 201–207, 1997.

[Schw 05] P. Schwaller, F. J. Haug, J. Michler, and J. Patscheider. "Nanocomposite Hard Coatings: Deposition Issues and Validation of their Mechanical Properties". *Advanced Engineering Materials*, Vol. 7, No. 5, pp. 318–322, 2005.

[Schw 95] D. Schweitzer. Master's thesis, Universität Augsburg, 1995.

[Seto 96] M. Setoyama, A. Nakayama, M. Tanaka, N. Kitagawa, and T. Nomura. "Formation of cubic-AlN in Ti/AlN superlattice". *Surface & coatings technology*, Vol. 86–87, No. 1-3, pp. 225–230, 1996.

[Shen 08] S. H. Sheng, R. F. Zhang, and S. Veprek. "Phase stabilities and thermal decomposition in the $\mathrm{Zr_{1-x}}$ $\mathrm{Al_xN}$ system studied by ab initio calculation and thermodynamic modeling". *Acta Materialia*, Vol. 56, No. 5, pp. 968–976, 2008.

[Shin 92] M. Shinn, L. Hultman, and S. A. Barnett. "Growth, structure, and microhardness of epitaxial TiN/NbN superlattices". *J. Mater. Res*, Vol. 7, No. 4, pp. 901–911, 1992.

[Simu 06] A. Šimůnek and J. Vackář. "Hardness of covalent and ionic crystals: First-principle calculations". *Phys. Rev. Lett.*, Vol. 96, p. 085501, 2006.

[Slat 64] J. C. Slater. "Atomic Radii in Crystals". *The Journal of Chemical Physics*, Vol. 41, No. 10, pp. 3199–3204, 1964.

[Sode 05] H. Söderberg, M. Odén, J. M. Molina-Aldareguia, and L. Hultman. "Nanostructure formation during deposition of $\mathrm{TiN/SiN_x}$ nanomultilayer films by reactive dual magnetron sputtering". *Journal of Applied Physics*, Vol. 97, p. 114327, 2005.

[Sode 06] H. Söderberg, M. Odén, T. Larsson, L. Hultman, and J. Molina-Aldareguia. "Epitaxial stabilization of cubic-$\mathrm{SiN_x}$ in $\mathrm{TiN/SiN_x}$ multilayers". *Applied Physics Letters*, Vol. 88, p. 191902, 2006.

[Sode 07a] H. Söderberg, J. Birch, L. Hultman, and M. Odén. "RHEED studies during growth of $\mathrm{TiN/SiN_x/TiN}$ trilayers on MgO (001)". *Surface Science*, Vol. 601, No. 11, pp. 2352–2356, 2007.

[Sode 07b] H. Söderberg, M. Odén, A. Flink, J. Birch, P. Persson, M. Beckers, and L. Hultman. "Growth and characterization of TiN/SiN (001) superlattice films". *J. Mater. Res*, Vol. 22, No. 11, pp. 3255–3264, 2007.

[Soto 04] G. Soto, W. de la Cruz, and M. H. Farías. “XPS, AES, and EELS characterization of nitrogen-containing thin films”. *Journal of Electron Spectroscopy and Related Phenomena*, Vol. 135, No. 1, pp. 27–39, 2004.

[Spen 01] P. Spencer. “Thermodynamic prediction of metastable coating structures in PVD processes”. *Zeitschrift für Metallkunde*, Vol. 92, No. 10, pp. 1145–1150, 2001.

[Spen 90] P. J. Spencer and H. Holleck. “Application of a thermochemical data bank system to the calculation of metastable phase formation during PVD of carbide, nitride, and boride coatings”. *High Temperature Science*, Vol. 27, pp. 295–309, 1990.

[Spro 05] W. D. Sproul, D. J. Christie, and D. C. Carter. “Control of reactive sputtering processes”. *Thin Solid Films*, Vol. 491, No. 1-2, pp. 1–17, 2005.

[Spro 98] W. D. Sproul. “High-rate reactive DC magnetron sputtering of oxide and nitride superlattice coatings”. *Vacuum*, Vol. 51, No. 4, pp. 641–646, 1998.

[Stam 02] C. Stampfl and C. G. V. de Walle. “Theoretical investigation of native defects, impurities, and complexes in aluminum nitride”. *Physical Review B*, Vol. 65, No. 15, p. 155212, 2002.

[Ston 09] G. G. Stoney. “The Tension of Metallic Films Deposited by Electrolysis”. *Proceedings of the Royal Society of London*, Vol. 82, No. 553, pp. 172–175, 1909.

[Stue 08] M. Stueber, H. Holleck, H. Leiste, K. Seemann, S. Ulrich, and C. Ziebert. “Concepts for the design of advanced nanoscale PVD multilayer protective thin films”. *Journal of Alloys and Compounds*, 2008. Article in press; doi:10.1016/j.jallcom.2008.08.133.

[Sund 86] J. E. Sundgren and H. T. G. Hentzell. “A review of the present state of art in hard coatings grown from the vapor phase”. *Journal of Vacuum Science & Technology A*, Vol. 4, pp. 2259–2279, 1986.

[Swan 83] R. Swanepoel. “Determination of the thickness and optical constants of amorphous silicon”. *Journal of Physics E: Scientific Instruments*, Vol. 16, No. 12, pp. 1214–1222, 1983.

[Swan 84] R. Swanepoel. “Determination of surface roughness and optical constants of inhomogeneous amorphous silicon films”. *Journal of Physics E: Scientific Instruments*, Vol. 17, pp. 896–903, 1984.

[Swif 82] P. Swift. “Adventitious carbon – the panacea for energy referencing?”. *Surface and Interface Analysis*, Vol. 4, No. 2, pp. 47–51, 1982.

[Szlu 05] I. Szlufarska, A. Nakano, and P. Vashishta. “A Crossover in the Mechanical Response of Nanocrystalline Ceramics”. *Science*, Vol. 309, No. 5736, pp. 911–914, 2005.

[Tani 01] Y. Taniyasu, M. Kasu, and N. Kobayashi. “Lattice parameters of wurtzite AlSiN ternary alloys”. *Applied Physics Letters*, Vol. 79, pp. 4351–4353, 2001.

[Tani 02] Y. Taniyasu, M. Kasu, and N. Kobayashi. “Intentional control of n-type conduction for Si-doped AlN and $\mathrm{Al_xGa_{1-x}N}$ ($0.42 \leq x < 1$)”. *Applied Physics Letters*, Vol. 81, No. 7, pp. 1255–1257, 2002.

[Tani 04] Y. Taniyasu, M. Kasu, and T. Makimoto. "Field emission properties of heavily Si-doped AlN in triode-type display structure". *Applied Physics Letters*, Vol. 84, No. 12, pp. 2115–2117, 2004.

[Tani 06a] Y. Taniyasu, M. Kasu, and T. Makimoto. "An aluminium nitride light-emitting diode with a wavelength of 210 nanometres". *Nature*, Vol. 441, No. 7091, pp. 325–328, 2006.

[Tani 06b] Y. Taniyasu, M. Kasu, and T. Makimoto. "Increased electron mobility in n-type Si-doped AlN by reducing dislocation density". *Applied physics letters*, Vol. 89, No. 18, pp. 182112–1–3, 2006.

[Tayl 78a] J. A. Taylor, G. M. Lancaster, A. Ignatiev, and J. W. Rabalais. "Interactions of ion beams with surfaces. Reactions of nitrogen with silicon and its oxides". *The Journal of Chemical Physics*, Vol. 68, p. 1776, 1978.

[Tayl 78b] J. A. Taylor, G. M. Lancaster, and J. W. Rabalais. "Chemical reactions of N_2^+ ion beams with group IV elements and their oxides". *Journal of Electron Spectroscopy and Related Phenomena*, Vol. 13, No. 3, pp. 435–444, 1978.

[Tayl 81a] J. A. Taylor. "Further examination of the Si KLL Auger line in silicon nitride thin films". *Applications of Surface Science*, Vol. 7, pp. 168–184, 1981.

[Tayl 81b] J. A. Taylor and J. W. Rabalais. "Reaction of N_2^+ beams with aluminum surfaces". *The Journal of Chemical Physics*, Vol. 75, No. 4, pp. 1735–1745, 1981.

[Thor 74] J. A. Thornton. "Influence of apparatus geometry and deposition conditions on the structure and topography of thick sputtered coatings". *Journal of Vacuum Science and Technology*, Vol. 11, No. 4, pp. 666–670, 1974.

[Thor 77] J. A. Thornton. "High Rate Thick Film Growth". *Annual Reviews in Materials Science*, Vol. 7, No. 1, pp. 239–260, 1977.

[Tjon 04] S. C. Tjong and H. Chen. "Nanocrystalline materials and coatings". *Materials Science & Engineering R*, Vol. 45, No. 1-2, pp. 1–88, 2004.

[Treu 05] C. P. O. Treutler. "Industrial use of plasma-deposited coatings for components of automotive fuel injection systems". *Surface & Coatings Technology*, Vol. 200, No. 5-6, pp. 1969–1975, 2005.

[Tsub 85] K. Tsubouchi and N. Mikoshiba. "Zero-Temperature-Coefficient SAW Devices on AlN Epitaxial Films". *Sonics and Ultrasonics, IEEE Transactions on*, Vol. SU-32, No. 5, pp. 634–644, 1985.

[Van 02] H. Van Swygenhoven. "Polycrystalline Materials: Grain Boundaries and Dislocations". *Science*, Vol. 296, No. 5565, pp. 66–67, 2002.

[Van 06] H. Van Swygenhoven and J. R. Weertman. "Deformation in nanocrystalline metals". *Materials Today*, Vol. 9, No. 5, pp. 24–31, 2006.

[Venn 06] P. Vennéguès and Z. Bougrioua. "Epitaxial orientation of III-nitrides grown on R-plane sapphire by metal-organic-vapor-phase epitaxy". *Applied Physics Letters*, Vol. 89, p. 111915, 2006.

[Vepr 00] S. Vepřek, A. Niederhofer, K. Moto, T. Bolom, H. Männling, P. Nesladek, G. Dollinger, and A. Bergmaier. "Composition, nanostructure and origin of the ultrahardness in nc-TiN/a-Si_3N_4/a-and nc-$TiSi_2$ nanocomposites with H_v= 80 to $\geq$ 105 GPa". *Surface & Coatings Technology*, Vol. 133–134, pp. 152–159, 2000.

[Vepr 04a] S. Vepřek, H. D. Männling, M. Jilek, and P. Holubar. "Avoiding the high-temperature decomposition and softening of $(Al_{1-x}Ti_x)N$ coatings by the formation of stable superhard nc-$(Al_{1-x}Ti_x)N$/a-Si_3N_4 nanocomposite". *Materials Science and Engineering A*, Vol. 366, pp. 202–205, 2004.

[Vepr 04b] S. Vepřek, H. D. Männling, A. Niederhofer, D. Ma, and S. Mukherjee. "Degradation of superhard nanocomposites by built-in impurities". *Journal of Vacuum Science & Technology B: Microelectronics and Nanometer Structures*, Vol. 22, No. 2, pp. L5–L9, 2004.

[Vepr 05] S. Vepřek, M. G. J. Vepřek-Heijman, P. Karvánková, and J. Procházka. "Different approaches to superhard coatings and nanocomposites". *Thin Solid Films*, Vol. 476, No. 1, pp. 1–29, 2005.

[Vepr 07a] S. Vepřek and M. G. J. Vepřek-Heijman. "The formation and role of interfaces in superhard nc-Me_nN/a-Si_3N_4 nanocomposites". *Surface & Coatings Technology*, Vol. 201, No. 13, pp. 6064–6070, 2007.

[Vepr 07b] S. Vepřek, M. G. J. Vepřek-Heijman, and R. Zhang. "Chemistry, physics and fracture mechanics in search for superhard materials, and the origin of superhardness in nc-TiN/a-Si_3N_4 and related nanocomposites". *Journal of Physics and Chemistry of Solids*, Vol. 68, No. 5-6, pp. 1161 – 1168, 2007. 7th International Conference of Solids State Chemistry 2006 (SSC 2006).

[Vepr 08] S. Vepřek and M. J. G. Vepřek-Heijman. "Industrial applications of superhard nanocomposite coatings". *Surface &Coatings Technology*, Vol. 202, No. 21, pp. 5063–5073, 2008.

[Vepr 81] S. Vepřek, Z. Iqbal, H. R. Oswald, F. A. Sarrot, J. J. Wagner, and A. P. Webb. "Lattice dilatation of small silicon crystallites-implications for amorphous silicon". *Solid State Commun.*, Vol. 39, pp. 509–512, 1981.

[Vepr 87] S. Vepřek, F. A. Sarott, and Z. Iqbal. "Effect of grain boundaries on the Raman spectra, optical absorption, and elastic light scattering in nanometer-sized crystalline silicon". *Physical Review B*, Vol. 36, No. 6, pp. 3344–3350, 1987.

[Vepr 95] S. Vepřek and S. Reiprich. "A concept for the design of novel superhard coatings". *Thin Solid Films*, Vol. 268, No. 1-2, pp. 64–71, 1995.

[Vepr 96] S. Vepřek, M. Haussmann, and S. Reiprich. "Superhard nanocrystalline W_2N/amorphous Si_3N_4 composite materials". *Journal of Vacuum Science & Technology A: Vacuum, Surfaces, and Films*, Vol. 14, No. 1, p. 46, 1996.

[Vepr 99] S. Vepřek. "The search for novel, superhard materials". *Journal of Vacuum Science & Technology A*, Vol. 17, pp. 2401–2420, 1999.

[Voev 97] A. A. Voevodin, S. V. Prasad, and J. S. Zabinski. "Nanocrystalline carbide/amorphous carbon composites". *Journal of Applied Physics*, Vol. 82, No. 2, pp. 855–858, 1997.

[Wagn 82] C. D. Wagner, D. E. Passoja, H. F. Hillery, T. G. Kinisky, H. A. Six, W. T. Jansen, and J. A. Taylor. “Auger and photoelectron line energy relationships in aluminum–oxygen and silicon–oxygen compounds”. *Journal of Vacuum Science and Technology*, Vol. 21, No. 4, pp. 933–944, 1982.

[Wall 04] C. G. V. de Walle and J. Neugebauer. “First-principles calculations for defects and impurities: Applications to III-nitrides”. *Journal of Applied Physics*, Vol. 95, No. 8, pp. 3851–3879, 2004.

[Wang 96] C. M. Wang, X. Pan, M. Rühle, F. L. Riley, and M. Mitomo. “Silicon nitride crystal structure and observations of lattice defects”. *Journal of Materials Science*, Vol. 31, No. 20, pp. 5281–5298, 1996.

[Weit 90] F. Weitzer, K. Remschnig, J. C. Schuster, and P. Rogl. “Phase Equilibria and Structural Chemistry in the Ternary Systems M–Si–N and M–B–N (M= Al, Cu, Zn, Ag, Cd, In, Sn, Sb, Au, Tl, Pb, Bi)”. *Journal of Materials Research*, Vol. 5, No. 10, pp. 2152–2159, 1990.

[Wert 83] G. K. Wertheim, S. B. DiCenzo, and S. E. Youngquist. “Unit Charge on Supported Gold Clusters in Photoemission Final State”. *Phys. Rev. Lett.*, Vol. 51, No. 25, pp. 2310–2313, 1983.

[Wert 88] G. K. Wertheim and S. B. DiCenzo. “Cluster growth and core-electron binding energies in supported metal clusters”. *Phys. Rev. B*, Vol. 37, No. 2, pp. 844–847, 1988.

[Wind 86a] B. Window and N. Savvides. “Charged particle fluxes from planar magnetron sputtering sources”. *Journal of Vacuum Science & Technology A: Vacuum, Surfaces, and Films*, Vol. 4, No. 2, pp. 196–202, 1986.

[Wind 86b] B. Window and N. Savvides. “Unbalanced dc magnetrons as sources of high ion fluxes”. *Journal of Vacuum Science and Technology A: Vacuum, Surfaces, and Films*, Vol. 4, No. 3, pp. 453–456, 1986.

[Wind 92] H. Windischmann. “Intrinsic stress in sputter-deposited thin films”. *Critical Reviews in Solid State and Materials Sciences*, Vol. 17, No. 6, pp. 547–596, 1992.

[Witt 00] M. Witthaut, R. Cremer, and D. Neuschuetz. “Electron spectroscopy of single-phase (Al, B) N films”. *Surface and Interface Analysis*, Vol. 30, No. 1, pp. 580–584, 2000.

[Witt 78] T. N. Wittberg, J. R. Hoenigman, W. E. Moddeman, C. R. Cothern, and M. R. Gulett. “AES and XPS of silicon nitride films of varying refractive indices”. *Journal of Vacuum Science and Technology*, Vol. 15, No. 2, pp. 348–352, 1978.

[Wrie 86] H. Wriedt. “The Al–N(Aluminum–Nitrogen) System”. *Bulletin of Alloy Phase Diagrams*, Vol. 7, No. 4, pp. 329–333, 1986.

[Xu 01] X. H. Xu, H. S. Wu, C. J. Zhang, and Z. H. Jin. “Morphological properties of AlN piezoelectric thin films deposited by DC reactive magnetron sputtering”. *Thin Solid Films*, Vol. 388, No. 1–2, pp. 62–67, 2001.

[Yash 98] P. Yashar, M. R. Pillai, J. Mirecki-Millunchick, and S. A. Barnett. “X-ray diffraction measurement of segregation-induced interface broadening in $\mathrm{In_xGa_{1-x}As/GaAs}$ superlattices”. *Journal of Applied Physics*, Vol. 83, No. 4, pp. 2010–2013, 1998.

[Yash 99] P. C. Yashar and W. D. Sproul. “Nanometer scale multilayered hard coatings”. *Vacuum*, Vol. 55, No. 3-4, pp. 179–190, 1999.

[Zehn 04] T. Zehnder, P. Schwaller, F. Munnik, S. Mikhailov, and J. Patscheider. “Nanostructural and mechanical properties of nanocomposite nc-TiC/aC:H films deposited by reactive unbalanced magnetron sputtering”. *Journal of Applied Physics*, Vol. 95, No. 8, pp. 4327–4334, 2004.

[Zema 04] H. Zeman, J. Musil, and P. Zeman. “Physical and mechanical properties of sputtered Ta–Si–N films with a high ($\geq$ 40 at.%) content of Si”. *Journal of Vacuum Science & Technology A: Vacuum, Surfaces, and Films*, Vol. 22, No. 3, pp. 646–649, 2004.

[Zerr 99] A. Zerr, G. Miehe, G. Serghiou, M. Schwarz, E. Kroke, R. Riedel, H. Fueß, P. Kroll, and R. Boehler. “Synthesis of cubic silicon nitride”. *Nature*, Vol. 400, No. 6742, pp. 340–342, 1999.

[Zhan 03] S. Zhang, D. Sun, Y. Fu, and H. Du. “Recent advances of superhard nanocomposite coatings: a review”. *Surface & Coatings Technology*, Vol. 167, No. 2-3, pp. 113–119, 2003.

[Zhan 04] C. H. Zhang, Z. J. Liu, K. Y. Li, Y. G. Shen, and J. B. Luo. “Microstructure, surface morphology, and mechanical properties of nanocrystalline TiN/amorphous SiN composite films synthesized by ion beam assisted deposition”. *Journal of Applied Physics*, Vol. 95, p. 1460, 2004.

[Zhan 06] Y. Zhang, H. Sun, and C. Chen. “Strain dependent bonding in solid $\mathrm{C_3N_4}$: High elastic moduli but low strength”. *Physical Review B*, Vol. 73, No. 6, p. 64109, 2006.

[Zhan 07a] R. F. Zhang, S. H. Sheng, and S. Veprek. “First principles studies of ideal strength and bonding nature of AlN polymorphs in comparison to TiN”. *Applied Physics Letters*, Vol. 91, p. 031906, 2007.

[Zhan 07b] R. F. Zhang, S. H. Sheng, and S. Veprek. “Mechanical strengths of silicon nitrides studied by ab initio calculations”. *Applied Physics Letters*, Vol. 90, p. 191903, 2007.

[Zhan 07c] R. F. Zhang and S. Veprek. “Crystalline-to-amorphous transition in $\mathrm{Ti_{1-x}Si_xN}$ solid solution and the stability of fcc SiN studied by combined ab initio density functional theory and thermodynamic calculations”. *Physical Review B*, Vol. 76, No. 17, p. 174105, 2007.

[Zhan 07d] R. F. Zhang and S. Veprek. “Metastable phases and spinodal decomposition in $\mathrm{Ti_{1-x}Al_xN}$ system studied by ab initio and thermodynamic modeling, a comparison with the $\mathrm{TiN–Si_3N_4}$ system”. *Materials Science & Engineering A*, Vol. 448, No. 1-2, pp. 111–119, 2007.

[Zhan 07e] R. F. Zhang and S. Veprřek. "Phase stabilities and spinodal decomposition in the $Cr_{1-x}Al_xN$ system studied by ab initio LDA and thermodynamic modeling: Comparison with the $Ti_{1-x}Al_xN$ and TiN/Si_3N_4 systems". *Acta Materialia*, Vol. 55, No. 14, pp. 4615–4624, 2007.

[Zhan 07f] S. Zhang, H. L. Wang, S. E. Ong, D. Sun, and X. L. Bui. "Hard yet Tough Nanocomposite Coatings- Present Status and Future Trends". *Plasma Process and Polymers*, Vol. 4, No. 3, p. 219, 2007.

[Zhan 08a] R. F. Zhang, S. H. Sheng, and S. Veprek. "Stability of TiBN solid solutions and the formation of nc-TiN/a-BN nanocomposites studied by combined ab initio and thermodynamic calculations". *Acta Materialia*, Vol. 56, No. 16, pp. 4440–4449, 2008.

[Zhan 08b] R. F. Zhang and S. Veprřek. "Phase stabilities of self-organized *nc*-TiN/*a*-Si_3N_4 nanocomposites and of $Ti_{1-x}Si_xN_y$ solid solutions studied by ab initio calculation and thermodynamic modeling". *Thin Solid Films*, Vol. 516, No. 8, pp. 2264–2275, 2008.

Curriculum Vitae

Name, surname: Pélisson, Aude
Date and place of birth: July, 3. 1980, Nantua (F)
Nationality: French

Formation:

- **1995 – 1998:** Lycée La Saulaie, Saint-Marcellin
  Baccalauréat Général Scientifique
  France
- **1998 – 2000:** **Preparatory School:**
  CPP (Cycle Préparatoire Polytechnique)
  INPG - Institut National Polytechnique de Grenoble,
  France
- **2000 – 2003:** **Engineering School:**
  ENSPG - École Nationale Supérieure de Physique de Grenoble, INPG,
  (3rd year as Eramus student at Trinity College, Dublin)
  France / Ireland
- **2003 – 2004:** **Master:**
  DESS / Nanotechnologies
  (Diplôme d'Etudes Supérieures Spécialisées),
  Université Claude Bernard - Lyon 1,
  France
- **2005 – 2009:** **Doctorate:**
  Laboratory for Nanoscale Materials Science,
  Empa, Swiss Federal Laboratories for Materials Testing and Research - Dübendorf
  & Philosophisch - Naturwissenschaftliche Fakultät,
  University of Basel,
  Switzerland

List of publications and communications

Publications

"Optically transparent hard coatings", A. Pélisson, F.J. Haug, M. Parlinska - Wojtan, J. Patscheider, *Empa Activity Report 2005*, pp. 8–9.

"PZT Films on Wafers and Fibers for MEMS Applications", R. Thapliyal, A. Pélisson, D. Logvinovich, M. Amberg, H.J. Hug, G. Fortunato, *IEEE international symposium on the application of ferroelectrics* (2006) 1–4.

"Microstructure and mechanical properties of Al-Si-N transparent hard coatings deposited by magnetron sputtering", A. Pélisson, M. Parlinska-Wojtan, H.J. Hug, J. Patscheider, *Surface and Coatings Technology*, **202** (2007) 884–889.

"Structure and Properties of AlN-SiN$_y$ nanoscaled multilayer thin films", A. Pélisson, M. Parlinska-Wojtan, H.J. Hug, J. Patscheider, *Empa Activity Report 2008*, p. 8.

"Charge referencing issues in XPS of insulators as evidenced in the case of Al-Si-N", A. Pélisson, H.J. Hug, J. Patscheider, *manuscript in preparation - to be submitted to Surface and Interface Analysis*, 2009.

"The issue of phase identification in nanostructured coatings of complex composition using photoelectron spectroscopy: the case of Al-Si-N hard coatings.", A. Pélisson, H.J. Hug, J. Patscheider, *manuscript in preparation - to be submitted to Surface and Coatings Technology*, 2009.

Posters

"Optically transparent hard coatings consisting of Al-Si-N", A. Pélisson, F.J. Haug, M. Parlinska, J. Patscheider, H. J. Hug, *Empa PhD Symposium*, October 20th, 2005, Dübendorf (Switzerland).

"Optically transparent hard coatings consisting of Al-Si-N", A. Pélisson, F.J.

Haug, M. Parlinska-Wojtan, J. Patscheider, H. J. Hug, *FOKO C, Empa's international research commission*, May 11th, 2006, Dübendorf (Switzerland).

"Optically transparent coatings of Al-Si-N for Wear Protection", A. Pélisson, M. Parlinska-Wojtan, F.J. Haug, H. J. Hug, J. Patscheider, *Empa PhD Symposium*, October 19th, 2006, St–Gallen (Switzerland).

"Optically transparent coatings of Al-Si-N for Wear Protection", A. Pélisson, M. Parlinska-Wojtan, F.J. Haug, J. Patscheider, *E-MRS Fall meeting*, September 4–8th, 2006, Warsaw (Poland).

Oral communications

"Revêtements durs optiquement transparents à base d'Al-Si-N", A. Pélisson, F.J. Haug, M. Parlinska-Wojtan, J. Patscheider, *Magnétron 2006*, June 7–8th, 2006, Grenoble (France).

"Al-Si-N Transparent Thin Films as Protective Coatings", A. Pélisson, H. J. Hug, J. Patscheider, *Gruppenseminar ESCA group, Universität Basel*, January 23rd, 2007, Basel (Switzerland).

"Al-Si-N Transparent Hard Coatings", A. Pélisson, M. Parlinska-Wojtan, H.J. Hug, J. Patscheider, *SPS (Swiss Physical Society) annual meeting*, February 20th, 2007, Zürich (Switzerland).

"Al-Si-N Transparent Hard Coatings", A. Pélisson, M. Parlinska-Wojtan, H.J. Hug, J. Patscheider, *ICMCTF (The International Conference on Metallurgical Coatings and Thin films)*, April 22–27th, 2007, San Diego (USA).

"Al-Si-N Transparent Hard Coatings", A. Pélisson, M. Parlinska-Wojtan, H.J. Hug, J. Patscheider, *E-MRS spring meeting*, Mai 28th–June 1st, 2007, Strasbourg (France).

"Synthesis and characterization of Al-Si-N transparent hard coatings", A. Pélisson, M. Parlinska-Wojtan, H. J. Hug, J. Patscheider, *Empa PhD Symposium*, November 21th, 2007, Dübendorf (Switzerland).

"Structural, mechanical and electronic properties of AlSiN hard coatings", A. Pélisson, M. Parlinska-Wojtan, H.J. Hug, J. Patscheider, *ICMCTF (The International Conference on Metallurgical Coatings and Thin films)*, April 26th–Mai 2nd, 2008, San Diego (USA).

"Al-Si-N Nanocomposite Transparent Hard Coatings", A. Pélisson, M. Parlinska-Wojtan, H.J. Hug, J. Patscheider, *FOKO C, Empa's international research commission*, June 12th, 2008, Dübendorf (Switzerland).

Acknowledgments

My PhD years draw to a close. Looking back in time, these were somehow tough but altogether very happy and enriching years. I really enjoyed being part of such an international and multidisciplinary lab. My thanks come therefore first to all my past and present fellow workers of the Laboratory for Nanoscale Materials Science at Empa: I had a great time with you all!

In particular, I would like to thank Prof. Hans Josef Hug for being my PhD supervisor and getting interested in the field of nanostructured hard coatings. Your enthusiasm, your eagerness to understand and your broader "physical" approach of the subject were always much helpful to me. Thanks for the many questions and for all our lively scientific discussions, especially towards the end of this thesis: it made me enjoy science and research, and it gave me a deeper insight into physics. I am deeply indebt to you for your commitment in my work.

I am also very grateful to Dr. Jörg Patscheider, my direct advisor and head of the Nanostructured Coatings group. Thanks for giving me the opportunity to work in your team, for your trust and for the freedom you gave me in my work. Thanks for being always available for these thousands of questions I had when playing around with the deposition machine or with my beloved X-ray diffractometer. Thanks also for giving me the opportunity to present my work at so many international conferences (and for helping me in preparing my written and oral contributions). This was just essential!

Thanks also to Prof. Peter Oelhafen for kindly accepting to be a referee on my thesis, and to Prof. Jochen Schneider, who accepted to sit as an external expert in my thesis jury.

This work would not have been possible without the scientific and technical support of many people on all the equipments I used to deposit and

characterize my samples, including: Dr. Jörg Patscheider for the deposition machine and the X-rays, Dr. Roland Hauert and Dr. Ulrich Müller for the XPS, Dr. Patrick Schwaller for the nanoindentation (Empa, Thun), Dr. Magdalena Parlinska-Wojtan and Dr. Myriam Aguirre for the TEM, Michael Stiefel for the SEM, Dr. Olga Guseva for the mechanical profilometry, Dr. Fernando Araujo de Castro and Dr. Thomas Geiger for the optical transmission measurements at Empa, Dr. Iris Mack for the optical transmission and spectroscopic ellipsometry measurements at the university of Basel. Special thanks to Günther Hobi for the overall technical support. What would it be without you... Special thanks also to Magdalena, for your patience and skills in TEM sample preparation and TEM imaging. You made wonders out of our CM30!

Thanks to Dr. Carlo Pignedoli and Dr. Daniele Passerone (Empa) for our fruitful scientific discussions and the simulation work performed on Si-doped AlN. Thanks also to Dr. Denis Music and Prof. Jochen Schneider (RWTH Aachen) for the on-going collaboration on the AlN/SiN$_y$ interface system.

Thanks to Lorenzo, for your "Italian touch", your good mood and our scientific discussions. Your daily presence was essential to me. All the best to Dominik, my successor as a PhD student in the Nanostructured Coatings group. It was great working with you over this last year.

Special thoughts to my fellow PhD (or ex-PhD) colleagues, especially Quang, Sébastien, Hervé, Rosa, Laura, Liliana and Vinzenz. For our scientific and non-scientific interactions, thanks also to Magda, Raphaelle, Peter, Sara, Miguel, Tobias, Andrew, Leo, Pablo, Claudiu, Karl... and the complete "125" team.

I am deeply indebt to Jörg, Hans, Dominik and Olivier for the detailed and constructive corrections of the present dissertation manuscript.

Finally, I would like to express my gratitude and my love to my parents, who always encouraged me to go on with my studies. They also gave me the opportunity to go abroad and become "European", even if it means I live now far away from them. My lasts thanks go to my beloved Olivier, for his love, his encouragements, and for bearing me during these last few years, months, weeks and days...

March 22th, 2009, Dübendorf